Quantum magnetism in three dimensions

Exploring phase diagrams and real materials using Functional Renormalization

Dissertation zur Erlangung des

naturwissenschaftlichen Doktorgrades

der Julius-Maximilians-Universität Würzburg

vorgelegt von

Tobias Leo Christian Müller

aus Würzburg

Würzburg 2022

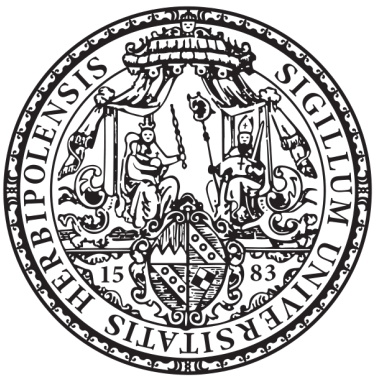

Eingereicht am 09. Mai 2022
bei der Fakultät für Physik und Astronomie

1. Gutachter: Prof. Dr. Ronny Thomale
2. Gutachter: Prof. Dr. Giorgio Sangiovanni
3. Gutachter: Prof. Dr. Jan von Delft
der Dissertation

Vorsitzende(r): Prof. Dr. Werner Porod

1. Prüfer: Prof. Dr. Ronny Thomale
2. Prüfer: Prof. Dr. Giorgio Sangiovanni
3. Prüfer: Prof. Dr. Vladimir Hinkov
4. Prüfer: Prof. Dr. Jan von Delft
im Promotionskolloquium

Tag des Promotionskolloquiums: 07. Oktober 2022

Dedicated to Leni, Jorik, and the one to be.

"*Fascinating.*"
Mr. Spock

Abstract

Magnetism is a phenomenon ubiquitously found in everyday life. Yet, together with superconductivity and superfluidity, it is among the few macroscopically realized quantum states. Although well-understood on a quasi-classical level, its microscopic description is still far from being solved. The interplay of strong interactions present in magnetic condensed-matter systems and the non-trivial commutator structure governing the underlying spin algebra prevents most conventional approaches in solid-state theory to be applied.

On the other hand, the quantum limit of magnetic systems is fertile land for the development of exotic phases of matter called spin-liquids. In these states, quantum fluctuations inhibit the formation of magnetic long-range order down to the lowest temperatures. From a theoretical point of view, spin-liquids open up the possibility to study their exotic properties, such as fractionalized excitations and emergent gauge fields. However, despite huge theoretical and experimental efforts, no material realizing spin-liquid properties has been unambiguously identified with a three-dimensional crystal structure. The search for such a realization is hindered by the inherent difficulty even for model calculations. As most numerical techniques are not applicable due to the interaction structure and dimensionality of these systems, a methodological gap has to be filled.

In this thesis, to fill this void, we employ the pseudo-fermion functional renormalization group (PFFRG), which provides a scheme to investigate ground state properties of quantum magnetic systems even in three spatial dimensions. We report the status quo of this established method and extend it by alleviating some of its inherent approximations. To this end, we develop a multi-loop formulation of PFFRG, including hitherto neglected terms in the underlying flow equations consistently, rendering the outcome equivalent to a parquet approximation. As a necessary prerequisite, we also significantly improve the numerical accuracy of our implementation of the method by switching to a formulation respecting the asymptotic behavior of the vertex functions as well as employing state-of-the-art numerical algorithms tailored towards PFFRG. The resulting codebase was made publicly accessible in the open-source code `PFFRGSolver.jl`.

We subsequently apply the technique to both model systems and real materials. Augmented by a classical analysis of the respective models, we scan the phase diagram of the three-dimensional body-centered cubic lattice up to third-nearest neighbor coupling and the Pyrochlore lattice up to second-nearest neighbor. In both systems, we uncover in addition to the classically ordered phases, an extended parameter regime, where a quantum paramagnetic phase appears, giving rise to the possibility of a quantum spin liquid.

Additionally, we also use the nearest-neighbor antiferromagnet on the Pyrochlore lattice as well as the simple cubic lattice with first- and third-nearest neighbor couplings as a testbed for multi-loop PFFRG, demonstrating, that the inclusion of higher loop orders has quantitative effects in paramagnetic regimes and that the onset of order can be signaled by a lack of loop convergence.

Turning towards material realizations, we investigate the diamond lattice compound $MnSc_2S_4$, explaining on grounds of *ab initio* couplings the emergence of a spiral spin liquid at low temperatures, but above the ordering transition. In the Pyrochlore compound $Lu_2Mo_2O_5N_2$, which is known to not magnetically order down to lowest temperatures, we predict a spin liquid state displaying a characteristic gearwheel pattern in the spin structure factor.

Zusammenfassung

Das Phänomen des Magnetismus ist allgegenwärtig im täglichen Leben und doch ist es, zusammen mit der Supraleitung und -fluidität, eines der wenigen makroskopisch realisierten Quantenphänomene. Auf quasi-klassischer Ebene ist Magnetismus gut verstanden, doch seine mikroskopische Beschreibung ist noch weit davon entfernt, als gelöst bezeichnet zu werden. Das Zusammenspiel von starken Wechselwirkungen, die in magnetischer kondensierte Materie am Werke sind, und der nicht-trivialen Kommutatorstruktur, die die zugrunde liegende Spin-Algebra bestimmt, verhindert, dass konventionelle Herangehensweisen der Festkörpertheorie angewendet werden können.

Andererseits ist der quantenmechanische Grenzfall magnetischer Systeme ein fruchtbarer Boden für die Herausbildung exotischer Phasen der Materie, die als Spin-Flüssigkeiten bezeichnet werden. In diesen Zuständen verhindern Quantenfluktuationen die Ausbildung einer langreichweitigen magnetischen Ordnung auch bei niedrigsten Temperaturen. Aus theoretischer Sicht eröffnen Spinflüssigkeiten die Möglichkeit, exotische Eigenschaften, wie fraktionalisierte Anregungen und emergente Eichfelder, zu studieren. Großen theoretischen und experimentellen Anstrengungen zum Trotz wurde jedoch bisher kein Material mit dreidimensionaler Kristallstruktur identifiziert, das unzweifelhaft die Eigenschaften von Spinflüssigkeiten aufweist. Die Suche nach einer solchen Realisierung wird von der Komplexität behindert, die sogar einfachen Modellrechnungen inhärent ist. Da die meisten numerischen Verfahren aufgrund der Wechselwirkungsstruktur und Dimensionalität der Systeme nicht anwendbar sind, bleibt eine methodische Lücke bestehen.

In dieser Arbeit benutzen wir die pseudo-fermionische funktionale Renormierungsgruppe (PFFRG), um diese zu füllen. Mit ihr realisieren wir ein Verfahren, um die Grundzustandseigenschaften von quantenmagnetischen Systemen in drei Raumdimensionen zu studieren,

Wir fassen den Status quo dieser bereits etablierten Methode zusammen und erweitern sie, indem wir einige ihrer inhärenten Näherungen abmildern. Dafür entwickeln wir eine Mehrschleifen-Formulierung der PFFRG, die bisher vernachlässigte Terme der zugrunde liegenden Flussgleichungen konsistent berücksichtigt und damit die PFFRG äquivalent zur Parquet-Näherung macht. Um dies zu erreichen, verbessern wir außerdem die numerische Genauigkeit der Methode signifikant, indem wir einerseits zu einer Formulierung wechseln, welche die Asymptotiken der Vertex-Funktionen explizit berücksichtigt und andererseits moderne Algorithmen, maßgeschneidert für die PFFRG, nutzt. Der daraus resultierenden Computercode wurde im Open-Source Paket `PFFRGSolver.jl` öffentlich zugänglich gemacht.

Im Anschluss wenden wir die Methode sowohl auf Modellsysteme, als auch echte Materialien an. Vor dem Hintergrund klassischer Analysen scannen wir die Phasendiagramme des dreidimensionalen raumzentrierten kubischen und des Pyrochlorgitters, wobei wir Wechselwirkungen bis zu drittnächsten beziehungsweise übernächsten Nachbarn berücksichtigen. In beiden Systemen finden wir, neben den klassisch geordneten Phasen, einen ausgedehnten Parameterraum, in dem eine quantenparamagnetische Phase im Phasendiagramm erscheint, welche die Möglichkeit einer Quantenspinflüssigkeitsphase eröffnet. Wir nutzen außerdem den Nächstnachbarantiferromagnet auf dem Py-

rochlorgitter und das kubische Gitter mit Nächst- und Drittnächstnachbarwechselwirkung als einen Prüfstand für die Vielschleifen-PFFRG, indem wir zeigen, dass die Berücksichtigung höherer Schleifenordnungen quantitative Auswirkungen in den paramagnetischen Regimen hat und außerdem magnetische Ordnung durch ein Fehlen der Schleifenkonvergenz signalisiert werden kann.

Abschließend wenden wir uns den echten Materialien zu und untersuchen $MnSc_2S_4$, welches eine Diamantgitterstruktur aufweist. Basierend auf *ab intio* Kopplungsstärken erklären wir das Auftreten einer Spiralspinflüssigkeit bei niedrigen Temperaturen, aber oberhalb des Ordnungsübergangs. Zudem sagen wir im Pyrochlormaterial $Lu_2Mo_2O_5N_2$, welches in Experimenten auch bei niedrigsten Temperaturen nicht magnetisch ordnet, einen Spinflüssigkeitszustand voraus, der sich durch ein charakteristisches Zahnradmuster im Spinstrukturfaktor auszeichnet.

Table of contents

Abstract v

Zusammenfassung vii

1 Introduction 1

I Classical Spins 9

2 Classical spin systems 11
2.1 The $S \to \infty$ limit . . . 11
2.2 Classical Heisenberg Hamiltonian and its ground state . . . 12

3 The Luttinger-Tisza method 13
3.1 From strong to weak constraint . . . 13
3.2 Exact cases: Bravais lattices and beyond . . . 15
3.2.1 Bravais lattices . . . 16
3.2.2 Two equivalent basis points . . . 16
3.3 General remarks . . . 17
3.3.1 Superposition of spiral states . . . 17
3.3.2 Non-coplanar spin states . . . 17
3.3.3 Connection to O($N \to \infty$) . . . 18

4 Iterative minimization 21
4.1 Constrained steepest descent . . . 21
4.2 Analysis tools . . . 22
4.2.1 Spin structure factor . . . 22
4.2.2 Real space diagnostics . . . 22
4.2.3 Competitive minimization . . . 22

II Pseudo-Fermion Functional Renormalization Group 25

5 Abrikosov Pseudo-Fermions 27
5.1 Operator mapping . . . 27
5.2 Gauge symmetry of the mapping . . . 28
5.3 Gauge symmetry of the pseudo-fermion Heisenberg Hamiltonian and Lagrangian . . . 29
5.4 Symmetries of pseudo-fermion Green's functions . . . 29
5.4.1 Time-translation invariance . . . 30
5.4.2 Time-reversal invariance . . . 30
5.4.3 Hermiticity of the Hamiltonian . . . 31
5.4.4 Lattice symmetries . . . 32
5.4.5 Crossing symmetries . . . 32
5.4.6 Local U(1) gauge symmetry . . . 32
5.4.7 Local particle-hole symmetry . . . 34
5.4.8 Summary of the symmetries . . . 34
5.5 Gauge-invariance of the pseudo-fermion Lagrangian . . . 35

6 Functional renormalization group 37
6.1 General setup . . . 37
6.2 Generating functionals . . . 38
6.3 Connecting different Green's and vertex functions . . . 41
6.3.1 From full to connected Green's functions . . . 41
6.3.2 Tree expansion . . . 41
6.4 Flow-equations . . . 43
6.4.1 Flow of the generating functionals for Green's functions . . . 44
6.4.2 Flow of the effective interaction . . . 45
6.4.3 Vertex function flow . . . 46
6.5 Truncation of the flow . . . 48
6.6 Initial conditions . . . 48

7 Pseudo-Fermion Functional renormalization group 51
7.1 Symmetry constrained parametrization of the self-energy . . . 51
7.2 Spin and real-space dependence of the two-particle vertex . . . 53
7.3 Multi-local flow equations . . . 54
7.4 Conventional frequency parametrization . . . 55
7.4.1 Parametrization of the two-particle vertex . . . 55
7.4.2 Parametrized flow equations . . . 57
7.5 Asymptotic frequency parametrization . . . 58
7.6 Choice of regulator . . . 61
7.6.1 Step regulator . . . 61
7.6.2 Smoothened frequency cutoff . . . 62
7.7 Susceptibilities . . . 63
7.8 Initial conditions . . . 64
7.9 Single occupation constraint . . . 65

7.10 Exact limits . . . 66
7.10.1 Large-S limit . . . 66
7.10.2 Large-N limit . . . 69

8 Multi-Loop extension to PFFRG 71
8.1 Katanin truncation as partial two-loop . . . 72
8.2 Derivation of Multi-loop corrections from general flow-equations . . . 73
8.2.1 Loop structure, cutting lines and reducibility . . . 73
8.2.2 Diagrammatic content of the two-particle vertex in Katanin-truncation . . . 74
8.2.3 Multi-loop flow of the two-particle vertex . . . 75
8.2.4 Multi-loop flow of the self-energy . . . 78
8.3 Peculiarities of PFFRG . . . 79

9 Numerical implementation of PFFRG 81
9.1 Lattice symmetries . . . 81
9.2 Frequency discretization . . . 82
9.2.1 Frequency discretization in the conventional implementation . . . 83
9.2.2 Frequency discretization in the improved implementation . . . 83
9.3 Frequency integration . . . 85
9.4 Differential equation solver . . . 85
9.5 Initial conditions . . . 86
9.6 Run-time scaling . . . 86

III Phase-diagrams of frustrated three-dimensional lattices 89

10 Body-Centered Cubic Lattice up to third-nearest-neighbor interactions 91
10.1 Classical Phase diagram . . . 91
10.1.1 Ferromagnetic J_1 . . . 92
10.1.2 Antiferromagnetic J_1 . . . 97
10.2 Quantum Phase diagram . . . 98
10.3 Nèel and Curie temperatures . . . 101

11 J_1-J_2 Heisenberg model on the Pyrochlore lattice 105
11.1 Classical phase diagram . . . 106
11.2 Quantum Phase Diagram . . . 111
11.3 Nearest-neighbor antiferromagnet in multi-loop . . . 117

12 J_1-J_3 Heisenberg model on the simple cubic lattice in multi-loop 121

IV Magnetic ordering and its absence in real material systems 125

13 Spiral spin liquid in $MnSc_2S_4$ 127
13.1 Model and classical analysis . . . 128

13.2 PFFRG results . . . 129
13.3 Further considerations . . . 132

14 Gearwheel spin liquid in $Lu_2Mo_2O_5N_2$ 137
14.1 Classical limit . . . 138
14.2 Quantum ground state . . . 140

15 Conclusion 141

V Appendices 145

A Flow equations in conventional parametrization 147
A.1 Selfenergy flow . . . 147
A.2 Spin vertex flow . . . 147
A.2.1 s-channel . . . 147
A.2.2 t-channel . . . 148
A.2.3 u-channel . . . 148
A.3 Density vertex flow . . . 149
A.3.1 s-channel . . . 149
A.3.2 t-channel . . . 149
A.3.3 u-channel . . . 150
A.4 Susceptibility . . . 150

B Flow equations in asymptotic parametrization 151
B.1 Selfenergy flow . . . 151
B.2 Spinvertex Flow . . . 152
B.2.1 s-channel . . . 152
B.2.2 t-channel . . . 152
B.2.3 u-channel . . . 154
B.3 Densityvertex Flow . . . 155
B.3.1 s-channel . . . 155
B.3.2 t-channel . . . 155
B.3.3 u-channel . . . 157
B.4 Susceptibility . . . 157

C Collection of real space lattices 159
C.1 Two-dimensional lattices . . . 159
C.1.1 Square lattice . . . 159
C.1.2 Triangular lattice . . . 159
C.1.3 Honeycomb lattice . . . 160
C.1.4 Kagome lattice . . . 160
C.2 Three-dimensional lattices . . . 160
C.2.1 Simple cubic lattice . . . 160

C.2.2 Body-centered cubic lattice . . . 161
C.2.3 Face-centered cubic lattice . . . 161
C.2.4 Diamond lattice . . . 161
C.2.5 Pyrochlore lattice . . . 162

D Exact integration of interpolating functions **163**

E Truncated unity in frequency space **165**
E.1 Spectral decomposition of functions . . . 165
E.2 Expansion of the flow equations . . . 166
E.3 Rotation between frequency parametrizations . . . 167
E.4 Numerical considerations . . . 168

Bibliography **171**

List of acronyms **185**

Acknowledgements **187**

CHAPTER 1

Introduction

Magnetic materials are ubiquitous in everyday life: from the humble fridge magnet through electric motors relying on strong ferromagnets for their basic functionality to hard drives in computers, where information is saved magnetically. Historically, magnetized lodestones have already been known 2500 years ago in both ancient Greece and China, where also their alignment with the earth's magnetic field was discovered, consequently leading to the development of the compass [1, 2].

In the following centuries, the notion of magnetic poles and their attraction and repulsion was formed, but a deeper theoretical understanding of magnetism even on a classical level was lacking till the 19th century, at the beginning of which Coulomb formulated the $1/r^2$ dependence of the interaction forces not only between electrical charges but also magnetic poles. In 1820, Hans-Christian Oersted laid the foundations of a unified theory of electromagnetism by discovering that currents create magnetic fields. Only one year later, Michael Faraday discovered induction as the complementary effect. All this culminated in the formulation of the fundamental equations of electrodynamics by James Clerk Maxwell in 1864, which, together with the Lorentz force acting on charges in electric and magnetic fields constitute the foundation of all classical understanding of magnetism is built on [1, 2].

Despite these efforts, the existence of (ferro-)magnetic materials remained an open question. Although the mean-field theory by Pierre Weiss offered an explanation for the thermodynamic properties of magnets in terms of magnetic domains [3], the microscopic origin of the magnetization could not be explained by classical notions, like circular currents, which would have to be in the order of gigaamperes in strength to explain the static magnetic fields known at the time.

Magnetism is not classical

This lack of a classical model turned out to be a fundamental one, as magnetism, like superconductivity and superfluidity, is one of the few macroscopic behaviors rooted in quantum effects. According to the *Bohr-van Leuwen theorem*, which was discovered very early in the development of quantum mechanics, a purely classical system cannot exhibit a finite thermal expectation value of the magnetization [4].

The proof of this theorem starts from system of N particles, which we couple to a magnetic field $\boldsymbol{B} = \boldsymbol{\nabla} \times \boldsymbol{A}$ derived from the corresponding vector potential $\boldsymbol{A}$. The magnetization of this system is given by

$$\langle \boldsymbol{M} \rangle = \frac{\partial F}{\partial \boldsymbol{B}}, \tag{1.1}$$

where $F = -\beta \ln Z$ is the free energy, which can be obtained from the canonical partition sum Z at inverse temperature β. The classical Hamiltonian $H(\boldsymbol{q}_i, \boldsymbol{p}_i)$ in terms of generalized coordinates $\boldsymbol{q}_i$ and corresponding

generalized momenta $\boldsymbol{p}_i$ can be coupled to the vector potential by means of the minimal substitution $\boldsymbol{p}_i \to \boldsymbol{p}_i - q_i \boldsymbol{A}_i$. Therefore, the partition sum of such a system can then be written as

$$Z = C(N) \prod_i \int \mathrm{d}\boldsymbol{p}_i \int \mathrm{d}\boldsymbol{q}_i \mathrm{e}^{-\beta H(\boldsymbol{q}_i, \boldsymbol{p}_i - q_i \boldsymbol{A}_i)} \tag{1.2}$$

with a suitable normalization constant $C(N)$. Clearly, as the momentum integration is carried out over all momenta, a shift $\boldsymbol{p}_i \to \boldsymbol{p}_i' = \boldsymbol{p}_i + q_i \boldsymbol{A}_i$ of the individual momenta leaves the partition sum invariant, but removes the dependence on the vector potential, i.e. the magnetic field, completely. Consequently, the magnetization in eq. (1.1) will vanish.

Quantum mechanics changes this conclusion in a very substantial way: As the phase space integration in eq. (1.2) is replaced by a trace over the Hilbert space of the system, a simple shift of variables is no longer possible, leaving room for finite magnetization even in the thermodynamic limit.

Why quantum magnetism is non-trivial

Having established, that magnetism necessitates a quantum mechanical treatment, we can readily see, that the non-commutativity of operators has a non-trivial impact on the analysis of magnetic systems.

As in classical mechanics, quantum magnetic moments are connected to a charge possessing some angular momentum. In the vast majority of cases, and in particular ones we consider in this thesis, these are electrons with their intrinsic quantized spin $S = 1/2$. Let us recall the quantum mechanical angular momentum operator $\hat{\boldsymbol{S}}$ and the corresponding commutation relations[1]

$$\left[\hat{S}^\alpha, \hat{S}^\beta\right] = \mathrm{i} \sum_{\gamma=1}^{3} \epsilon_{\alpha\beta\gamma} \hat{S}^\gamma \,, \tag{1.3}$$

where $\hat{S}^\alpha$ is the α-component of the vector operator $\hat{\boldsymbol{S}}$, as well as the ladder operators for the $\hat{S}^z$ eigenvalue of an eigenstate

$$\hat{S}^\pm = \hat{S}^x \pm i\hat{S}^y. \tag{1.4}$$

The simplest form of interaction between stationary magnetic moments proportional to these operators is given by the Heisenberg Hamiltonian

$$\hat{H}_\mathrm{H} = \sum_{i<j} J_{ij} \hat{\boldsymbol{S}}_i \cdot \hat{\boldsymbol{S}}_j, \tag{1.5}$$

with couplings J_{ij}. The sum is defined to run over each pair i, j exactly once. We will discuss the emergence of this Hamiltonian from purely fermionic systems shortly but will focus on the physics encoded in it first.

Considering eq. (1.5) for a one-dimensional (1D) spin-1/2 chain with purely nearest neighbor (NN) interactions, i.e. $J_{ij} = J$ for nearest neighbors and vanishing elsewhere, we can distinguish two cases.

Viewing for a moment the spin operators as classical vectors, clearly, a ferromagnetic (FM) configuration with all spins pointing to the same direction will be the ground state of this Hamiltonian for $J < 0$. This classical view[2] also holds true when restoring the operator nature of the spins. Rewriting the Heisenberg Hamiltonian in terms of ladder operators,

$$\hat{H}_\mathrm{H} = J \sum_{\langle i,j \rangle} \left(\frac{1}{2} \left(\hat{S}_i^+ \hat{S}_j^- + \hat{S}_i^- \hat{S}_j^+ \right) + \hat{S}_i^z \hat{S}_j^z \right), \tag{1.6}$$

[1] Throughout this thesis, we will use units in which $\hbar = 1$.
[2] We will show in Section 2.1, that this picture is indeed the classical limit of a spin system.

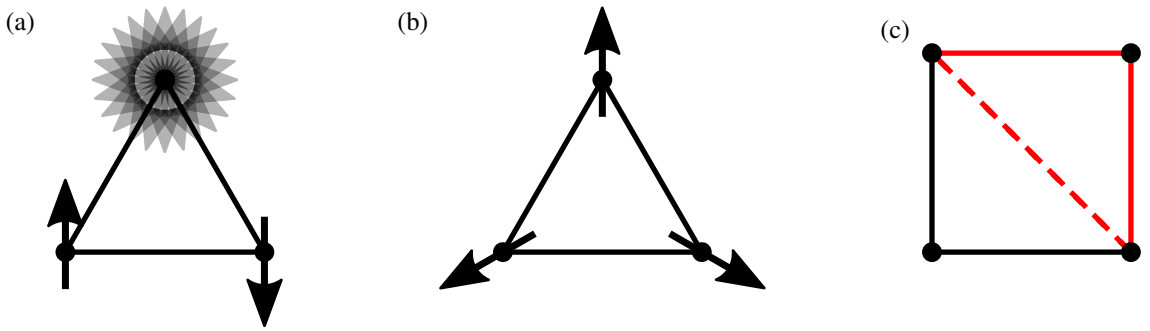

Figure 1.1: Illustration of frustration: (a) In an antiferromagnetically coupled triangle with two antiparallely aligned spins, the third spin cannot optimize its energy, it is frustrated. (b) Classically, this is solved by assuming a 120° order. (c) In a square lattice including next-nearest neighbor interactions (dashed), triangles are formed (red), which are frustrated for antiferromagnetic interactions, which are an example for geometric frustration.

using $\langle i, j \rangle$ to denote the sum over nearest neighbors, helps to establish the energy eigenvalue of the FM state of N spins, which we choose without loss of generality to be $|\uparrow\uparrow\uparrow\uparrow \ldots\rangle$, to be

$$\hat{H}_H \, |\uparrow\uparrow\uparrow\uparrow \ldots\rangle = N\frac{J}{4} \, |\uparrow\uparrow\uparrow \ldots\rangle \, , \tag{1.7}$$

as the ladder operator terms in eq. (1.6) vanish due to $\hat{S}^+$ annihilating the FM state.

Flipping the sign of J, classically an antiparallel configuration of neighboring spins, called Néel state, will minimize the energy. Analogous to the FM case, one would expect this ground state to carry over to the quantum model as well, however, the ladder operator contributions prevent the Néel state from being the exact ground state of eq. (1.6).

For illustration purposes, we consider the action of the combination of one raising and one lowering operator for the first two sites in the chain on the Néel state,

$$\hat{S}_1^- \hat{S}_2^+ \, |\uparrow\downarrow\uparrow\downarrow \ldots\rangle = |\downarrow\uparrow\uparrow\downarrow \ldots\rangle \, , \tag{1.8}$$

which yields a state orthogonal to the original Néel one. This means, that the ground state of the antiferromagnetic (AF) chain has to be a superposition of spin configurations, i.e. a highly entangled state, which has no classical analog.

These results generalize to higher dimensions, meaning, that conceptually FM and AF interactions have very different implications in a quantum model. While for the former, the classical intuition of a FM order still is valid, the latter opens up the possibility for quantum effects to severely change physics compared to a classical model, purely due to the non-commutativity of spin operators, here encoded in the existence of ladder operators. In the most extreme cases, quantum fluctuations can even destroy classical orders, leading to a more exotic state of matter with no classical analog.

Frustration as a path to destroy order

Quantum effects alone, however, will in most cases not lead to the absence of magnetic long-range order. The second main ingredient to achieve such a state is known as *frustration*, which describes the situation, where not all interactions in a system can be fulfilled simultaneously. To illustrate this, consider three spins arranged in a triangle, coupled AF to each other, as illustrated in Figure 1.1(a). Orienting the first spin, without loss of generality, upwards, the second spin will point downwards. The third spin would have to point downwards as well, to minimize its interaction with

the first one, but upwards to be antiparallel to the second. The interaction is frustrated. The classical (and in this case also quantum mechanical) solution to this specific problem is for the spins to assume an angle of 120° with respect to each other, as shown in Figure 1.1(b).

As this frustration is only determined by the underlying geometry of the spin arrangement, it is called *geometric frustration*, in contrast to *parametric frustration* induced by the interplay between different interactions. This is for example the case for NN and next-to-nearest neighbor (NNN) AF interactions on the square lattice, which form again a triangle, cf. Figure 1.1(c).

Quantum spin liquids

The interplay of quantum fluctuations and frustration can lead to the emergence of spin states, which lack the magnetic long-range order generically found in classical spin models. Prime examples are the valence-bond solids, realized as exact ground states in the two-dimensional (2D) Shastry-Sutherland model [5] and very recently on the Maple-Leaf lattice [6]. Here spins pair up with one of their neighbors to form spin singlets, thereby optimizing the energy along the bond connecting the pair, while nullifying the contributions from all other bonds. The localization of the singlets, however, relies on the peculiar structure of the lattice models, which favors the potential energy gain over one in kinetic energy.

Even before the discovery of the exact valence-bond solids, Anderson proposed the resonating valence bond (RVB) state [7, 8], which takes into account this peculiar interplay. Instead of selecting a unique singlet covering of a lattice, the RVB is constructed as a superposition of all coverings, allowing for an energy gain by fluctuations between the different coverings. Although originally proposed as a ground state for the triangular NNAF, which however is now established to host an ordered state [9], it is believed to be closely connected to the notion of high-T_C superconductivity in cuprate materials [10]. As this state breaks (in contrast to the valence-bond solid) no symmetries of the original Hamiltonian and also is paramagnetic, i.e. it exhibits no long-range magnetic order, it is the first example of a *quantum spin liquid* [11–13]. Although very commonly used, this term is only loosely defined, mainly by the abovementioned absence of long-range order despite strong interactions. Therefore, it is extremely challenging to positively identify a quantum spin liquid both in experimental and theoretical analysis of both models and materials.

This does, however, not exclude the possibility of explicitly constructing quantum spin liquid states. For example, in 1987 Kalmeyer and Laughlin connected quantum spin liquids to the fractional quantum hall effect by constructing a chiral spin-liquid state [14]. In the same year, the RVB wave functions proposed in connection with the cuprate family [10, 15] were the first to utilize a parton decomposition of the spin operators into two fermions, in modern language called spinons, to construct according quantum spin-liquid wave functions. To this end, they obtain the ground state of a mean-field Ansatz on the level of partons and subsequently project this state onto its spin-$1/2$, a process called Gutzwiller projection. This approach was later formalized by Xiao-Gang Wen [16] and used to classify spin liquid Ansätze allowed by the underlying lattice symmetry according to their projective symmetry group in spinon space [17].

From electrons to spins: the Heisenberg model

Knowing the possible physics emerging from a pure spin model, the question remains, how a Hamiltonian like eq. (1.5) can be relevant in a condensed matter setting, which is dominated by electronic physics.

As its main ingredient, a spin Hamiltonian necessitates localized degrees of freedom, which naturally arise in Mott insulators, in which the electron mobility is greatly reduced due to strong interactions gapping the spectrum, thereby rendering them localized in the atomic lattice. The simplest approach to capture this physics is the Hubbard model [18–23]

$$\hat{H} = -\sum_{\substack{i,j \\ \sigma=\uparrow,\downarrow}} t_{ij}\hat{c}^{\dagger}_{i\sigma}\hat{c}_{j\sigma} + U\sum_{i}\hat{c}^{\dagger}_{i\uparrow}\hat{c}_{i\uparrow}\hat{c}^{\dagger}_{i\downarrow}\hat{c}_{i\downarrow}, \tag{1.9}$$

which captures the main contribution of the Coulomb repulsion between electrons as a local Hubbard-interaction term U, while the band structure is encoded in the hopping t_{ij}. In the strongly interacting limit $U \to \infty$ at half-filling, appropriate for Mott insulators, the ground state of this Hamiltonian will consist of exactly one electron per site. Expanding eq. (1.9) around this limiting state to second order in t_{ij}, one finds the Heisenberg term [24]

$$\hat{H}_{\text{eff}} = \sum_{i,j}\frac{4t_{ij}^2}{U}\hat{\boldsymbol{S}}_i \cdot \hat{\boldsymbol{S}}_j, \tag{1.10}$$

where $\hat{\boldsymbol{S}}_i = \sum_{\sigma,\sigma'=\uparrow,\downarrow}\hat{c}^{\dagger}_{i\sigma}\boldsymbol{\sigma}\hat{c}_{i\sigma'}$ is the spin operator of the electron at site i.

As the interaction strength $4t_{ij}^2/U$ is strictly positive, this represents an antiferromagnetic Heisenberg model, *a posteriori* justifying both the choice of Hamiltonian eq. (1.5) and the subsequent discussion of antiferromagnetic couplings. This sign of interaction is in contrast to what one would naively expect from magnetic dipole-dipole interactions, which are ferromagnetic in nature.

There is a simple picture to understand AF interactions: for electrons to gain any kinetic energy through the perturbing hopping, there has to be the possibility to move to another lattice space and back again. According to the Pauli exclusion principle, with one electron per site, this is only possible (without spin flips), if the two sites connected by t_{ij} have spin oriented in different directions, i.e. they form an AF arrangement.

In real materials, this *direct exchange* of particles between magnetic sites is typically obstructed by interstitial non-magnetic atoms. A hopping path over the orbitals of these is called *superexchange* and the exact details of the sign and spatial structure of the orbitals involved in this process will influence both the strength and even sign of the Heisenberg coupling. This opens up the existence of both FM and AFcouplings in real materials.

Numerical approaches to quantum magnets

As we have established by now, quantum spin models can give rise to both theoretically and experimentally compelling states of matter. In particular, in three-dimensional (3D) crystals, in contrast to for example the NNAF on the 2D Kagome lattice [25–27], there has not yet been unambiguously found a spin liquid state in a Heisenberg model. This is mostly due to the fact, that there is a distinct lack of computational methods applicable to this dimension.

Exact Diagonalization

Exact diagonalization builds upon the idea of representing the Hilbert space of a finite system by vectors, which in turn leads to a representation of operators on this space as matrices. The latter, specifically the Hamilton operator, subsequently can be numerically diagonalized using standard algorithms, which allows obtaining both the energy spectrum of this system and the corresponding eigenstates exactly.

In interacting systems, however, these eigenfunctions no longer can be decomposed into products of single-particle states, such that the whole Hilbert space has to be considered. For systems consisting of n spins, the number of basis

states scales as 2^n. With the size of the Hamiltonian matrix being proportional to the square of this number, memory constraints in the numerical implementation limit the method to a low number of spins. Especially in 3D, this poses a severe problem, as it will induce severe finite-size effects in the calculations.

Quantum Monte Carlo

The quantum Monte-Carlo (QMC) method is another (statistically) exact method. Here the goal is to calculate the actual partition sum of the quantum system numerically using stochastic quadrature algorithms. In principle, 3D systems do not pose an inherent obstacle to this method, however for frustrated problems one usually encounters what is known as a *sign problem*. Here the integrand of the partition sum changes its sign for different configurations of the system, spoiling convergence of the stochastic sampling of the integral. This leads to a critical slow down of the calculations. While theoretically still an exact method, obtaining meaningful results would necessitate impractically long calculation times.

Density matrix renormalization group

The density matrix renormalization group (DMRG) [28, 29], in contrast to the previously mentioned methods, is an approximate scheme. The general idea is to approximate the ground state wave-function of a quantum mechanical system by a matrix product state, which can be efficiently represented numerically. DMRG now provides a procedure to consistently adjust the internal degrees of freedom of this state to better approximate the true ground state.

The method works extremely efficiently in 1D where correlations between spins die off quickly. Higher-dimensional systems, however, have to be implemented by mapping back to an effective 1D chain of spins, which however will induce longer-range correlations in the effective wave-function. This extremely enlarges the internal degrees of freedom of the matrix product state, which have to be taken into account to describe the system, rendering DMRG inaccurate, especially in 3D systems.

Variational Monte Carlo

Variational Monte Carlo, although being a method exact for a given family of ground state Ansätze, has the limitation, that it is biased, in contrast to all aforementioned schemes. The basic idea is to parton-decompose the spin Hamiltonian and employ a mean-field description of the resulting fermions. The ground state of this mean-field then is Gutzwiller projected, i.e. only the contained subspace corresponding to physical spins is retained and taken as an approximation to the true ground state of the system. During a variational Monte Carlo run, the parameters of the fermionic mean-field are adjusted to minimize the energy to obtain an as accurate as possible description of the target spin system.

This method is excellent for testing various spinon mean-field quantum spin liquid Ansätze for a known quantum paramagnetic system, but, by design, the method is limited to only the mean-field couplings assumed from the beginning and thus does not allow to determine the ground state of a generic spin system in an objective way.

Pseudo-fermion functional renormalization group

The PFFRG fills in the gap left by the other methods. It is an unbiased field theoretical method, taking into account both quantum fluctuations and classical ordering tendencies. This is done by tracking the evolution and mutual influence of different diagrammatic channels in the quantum system from a high energy scale, where only microscopic interactions are relevant, down to the scale-free fully correlated ground state.

Although it is also approximate, including only correlations up to a finite distance and at the same time neglecting expectation values of three or more spins, it has been proven to give excellent predictions both of phase diagrams [30–32] and real material properties [33–35] of 3D quantum magnetic systems. Therefore, this is the method of our choice, which we will employ and extend in this thesis.

Outline

This thesis is structured as follows. Before tackling the full quantum model, we first discuss the classical limit of spin systems in Part I, as it is more intuitive to think about vectors than quantum spins. Here we first define in Chapter 2 what is exactly meant by classical spin limit. In Chapter 3, we subsequently introduce the Luttinger-Tisza method as an analytical approach to solving classical spin systems, explicitly discussing its domain of applicability and relation to the approximate O($N \to \infty$) limit. In Chapter 4, as a complementary numerical method, we introduce the iterative minimization. In Part II the PFFRG is introduced as the numerical method of choice to treat quantum spin systems within this thesis. After the introduction of the Abrikosov pseudo-fermion decomposition in Chapter 5 and an introduction to functional renormalization group (FRG) in general in Chapter 6, we recapitulate the previously developed PFFRG in Chapter 7, while at the same time introducing a better-suited frequency parametrization of the vertex functions. In Chapter 8 we extend the formalism to include multi-loop contributions in the flow equations, which is the main technical advancement of this thesis, together with the improvements of its numerical implementation described in Chapter 9.

In Part III we apply the techniques developed to three prototypical three-dimensional spin models to produce their phase diagrams hitherto not discussed in literature. In Chapter 10, the body-centered cubic (BCC) lattice with interactions up to NNN level is discussed both on classical and quantum levels, unveiling the existence of quantum paramagnetic regimes emerging due to parametric frustration from the classically ordered phases. In Chapter 11 we repeat the analysis on the geometrically frustrated Pyrochlore lattice, considering Heisenberg interactions up to NN, uncovering an extended quantum paramagnetic regime even for a spin-1 model. We also apply the multiloop extension of PFFRG to discuss its effects on the findings for the NNAF on this lattice. As a final model, we investigate the cubic lattice including first and third NN interactions to demonstrate the multi-loop extension of PFFRG in an ordered regime.

In Part IV we shift focus towards models for real quantum magnetic materials, starting in Chapter 13 with a discussion of the spiral spin liquid in the diamond lattice material $MnSc_2S_4$, followed by uncovering the signatures of a gearwheel quantum spin liquid in the Pyrochlore compound $Lu_2Mo_2O_5N_2$ in Chapter 14.

We conclude in Chapter 15 and give an outlook on the future of PFFRG and three-dimensional quantum magnetism.

I

Classical Spins

In this part, we take a detour to the classical limit of spin systems and numerical methods to find their ground states.
After introducing the limit itself, we review the analytical Luttinger-Tisza approximation based on Reference [36], adding a physical interpretation of its output even when it is not fully applicable. As an analytical approach we introduce iterative minimization based on References [37] and [38].

CHAPTER 2

Classical spin systems

Quantum mechanics in general is often perceived as an unintuitive theory, as it does not fit our day-to-day perception of the world, which is governed by classical physics. This is especially true for quantum spins, which, due to their peculiar commutator structure, defy the notion of them behaving as a vector quantity.

Although quantum magnetism is an inherently quantum mechanical phenomenon, as discussed in Section 1, one can still define a meaningful classical limit. This stands in contrast to the other macroscopic quantum effects, i.e. superconductivity and superfluidity, which rely on the coherent superposition of quantum mechanical objects.

2.1 The $S \to \infty$ limit

The classical limit of spin systems can be obtained by performing the limit, where the spin length S is taken to infinity[1], effectively replacing the spin operator $\hat{\boldsymbol{S}}$ by a classical unit vector $\boldsymbol{s}$. This limit can be proven rigorously as done in References [39] and [40], but we will take in the following a more illustrative approach, which leads to the same conclusions.

Firstly, we define a rescaled spin operator

$$\hat{\boldsymbol{s}} = \frac{1}{S}\hat{\boldsymbol{S}}, \tag{2.1}$$

where we have divided by the spin length to obtain a quantity, which is sensibly defined in the limit $S \to \infty$. Note, that

$$\left\langle \hat{\boldsymbol{s}}^2 \right\rangle = \frac{S(S+1)}{S^2} \to 1 \quad \text{as} \quad S \to \infty, \tag{2.2}$$

i.e. $\hat{\boldsymbol{s}}$ is normalized in this limit. To motivate, that it indeed behaves as a classical vector, we consider the commutation relations for the components of the rescaled spin operator, given by

$$\left[\hat{s}^i, \hat{s}^j\right] = \frac{\mathrm{i}}{S}\sum_k \epsilon_{ijk}\hat{s}^k \to 0 \quad \text{as} \quad S \to \infty. \tag{2.3}$$

This implies, that in the infinite spin length limit, the components of the rescaled spin can be measured independently. In conjunction with the commutator, also the difference between subsequent eigenvalues of the spin components $\Delta = \frac{1}{S}$ vanishes, rendering the components well-defined continuous variables, only constrained by the unit length requirement given above.

[1] Instead of the spin quantum number S, one could equally well refer to root of the spin-square expectation value, $\sqrt{S(S+1)}$, as the spin length. We choose the former, as it simplifies notation and is equivalent in the large-S limit.

In total, the classical limit of a spin operator is given by

$$\lim_{S\to\infty} \frac{1}{S}\hat{\boldsymbol{S}} = \boldsymbol{s}, \tag{2.4}$$

where $\boldsymbol{s}$ is a three-component unit vector.

2.2 Classical Heisenberg Hamiltonian and its ground state

Having found the classical limit of a single spin operator, we are now also able to determine the classical spin Hamiltonian and its connection to its quantum version. To this end, we perform the limit (2.4) in the quantum Heisenberg Hamiltonian eq. (1.5), giving

$$H_{\mathrm{cl}} = \sum_{i,j} J_{i,j}\boldsymbol{s}_i \cdot \boldsymbol{s}_j \tag{2.5}$$

under the constraints

$$\boldsymbol{s}_i^2 = 1 \quad \forall i. \tag{2.6}$$

Note, that we have rescaled the Hamiltonian $H_{\mathrm{cl}} = H/S^2$, such that it is finite in the $S \to \infty$ limit. In the following, we will drop subscript cl, as it will be clear from context, if this rescaling was performed.

Determining the classical ground state of the Heisenberg model, therefore, amounts to finding the spin configuration $\{\boldsymbol{s}_i\}$, that minimizes (2.5). Although superficially one would expect this task to be easily solvable using vector calculus, this minimization problem, due to the indefiniteness of the interaction matrix $J_{i,j}$ is a non-convex quadratically constrained quadratic optimization, which is known to be computationally NP-hard [41]. Therefore, even in the classical spin limit, in general, we have to resort to approximate methods, two of which we will discuss in the following chapters. However, we will see, that in certain classes of lattices, their corresponding underlying symmetries render these methods exact.

CHAPTER 3

The Luttinger-Tisza method

An extremely powerful approach to determining the classical Heisenberg ground state is the approximate Luttinger-Tisza method [36]. Initially, it was developed for small spin clusters on the simple cubic lattice [42] and later also found to work for Ising spins on three-dimensional Bravais lattices [43]. A generalization to non-Bravais lattices was given shortly after [44]. The method recently found its renaissance due to the increasing interest in three-dimensional magnetic materials with Octahedral [37] and Pyrochlore [38] magnetic lattices. Our discussion of the method will follow its description given in Reference [36].

3.1 From strong to weak constraint

The most prominent symmetry, almost always exploited in condensed matter systems, is the periodicity of the underlying lattice. To this end, we define the Fourier transform of the classical spins on sublattice α in the ith unit cell as

$$\boldsymbol{s}_{i\alpha} = \sum_{\boldsymbol{q}\in\mathrm{BZ}} \mathrm{e}^{\mathrm{i}\boldsymbol{q}\cdot\boldsymbol{r}_{i\alpha}} \boldsymbol{s}_{\alpha}(\boldsymbol{q}), \tag{3.1}$$

where the sum on the r.h.s. runs over the first Brillouin zone (BZ) of the lattice and $\boldsymbol{r}_i$ is the Bravais vector of the ith unit cell. Note, that this discrete Fourier transform implicitly assumes a finite real space spin system consisting of N unit cells. This is primarily done for notational convenience, but generalizes trivially to infinite systems using the Fourier series. We will not make a notational distinction between the spin $\boldsymbol{s}_{i\alpha}$ and its Fourier transform $\boldsymbol{s}_{\alpha}(\boldsymbol{q})$, but rely on their arguments to clarify which space we treat the objects in.

Plugging the transform into eq. (2.5), we obtain the energy per unit cell

$$\mathcal{E} = H/N = \sum_{\boldsymbol{q},\mu,\nu} J_{\mu,\nu}(\boldsymbol{q})\, \boldsymbol{s}_{\mu}(\boldsymbol{q}) \cdot \boldsymbol{s}^{*}_{\nu}(\boldsymbol{q}), \tag{3.2}$$

where we have used $\boldsymbol{s}_{\alpha}(-\boldsymbol{q}) = \boldsymbol{s}^{*}_{\alpha}(\boldsymbol{q})$ due to real space spins $\boldsymbol{s}_{i\alpha}$ being real. The Fourier transform of the couplings, called Luttinger-Tisza matrix, is defined as

$$J_{\mu,\nu}(\boldsymbol{q}) = \sum_{j} J_{i\mu,j\nu}\, \mathrm{e}^{\mathrm{i}\boldsymbol{q}\cdot(\boldsymbol{r}_{i\mu}-\boldsymbol{r}_{j\nu})}. \tag{3.3}$$

Note, that, due to translational symmetry, the distance vector $\boldsymbol{r}_{i\mu} - \boldsymbol{r}_{j\nu}$ between sites in unit cell i on sublattice μ and unit cell j and sublattice ν is independent of i.

Equation (3.2) suggests, that the ground state of the classical spin system should be connected to the ordering vector q, for which the smallest eigenvalue of the Luttinger-Tisza matrix is minimized. This conclusion, however, can only be drawn, if we relax the spin length constraint eq. (2.6) to only be fulfilled on average, as we will find.

To be able to incorporate the spin length constraint into the calculations and at the same time make the reasoning more rigorous, we introduce Lagrange multipliers $\lambda_{i\mu}$ for the constraints eq. (2.6), leading to

$$H_{\text{strong}} = \sum_{i\mu,j\nu} J_{i\mu,j\nu}\, \boldsymbol{s}_{i\mu} \cdot \boldsymbol{s}_{j\nu} - \sum_{i\mu} \frac{\lambda_{i\mu}}{2} (\boldsymbol{s}_{i\mu}{}^2 - 1) \tag{3.4}$$

to be minimized with respect to both the spins and Lagrange multipliers at the same time. The strong spin length constrained is here traded for an even larger space, the minimization has to be done in, by adding one additional minimization parameter per site. Additionally, the $\lambda_{i\mu}$ are, in general, not constrained by the underlying lattice symmetries, in contrast to the couplings $J_{i\mu,j\nu}$ [36]. Therefore, a straightforward Fourier transform similar to eq. (3.1), generically will not be periodic in spin space for the Lagrange multipliers and consequently not simplify the calculations[1].

The idea of Luttinger and Tisza [42] is now to relax the *strong spin length constraint* eq. (2.6) by only enforcing it after summing over all lattice sites, i.e. on average. This leads to the single *weak constraint*

$$\sum_{i,\mu} \boldsymbol{s}_{imu}{}^2 = N_s, \tag{3.5}$$

where by N_s we denote the total number of spins in the system. Clearly, the set of states fulfilling eq. (3.5) is a superset of the true classical spin configurations subject to the strong constraint eq. (2.6).

Weakening the constraint means, that now only one Lagrange multiplier λ, constant over the whole system, is sufficient to take it into account in the minimization, i.e. the function to minimize reduces to

$$H_{\text{weak}} = \sum_{i\mu,j\nu} J_{i\mu,j\nu} \boldsymbol{s}_{i\mu} \cdot \boldsymbol{s}_{j\nu} - \frac{\lambda}{2} \left(\sum_{i\mu} \boldsymbol{s}_{i\mu}{}^2 - N_s \right). \tag{3.6}$$

The stationary state of this function now has to be found with respect to both Λ and the spins $\boldsymbol{s}_{i\mu}$. The former leads to the condition

$$\frac{\partial H_{\text{weak}}}{\partial \lambda} = \sum_{i,\mu} \boldsymbol{s}_{i\mu}{}^2 - N_s = 0, \tag{3.7}$$

i.e. the *weak constraint*, by construction. Extremalizing w.r.t. the spins, on the other hand, gives

$$\frac{\partial H_{\text{weak}}}{\partial \boldsymbol{s}_{i\mu}} = \sum_{j\nu} J_{i\mu,j\nu}\, \boldsymbol{s}_{j\nu} - \lambda\, \boldsymbol{s}_{i\mu} = 0, \tag{3.8}$$

which reduces, after Fourier transform, to the Eigenvalue problem

$$\sum_{\nu} J_{\mu,\nu}(\boldsymbol{q})\, \boldsymbol{s}_{\nu}(\boldsymbol{q}) = \lambda \boldsymbol{s}_{\mu}(\boldsymbol{q}) \quad \forall \boldsymbol{q} \tag{3.9}$$

for the Fourier transformed interaction matrix, where the Lagrange multiplier λ takes on the role of the eigenvalue. The energy minimization now amounts to finding the Luttinger-Tisza ordering vector $\boldsymbol{q}_{\text{LT}}$, for which the lowest eigenvalue

[1] In addition to the lower symmetry of the Lagrange multipliers, the strictly local nature of the constraint term will lead to a convolution in Fourier space, additionally complicating the search for a minimal energy state.

band of the Luttinger-Tisza matrix takes on its minimum value within the first BZ. Note, that this vector will not be unique: firstly, $J_{\mu,\nu}(\boldsymbol{q})$ is subject to the lattice symmetries, typically leading to multiple symmetry equivalent energy minima in reciprocal space. Secondly, independently of the lattice, ordering vectors will always come in pairs $\pm\boldsymbol{q}$, as due to the real space interaction matrix $J_{i\mu,j\nu}$ being real and symmetric, its Fourier transform has to fulfill $J_{\mu,\nu}(\boldsymbol{q}) = J_{\mu,\nu}(-\boldsymbol{q})^* = J_{\nu,\mu}(\boldsymbol{q})^*$, i.e. it is hermitian for a given $\boldsymbol{q}$ and complex conjugated under reflection in reciprocal space, leaving the real spectrum of the matrix invariant. Therefore, in the following discussions, we will this not consider to be a degeneracy of the ground state, as it is always present.

The energy of the Luttinger-Tisza eigenstate can be found, using the weak constraint eq. (3.5) in reciprocal space

$$\sum_{\mathbf{q},\mu} \left|\boldsymbol{s}_\mu(\boldsymbol{q})\right| = N_b, \tag{3.10}$$

where $N_b = {}^{N_s}/_{N}$ is the number of sites constituting the basis of the lattice, together with eq. (3.9) and eq. (3.2) to be

$$\mathcal{E} = N_b\,\lambda. \tag{3.11}$$

Let us finally consider the real space representation of the Luttinger-Tisza state. To this end, we denote the normalized eigenvector of the Luttinger-Tisza matrix corresponding to the minimal eigenvalue at $\boldsymbol{q}_{\mathrm{LT}}$ as $\boldsymbol{\psi}$. Note, that this is a vector in sublattice rather than spin space. Due to rotational invariance of the Heisenberg model, everything discussed so far holds for each component S^α of the spin vector separately, which means, we can scale the eigenvectors by a factor c_α for each spin component α, i.e. $s^\alpha_\mu(\boldsymbol{q}_{\mathrm{LT}}) = c_\alpha\psi_\mu$. To build a configuration of real vector spins, we also have to consider the energetically degenerate eigenstate for $-\boldsymbol{q}_{\mathrm{LT}}$, which has eigenvector $s^\alpha_\mu(-\boldsymbol{q}_{\mathrm{LT}}) = {c_\alpha}^*{\psi_\mu}^*$. In real space, using eq. (3.1), the most general Luttinger-Tisza state therefore is

$$\boldsymbol{s}^{\mathrm{LT}}_{i\mu} = \sum_{\alpha=1,2,3} \hat{\boldsymbol{x}}_\alpha \left(c_\alpha\psi_\mu \mathrm{e}^{\mathrm{i}\boldsymbol{q}_{\mathrm{LT}}\cdot\boldsymbol{r}_{i\mu}} + {c_\alpha}^*{\psi_\mu}^*\mathrm{e}^{-\mathrm{i}\boldsymbol{q}_{\mathrm{LT}}\cdot\boldsymbol{r}_{i\mu}}\right), \tag{3.12}$$

where $\hat{\boldsymbol{x}}_\alpha$ represent the Cartesian unit vectors. Using spin rotation symmetry to eliminate one spin component and demanding, that ${\boldsymbol{s}_{i,\mu}}^2$ should be independent of the unit cell i, we can restrict the state to a set of spirals on the sublattices [36]

$$\boldsymbol{s}^{\mathrm{LT}}_{i,\mu} = c|\psi_\mu| \begin{pmatrix} \cos\left(\boldsymbol{q}_{\mathrm{LT}}\cdot\boldsymbol{r}_{i\mu} + \phi_\mu\right) \\ \pm\sin\left(\boldsymbol{q}_{\mathrm{LT}}\cdot\boldsymbol{r}_{i\mu} + \phi_\mu\right) \\ 0 \end{pmatrix}, \tag{3.13}$$

where $c \in \mathbb{R}$ and $\psi_\mu = |\psi_\mu|\exp\{\mathrm{i}\phi_\mu\}$. The sign in the second component is the chirality of the spirals, which is not fixed by the Heisenberg model.

3.2 Exact cases: Bravais lattices and beyond

Having found the real space expression for the Luttinger-Tisza state eq. (3.13), we can now recast the strong constraint eq. (2.6) in terms of the Luttinger-Tisza eigenvectors, leading to the condition, that

$$c^2|\psi_\mu|^2 = 1\ \forall\mu, \tag{3.14}$$

i.e. the components of the Luttinger-Tisza vectors have to be equal on all sublattices, as their modulus can always be compensated by the free parameter c. In general, this is not fulfilled, but there are two very general classes of Lattices, this condition will always be satisfied.

3.2.1 Bravais lattices

The simplest case is the one of a Bravais lattice, featuring only a single sublattice, which renders the Luttinger-Tisza eigenvectors simple scalars within sublattice space. This means, there is only one component ψ_μ and setting $c^2 = 1/\psi_\mu$ satisfies eq. (3.14). This proves, what is referred to as the *spiral theorem for Bravais lattices* in literature [36, 44, 45]:

> The classical ground state of a Heisenberg model with arbitrary interactions on a Bravais lattice is always a coplanar spiral given by eq. (3.13).

This in turn implies, that any non-coplanar magnetic ground states on Bravais lattices cannot originate from a pure Heisenberg model, but other interactions have to be present.

3.2.2 Two equivalent basis points

A second quite general class of lattices, where the Luttinger-Tisza method gives the true ground state, is the one with exactly two basis points per unit cell, which are equivalent under space group transformations.

To clarify this statement, let us analyze the Luttinger-Tisza matrix $J_{\mu,\nu}(\boldsymbol{q})$ as defined in eq. (3.3). For a two basis point lattice, it is a hermitian, $\boldsymbol{q}$-dependent 2×2 matrix, which can in general be expanded in terms of Pauli-matrices and the identity as

$$J_{\mu,\nu}(\boldsymbol{q}) = a_0(\boldsymbol{q})\mathbb{1}_{\mu,\nu} + a_x(\boldsymbol{q})\sigma^x_{\mu,\nu} + a_y(\boldsymbol{q})\sigma^y_{\mu,\nu} + a_z(\boldsymbol{q})\sigma^z_{\mu,\nu}. \tag{3.15}$$

The Luttinger-Tisza eigenvectors for such a lattice are then (up to normalization) given by

$$\psi^\pm = \begin{pmatrix} \frac{a_z(\boldsymbol{q}) \pm \sqrt{a_x(\boldsymbol{q})^2 + a_y(\boldsymbol{q})^2 + a_z(\boldsymbol{q})^2}}{a_x(\boldsymbol{q}) - \mathrm{i}a_y(\boldsymbol{q})} \\ 1 \end{pmatrix} \tag{3.16}$$

If the two sublattices are equivalent by a space-group symmetry operation, this in particularly means, that interactions between spins located on the same sublattice have to be the same, regardless of which sublattices they are located on. In terms of the Luttinger-Tisza matrix, this means, that the diagonal entries have to be the same, i.e. $a_z(\boldsymbol{q})$ has to vanish. This simplifies the Luttinger-Tisza eigenvector to

$$\psi^\pm = \begin{pmatrix} \pm \frac{\sqrt{a_x(\boldsymbol{q})^2 + a_y(\boldsymbol{q})^2}}{a_x(\boldsymbol{q}) - \mathrm{i}a_y(\boldsymbol{q})} \\ 1 \end{pmatrix}, \tag{3.17}$$

which obviously fullfills $|\psi^\pm_1| = |\psi^\pm_2| = 1$, therefore fulfilling the strong constraint eq. (3.14). This proves the *spiral theorem for lattices with two equivalent basis points*:

> The ground state of a classical Heisenberg model on a lattice with exactly two symmetry equivalent basis points per unit cell is always a coplanar spiral given by eq. (3.13).

A prime example for this class of lattices is the Diamond structure, where we will apply the Luttinger-Tisza method in Chapter 13.

3.3 General remarks

To round up our discussion of the Luttinger-Tisza method, we collect some generic findings, which hold true, regardless of the specific lattice underlying the spin model under investigation.

3.3.1 Superposition of spiral states

Up to now, we have implicitly assumed, that there is a unique reciprocal vector $\boldsymbol{q}_{\mathrm{LT}}$ within the first BZ characterizing the Luttinger-Tisza state. On most lattices in two or more dimensions, however, this is only true, if this ordering vector is at special high symmetry points. Away from these, due to rotational and mirror symmetries, there will always be a set of symmetry equivalent reciprocal vectors with the same minimal energy eigenvalue of the Luttinger-Tisza matrix[2].

As the states are found by solving the linear eigenvalue problem of the Luttinger-Tisza matrix eq. (3.9), one would expect the superposition of two spiral states, as parametrized in eq. (3.13), to also form a ground state of the full classical model, given this is true for the individual spirals. The strong spin length constraint, eq. (2.6), on the other hand, is intrinsically non-linear, which will render this assumption false in general. Suppose, we form of a linear combination $\boldsymbol{s}_{i\mu}$ of two spin spirals $\boldsymbol{s}'_{i\mu}$ and $\boldsymbol{s}''_{i\mu}$ with ordering vectors $\boldsymbol{q}'_{\mathrm{LT}}$ and $\boldsymbol{q}''_{\mathrm{LT}}$, respectively, as defined in eq. (3.13), according to

$$\boldsymbol{s}_{i\mu} = a\boldsymbol{s}'_{i\mu} + b\boldsymbol{s}''_{i\mu} \tag{3.18}$$

with real prefactors a and b, then the resulting

$$(\boldsymbol{s}_{i\mu})^2 = a^2 + b^2 + 2\,a\,b\,c'|\psi'_\mu|\,c''|\psi''_\mu|\cos\Big((\boldsymbol{q}'_{\mathrm{LT}} - \boldsymbol{q}''_{\mathrm{LT}})\cdot\boldsymbol{r}_{i\mu} + (\phi'_\mu - \phi''_\mu)\Big) \tag{3.19}$$

is a priori dependent on the lattice site $\boldsymbol{r}_{i\mu}$ and therefore the strong constraint can not be fulfilled for arbitrary $\boldsymbol{q}'_{\mathrm{LT}}$ and $\boldsymbol{q}''_{\mathrm{LT}}$ [36].

We would like to highlight two special exceptions to this rule:

1. If $\boldsymbol{q}'_{\mathrm{LT}} - \boldsymbol{q}''_{\mathrm{LT}}$ is a reciprocal lattice vector and $(\boldsymbol{q}'_{\mathrm{LT}} - \boldsymbol{q}''_{\mathrm{LT}})\cdot\boldsymbol{r}_\mu = -(\phi'_\mu - \phi''_\mu)$, i.e. the phase difference in the spirals within one unit cell cancels out the relative angle induced by the spiraling. This is trivially the case in Bravais lattices.

2. $|\psi'_\mu|$ vanishes on sublattices, where $|\psi''_\mu|$ is non-zero and vice versa.

The latter case implies another larger ground state degeneracy: due to the eigenvector structure, the spins corresponding to the different ordering vectors are independent of each other, which allows for the two sets to be rotated freely with respect to each other, introducing two continuous degrees of freedom into the ground state. This trivially generalizes to more than two ordering vectors.

3.3.2 Non-coplanar spin states

From our discussion of the exactness of the Luttinger-Tisza method on both Bravais lattices and ones with two equivalent basis sites in Section 3.2 and the explicit parametrization of the Luttinger-Tisza eigenstate as a planar spiral in eq. (3.13), we can immediately deduce, that for these two classes of lattices, there cannot exist a true non-coplanar classical ground state. By true, we mean, that there is still the possibility of internal rotational freedom in a given

[2] Note, that space inversion is the only symmetry, which will not induce additional reciprocal vectors, as the sign of the ordering vector does not matter.

state, as discussed in the previous section, but at least one fully coplanar spin configuration will always be part of the ground-state manifold.

To find classical states ground states, in which spins are *forced* to point in three linearly independent directions, we, therefore, have to consider lattices with at least two inequivalent or three symmetry-equivalent basispoints per unit cell. However, even in these cases, Luttinger-Tisza eigenstates will generally form coplanar spirals, as parametrized by eq. (3.13). The only known possibility, to construct such non-coplanar states, is the cuboctahedral order on the Kagome [46, 47] and Octochlore lattices [37]. Here the ordering vector is commensurate, such that spins separated by a lattice vector are antiparallel. Additionally, the corresponding Luttinger-Tisza eigenvector only has non-zero weight on two of the three basis points and for the symmetry equivalent reciprocal vectors, the sublattice combinations supporting the state are different. These features allow the state to have different ordering vectors for different spin components on different basis points, forcing the spins to form a non-coplanar spin structure.

From this we can formulate three necessary, but not sufficient, conditions to construct non-coplanar Luttinger-Tisza eigenstates:

1. The lattice has to feature at least two non-equivalent or three equivalent basis points.
2. The Luttinger-Tisza eigenvector corresponding to the ordering vector has to feature zeros, otherwise, the ground state would be a planar spiral.
3. The ordering vector has to be commensurate, otherwise, the ordering cannot be constrained to a single spin direction, which prevents normalization.

3.3.3 Connection to $\mathrm{O}(N \to \infty)$

Apart from the classes of lattices discussed in the previous section, the Luttinger-Tisza method generically does not yield a classical ground state. In a lattice featuring symmetry inequivalent or more than two symmetry equivalent basis points, typically eq. (3.14) is not fulfilled, i.e. spins in the Luttinger-Tisza approximation have different lengths on different basis sites.

We can, however, still extract physically meaningful information from the Luttinger-Tisza result on these lattices. To this end, we turn to a mean-field approach for generalized spin systems [48, 49].

In our discussion of the classical spin limit, we found, that in the limit $S \to \infty$, quantum spin operators turn into normalized three-vectors, cf. eq. (2.4). The corresponding Classical Hamiltonian, eq. (2.5), features a full global $O(3)$ symmetry of the classical spins, i.e. it is invariant under

$$\boldsymbol{s}_i \to R\boldsymbol{s}_i \quad \text{with} \quad R \in O(3). \tag{3.20}$$

As a first step, we generalize this symmetry by elevating $O(3) \to O(N)$, which implies also promoting $\boldsymbol{s}$ to a N-component vector, while at the same time preserving normalization of the spins.

The mean-field free energy of this system is to second order in the spins given by [48, 49]

$$\mathcal{F} = \sum_{\boldsymbol{q},\mu,\nu} \left(\frac{NT}{2}\delta^{\mu\nu} + J_{\mu\nu}(\boldsymbol{q}) \right) \boldsymbol{s}_\mu(\boldsymbol{q}) \cdot \boldsymbol{s}_\nu(-\boldsymbol{q}), \tag{3.21}$$

where the first term, diagonal in sublattice space, originates in the second order expansion of the entropy, while the second one is just the internal energy. Using the eigenvalues $\lambda^\alpha(\boldsymbol{q})$ and corresponding normalized eigenvectors $\psi^\alpha(\boldsymbol{q})$

of the interaction matrix $J_{\mu\nu}(\boldsymbol{q})$, the spin-spin correlator

$$\left\langle \boldsymbol{s}_\mu(\boldsymbol{q}) \cdot \boldsymbol{s}_\nu(\boldsymbol{q}') \right\rangle = \int \mathcal{D}\{\boldsymbol{s}\}\, \boldsymbol{s}_\mu(\boldsymbol{q}) \cdot \boldsymbol{s}_\nu(\boldsymbol{q}') \mathrm{e}^{-\mathcal{F}/T} / \mathcal{Z} \tag{3.22}$$

$$= \sum_\alpha \frac{N \psi_\mu^\alpha(\boldsymbol{q}) \psi_\nu^\alpha(\boldsymbol{q}') \delta(\boldsymbol{q} + \boldsymbol{q}')}{N + 2\lambda^\alpha(\boldsymbol{q})/T} \tag{3.23}$$

can be solved using standard Gaussian integration. The partition sum is defined by

$$\mathcal{Z} = \int \mathcal{D}\{\boldsymbol{s}\}\, \mathrm{e}^{-\mathcal{F}/T} \tag{3.24}$$

This mean-field, being a saddle point approximation of the full $O(N)$ spin model, neglecting terms $O(\boldsymbol{s}^4)$, clearly does not capture the full physics present in the model. Setting $\mu = \nu$ in eq. (3.23), one immediately realizes, that due to the finite eigenvalues $\lambda^\alpha(\boldsymbol{q})$, the strong constraint eq. (2.6) is not fulfilled for any finite N, but only

$$\lim_{N\to\infty} \left\langle \boldsymbol{s}_\mu(\boldsymbol{q}) \cdot \boldsymbol{s}_\mu(-\boldsymbol{q}) \right\rangle = 1. \tag{3.25}$$

This precisely is the limit, in which the mean-field becomes exact, as fluctuations within the infinite-dimensional spin space will not lead to renormalization of the results [50–52].

Considering the temperature dependence of eq. (3.23), we find, that there will be a divergence of the correlations at $T_{\mathrm{MF}}^c = -2/N \min(\lambda^\alpha(\boldsymbol{q}))$, which signals a phase transition. Here the minimum of the eigenvalues is taken over the whole BZ. This temperature will always be finite, even on lattices, like Kagome or Pyrochlore, where the classical ground state is known to be disordered. The reason for this inaccuracy lies in the inconsistency with which the correlations are calculated: in setting up the mean-field eq. (3.21), we have neglected correlations between the spins, or, to be more precise, the molecular field. The subsequent calculation of the correlations of the order parameter from the result of the mean-field approximation will therefore inherently yield inconsistent results. An established method to deal with this shortcoming is the *self-consistent Gaussian approximation*, which also takes into account fluctuations of the molecular field itself [50–52]. For illustration purposes, however, we have in this section taken the more inaccurate, but also more instructive and easier-to-follow approach.

To round up this discussion, let us connect back to the Luttinger-Tisza method: The eigenvalues and eigenvectors used to construct eq. (3.23) are exactly the ones, that determine the Luttinger-Tisza energy landscape and eigenstates. Therefore, we can view eq. (3.23) for $N = 3$ as a Luttinger-Tisza mean-field spin structure factor. Additionally, the reciprocal vector, determined by the minimal energy eigenvalue, at which the structure factor diverges, is exactly the one found from the Luttinger-Tisza approach in the ground state.

Combining the above results, we conclude, that not only is Luttinger-Tisza equivalent to an $O(N \to \infty)$ mean-field, but additionally both approaches support each other with valuable contributions: Luttinger-Tisza provides a parametrization for the real-space spin structure in the limit $O(3)$, when applicable, while the $N \to \infty$ limit provides an expression for a spin-structure factor and physical interpretation of the results.

CHAPTER 4

Iterative minimization

In the cases, where the Luttinger-Tisza eigenstate is not a normalizable spin configuration, we have to resort to other methods to find a candidate for the classical ground state spin configuration. To this end, we will employ the iterative minimization method [37, 38], capable of finding local energy minima in configuration space.

4.1 Constrained steepest descent

The idea behind iterative minimization is to use a steepest descent algorithm, which is known to converge to a solution even for non-linear minimization problems [53], as we face when minimizing the classical Heisenberg Hamiltonian eq. (2.5).

We start from a random spin configuration on a finite lattice, consisting of L unit cells along each direction, i.e. we consider $N_s = L^d N_b$ spins, where d is the dimensionality of the lattice and N_b the number of basis sites. From experience, we find, that the real space cluster used in the scheme should not violate the symmetries of the underlying lattice in order to capture the correct physics.

Upon this state we perform single spin updates by choosing a random lattice point i and rotating the spin $\boldsymbol{s}_i$ residing there antiparallel to its local field originating from its coupling to the neighboring spins

$$\boldsymbol{h}_i = \frac{\delta H}{\delta \boldsymbol{s}_i} = \sum_j J_{i,j} \boldsymbol{s}_j, \tag{4.1}$$

therefore simultaneously minimizing the total energy and satisfying the strong spin length constraint eq. (2.6). A full lattice update, after which the total energy is calculated using eq. (2.5) and checked for convergence, consists of N_s such single-spin updates. This scheme can be viewed as a variant of classical Monte Carlos at zero temperature, using metropolis updates, where only optimal updates are proposed and accepted.

As we work in real space, we naturally will detect spontaneous symmetry breaking, not detectable by Fourier space methods such as Luttinger-Tisza. The finite real space lattice we complement with periodic boundary conditions, although open and twisted ones are in principle also possible. In the latter case, however, we observe severe finite-size effects due to the different environment of spins at the boundary and also the formation of domains with differently symmetry broken states.

Although this scheme is not guaranteed to converge to the global energy minimum, we find, that in all phases with exactly known ground state parametrization, e.g. where Luttinger-Tisza is exact, the iterative minimization recovers this state. To judge the quality of the converged ground state of a single minimization run and to maximize the likelihood to find the true ground state, we carry out the minimization starting from multiple random initial conditions. We then take the state with the lowest energy over these runs as the best approximation to the true one. The distribution

of energies additionally allows us to judge the energy landscape of the model, i.e. how frequent local energy minima occur.

4.2 Analysis tools

The real space spin configuration with minimal energy produced by iterative minimization is not the most intuitive object to work with, on one hand, due to its typically large number of spins N_s, on the other hand, the $O(3)$ symmetry of the Heisenberg model means, that the spin orientation after the minimization is usually not such, that e.g. spirals are easily visible. Therefore, we use several tools to further analyze the obtained state.

4.2.1 Spin structure factor

To directly probe the ordering wave vectors contained in the numerically obtained ground state, we calculate the spin structure factor

$$F(\boldsymbol{k}) = \frac{1}{N_s}\left|\sum_i \boldsymbol{s}_i e^{i\boldsymbol{k}\cdot\boldsymbol{r}_i}\right|^2, \tag{4.2}$$

where the sum runs over all lattice sites i. It captures the spectral composition of the state and develops sharp peaks at the ordering vectors for spin states governed by a single wave vector. For more complicated states, there are subdominant peaks present, which will carry a fraction of the total spectral weight.

4.2.2 Real space diagnostics

Although extremely useful in the case of single-$\boldsymbol{q}$ states, the spin structure factor does not fully characterize the real space configuration for states governed by multiple wave vectors. To get a better understanding of their structure and find possible parametrizations, we employ a series of real space diagnostics. Firstly, the spin inertia tensor [37]

$$M^{\mu\nu} = \frac{1}{N_s}\sum_i (\boldsymbol{s}_i)^\mu (\boldsymbol{s}_i)^\nu \tag{4.3}$$

encodes the information about preferred directions in spin space in its eigenvalues and -vectors. A collinear spin state has only one non-vanishing eigenvalue with its corresponding eigenvector giving the direction the collinear state points to in spin space. Similarly, a coplanar state features two finite eigenvalues, where the corresponding eigenvectors span the plane the spins of the state reside in. Finally, a non-coplanar state will feature three finite eigenvalues.

Typically, using the rotational symmetry of the Heisenberg model to align the eigenvectors in spin space with the cardinal directions in real space, will help uncover the state's structure. For further visual inspection, we use a common origin plot by shifting all spin vectors of the lattice, such that they start at the same point. This will reveal any lattice commensurability within the state, as then only a finite set of spin orientations will be visible.

As a final real space diagnostic, a fit of linear combinations of single-$\boldsymbol{q}$ states governed by dominant and subdominant ordering vectors, as found using the spin structure factor, can reveal a clearer picture of the state.

4.2.3 Competitive minimization

The starting point for iterative minimization does not necessarily have to be a random initial configuration, but any configuration can be used. This is useful in two ways: firstly, having obtained a candidate ground state parametrization,

we can use such a state as the initial configuration, to check, if it is (a) indeed a (local) energy minimum of the system and (b) how it is modified by minimization if it is not. Secondly, especially at phase boundaries, we can swap iteratively obtained configurations of neighboring phases, preferably from deep within the respective phase, to check, if the location of the phase boundary is correctly determined. This we dub *competitive minimization*. Of course, this is not only constrained to the vicinity of phase boundaries but can always be used to cross-check, if the iteratively-found ground state has indeed competitive energy or minimization procedure just got stuck in local minima.

II

Pseudo-Fermion Functional Renormalization Group

This part introduces the pseudo-fermion functional renormalization group as a methodological approach to quantum spin systems.
After a pedagogical review of Abrikosov pseudo-fermions with an emphasis on their inherent symmetries and the functional renormalization group, as well as their fusion into the pseudo-functional renormalization group method, we extend this formalism to a multi-loop formulation and discuss the state-of-the-art numerical implementation of the equations.

CHAPTER 5

Abrikosov Pseudo-Fermions

The inherent difficulty in solving any spin Hamiltonian can be traced back to the algebra of the spin operators $\hat{\boldsymbol{S}}$. As they are generators of rotations in spin space, they fulfill the defining commutation relations of the Lie-algebra $\mathfrak{su}(2)$

$$\left[S^i, S^j\right] = \mathrm{i}\hbar \sum_{k=1}^{3} \epsilon_{ijk} S^k, \tag{5.1}$$

which in turn necessitates the spin states to form a representation of the Lie-Group SU(2).

These operators fulfill neither fermionic anticommutation relations nor canonical bosonic commutators, which prevents most methods of condensed matter physics to be applied to them, as Wick's theorem [54] in its standard formulation does not hold [55, 56]. To circumvent this problem, we will introduce pseudo-particles with canonical commutation relations, which are then amenable to standard diagrammatic techniques.

5.1 Operator mapping

We choose a representation of the spin operators in terms of two species of fermions $c_\uparrow$ and $c_\downarrow$ introduced originally by Abrikosov [57] given by

$$S^\mu = \frac{1}{2} \sum_{\alpha,\beta=\uparrow,\downarrow} c^\dagger_\alpha \sigma^\mu_{\alpha\beta} c_\beta, \tag{5.2}$$

where σ^μ ($\mu \in \{1,2,3\}$) are the standard Pauli matrices. Clearly, this representation fulfills the necessary commutation relations eq. (5.1), but brings along a different complication: by splitting up the spin operators into two fermions, we have doubled the size of the Hilbert space, which now consists of the four states

$$\begin{aligned} &\left|0_\uparrow, 0_\downarrow\right\rangle && \left|1_\uparrow, 0_\downarrow\right\rangle = c^\dagger_\uparrow \left|0_\uparrow, 0_\downarrow\right\rangle \\ &\left|0_\uparrow, 1_\downarrow\right\rangle = c^\dagger_\downarrow \left|0_\uparrow, 0_\downarrow\right\rangle && \left|1_\uparrow, 1_\downarrow\right\rangle = c^\dagger_\uparrow c^\dagger_\downarrow \left|0_\uparrow, 0_\downarrow\right\rangle = -c^\dagger_\downarrow c^\dagger_\uparrow \left|0_\uparrow, 0_\downarrow\right\rangle, \end{aligned} \tag{5.3}$$

of which only the states filled with a single fermion correspond to a physical spin state corresponding to the mapping $|\uparrow\rangle \equiv \left|1_\uparrow, 0_\downarrow\right\rangle$ and $|\downarrow\rangle \equiv \left|0_\uparrow, 1_\downarrow\right\rangle$. The additional states filled with none or two fermions, $\left|0_\uparrow, 0_\downarrow\right\rangle$ and $\left|1_\uparrow, 1_\downarrow\right\rangle$, respectively, have, in contrast, no counterpart in the physical Hilbert space of the original spins.

To cure this overcounting, we have to complement the operator mapping eq. (5.2) by the single occupation constraint

$$c^\dagger_{i\downarrow} c_{i\downarrow} + c^\dagger_{i\uparrow} c_{i\uparrow} = 1. \tag{5.4}$$

to construct a faithful mapping between the Hilbert spaces of spin ½ and Abrikosov pseudo fermions. Note, that this identity has to hold on an operator level.

5.2 Gauge symmetry of the mapping

The restriction to half-filling in pseudo-fermion space introduced by eq. (5.4) implies an additional ambiguity in the pseudo-fermion description. As both none and doubly occupied fermionic states are not physical, the choice of the fermionic vacuum we implicitly made in eq. (5.3), namely by constructing all other states from $|0_\uparrow, 0_\downarrow\rangle$, is not unique. By, e.g., interchanging fermionic creation and annihilation operators appropriately, one can as well start from $|1_\uparrow, 1_\downarrow\rangle$ as the fermionic vacuum. Indeed, one can rotate the description continuously between these two cases independently for each spin operator in a lattice model, leading to an inherent SU(2) gauge symmetry of the pseudo-fermion description.

To formalize this intuitive picture, we introduce the matrix operator [58]

$$\Psi = \begin{pmatrix} c_\uparrow & c_\downarrow^\dagger \\ c_\downarrow & -c_\uparrow^\dagger \end{pmatrix}, \tag{5.5}$$

which allows us to express the mapping eq. (5.2) as

$$S^\mu = -\frac{1}{4} \operatorname{Tr}\left[\sigma^\mu \Psi \Psi^\dagger\right]. \tag{5.6}$$

In this form, it becomes clear, that the mapping is invariant under a right-multiplication with an SU(2) matrix according to

$$\Psi \to \Psi U^\dagger, \qquad U \in \mathrm{SU}(2), \tag{5.7}$$

i.e. a SU(2) transformation intermixing creation and annihilation operators of up- and down spins. This gauge symmetry, in turn, leads to an intermixing of the two possible vacua $|0_\uparrow, 0_\downarrow\rangle$ and $|1_\uparrow, 1_\downarrow\rangle$ due to their definitions eq. (5.3). As operator expectation values are always taken with respect to a specific vacuum, therefore only the U(1) and $\mathbb{Z}_2$ subgroup of the full SU(2) gauge symmetry can be exploited, as they will lead to a pure, rather than mixed, vacuum state. The former amounts to multiplying the operators with a complex phase, leaving the vacuum invariant, while the latter represents a particle-hole transformation given by

$$U_{\mathbb{Z}_2} = \begin{pmatrix} 0 & 1 \\ -1 & 0 \end{pmatrix}. \tag{5.8}$$

Under this transformation, $|0_\uparrow, 0_\downarrow\rangle$ and $|1_\uparrow, 1_\downarrow\rangle$ swap their roles. Both these subgroups of the full SU(2) symmetry, therefore, lead to well-defined expectation values, which can be brought into relation with each other.

For completeness, let us mention, that the single occupation constraint eq. (5.4) can also be recast in terms of the matrix operator eq. (5.5), by realizing, that half filling additionally implies the operator identities

$$c_{i\uparrow}^\dagger c_{i\downarrow}^\dagger = c_{i\uparrow} c_{i\downarrow} = 0, \tag{5.9}$$

as for exactly one fermion, we can neither create nor annihilate two fermions at the same site.

Together, Equations (5.4) and (5.9) can be recast as the vector equation

$$G^\mu = \frac{1}{4}\,\mathrm{Tr}\left[\sigma^\mu \Psi_i^\dagger \Psi_i\right] = 0. \tag{5.10}$$

Using the cyclicity of the trace, an SU(2) transformation according to eq. (5.7) corresponds to transforming the Pauli matrix in eq. (5.10) according to

$$\sigma^\mu \to U^\dagger \sigma^\mu U = R^\mu_\nu \sigma_\nu, \tag{5.11}$$

where we have used, that any SU(2) transformation on a Pauli matrix will correspond to an O(3) rotation R in Pauli matrix space. This means, although superficially superfluous, and equivalent to the half-filling constraint, the additional operator identities in eq. (5.9) will be generated under the action of the SU(2) gauge symmetry of the pseudo-fermion representation. The special case of a particle-hole symmetry eq. (5.8) does not mix the components of the constraint vector G^μ defined in eq. (5.10), but only flips the sign of its y component.

Using the relation between O(3) and SU(2) backward, we can straightforwardly show, that any rotation in spin space corresponds to an $SU(2)$ transformation of the corresponding fermionic operators:

$$\begin{aligned} R^\mu_\nu \boldsymbol{S}^\nu_i &= -\frac{1}{4}\,\mathrm{Tr}\left[(R^\mu_\nu \sigma^\nu)\Psi_i \Psi_i^\dagger\right] && (5.12)\\ &= -\frac{1}{4}\,\mathrm{Tr}\left[U^\dagger \sigma^\nu U \Psi_i \Psi_i^\dagger\right] && (5.13)\\ &= -\frac{1}{4}\,\mathrm{Tr}\left[\sigma^\nu (U\Psi_i)(U\Psi_i)^\dagger\right]. && (5.14) \end{aligned}$$

5.3 Gauge symmetry of the pseudo-fermion Heisenberg Hamiltonian and Lagrangian

Having defined the pseudo-fermion mapping, we now are able to rewrite the Heisenberg Hamiltonian eq. (1.5) in fermionic language, leading to

$$H = \frac{1}{4}\sum_{i,j,\mu,\nu,\rho,\sigma} J_{ij} c^\dagger_{i\mu} c_{i\nu} c^\dagger_{j\rho} c_{j\sigma} \boldsymbol{\sigma}_{\mu\nu} \cdot \boldsymbol{\sigma}_{\rho\sigma}, \tag{5.15}$$

where the prefactor comes from the mapping of the spin operators to pseudo-fermions. The quadratic form of this Hamiltonian makes it apparent, that spin systems inherently are strongly interacting. In particular, the absence of a quadratic, i.e. kinetic, term in the Hamiltonian prevents the notion of a non-interacting pseudo-fermion system due to the vanishing kinetic energy scale. Therefore, perturbative expansions of the problem around a Gaussian theory are not possible, calling for more sophisticated many-body methods to analyze the problem, such as the functional renormalization group (FRG) we will introduce in Chapter 6.

5.4 Symmetries of pseudo-fermion Green's functions

The Heisenberg Hamiltonian features a series of symmetries, both physical ones, such as hermiticity and time-reversal invariance, and, most importantly for practical calculations, the local SU(2) gauge symmetry of the pseudo-fermion

mapping. In this section, we will, following the presentation in Reference [59], summarize these symmetries and their implications on the important one- and two-particle Green's functions[1].

To fix notation, we define the one-particle Green's function

$$G(1';1) = \left\langle c^\dagger_{1'} c_1 \right\rangle \tag{5.16}$$

and its two-particle counterpart

$$G(1',2';1,2) = \left\langle c^\dagger_{1'} c^\dagger_{2'} c_1 c_2 \right\rangle, \tag{5.17}$$

where we use multi-indices $j = (i_j, \mathrm{i}\omega_j, \mu_j)$, capturing the site index i_j, Matsubara frequency[2] ω_j and spin index μ_j. Primed indices, corresponding to creation operators, we refer to as outgoing indices, whereas the unprimed indices corresponding to annihilation operators, we call incoming indices.

5.4.1 Time-translation invariance

We start our discussion of symmetries with the invariance of the pseudo-fermion Hamiltonian under translations in imaginary time, which is manifestly seen in eq. (5.15) by the absence of any explicit time or Matsubara frequency dependence. This implies, that all Green's functions only are dependent on imaginary time differences, which, after Fourier transform, leads to a Matsubara frequency conservation. Therefore, the sum of incoming Matsubara frequencies has to equal the sum of outgoing ones. For the Green's functions, we can sum up this discussion in the relations

$$G(1';1) = G(1';1)\delta_{\omega_{1'},\omega_1} \tag{5.18}$$

and

$$G(1',2';1,2) = G(1',2';1,2)\delta_{\omega_{1'}+\omega_{2'},\omega_1+\omega_2}. \tag{5.19}$$

These reduce the dependence of these correlators by one frequency, which can be expressed as a linear combination of the others. Note, that this relation, when formulated in terms of real frequencies, is equivalent to conservation of energy in the Green's functions.

5.4.2 Time-reversal invariance

Another important physical symmetry relating to imaginary time is reversing its direction. The effect of time reversal on spins is to flip their direction, i.e. $\boldsymbol{S} \to -\boldsymbol{S}$. Additionally, time-reversal has to be antiunitary and therefore contain a complex conjugation in its action. This can be understood easily considering the time evolution operator $\exp(-\mathrm{i}Ht)$. For it to be invariant under time reversal for an invariant Hamiltonian, the imaginary i has to flip sign, compensating the sign change in time t.

The action of time-reversal $\mathcal{T}$ on the fermionic operators can be implemented as

$$\mathcal{T}\begin{pmatrix} c^\dagger_{i\mu} \\ c_{i\mu} \end{pmatrix}\mathcal{T}^{-1} = \begin{pmatrix} \mathrm{e}^{\mathrm{i}\pi\mu/2} c^\dagger_{i\bar{\mu}} \\ \mathrm{e}^{-\mathrm{i}\pi\mu/2} c_{i\bar{\mu}} \end{pmatrix}, \tag{5.20}$$

[1] In literature, n-particle functions are also called $2n$-point functions. We choose the former name, referring to the number of pairs of creation and annihilation operators within an expectation value, signifying the number of particles involved, while the latter refers to the number of operators itself, or equivalently the number of external arguments to the function.

[2] For clarity, we drop the discrete index of the Matsubara frequencies.

where the notation $\bar{\mu} = -\mu$ is a shorthand to indicate the flip of the spin index with $\mu = \pm 1$ representing spin up/down.

Using this relation on the two-particle Green's function eq. (5.16), we find for time-reversal invariant systems the relation

$$G(1';1) = \mathrm{e}^{\mathrm{i}\pi(\mu_{1'}-\mu_1)/2} G(i_{1'}, -\mathrm{i}\omega_{1'}, \bar{\mu}_{1'}; i_1, -\mathrm{i}\omega_1, \bar{\mu}_1)^*. \tag{5.21}$$

Here the complex conjugation is only meant to act on the Green's function itself, but not on its arguments, where we have explicitly added the negative sign for the Matsubara frequency arguments.

The origin of this complex conjugation is the antiunitarity of time-reversal, as expectation values of an operator A transform as $\langle A \rangle \to \left\langle \mathcal{T} A \mathcal{T}^{-1} \right\rangle^*$.

The phase factor $\mathrm{e}^{\mathrm{i}\pi(\mu_{1'}-\mu_1 n_{oprime})/2}$ can be simplified using the fact, that $\mu = \pm 1$ to

$$\mathrm{e}^{\mathrm{i}\pi(\mu_{1'}-\mu_1)/2} = \mu_{1'}\mu_1, \tag{5.22}$$

as can be easily verified by considering all possible combinations of the spin indices.

Similarly, the two-particle vertex obeys the relation

$$G(1',2';1,2) = \mu_{1'}\mu_{2'}\mu_1\mu_2 G(i_{1'}, -\mathrm{i}\omega_{1'}, \bar{\mu}_{1'}, i_{2'}, -\mathrm{i}\omega_{2'}, \bar{\mu}_{2'}; i_1, -\mathrm{i}\omega_1, \bar{\mu}_1, i_2, -\mathrm{i}\omega_2, \bar{\mu}_2)^*. \tag{5.23}$$

Please note, that time-reversal symmetry of a magnetic system is already spoiled when coupling to an external magnetic field $\boldsymbol{B}$ via a term $\boldsymbol{S} \cdot \boldsymbol{B}$ and also by interactions involving an odd number of spins. As, however, time-reversal symmetry will turn out crucial for the performance of our calculations, we will refrain from adding such terms, although the formalism is in principle capable of handling these.

5.4.3 Hermiticity of the Hamiltonian

Representing the energy as a physical observable, the Hamiltonian necessarily has to be a hermitian operator. This allows us to obtain relations involving the complex conjugate of expectation values. As the density operator, being an exponential of the Hamiltonian, is invariant under hermitian conjugation, complex conjugation of such expectation values is equivalent to a hermitian conjugation of the operators contained in these. Carrying out the hermitian conjugate exchanges creation and annihilation operators, reverses their order and, due to complex conjugation, reverses the sign of the Matsubara frequency.

From this process, we obtain the relation

$$G(1';1) = G(i_1, -\mathrm{i}\omega_1, \mu_1; i_{1'}, -\mathrm{i}\omega_{1'}, \mu_{1'})^* \tag{5.24}$$

for the one-particle Green's function and

$$G(1',2';1,2) = G(i_1, -\mathrm{i}\omega_1, \mu_1, i_2, -\mathrm{i}\omega_2, \mu_2; i_{1'}, -\mathrm{i}\omega_{1'}, \mu_{1'}, i_{2'}, -\mathrm{i}\omega_{2'}, \mu_{2'})^* \tag{5.25}$$

for the two-particle one. By themselves, these relations already give some insight into the analytical structure of the Green's functions, however a combination with the time-reversal relations Equations (5.22) and (5.23) will lead to new relations for the whole Green's function, rather than their real and imaginary parts separately,

5.4.4 Lattice symmetries

As a last physical symmetry, we discuss the one associated with the underlying lattice of the Heisenberg Hamiltonian in eq. (5.15). Although the specific symmetry group highly depends on the specific lattice considered, the effect on Green's functions can be stated universally, as the lattice symmetry always maps one lattice point i onto another point $\mathrm{L}(i)$ within the lattice. In operator language, this transformation, defining a suitable unitary symmetry operator $\mathcal{L}$, reads

$$\mathcal{L}\begin{pmatrix} c^\dagger_{i\mu} \\ c_{i\mu} \end{pmatrix}\mathcal{L}^{-1} = \begin{pmatrix} c^\dagger_{\mathrm{L}(i)\mu} \\ c_{\mathrm{L}(i)\mu} \end{pmatrix}. \tag{5.26}$$

As the Hamiltonian, being defined on the lattice, is by definition invariant under such transformations[3], the Green's functions are as well, leading to the relations

$$G(1';1) = G(\mathrm{L}(i_{1'}), \mathrm{i}\omega_{1'}, \mu_{1'}; \mathrm{L}(i_1), \mathrm{i}\omega_1, \mu_1) \tag{5.27}$$

for the one-particle Green's function and likewise

$$G(1',2';1,2) = G(\mathrm{L}(i_{1'}), \mathrm{i}\omega_{1'}, \mu_{1'}, \mathrm{L}(i_{2'}), \mathrm{i}\omega_{2'}, \mu_{2'}; \mathrm{L}(i_1), \mathrm{i}\omega_1, \mu_1, \mathrm{L}(i_2), \mathrm{i}\omega_2, \mu_2) \tag{5.28}$$

in the two-particle case.

As any lattice symmetry group contains a translational symmetry subgroup by definition, this implies we can always map back at least one of the site arguments onto a site in a given reference unit cell. Furthermore, if all sites in the lattice are equivalent, there will be an additional symmetry within that unit cell, that allows us to select a single reference point we can map one of the points onto[4].

5.4.5 Crossing symmetries

Before turning towards the gauge symmetries of the pseudo-fermion mapping, let us briefly mention another symmetry of any Green's function, which derives from their definition of expectation values combined with the canonical anticommutation relations of fermionic operators. Using the latter to swap the two annihilation or creation operators in the definition eq. (5.23) of the two-particle vertex, we find, that this Green's function is invariant under exchange of the incoming or outgoing indices, up to a sign, i.e.

$$G(1',2';1,2) = -G(2',1';1,2) = -G(1',2';2,1) = G(2',1';2,1)\,. \tag{5.29}$$

This is commonly referred to as crossing symmetry of the Green's function, as in a diagrammatic language it corresponds to crossing the incoming or outgoing legs of a given diagram.

5.4.6 Local $\mathrm{U}(1)$ gauge symmetry

Having exhausted all symmetries of the Green's functions, which hold for general fermionic systems respecting the discussed physical symmetries, we now explore the additional constraints the pseudo-fermion mapping imposes on these objects. As already discussed in Section 5.2, the single occupation constraint accompanying the mapping of

[3] We treat any symmetry breaking imposed by couplings not compatible with the full symmetry of the lattice by defining a new lattice compatible with the coupling symmetries.

[4] In the case of n symmetry inequivalent points in the unit cell, we have to consider n of these reference points.

spin operators to bosons introduces a local SU(2) gauge symmetry. As however, the vacuum is not invariant under this group, only two subgroups of the full symmetry can be exploited for expectation values. The first one, we want to discuss, is the local U(1) symmetry.

The action of this group amounts to rotating the complex phase of an operator at site i by an angle ϕ_i, i.e. the operators transform as

$$\mathcal{U}_\phi \begin{pmatrix} c^\dagger_{i\mu} \\ c_{i\mu} \end{pmatrix} \mathcal{U}_\phi^{-1} = \begin{pmatrix} \mathrm{e}^{\mathrm{i}\phi_i} c^\dagger_{i\mu} \\ \mathrm{e}^{-\mathrm{i}\phi_i} c_{i\mu} \end{pmatrix}. \tag{5.30}$$

Again, applying the symmetry transform to the Green's functions yields

$$G(1';1) = \mathrm{e}^{\mathrm{i}(\phi_{i_{1'}} - \phi_{i_1})} G(1';1) \tag{5.31}$$

and

$$G(1',2';1,2) = \mathrm{e}^{\mathrm{i}(\phi_{i_{1'}} + \phi_{i_{2'}} - \phi_{i_1} - \phi_{i_2})} G(1',2';1,2) \tag{5.32}$$

for the one- and two-particle Greens functions, respectively.

To allow for non-vanishing Green's functions, the phase factors in Equations (5.31) and (5.32) have to equal unity. The individual phases ϕ_i on different lattice points, however, can be chosen independently, such that for the total phase to vanish, incoming and outgoing sites have to be pairwise equal. This means in the one-particle case, the Green's function becomes purely local, i.e.

$$G(1';1) = G(1';1)\delta_{i_{1'} i_1}, \tag{5.33}$$

while the two-particle Green's function features two possible combinations of incoming an outgoing sites

$$G(1',2';1,2) = G(1',2';1,2)\delta_{i_{1'} i_1}\delta_{i_{2'} i_2} - G(2',1';1,2)\delta_{i_{1'} i_2}\delta_{i_{2'} i_1}. \tag{5.34}$$

In the second term, we have already explicitly incorporated the crossing-symmetry eq. (5.29) in the parametrization, leading to a direct and crossed term in terms of real space indices. This implies, that in any given correlator, for it to be non-vanishing, there must be an equal number of creation and annihilation operators at the same site present, rendering the particle number at each site a conserved quantity. This is in analogy to a global U(1) symmetry, which implies total particle number conservation.

We can understand this constraint most easily in the light of the pseudo-fermion mapping eq. (5.2). Here, every spin operator, defined at a particular point i in the lattice decomposes into one creation and annihilation operator, which both have to carry the same lattice index i as the original spin operator. The U(1) symmetry now guarantees, that only correlations consistent with this parametrization can be generated by the system.

This multi-locality constraint on the Green's functions has profound implications on what forms the best basis to treat multi-fermion systems formally. Itinerant fermions, which one usually deals with, tend to delocalize, which usually renders a momentum-space picture more appropriate. The locality of the pseudo-fermions, which is already encoded in the Heisenberg Hamiltonian eq. (5.15) in the absence of a kinetic hopping term, implies, that the Green's functions are constant in momentum space. In direct space, however, lattice summations will be extremely simplified, as we will see in Section 7.3, rendering a real space description the more convenient picture for pseudo-fermions.

$G(1';1)$	$= G(1';1)\delta_{i_{1'}i_1}$	(U(1))
$G(1';1)\delta_{i_{1'}i_1}$	$= G(\mathrm{L}(i_{1'}), \mathrm{i}\omega_{1'}, \mu_{1'}; \mathrm{L}(i_1), \mathrm{i}\omega_1, \mu_1)\delta_{i_{1'}i_1}$	(L)
$G(1';1)\delta_{i_{1'}i_1}$	$= G(1';1)\delta_{i_{1'}i_1}\delta_{\omega_{1'},\omega_1}$	(TT)
$G(1';1)\delta_{i_{1'}i_1}$	$= -\mu_{1'}\mu_1 G(i_1, -\mathrm{i}\omega_1, \bar{\mu}_1; i_{1'}, -\mathrm{i}\omega_{1'}, \bar{\mu}_{1'})\delta_{i_{1'}i_1}$	(PH)
$G(1';1)\delta_{i_{1'}i_1}$	$= \mu_{1'}\mu_1 G(i_{1'}, -\mathrm{i}\omega_{1'}, \bar{\mu}_{1'}; i_1, -\mathrm{i}\omega_1, \bar{\mu}_1)^*\delta_{i_{1'}i_1}$	(TR)
$G(1';1)\delta_{i_{1'}i_1}$	$= G(i_1, -\mathrm{i}\omega_1, \mu_1; i_{1'}, -\mathrm{i}\omega_{1'}, \mu_{1'})^*\delta_{i_{1'}i_1}$	(H)

Table 5.1: Symmetry relations of the one-particle correlation function for pseudo-fermion Hamiltonians. The combined index $j = (i_j, \mathrm{i}\omega_j, \mu_j)$ is used as shorthand for site index i_j, Matsubara frequency $\mathrm{i}\omega_j$ and spin index μ_j for incoming (unprimed) and outgoing (primed) parameters. The labels are shorthands for the underlying symmetry of the relations: TR denotes time-reversal, TT time translation, L lattice symmetries, H hermitian conjugation, X crossing symmetry in both incoming and outgoing particles and PH1/2 is a particle-hole transformation for particle 1/2.

5.4.7 Local particle-hole symmetry

The second subgroup of the SU(2) gauge symmetry, we want to discuss, is the $\mathbb{Z}_2$ subgroup, which amounts to a local particle-hole transformation

$$\mathcal{Z}_i \begin{pmatrix} c^\dagger_{i\mu} \\ c_{i\mu} \end{pmatrix} \mathcal{Z}_i^{-1} = \begin{pmatrix} \mu c_{i\bar{\mu}} \\ \mu c^\dagger_{i\bar{\mu}} \end{pmatrix}, \tag{5.35}$$

which also swaps spin sectors. As shown in the previous section, the Green's functions are multi-local in real space, which allows us to apply the transformation directly to the appropriately parametrized Green's functions, yielding

$$G(1';1)\delta_{i_{1'}i_1} = -\mu_1\mu_1 G(i_1, -\mathrm{i}\omega_1, \bar{\mu}_1; i_{1'}, -\mathrm{i}\omega_{1'}, \bar{\mu}_{1'})\delta_{i_{1'}i_1} \tag{5.36}$$

for the one-particle case. The negative sign is due to an anticommutation within the expectation value defining the Green's function, while the inversion of frequency is due to the swapping of creation and annihilation operators, which flips the energy spectrum.

For the two-particle case, we analogously find, by applying the local transform to the two independent sites separately

$$\begin{aligned} G(1',2';1,2)\delta_{i_{1'}i_1}\delta_{i_{2'}i_2} &= -\mu_{1'}\mu_1 G(i_1, -\mathrm{i}\omega_1, \bar{\mu}_1, 2'; i_{1'}, -\mathrm{i}\omega_{1'}, \bar{\mu_{1'}}, 2)\delta_{i_{1'}i_1}\delta_{i_{2'}i_2} && (5.37) \\ &= -\mu_{2'}\mu_2 G(1', i_2, -\mathrm{i}\omega_2, \bar{\mu}_2; 1, i_{2'}, -\mathrm{i}\omega_{2'}, \bar{\mu_{2'}})\delta_{i_{1'}i_1}\delta_{i_{2'}i_2}. && (5.38) \end{aligned}$$

Note, that even in the case of $i_1 = i_2$, the two relations Equations (5.37) and (5.38) hold separately. This is due to the fact, that the labels 1 and 2 in i_1 and i_2 directly connect to which original spin operator the individual fermions are part of. As the relations are obtained from the symmetry of this operator mapping, even for $i_1 = i_2$ no intermixing of the pseudo-fermions corresponding to different spin operators will take place.

5.4.8 Summary of the symmetries

For reference, we summarize all symmetry relations of the one-particle Green's function in Table 5.1 and the ones for the two-particle one in Table 5.2.

We can divide the symmetries into two groups. The first one reduces the dependence of the Green's functions on the external degrees of freedom: The local U(1) symmetry renders the one(two)-particle function (bi-)local,

$$G(1',2';1,2) = G(1',2';1,2)\delta_{i_{1'}i_1}\delta_{i_{2'}i_2} - G(2',1';1,2)\delta_{i_{1'}i_2}\delta_{i_{2'}i_1} \tag{U(1)}$$

$$G(1',2';1,2)\delta_{i_{1'}i_1}\delta_{i_{2'}i_2} = G(\mathrm{L}(i_{1'}),\mathrm{i}\omega_{1'},\mu_{1'},\mathrm{L}(i_{2'}),\mathrm{i}\omega_{2'},\mu_{2'};\mathrm{L}(i_1),\mathrm{i}\omega_1,\mu_1,\mathrm{L}(i_2),\mathrm{i}\omega_2,\mu_2)\delta_{i_{1'}i_1}\delta_{i_{2'}i_2} \tag{L}$$

$$G(1',2';1,2)\delta_{i_{1'}i_1}\delta_{i_{2'}i_2} = G(1',2';1,2)\delta_{i_{1'}i_1}\delta_{i_{2'}i_2}\delta_{\omega_{1'}+\omega_{2'},\omega_1+\omega_2} \tag{TT}$$

$$G(1',2';1,2)\delta_{i_{1'}i_1}\delta_{i_{2'}i_2} = -\mu_{1'}\mu_1 G(i_1,-\mathrm{i}\omega_1,\bar{\mu}_1,2';i_{1'},-\mathrm{i}\omega_{1'},\bar{\mu_{1'}},2)\delta_{i_{1'}i_1}\delta_{i_{2'}i_2} \tag{PH1}$$

$$G(1',2';1,2)\delta_{i_{1'}i_1}\delta_{i_{2'}i_2} = -\mu_{2'}\mu_2 G(1',i_2,-\mathrm{i}\omega_2,\bar{\mu}_2;1,i_{2'},-\mathrm{i}\omega_{2'},\bar{\mu_{2'}})\delta_{i_{1'}i_1}\delta_{i_{2'}i_2} \tag{PH2}$$

$$G(1',2';1,2)\delta_{i_{1'}i_1}\delta_{i_{2'}i_2} = \mu_{1'}\mu_{2'}\mu_1\mu_2 G(i_{1'},-\mathrm{i}\omega_{1'},\bar{\mu}_{1'},i_{2'},-\mathrm{i}\omega_{2'},\bar{\mu}_{2'};i_1,-\mathrm{i}\omega_1,\bar{\mu}_1,i_2,-\mathrm{i}\omega_2,\bar{\mu}_2)^*\delta_{i_{1'}i_1}\delta_{i_{2'}i_2} \tag{TR}$$

$$G(1',2';1,2)\delta_{i_{1'}i_1}\delta_{i_{2'}i_2} = G(i_1,-\mathrm{i}\omega_1,\mu_1,i_2,-\mathrm{i}\omega_2,\mu_2;i_{1'},-\mathrm{i}\omega_{1'},\mu_{1'},i_{2'},-\mathrm{i}\omega_{2'},\mu_{2'})^*\delta_{i_{1'}i_1}\delta_{i_{2'}i_2} \tag{H}$$

$$G(1',2';1,2)\delta_{i_{1'}i_1}\delta_{i_{2'}i_2} = G(2',1';2,1)\delta_{i_{1'}i_1}\delta_{i_{2'}i_2} \tag{X}$$

Table 5.2: Symmetry relations of the two-particle correlation function for pseudo-fermion Hamiltonians. The combined index $j = (i_j, \mathrm{i}\omega_j, \mu_j)$ is used as shorthand for site index i_j, Matsubara frequency $\mathrm{i}\omega_j$ and spin index μ_j for incoming (unprimed) and outgoing (primed) parameters. The labels are shorthands for the underlying symmetry of the relations, for details see main text.

greatly reducing their spatial dependence. Additionally, lattice symmetries (L) reduce these dependencies further, as translational invariance always allows to set one of these local points to a reference one. In frequency-space, time-translational invariance (TT) has a similar effect, reducing the number of frequency arguments by one.

The second group of symmetries establishes relations within the remaining structure of the Green's functions: In this group falls the remaining part of the lattice symmetries. Furthermore, the local particle-hole symmetry, which induces one symmetry relation (PH) in the one-particle case and two, (PH1) and (PH2), in the two-particle one, one for each site index, in the two-particle case. Time-reversal (TR) and Hermitian (H) symmetry as a special case induce relations for the real and imaginary parts of the Green's function separately. For the case of the two-particle Green's function, we also have the combined crossing symmetry in both incoming and outgoing arguments (X), but not the separate version for one of the species of arguments only. This is due to the bilocality constraint following from (U(1)), which already decomposes the vertex into two components, which are related by an individual crossing symmetry, as shown in eq. (5.29).

5.5 Gauge-invariance of the pseudo-fermion Lagrangian

Having discussed the symmetries of both the Heisenberg Hamiltonian and the Green's functions, we still have to see, how the gauge symmetry affects the Lagrangian, which we need for a field-theoretic treatment of pseudo-fermion systems. To this end, we bring the Heisenberg Hamiltonian in a for our purpose more convenient form

$$H = -\frac{1}{16}\sum_{i,j,\mu}\mathrm{Tr}\left[\sigma^\mu\Psi_i\Psi_i^\dagger\right]\mathrm{Tr}\left[\sigma^\mu\Psi_j\Psi_j^\dagger\right]. \tag{5.39}$$

Here, we immediately see, that the Heisenberg model is invariant both under a local gauge transformation SU(2) gauge transformation according to eq. (5.7),

$$\Psi_i \to \Psi_i U_i^\dagger, \qquad U_i \in \mathrm{SU}(2), \tag{5.40}$$

where the matrix U_i can be site-dependent, as well as a global rotation in spin space as given by eq. (5.14). For field-theoretical treatments, we will need the Lagrangian of this system [58]

$$L = \mathrm{i} \sum_{i,\mu} c^\dagger_{i\mu} \frac{\partial}{\partial t} c_{i\mu} - H, \tag{5.41}$$

which is by means of integration by parts up to a constant term equivalent to the manifestly gauge invariant form

$$L = \frac{\mathrm{i}}{2} \sum_i \mathrm{Tr} \left[\Psi_i \frac{\partial}{\partial t} \Psi_i^\dagger \right] - H. \tag{5.42}$$

To include the single-occupation per site constraints in this formulation, we add three Lagrange multipliers A^μ enforcing the three components of eq. (5.10), adding a term $\mathrm{Tr}\left[\Psi_i (\boldsymbol{A} \cdot \boldsymbol{\sigma}) \Psi_i^\dagger\right]$ to the Lagrangian. This term, however, is nothing else than a coupling of the matrix valued field Ψ to the temporal component of a SU(2) gauge field $\boldsymbol{A} \cdot \boldsymbol{\sigma}$, given we allow for fluctuations of the Lagrange multipliers, promoting them to fields.

This view even allows for time-dependent gauge transformations, which would not leave the kinetic term in eq. (5.42) invariant, due to time derivative terms of the transformation not being cancelled. Demanding a suitable transformation of the gauge field

$$\boldsymbol{A} \cdot \boldsymbol{\sigma} \to U^\dagger (\boldsymbol{A} \cdot \boldsymbol{\sigma} - \mathrm{i} \frac{\partial}{\partial t}) U, \tag{5.43}$$

heals this invariance, promoting the local SU(2) gauge invariance to a time-dependent one. The Lagrangian fully invariant under the local and time-dependent gauge symmetry of the SU(2) symmetry of the pseudo-fermions therefore reads

$$L = \frac{1}{2} \sum_i \mathrm{Tr} \left[\Psi_i (\mathrm{i} \frac{\partial}{\partial t} + \boldsymbol{A} \cdot \boldsymbol{\sigma}) \Psi_i^\dagger \right] - H. \tag{5.44}$$

CHAPTER 6

Functional renormalization group

The reformulation of the spin Heisenberg Hamiltonian eq. (1.5) in terms of fermionic operators, as discussed in the previous chapter, opens up the possibility of employing standard many-body techniques developed for itinerant fermionic systems. The explicit form of eq. (5.15), however, at the same time severely restricts the applicable techniques. The pseudo-fermions representing localized magnetic moments results in the absence of a kinetic term in the Hamiltonian, which is prohibited by the SU(2) gauge symmetry introduced by the mapping, cf. Section 5.4.6. This lack of a hopping term implies that perturbative approaches, which usually assume the interaction term to be small compared to the kinetics, allowing for an expansion around a non-interacting state.

A non-perturbative approach originally developed in the context of high-energy physics, where especially dealing with the strong nuclear force, breakdown of perturbation theory is ubiquitous, is the FRG [60–62], which extends the ideas of the Wilsonian renormalization group [63, 64] to Green's and vertex functions. Here it has been successfully applied to, e.g., electroweak physics [65], quantum chromodynamics [66–69] and models of quantum gravity [70, 71].

In the context of condensed matter systems, FRG historically was introduced by Wilson in the context of the Kondo problem [72]. More recently, it was utilized to investigate zero dimensional systems such as quantum dots [73–76], Luttinger-Liquid physics in one-dimensional (1D) [77–79] and extensive studies were performed on the Hubbard model [80–90] with respect to superconducting and magnetic instabilities. Using multi-orbital extensions [91] of the method together with *ab initio* models, superconductivity in copper [92], iron [92–96] and nickel-based superconductors [97] were investigated.

In the realm of spin system, which are the main focus of our work, FRG was introduced by Reuther in References [98] and [99] in terms of the Abrikosov pseudo-fermions discussed in Chapter 5. However, before laying out the details of this implementation in Chapter 7, in the current section, we want to introduce the general FRG formalism, without focussing on a particular implementation.

As there is a plethora of reviews [73, 79, 91, 100–102] and textbooks [103] on the method, we aim at giving as concise of an introduction as while being pedagogical enough to follow the derivation of the FRG flow-equations from scratch. In the subsequent discussion, we will follow closely the notation of Reference [99] in this discussion.

6.1 General setup

The main idea behind the renormalization group in general and FRG in particular, is, to make a connection between the fully correlated many-body problem and an effective microscopic description of the same system, based on a single-particle picture.

This connection is made by defining a path through the space of physical models, starting from the microscopic Hamiltonian description, gradually including correlations corresponding to the low-energy sector, till the description arrives at the full physical model.

The most pictorial description of this procedure is the block spin renormalization group due to Kadanoff [104], which prescribes renormalization procedure in real space, grouping together localized spins to coarsen the system and include spatially longer-range correlations into its description.

The FRG aims at a similar procedure, while operating at a more general and formal level. Starting point is a generic fermionic system, described by the Hamiltonian

$$H = H_0 + H_{\text{int}} \tag{6.1}$$

with a kinetic term

$$H_0 = \sum_{k,k'} \zeta_{k,k'} c^\dagger_{k'} c_k, \tag{6.2}$$

where $c^\dagger$ (c) are fermionic creation (annihilation) operators. The indices k, k' represent a full set of generalized quantum numbers labeling the fermions. If one or more of these are continuous the summation implies a suitably normalized integration over the respective quantum numbers. $\zeta_{k,k'}$ is a generalized hopping matrix.

We furthermore consider a generic biquadratic interaction of the form

$$H_{\text{int}} = \sum_{k_1,k_1',k_2,k_2'} V_{k_1,k_2;k_1',k_2'} c^\dagger_{k_1} c^\dagger_{k_2'} c_{k_2} c_{k_1}, \tag{6.3}$$

where the interaction matrix V is antisymmetric under pairwise exchange of indices.

6.2 Generating functionals

Before deriving the FRG equations, we repeat the main elements of the path integral representation of Green's functions, mainly to fix our notation for the following discussions. To this end, we start from the functional integral representation of the partition function given by

$$\begin{aligned}\mathcal{Z} &= \text{Tr}\left[e^{-\beta H}\right] \\ &= \int \mathcal{D}[\bar{\Psi},\Psi] \exp\left[-\int_0^\beta \mathrm{d}\tau \left(\sum_{k,k'} \bar{\Psi}_{k'}(\tau+0^+)(\partial_\tau + \xi_{k,k'})\Psi_k(\tau) \right.\right. \\ &\qquad \left.\left. + \sum_{\substack{k_1,k_1',\\ k_2,k_2'}} \bar{\Psi}_{k_1'}(\tau+0^+)\bar{\Psi}_{k_2'}(\tau+0^+) V_{k_1,k_2;k_1',k_2'} \Psi_{k_2}(\tau)\Psi_{k_1}(\tau)\right)\right]\end{aligned} \tag{6.4}$$

where we replaced the creation and annihilation operators by Grassmann fields Ψ and $\bar{\Psi}$, which are dependent on imaginary time τ. This dependence is periodic with the inverse temperature β. Therefore, the imaginary frequency representation of the fields is given in terms of a discrete Fourier series

$$\Psi_k(\tau) = \frac{1}{\beta}\sum_{\omega_n} \Psi_k(\mathrm{i}\omega_n)\mathrm{e}^{-\mathrm{i}\omega_n\tau} \tag{6.5}$$

with fermionic Matsubara frequencies $\omega_n = (2n+1)\pi/\beta$ ($n \in \mathbb{Z}$). The corresponding inverse transform reads

$$\Psi_k(\mathrm{i}\omega_n) = \int_0^\beta \mathrm{d}\tau\ \Psi_k(\tau)\mathrm{e}^{-\mathrm{i}\omega_n\tau}. \tag{6.6}$$

Introducing the compact notation

$$\left(\bar{\Psi}, A\Psi\right) \equiv \sum_{1,1'} \bar{\Psi}_{1'} A_{1'1} \Psi_1, \tag{6.7}$$

with the multi-index $1 = (\mathrm{i}\omega_1, k_1)$ and again treating sums over this index as sums/integrals over all contained indices, we can rewrite the partition function in the compact form

$$\frac{\mathcal{Z}}{\mathcal{Z}_0} = \frac{1}{\mathcal{Z}_0}\int \mathcal{D}[\bar{\Psi},\Psi]\,\mathrm{e}^{\left(\bar{\Psi},G_0^{-1}\Psi\right) - S_{\mathrm{int}}}, \tag{6.8}$$

where we divide by the noninteracting partition function $\mathcal{Z}_0 = \mathrm{Tr}\left[e^{-\beta H_0}\right]$ to cancel additional factors from possibly changing the integration measure. The inverse bare propagator is given by

$$(G_0^{-1})_{1,1'} = (\mathrm{i}\omega_1 - \xi_{k_1,k_{1'}})\delta(\mathrm{i}\omega_1 - \mathrm{i}\omega_{1'}) \tag{6.9}$$

and we defined the interacting part of the action

$$S_{\mathrm{int}} = \frac{1}{\beta}\sum_{\substack{1,1',\\2,2'}} \delta_{\mathrm{i}\omega_1'+\mathrm{i}\omega_2'-\mathrm{i}\omega_1-\mathrm{i}\omega_2} V_{k_1',k_2';k_1,k_2}\bar{\Psi}_{k_1'}(\mathrm{i}\omega_1')\bar{\Psi}_{k_2'}(\mathrm{i}\omega_2')\Psi_{k_2}(\mathrm{i}\omega_2)\Psi_{k_1}(\mathrm{i}\omega_1). \tag{6.10}$$

From a physical point of view, the objects of interest are the m-particle Green's functions, which are the (imaginary) time-ordered expectation values of m creation and annihilation operators

$$G_m(1',\ldots,m';1,\ldots,m) = (-1)^m\left\langle T\left\{c_{1'}^\dagger\ldots c_{m'}^\dagger c_m\ldots c_1\right\}\right\rangle \tag{6.11}$$

$$= \frac{1}{\mathcal{Z}}\int D[\bar{\Psi},\Psi]\,\bar{\Psi}_{k_1'}(\tau_1')\ldots\bar{\Psi}_{k_m'}(\tau_m')\Psi_{k_m}(\tau_m)\ldots\Psi_{k_1}(\tau_1)e^{\left(\bar{\Psi},G_0^{-1}\Psi\right) - S_{\mathrm{int}}}, \tag{6.12}$$

as these govern the behavior of the quantum system.

The functional integral form eq. (6.12) of this definition hints towards the possibility of defining a generating functional for all Green's function. To this end, we introduce two further Grassmann fields η and $\bar{\eta}$, called source field, and couple these to the original fermionic fields, leading to the generating functional for Green's functions

$$\begin{aligned}\mathcal{W}[\eta,\bar{\eta}] &= \frac{1}{\mathcal{Z}}\int \mathcal{D}[\bar{\Psi},\Psi]e^{\left(\bar{\Psi},G_0^{-1}\Psi\right)-S_{int}-\left(\bar{\Psi},\eta\right)-\left(\bar{\eta},\Psi\right)}\\ &= \frac{\mathcal{Z}[\eta,\bar{\eta}]}{\mathcal{Z}}.\end{aligned} \tag{6.13}$$

Here we have defined an extension $\mathcal{Z}[\eta,\bar{\eta}]$ of the partition sum including the coupling to the source field. The normalization is chosen such that $\mathcal{W}[0,0] = 1$.

From eq. (6.13) we can derive all m-particle Green's functions by taking functional derivatives with respect to the source field and setting them to zero afterward:

$$G_m(1',\dots,m';1,\dots,m) = (-1)^m \frac{\delta}{\delta\bar{\eta}_{1'}}\dots\frac{\delta}{\delta\bar{\eta}_{m'}}\frac{\delta}{\delta\eta_1}\dots\frac{\delta}{\delta\eta_m}\,\mathcal{W}[\eta,\bar{\eta}]\Big|_{\eta=\bar{\eta}=0}. \tag{6.14}$$

The factor $(-1)^m$ is inserted to cancel the signs from the anticommutativity of the Graßmann derivatives. The full Green's functions, however, are cumbersome to work with, as generic operator expectation values always require a cancellation of the disconnected parts of the involved Green's functions [105]. The latter, in a diagrammatic language, can be decomposed into products of two or more other fully connected diagrams, which are not mutually connected.

It is therefore convenient, to distill the fully connected parts of eq. (6.14) from the beginning to avoid the technicalities, which subtractions of (possibly) divergent disconnected parts are accompanied by.

Conveniently, by taking the logarithm of $\mathcal{W}[\eta,\bar{\eta}]$, we obtain the generating functional

$$\mathcal{W}^c[\eta,\bar{\eta}] = \ln(\mathcal{W}[\eta,\bar{\eta}]), \tag{6.15}$$

from which we can obtain the connected m-particle Green's functions by taking functional derivatives analogous to eq. (6.14) [105]:

$$G^c_m(1',\dots,m';1,\dots,m) = (-1)^m \frac{\delta}{\delta\bar{\eta}_{1'}}\dots\frac{\delta}{\delta\bar{\eta}_{m'}}\frac{\delta}{\delta\eta_1}\dots\frac{\delta}{\delta\eta_m}\,\mathcal{W}^c[\eta,\bar{\eta}]\Big|_{\eta=\bar{\eta}=0}. \tag{6.16}$$

Although this new functional reduces the redundant information contained in the full generating functional $\mathcal{W}$ by excluding unconnected contributions, there is still more redundancy in this description: some diagrams can be separated into two mutually unconnected parts by cutting a single line, i.e. they are just products of multiply connected parts and a suitable connecting propagator. For a full description of the physical system, it suffices therefore to know just these one-particle irreducible (1PI) quantities with amputated external legs [105].

The functional generating those objects is the effective action Γ, which can be obtained from $\mathcal{W}^c$ by means of a Legendre transformation

$$\Gamma[\bar{\phi},\phi] = -\mathcal{W}^c[\eta,\bar{\eta}] - (\bar{\phi},\eta) - (\bar{\eta},\phi) + \left(\bar{\phi},G_0^{-1}\phi\right), \tag{6.17}$$

where $\eta,\bar{\eta}$ are now to be treated as functionals of the conjugate external fields $\phi,\bar{\phi}$, obtained by inverting the definitions

$$\phi = -\frac{\delta\mathcal{W}^c}{\delta\bar{\eta}} \qquad \bar{\phi} = \frac{\delta\mathcal{W}^c}{\delta\eta} \tag{6.18}$$

of the latter.

The amputated m-particle vertex γ_m functions can in turn be computed as derivatives of eq. (6.17) with respect to the external fields

$$\gamma_m(1',\dots,m';1,\dots,m) = \frac{\delta}{\delta\bar{\phi}_{1'}}\dots\frac{\delta}{\delta\bar{\phi}_{m'}}\frac{\delta}{\delta\phi_m}\dots\frac{\delta}{\delta\phi_1}\,\Gamma\left[\bar{\phi},\phi\right]\Big|_{\phi=\bar{\phi}=0} \tag{6.19}$$

Note that the definition of the effective action in eq. (6.17) differs from the one used, e.g., in perturbative FRG by the Gaussian term $\left(\bar{\phi},G_0^{-1}\phi\right)$ in the external fields. We include this term to both connect to existing pseudo-fermion functional renormalization group (PFFRG) literature and to simplify the connection between the two-particle vertex and the self-energy, as we will show by relating the second derivatives of the Γ and $\mathcal{W}^c$.

6.3 Connecting different Green's and vertex functions

In the previous section, we have heavily relied on the fact, that Green's functions can be reduced to their connected parts and these in turn can be expressed using one-particle irreducible vertex functions. For a full derivation, we defer the interested reader to the excellent discussions in References [103] and [105]. In the following, we collect the main results on the one- and two-particle functions we will use in our implementation of FRG.

6.3.1 From full to connected Green's functions

Starting from the one-particle Green's function as the most instructive example, we can use the relations between Green's functions and their generating functionals in Equations (6.14) and (6.16) together with the definitions of the latter given in Equations (6.13) and (6.15) to relate

$$\begin{aligned} G_1(1';1) &= -\frac{\delta}{\delta\bar{\eta}_{1'}}\frac{\delta}{\delta\eta_1}\,\mathcal{W}[\eta,\bar{\eta}]\Big|_{\eta=\bar{\eta}=0} \\ &= -\frac{1}{\mathcal{Z}}\frac{\delta}{\delta\bar{\eta}_{1'}}\frac{\delta}{\delta\eta_1}\,\mathcal{Z}[\eta,\bar{\eta}]\Big|_{\eta=\bar{\eta}=0} \\ &= -\left[\frac{1}{\mathcal{Z}[\eta,\bar{\eta}]}\frac{\delta}{\delta\bar{\eta}_{1'}}\frac{\delta}{\delta\eta_1}\mathcal{Z}[\eta,\bar{\eta}]\right]_{\eta=\bar{\eta}=0} \\ &= -\frac{\delta}{\delta\bar{\eta}_{1'}}\frac{\delta}{\delta\eta_1}\,\mathcal{W}^c[\eta,\bar{\eta}]\Big|_{\eta=\bar{\eta}=0} = G_1^c(1';1). \end{aligned} \tag{6.20}$$

This confirms the rather obvious notion, that a one-particle Green's function will always consist of connected diagrams.

The simplest non-trivial relation is found for the two-particle Green's function along similar lines

$$\begin{aligned} G_2(1',2';1,2) &= (-1)^2\frac{1}{\mathcal{Z}}\frac{\delta}{\delta\bar{\eta}_{1'}}\frac{\delta}{\delta\bar{\eta}_{2'}}\frac{\delta}{\delta\eta_1}\frac{\delta}{\delta\eta_2}\,\mathcal{Z}[\eta,\bar{\eta}]\Big|_{\eta=\bar{\eta}=0} \\ &= \frac{1}{\mathcal{Z}}\left[\frac{\delta}{\delta\bar{\eta}_{1'}}\frac{\delta}{\delta\eta_1}\mathcal{Z}[\eta,\bar{\eta}]\frac{\delta}{\delta\bar{\eta}_{2'}}\frac{\delta}{\delta\eta_2}\mathcal{W}^c[\eta,\bar{\eta}]\right]_{\eta=\bar{\eta}=0} \\ &= \left[\frac{\delta}{\delta\bar{\eta}_{1'}}\frac{\delta}{\delta\bar{\eta}_{2'}}\frac{\delta}{\delta\eta_1}\frac{\delta}{\delta\eta_2}\mathcal{W}^c[\eta,\bar{\eta}] + \left(\frac{\delta}{\delta\bar{\eta}_{1'}}\frac{\delta}{\delta\eta_1}\mathcal{W}^c[\eta,\bar{\eta}]\right)\left(\frac{\delta}{\delta\bar{\eta}_{2'}}\frac{\delta}{\delta\eta_2}\mathcal{W}^c[\eta,\bar{\eta}]\right)\right]_{\eta=\bar{\eta}=0} \\ &= G_2^c(1',2';1,2) + G_1^c(1';1)G_1^c(2';2). \end{aligned} \tag{6.21}$$

This decomposition of the full two-particle Green's function into its connected counterpart and products of connected one-particle functions generalizes to m-particle Green's functions, which similarly can be decomposed in connected m-particle Green's functions and products of $n < m$ particle ones [103, 105]. With this realization, we also gain an *a posteriori* justification, that $\mathcal{W}^c$ actually generates connected Green's functions.

6.3.2 Tree expansion

A similar connection, commonly known as *tree expansion* can be made between the connected Green's and the vertex functions generated by the effective interaction Γ. We again illustrate this on the level of one- and two-particle connected Green's functions.

This process, however, is a bit more involved, as the definition of the effective action eq. (6.17) involves a change of field variables in the functional via Legendre transform. We therefore start out derivation by calculating the first derivatives of the effective action with respect to the new field variables

$$\begin{aligned}\frac{\delta\Gamma}{\delta\phi_1} &= -\left(\frac{\delta\mathcal{W}^c}{\delta\eta}, \frac{\delta\eta}{\delta\phi_1}\right) - \left(\frac{\delta\mathcal{W}^c}{\delta\bar{\eta}}, \frac{\delta\bar{\eta}}{\delta\phi_1}\right) + \bar{\eta}_1 - \left(\bar{\phi}\, G_0^{-1}\right)_1 + \left(\bar{\phi}, \frac{\delta\eta}{\delta\phi_1}\right) - \left(\frac{\delta\bar{\eta}}{\delta\phi_1}, \phi\right) \\ &= -\left(\bar{\phi}, \frac{\delta\eta}{\delta\phi_1}\right) - \left(\phi, \frac{\delta\bar{\eta}}{\delta\phi_1}\right) + \bar{\eta}_1 - \left(\bar{\phi}\, G_0^{-1}\right)_1 + \left(\bar{\phi}, \frac{\delta\eta}{\delta\phi_1}\right) - \left(\frac{\delta\bar{\eta}}{\delta\phi_1}, \phi\right) \\ &= \bar{\eta}_1 - \sum_2 \bar{\phi}_2 \left(G_0^{-1}\right)_{21}\end{aligned} \tag{6.22}$$

$$\begin{aligned}\frac{\delta\Gamma}{\delta\bar{\phi}_1} &= -\left(\frac{\delta\mathcal{W}^c}{\delta\eta}, \frac{\delta\eta}{\delta\bar{\phi}_1}\right) - \left(\frac{\delta\mathcal{W}^c}{\delta\bar{\eta}}, \frac{\delta\bar{\eta}}{\delta\bar{\phi}_1}\right) - \eta_1 + \left(G_0^{-1}\phi\right)_1 + \left(\bar{\phi}, \frac{\delta\eta}{\delta\bar{\phi}_1}\right) - \left(\frac{\delta\bar{\eta}}{\delta\bar{\phi}_1}, \phi\right) \\ &= -\eta_1 + \sum_2 \left(G_0^{-1}\right)_{12} \phi_1,\end{aligned} \tag{6.23}$$

where we used eq. (6.18) to simplify the relations.

These we can now can use as a starting point to connect the second derivatives of the generating functionals by using the chain rule of differentiation, by considering

$$\begin{aligned}\delta_{11'} = \frac{\delta\phi_1}{\delta\phi_{1'}} &= -\frac{\delta}{\delta\phi_{1'}} \frac{\delta\mathcal{W}^c}{\delta\bar{\eta}_1} \\ &= -\left(\frac{\delta\eta}{\delta\phi'_1}, \frac{\delta^2\mathcal{W}^c}{\delta\eta\delta\bar{\eta}_1}\right) - \left(\frac{\delta\bar{\eta}}{\delta\phi'_1}, \frac{\delta^2\mathcal{W}^c}{\delta\bar{\eta}\delta\bar{\eta}_1}\right) \\ &= \sum_2 \left[\left(\frac{\delta^2\Gamma}{\delta\phi_{1'}\delta\bar{\phi}_2} - \left(G_0^{-1}\right)_{21'}\right) \frac{\delta^2\mathcal{W}^c}{\delta\eta_2\delta\bar{\eta}_1} - \frac{\delta^2\Gamma}{\delta\phi_{1'}\delta\phi_2} \frac{\delta^2\mathcal{W}^c}{\delta\bar{\eta}_2\delta\bar{\eta}_1}\right],\end{aligned} \tag{6.24}$$

and

$$\begin{aligned}0 = \frac{\delta\bar{\phi}_1}{\delta\phi_{1'}} &= \sum_2 \left[\left(-\frac{\delta^2\Gamma}{\delta\phi_{1'}\delta\bar{\phi}_2} + \left(G_0^{-1}\right)_{21'}\right) \frac{\delta^2\mathcal{W}^c}{\delta\eta_2\delta\eta_1} - \frac{\delta^2\Gamma}{\delta\phi_{1'}\delta\phi_2} \frac{\delta^2\mathcal{W}^c}{\delta\bar{\eta}_2\delta\eta_1}\right].\end{aligned} \tag{6.25}$$

Similar expressions for $\delta\bar{\phi}_1/\delta\bar{\phi}_{1'}$ and $\delta\phi_1/\delta\bar{\phi}_{1'}$ can be computed. Combining all these equations, we find the matrix relation [98]

$$\mathcal{V} = \begin{pmatrix} \frac{\delta^2\mathcal{W}^c}{\delta\bar{\eta}\delta\eta} & -\frac{\delta^2\mathcal{W}^c}{\delta\bar{\eta}\delta\bar{\eta}} \\ -\frac{\delta^2\mathcal{W}^c}{\delta\eta\delta\eta} & \frac{\delta^2\mathcal{W}^c}{\delta\eta\delta\bar{\eta}} \end{pmatrix} = \begin{pmatrix} \frac{\delta^2\Gamma}{\delta\bar{\phi}\delta\phi} + G_0^{-1} & \frac{\delta^2\Gamma}{\delta\bar{\phi}\delta\bar{\phi}} \\ \frac{\delta^2\Gamma}{\delta\phi\delta\phi} & \frac{\delta^2\Gamma}{\delta\phi\delta\bar{\phi}} - \left(G_0^{-1}\right)^T \end{pmatrix}^{-1}. \tag{6.26}$$

Setting the external fields η and $\bar{\eta}$ to zero on both sides of eq. (6.26) and assuming, that the second derivatives of the free energy with respect to two fields of the same kind is vanishing[1], we find for the upper left component of eq. (6.26)

$$G_1^c(1';1) = \frac{\delta^2\mathcal{W}^c}{\delta\bar{\eta}_{1'}\delta\eta_1}\bigg|_{\eta=\bar{\eta}=0} = \left(\frac{\delta^2\Gamma}{\delta\bar{\phi}'_1\delta\phi_1}\bigg|_{\phi=\bar{\phi}=0} + G_0^{-1}(1';1)\right)^{-1} = \left(\gamma_1(1';1) + G_0^{-1}(1';1)\right)^{-1}. \tag{6.27}$$

[1] This has always to be the case, as long as the particle number is conserved, which is especially true for Abrikosov Pseudo-Fermions, as a result of the SU(2) gauge symmetry inherent in this mapping, see Section 5.2.

Now eq. (6.27) is simply Dyson's equation, where the one-particle vertex γ_1 takes on the role of the negative self-energy Σ:

$$\gamma_1 = -\Sigma\,. \tag{6.28}$$

Note, that we have found this identity directly, as we have included the Gaussian part in eq. (6.17). If we had taken a pure Legendre transform $\mathcal{W}^c$ without the Gaussian part, eq. (6.28) would contain an additive inverse bare propagator on the right-hand side. The addition of the Gaussian part is however only relevant for the one-particle vertex, as it vanishes due to the higher derivatives of $\mathcal{W}^c$ with respect to the source fields taken to calculate $m > 2$-particle vertices.

The tree expansion for the connected two-particle Green's function G_2^c follows the same line of argument, starting from higher derivatives of the field ϕ and $\bar{\phi}$ with respect to themselves. As this calculation is more involved, we refer the interested reader to References [103] and [105] for details and only cite the result. The connected two-particle Green's function can be expressed as a two-particle vertex function with a single-particle Green's function attached to each of the external legs:

$$G_2^c(1',2';1,2) = \sum_{3',4',3,4} G_1^c(1';3')G_1^c(2';4')\gamma_2(3',4';3,4)G_1^c(3;1)G_1^c(4;2). \tag{6.29}$$

As, according to eq. (6.20) connected and full one-particle Green's function are equivalent, G_1^c in eq. (6.29) can equally well be replaced by G_1.

6.4 Flow-equations

Having discussed the definitions of the relevant generating functionals as well as the connections of the different Green's and vertex functions one can obtain from these, we are now well-equipped to derive the so-called flow equations of FRG. In particular, we aim for an renormalization group (RG) equation for the effective action defined in eq. (6.17), as it both contains all physical information and, at the same time, we can deduce sensible initial conditions for the flow, as we will show in Section 6.6.

The FRG aims at connecting the microscopic physical model, only containing high-energy degrees of freedom, in a controlled way to the low energy model containing all correlations induced by interactions, as already discussed in the beginning of this chapter. This is achieved by defining a path through the space of physical models, which connects these two limits and along its way includes more and more low-energy degrees of freedom.

In FRG such a flow is implemented in frequency space by introducing a multiplicative regulator function $R(\omega,\Lambda)$ in the free propagator, which suppresses all degrees of freedom below a cut-off Λ. Then, starting from the high-energy limit $\Lambda \to \infty$ the full theory can be obtained by lowering the cut-off down to $\Lambda = 0$.

We, therefore, have to consider a regulated bare propagator

$$G_0(i\omega) \to G_0^\Lambda(i\omega) = R(\omega,\Lambda)G_0(i\omega), \tag{6.30}$$

which depends on the scale by means of the regulator. To implement the desired RG flow, the regulator function has to fulfill

$$R(\omega,\Lambda) = \begin{cases} 0 & \text{for} \quad \Lambda \to \infty \\ 1 & \text{for} \quad \Lambda \to 0, \end{cases} \tag{6.31}$$

meaning, that

$$G_0^\Lambda = \begin{cases} 0 & \text{for} \quad \Lambda \to \infty \\ G_0 & \text{for} \quad \Lambda \to 0. \end{cases} \tag{6.32}$$

This implies, that the regulator effectively freezes out all fluctuations with $\omega \lesssim \Lambda$ and therefore at $\Lambda \to \infty$ no correlations can build up. In principle, one could also use a momentum space regulator, as regularly done for itinerant fermion systems citePlatt2013, but due to the strict locality of the pseudo-fermion Hamiltonian discussed in Section 5.4.6 we will refrain from this possibility and use the frequency regulator discussed here.

Replacing all propagators according to eq. (6.30), all generating functionals and consequently all Green's and vertex functions acquire a dependence on the flow parameter Λ.

6.4.1 Flow of the generating functionals for Green's functions

As a first intermediate step, we will derive the flow equation for the generating functional of the connected m-particle Green's functions $\mathcal{W}^c$ defined in eq. (6.15). We, however, not only implement the replacement of the propagators eq. (6.30), but for convenience, we also change $\mathcal{Z} \to \mathcal{Z}_0^\Lambda$ in the denominator. This modifies $\mathcal{W}^c$ and therefore the effective action only by an additional constant $\ln\left(\mathcal{Z}^\Lambda / \mathcal{Z}_0^\Lambda\right)$, independent of the external fields, such that both the connected Green's functions and vertex functions are unchanged by this replacement.

To derive the flow equations we now take the derivative of eq. (6.15) after doing the replacements and find

$$\begin{aligned}
\frac{\mathrm{d}\mathcal{W}^{c,\Lambda}}{\mathrm{d}\Lambda} =& \frac{1}{\mathcal{W}^\Lambda}\frac{\mathrm{d}}{\mathrm{d}\Lambda}\left[\frac{1}{\mathcal{Z}_0^\Lambda}\int D[\bar\Psi,\Psi] \mathrm{e}^{\left(\bar\Psi,\left(G_0^\Lambda\right)^{-1}\Psi\right) - S_{\mathrm{int}} - \left(\bar\Psi,\eta\right) - \left(\bar\eta,\Psi\right)}\right] \\
=& \frac{1}{\mathcal{W}^\Lambda}\frac{1}{\mathcal{Z}_0^\Lambda}\int D[\bar\Psi,\Psi]\left(\bar\Psi, \frac{\mathrm{d}\left(G_0^\Lambda\right)^{-1}}{\mathrm{d}\Lambda}\Psi\right) e^{\left(\bar\Psi,\left(G_0^\Lambda\right)^{-1}\Psi\right) - S_{\mathrm{int}} - \left(\bar\Psi,\eta\right) - \left(\bar\eta,\Psi\right)} - \frac{1}{\mathcal{Z}_0^\Lambda}\frac{\mathrm{d}\mathcal{Z}_0^\Lambda}{\mathrm{d}\Lambda} \\
=& -\frac{1}{\mathcal{W}^\Lambda}\left(\frac{\delta}{\delta\eta}, \frac{\mathrm{d}\left(G_0^\Lambda\right)^{-1}}{\mathrm{d}\Lambda}\frac{\delta}{\delta\bar\eta}\right)\mathcal{W}^\Lambda - \frac{1}{\mathcal{Z}_0^\Lambda}\int D[\bar\Psi,\Psi]\left(\bar\Psi, \frac{\mathrm{d}\left(G_0^\Lambda\right)^{-1}}{\mathrm{d}\Lambda}\Psi\right)\mathrm{e}^{\left(\bar\Psi,\left(G_0^\Lambda\right)^{-1}\Psi\right)} \\
=& -\frac{1}{\mathcal{W}^\Lambda}\left(\frac{\delta}{\delta\eta}, \frac{\mathrm{d}\left(G_0^\Lambda\right)^{-1}}{\mathrm{d}\Lambda}\frac{\delta}{\delta\bar\eta}\right)\mathcal{W}^\Lambda - \sum_{1,1'}\left(\frac{\mathrm{d}\left(G_0^\Lambda\right)^{-1}}{\mathrm{d}\Lambda}\right)_{1,1'}\frac{1}{\mathcal{Z}_0^\Lambda}\int D[\bar\Psi,\Psi]\bar\Psi_1\Psi_{1'}\mathrm{e}^{\left(\bar\Psi,\left(G_0^\Lambda\right)^{-1}\Psi\right)} \\
=& -\frac{1}{\mathcal{W}^\Lambda}\left(\frac{\delta}{\delta\eta}, \frac{\mathrm{d}\left(G_0^\Lambda\right)^{-1}}{\mathrm{d}\Lambda}\frac{\delta}{\delta\bar\eta}\right)\mathcal{W}^\Lambda - \sum_{1,1'}\left(\frac{\mathrm{d}\left(G_0^\Lambda\right)^{-1}}{\mathrm{d}\Lambda}\right)_{1,1'}\left(G_0^\Lambda\right)_{1',1} \\
=& -\frac{1}{\mathcal{W}^\Lambda}\left(\frac{\delta}{\delta\eta}, \frac{\mathrm{d}\left(G_0^\Lambda\right)^{-1}}{\mathrm{d}\Lambda}\frac{\delta}{\delta\bar\eta}\right)\mathcal{W}^\Lambda - \mathrm{Tr}\left[\frac{\mathrm{d}\left(G_0^\Lambda\right)^{-1}}{\mathrm{d}\Lambda}G_0^\Lambda\right],
\end{aligned} \tag{6.33}$$

where we used, the definition of the bare propagator in functional integral language in the second-to-last step. To connect to the effective action we have to simplify the first term in (6.33) further by using (6.15) and explicitly taking the derivatives to find

$$
\begin{aligned}
\frac{\mathrm{d}\mathcal{W}^{c,\Lambda}}{\mathrm{d}\Lambda} &= -\,\mathrm{e}^{-\mathcal{W}^{c,\Lambda}} \sum_{1,1'} \left(\frac{\mathrm{d}\left(G_0^\Lambda\right)^{-1}}{\mathrm{d}\Lambda}\right)_{1,1'} \frac{\delta}{\delta\eta_1}\frac{\delta}{\delta\bar{\eta}_{1'}} \mathrm{e}^{\mathcal{W}^{c,\Lambda}} - \mathrm{Tr}\left[\frac{\mathrm{d}\left(G_0^\Lambda\right)^{-1}}{\mathrm{d}\Lambda} G_0^\Lambda\right] \\
&= -\,\mathrm{e}^{-\mathcal{W}^{c,\Lambda}} \sum_{1,1'} \left(\frac{\mathrm{d}\left(G_0^\Lambda\right)^{-1}}{\mathrm{d}\Lambda}\right)_{1,1'} \frac{\delta}{\delta\eta_1} \mathrm{e}^{\mathcal{W}^{c,\Lambda}} \frac{\delta\mathcal{W}^{c,\Lambda}}{\delta\bar{\eta}_{1'}} - \mathrm{Tr}\left[\frac{\mathrm{d}\left(G_0^\Lambda\right)^{-1}}{\mathrm{d}\Lambda} G_0^\Lambda\right] \\
&= -\sum_{1,1'} \left(\frac{\mathrm{d}\left(G_0^\Lambda\right)^{-1}}{\mathrm{d}\Lambda}\right)_{1,1'} \frac{\delta\mathcal{W}^{c,\Lambda}}{\delta\eta_1}\frac{\delta\mathcal{W}^{c,\Lambda}}{\delta\bar{\eta}_{1'}} - \sum_{1,1'} \left(\frac{\mathrm{d}\left(G_0^\Lambda\right)^{-1}}{\mathrm{d}\Lambda}\right)_{1,1'} \frac{\delta^2\mathcal{W}^{c,\Lambda}}{\delta\eta_1\delta\bar{\eta}_{1'}} - \mathrm{Tr}\left[\frac{\mathrm{d}\left(G_0^\Lambda\right)^{-1}}{\mathrm{d}\Lambda} G_0^\Lambda\right] \\
&= -\,\mathrm{Tr}\left[\frac{\mathrm{d}\left(G_0^\Lambda\right)^{-1}}{\mathrm{d}\Lambda} G_0^\Lambda\right] + \mathrm{Tr}\left[\left(\frac{\mathrm{d}\left(G_0^\Lambda\right)^{-1}}{\mathrm{d}\Lambda}\right)\frac{\delta^2\mathcal{W}^{c,\Lambda}}{\delta\bar{\eta}\delta\eta}\right] - \left(\frac{\delta\mathcal{W}^{c,\Lambda}}{\delta\eta}, \frac{\mathrm{d}\left(G_0^\Lambda\right)^{-1}}{\mathrm{d}\Lambda}\frac{\delta\mathcal{W}^{c,\Lambda}}{\delta\bar{\eta}}\right)
\end{aligned}
\tag{6.34}
$$

This flow equation is the starting point for a field theoretical method known as exact renormalization group.

6.4.2 Flow of the effective interaction

For FRG, however, we want to focus on the flow of the effective action, defined in eq. (6.17). To arrive there, we first have to note, that by changing the independent variable from η to ϕ in the Legendre transform means, that the former acquire a dependence on the renormalization scale Λ by the relation eq. (6.18), while the latter, being an external source field, do not.

Taking the derivative of eq. (6.17) the flow is found to be

$$
\begin{aligned}
\frac{\mathrm{d}\Gamma^\Lambda}{\mathrm{d}\Lambda} &= -\frac{\mathrm{d}\mathcal{W}^{c,\Lambda}[\eta^\Lambda,\bar{\eta}^\Lambda]}{\mathrm{d}\Lambda} - \left(\bar{\phi}, \frac{\partial\eta^\Lambda}{\partial\Lambda}\right) - \left(\frac{\partial\bar{\eta}^\Lambda}{\partial\Lambda}, \phi\right) + \left(\bar{\phi}, \frac{\partial\left(G_0^\Lambda\right)^{-1}}{\partial\Lambda}\phi\right) \\
&= -\frac{\partial\mathcal{W}^{c,\Lambda}}{\partial\Lambda} - \sum_1 \left(\frac{\partial\eta_1^\Lambda}{\partial\Lambda}\frac{\delta\mathcal{W}^{c,\Lambda}}{\delta\eta_1^\Lambda} + \frac{\partial\bar{\eta}_1^\Lambda}{\partial\Lambda}\frac{\delta\mathcal{W}^{c,\Lambda}}{\delta\bar{\eta}_1^\Lambda}\right) - \left(\bar{\phi}, \frac{\partial\eta^\Lambda}{\partial\Lambda}\right) - \left(\frac{\partial\bar{\eta}^\Lambda}{\partial\Lambda}, \phi\right) + \left(\bar{\phi}, \frac{\partial\left(G_0^\Lambda\right)^{-1}}{\partial\Lambda}\phi\right) \\
&= -\frac{\partial\mathcal{W}^{c,\Lambda}}{\partial\Lambda} + \left(\bar{\phi}, \frac{\partial\left(G_0^\Lambda\right)^{-1}}{\partial\Lambda}\phi\right).
\end{aligned}
\tag{6.35}
$$

Note the order of the factors in the second term of eq. (6.35), which have been simplified using eq. (6.18). Substituting eq. (6.34) we can remove the dependence on $\mathcal{W}^{c,\Lambda}$

$$
\begin{aligned}
\frac{\mathrm{d}\Gamma^\Lambda}{\mathrm{d}\Lambda} &= \mathrm{Tr}\left[\frac{\mathrm{d}\left(G_0^\Lambda\right)^{-1}}{\mathrm{d}\Lambda} G_0^\Lambda\right] - \mathrm{Tr}\left[\left(\frac{\mathrm{d}\left(G_0^\Lambda\right)^{-1}}{\mathrm{d}\Lambda}\right)\frac{\delta^2\mathcal{W}^{c,\Lambda}}{\delta\bar{\eta}\delta\eta}\right] - \left(\bar{\phi}, \frac{\partial\left(G_0^\Lambda\right)^{-1}}{\partial\Lambda}\phi\right) + \left(\bar{\phi}, \frac{\partial\left(G_0^\Lambda\right)^{-1}}{\partial\Lambda}\phi\right) \\
&= \mathrm{Tr}\left[\frac{\mathrm{d}\left(G_0^\Lambda\right)^{-1}}{\mathrm{d}\Lambda} G_0^\Lambda\right] - \mathrm{Tr}\left[\left(\frac{\mathrm{d}\left(G_0^\Lambda\right)^{-1}}{\mathrm{d}\Lambda}\right)\mathcal{V}_{1,1}^\Lambda\right],
\end{aligned}
\tag{6.36}
$$

where $\mathcal{V}_{1,1}^\Lambda$ is the upper left component of eq. (6.26).

Equation (6.36), also known as Wetterich equation [62], is the central object of FRG, which we will in the following make amenable to numerical treatment.

6.4.3 Vertex function flow

Although representing an exact relation, the flow of the effective Action eq. (6.36) in its current form is not suitable for numerical investigations. As the physically interesting vertex functions can only be obtained from Γ by the means of functional derivatives, one would be faced to track the complete functional structure in a solution of eq. (6.36). Both analytically and numerically, this is an insurmountable task, such that we resort to further refining this equation.

To this end, consider the definition of the vertex functions in eq. (6.19). From it, we can infer an expansion of the effective action in terms of the source fields

$$\Gamma^\Lambda = \sum_{k=1}^{\infty} \frac{(-1)^k}{k!} \sum_{1',\dots,k'} \sum_{1,\dots,k} \gamma_k^\Lambda(1',\dots,k';1,\dots,k)\bar{\phi}_{1'}\dots\bar{\phi}_{k'}\phi_k\dots\phi_1, \tag{6.37}$$

which we can substitute directly into the left-hand side of eq. (6.36). Expanding also the right-hand side of this equation and comparing coefficients will lead to a set of flow equations for the m-paricle vertices. To this end, we rewrite $\mathcal{V}$ aiming at the use of a geometric series according to

$$\mathcal{V}^\Lambda = \begin{pmatrix} \frac{\delta^2\Gamma^\Lambda}{\delta\bar{\phi}\delta\phi} + \left(G_0^\Lambda\right)^{-1} & \frac{\delta^2\Gamma^\Lambda}{\delta\bar{\phi}\delta\bar{\phi}} \\ \frac{\delta^2\Gamma^\Lambda}{\delta\phi\delta\phi} & \frac{\delta^2\Gamma^\Lambda}{\delta\phi\delta\bar{\phi}} - \left[\left(G_0^\Lambda\right)^{-1}\right]^T \end{pmatrix}^{-1} \tag{6.38}$$

$$= \left[1 - \begin{pmatrix} -G^\Lambda & 0 \\ 0 & \left[G_0^\Lambda\right]^T \end{pmatrix} \begin{pmatrix} \mathcal{U}^\Lambda & \frac{\delta^2\Gamma^\Lambda}{\delta\bar{\phi}\delta\bar{\phi}} \\ \frac{\delta^2\Gamma^\Lambda}{\delta\phi\delta\phi} & -\mathcal{U}^\Lambda \end{pmatrix}\right]^{-1} \cdot \begin{pmatrix} -G^\Lambda & 0 \\ 0 & \left[G^\Lambda\right]^T \end{pmatrix}, \tag{6.39}$$

where we have defined the shorthand $\mathcal{U}^\Lambda = \frac{\delta^2\Gamma^\Lambda}{\delta\bar{\phi}\delta\phi} - \gamma_1$. This enables us to perform an expansion of the upper left entry of $\mathcal{V}^\Lambda$ in terms of propagators

$$\mathcal{V}_{1,1}^\Lambda = G^\Lambda - G^\Lambda\mathcal{U}^\Lambda G^\Lambda + G^\Lambda\mathcal{U}^\Lambda G^\Lambda\mathcal{U}^\Lambda G^\Lambda - G^\Lambda\frac{\delta^2\Gamma^\Lambda}{\delta\bar{\phi}\delta\bar{\phi}}\left[G^\Lambda\right]^T\frac{\delta^2\Gamma^\Lambda}{\delta\phi\delta\phi}G^\Lambda + \dots \tag{6.40}$$

Please note, that in this expansion the double derivatives with respect to the same kind of field do not vanish even in symmetry unbroken phases, as source fields are not set to zero in this calculation.

Finally, combining the Wetterich equation eq. (6.36), the vertex expansion of the effective action eq. (6.37) and the expansion of the matrix $\mathcal{V}$ eq. (6.40), we can find the flow equations for the one- and two-particle vertices by comparing the coefficients in the Wetterich equation for terms quadratic and quartic in the source field, respectively.

For the two-particle vertex, we find

$$\frac{\mathrm{d}}{\mathrm{d}\Lambda}\gamma_1^\Lambda(1';1) = \sum_{2',2}\gamma_2^\Lambda(1',2';1,2)S^\Lambda(2,2') \tag{6.41}$$

with the so-called single-scale propagator

$$S^\Lambda = G^\Lambda\frac{\mathrm{d}\left(G_0^\Lambda\right)^{-1}}{\mathrm{d}\Lambda}G^\Lambda = -\frac{\mathrm{d}}{\mathrm{d}\Lambda}\,G^\Lambda\Big|_{\gamma_1^\Lambda=\text{const}} \tag{6.42}$$

as the derivate of the full propagator with respect to the scale Λ without considering the scale dependence of the one-particle vertex, i.e. not including the contributions of the self-energy flow.

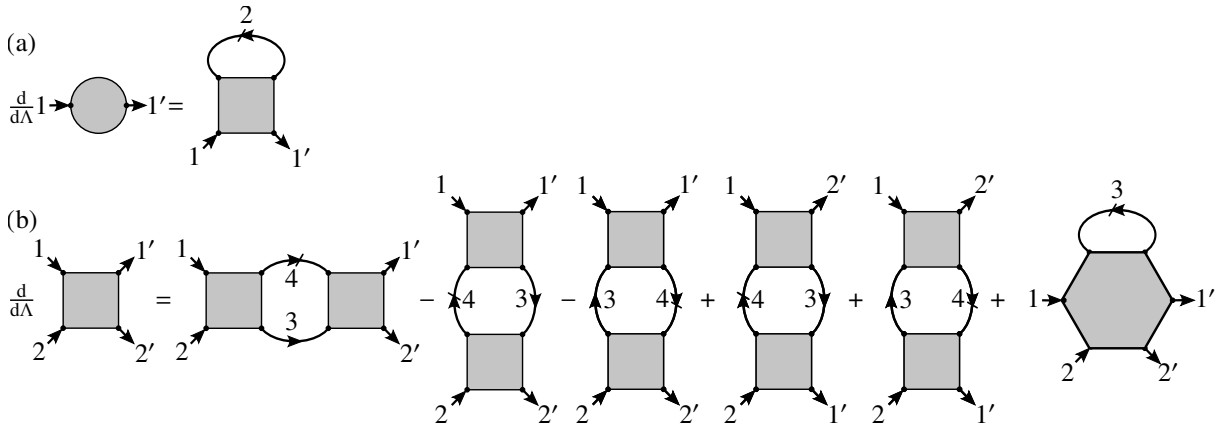

Figure 6.1: Diagrammatic representation of the FRG flow equations of the (a) one-particle (circle, eq. (6.41)) and (b) two-particle vertex (square, eq. (6.43)). The hexagon denotes the three-particle vertex, arrows represent full Green's functions G^Λ, while slashed arrows are single scale propagators S^Λ. The label corresponding to a propagator means, that it depends on both the primed and unprimed variable.

From eq. (6.41) we immediately see, that the two-particle vertex couples both to itself, as it is part of the full propagator G^Λ via Dyson's equation eq. (6.27), but also to the two-particle vertex γ_2^Λ. This is a recurring theme, as in the flow for the two-particle vertex

$$\begin{aligned}\gamma_2^\Lambda(1',2';1,2) = \sum_{3',4',3,4} \big[&\gamma_2^\Lambda(1',2';3,4)\gamma_2^\Lambda(3',4';1,2)\\ &-\gamma_2^\Lambda(1',4';1,3)\gamma_2^\Lambda(3',2';4,2) - (3'\leftrightarrow 4', 3\leftrightarrow 4)\\ &+\gamma_2^\Lambda(2',4';1,3)\gamma_2^\Lambda(3',1';4,2) + (3'\leftrightarrow 4', 3\leftrightarrow 4)\big]\\ &\times G^\Lambda(3,3')S^\Lambda(4,4')\\ +\sum_{3',3}&\gamma_3^\Lambda(1',2',3';1,2,3)S^\Lambda(2,3')\end{aligned} \tag{6.43}$$

also one- (through G^Λ), two- and even three-particle vertices enter.

Along the same lines, one can calculate flow equations for all m-particle vertices. As exemplified here, these equations will depend on all other vertices up to the $(m+1)$-particle order. Therefore, the vertex flow equations form an infinite system of coupled ordinary differential equations.[2] This is the direct result of the appearance of second derivatives with respect to external sources in $\mathcal{V}_{1,1}^\Lambda$.

A diagrammatic representation of the flow equations is shown in Figure 6.1. It decomposes into four classes of diagrams: the first line in eq. (6.43), corresponding to the first diagram in Figure 6.1(b) is the particle-particle diagram, also called s-channel in literature[3]. The second line of eq. (6.43) (second and third diagram) are called direct particle-hole diagrams or alternatively t-channel. The crossed particle hole terms are found in the third line of eq. (6.43) (fourth and fifth diagram), which are also dubbed u-channel contributions. The last contribution (fourth line/last diagram) concerns the influence of the three-particle vertex on the flow of γ_2. This part will be the focus of the approximations we employ in the following section.

[2] The flow equations are often considered to be integro-differential equations. This notion is however wrong, as the integrals on the right-hand side, included in the multi-index sums, do not run over the scale Λ, which is the variable with respect to which the derivatives are taken. The frequency integrals therefore only constitute scalar product-like couplings within the functional vector space of the vertex functions.

[3] In the literature on itinerant fermion FRG s-, t- and u-channel are also referred to as parallel (p), crossed (x) and antiparallel (a) diagrams.

6.5 Truncation of the flow

As an infinite set of differential equations is not amenable to a numerical treatment, we have to introduce an approximation, which truncates this hierarchy after a finite number of equations. Note, that, up to now, the derivation of the flow equations was completely exact.

The most commonly employed simplification is done, by setting all m-particle vertices with $m \geq 3$ to zero

$$\gamma^{\Lambda}_{m\geq 3} \equiv 0, \tag{6.44}$$

effectively removing all three- and higher-particle correlations from the system. For itinerant fermions, this can be justified by a power-counting argument, as the three-particle vertex has to be of higher order in the initial interaction than the two-particle one [84, 91]. This in turn means, that for small enough interactions with respect to the bandwidth, the three-particle vertex can be neglected as long as the system does not flow to strong coupling.

For purely interacting systems like the Abrikosov pseudo-fermions we will deal with, this approximation, however, is *a priori* not justified and indeed does not capture the relevant physics in the sense, that no quantum paramagnetic behavior shows up in the corresponding calculations [59, 98, 99].

It was, however, realized early on [98, 99], that the so-called Katanin substitution [106] cures this problem. It amounts to a replacement of the single scale propagator with the full scale-derivative of the full propagator

$$S^{\Lambda} = -\frac{\mathrm{d}}{\mathrm{d}\Lambda} G^{\Lambda}\Big|_{\gamma_1^{\Lambda}=\text{const}} \rightarrow S^{\Lambda}_{\text{kat}} = -\frac{\mathrm{d}}{\mathrm{d}\Lambda} G^{\Lambda}\Big|_{\gamma_1^{\Lambda}=\text{const}} = S^{\Lambda} + \left(G^{\Lambda}\right)^2 \frac{\mathrm{d}}{\mathrm{d}\Lambda}\gamma_1^{\Lambda}. \tag{6.45}$$

in the flow equation for the two-particle vertex, but not the one-particle one.

Such a substitution has been shown to improve the fulfillment of the Ward identities to a consistent order of the approximation [106]. We will use this scheme in the remainder of this thesis.

The Katanin truncation can also be viewed as including parts of the three-particle vertex contributions back into the flow of the two-particle vertex. We will discuss this notion in more detail in Section 8.1.

6.6 Initial conditions

As any differential equation, we have to supply the flow equations Equations (6.41) and (6.43) with initial conditions. These can be found in an involved formal derivation, utilizing the generating functional for amputated connected Green's functions we have not considered here [107]. Instead, we will here take a more intuitive route: At the initial cut-off $\Lambda \rightarrow \infty$, all propagator lines, that could constitute diagrams contributing to the effective action vanish due to the regulator introduced in FRG. Hence, the only diagrammatic contributions to the one-particle irreducible vertex functions, and therefore the effective action, are constituted solely by the interactions present in the microscopic action, given by eq. (6.10), and we conclude

$$\Gamma^{\Lambda\rightarrow\infty} = S_{\text{int}}. \tag{6.46}$$

Inserting the vertex expansion eq. (6.37) and comparing coefficients, we end up at the initial conditions for the specific quartic interaction term defined in eq. (6.10), which are given by

$$\gamma_1^{\Lambda\rightarrow\infty} = 0 \tag{6.47}$$

$$\gamma_2^{\Lambda\to\infty}(1',2';1,2) = 4V_{1',2';1,2} \tag{6.48}$$

$$\gamma_{m\geq 3}^{\Lambda\to\infty} = 0. \tag{6.49}$$

To conclude the discussion of initial conditions, let us note another reason for relying on the flow of the effective action instead of building up from eq. (6.34), which describes the scale derivative of the generating functional for the connected Green's functions $\mathcal{W}^c$.

Starting from its definition in eq. (6.15), combined with the definition of the generating functional for interacting Green's functions eq. (6.13), we find

$$\mathcal{W}^c = \ln(\mathcal{Z}[\eta,\bar{\eta}]) - \ln(\mathcal{Z}). \tag{6.50}$$

Taking now the limit $\Lambda \to \infty$, implying $G_0^{\Lambda\to\infty} \to 0$, we find from eq. (6.13), that $\mathcal{Z}[\eta,\bar{\eta}] \to \mathcal{Z}$, i.e. the interactions become negligible compared to the kinetic part of the action. This implies, that $\mathcal{W}^c \to 0$ in the initial limit $\Lambda \to \infty$, removing any notion of the interactions defining the physical system and rendering the initial condition problem given by eq. (6.34) ill-defined.

CHAPTER 7

Pseudo-Fermion Functional renormalization group

Having introduced both the Abrikosov pseudo-fermion representation and its properties in Chapter 5, as well as the general formalism of FRG in Chapter 6, our goal now is to fuse both together, resulting in the pseudo-fermion functional renormalization group (PFFRG). To this end, we will use the symmetry relations obtained in Section 5.4 to establish the parametrization of one- and two-particle vertices as well as the corresponding flow equations.

7.1 Symmetry constrained parametrization of the self-energy

As a first step, we want to analyze the one-particle vertex γ_1, following closely the derivation given in Reference [59]. As it generically is equivalent to the self-energy (up to a sign), cf. eq. (6.28), we from hereon will switch notation and only consider the pseudo-fermionic self-energy $\Sigma^\Lambda(1';1)$.

To better understand its properties, recall Dyson's equation, eq. (6.27), which relates the connected Green's function and the self-energy. The former is, according to eq. (6.20) equivalent to the full Green's function. Upon inspection of Table 5.1 we realize, that the full one-particle Green's function for any pseudo-fermionic system has to be diagonal in all its quantum numbers, as we will outline in the following.

The local U(1) symmetry guarantees locality in real space. In combining with the lattice space group symmetries, we find, that there even cannot be any dependence on the explicit real space coordinate, as we can map any real space point back to a given reference point using translations.[1] Time-translation invariance dictates diagonality in Matsubara frequency space due to energy conservation according to Noether's theorem [108].

As an intermediate result, we collect these findings in the parametrization

$$G(1',1) = \left(G^\nu(\omega_1)\sigma^\nu_{\mu_{1'}\mu_1}\right)\delta_{i_{1'}i_1}\delta_{\omega_{1'},\omega_1}, \tag{7.1}$$

where we have expanded the remaining spin structure in terms of Pauli matrices. A sum over $\nu \in \{0,1,2,3\}$ is implied, where σ^1, σ^2 and σ^3 denote the standard Pauli matrices, which are supplemented by the 2×2 unit matrix σ^0.

Combining hermitian and time-reversal symmetry, we find the relation

$$G^\nu(\omega_1)\sigma^\nu_{\mu_{1'}\mu_1} = \mu_{1'}\mu_1 G^\nu(\omega_1)\sigma^\nu_{\bar{\mu}_1\bar{\mu}_{1'}}, \tag{7.2}$$

[1] This is only strictly true for Archimedean lattices, which only feature equivalent lattice sites. If there are n symmetry inequivalent classes of sites in the lattice, we would have to consider n components of the one-particle Green's function.

which we can simplify realizing, that

$$\mu_{1'}\mu_1\sigma^{\nu}_{\bar{\mu}_1\bar{\mu}_{1'}} = \mu_{1'}\mu_1\left(\sigma^{\nu}_{\bar{\mu}_{1'}\bar{\mu}_1}\right)^* = \xi(\nu)\sigma^{\nu}_{\mu_{1'}\mu_1} \tag{7.3}$$

with

$$\xi(\nu) = \begin{cases} 1 & \nu = 0 \\ -1 & \nu \in \{1,2,3\}. \end{cases} \tag{7.4}$$

This relation is purely based on the properties of Pauli matrices and will help to remove the spin-dependent prefactors of the symmetry relations in all following discussions.

For the one-particle Green's function, this simplifies the combined time-reversal and hermitian symmetry eq. (7.2) to

$$G^{\nu}(\omega_1) = \xi(\nu)G^{\nu}(\omega_1), \tag{7.5}$$

implying, that only the $\nu = 0$ component is non-vanishing, rendering the one-particle Green's function diagonal in the spin index.

Along the same lines, we find that particle-hole symmetry leads to a symmetry statement with respect to the frequency argument of G^{ν}

$$G^{\nu}(\omega_1) = -\xi(\nu)G^{\nu}(-\omega_1), \tag{7.6}$$

i.e. the non-vanishing $\nu = 0$ component of the Green's function is antisymmetric in frequency space.

Finally, by combining time-reversal and particle hole symmetry, we can conclude, that

$$G^{\nu}(\omega_1) = -\xi(\nu)G^{\nu}(\omega_1)^*. \tag{7.7}$$

Therefore, in total, the one-particle Green's function can be parametrized as

$$G(1',1) = G(\omega_1)\delta_{i_{1'}i_1}\delta_{\omega_{1'},\omega_1}\delta_{\mu_{1'},\mu_1} \tag{7.8}$$

with an imaginary antisymmetric function $G(\omega)$. To connect to the one-particle vertex function we have to invoke Dyson's equation eq. (6.27). Realizing, that for a generic pseudo-fermionic Hamiltonian given in eq. (5.15), which lacks any kinetic term, the non-interacting one-particle Green's function $G_0(\omega)$ is given by

$$G_0(\omega) = \frac{1}{\mathrm{i}\omega}. \tag{7.9}$$

This means, that Dyson's equation assumes the simple form

$$G(1';1) = \frac{1}{\mathrm{i}\omega_1\delta_{\omega_{1'},\omega_1} - \Sigma(1';1)}\,. \tag{7.10}$$

Combining this with the parametrization eq. (7.8), we realize, that the diagonality in spin, real space and frequency carries directly over from the one-particle Green's function to the self-energy, leading to a similar parametrization

$$\Sigma(1';1) = \Sigma(\omega_1)\delta_{i_{1'}i_1}\delta_{\omega_{1'},\omega_1}\delta_{\mu_{1'},\mu_1}\,. \tag{7.11}$$

with $\Sigma(\omega)$ being purely imaginary and antisymmetric.

This parametrization relies heavily on the presence of time-reversal symmetry. Its breaking, e.g. by including magnetic fields in the Hamiltonian, would destroy this extremely simple structure by both introducing a real part and a spin structure to the self-energy.

7.2 Spin and real-space dependence of the two-particle vertex

Similar to the self-energy, we now aim at a representation of the two-particle vertex, completely dictated by the symmetries of the pseudo-fermion Green's functions, summarized in Table 5.2. To this end, we first note, that by combining the relation between full and connected two-particle Green's function, eq. (6.21), with the tree expansion of the latter, eq. (6.29), we find

$$G_2(1',2';1,2) = \sum_{3',4',3,4} G_2^c(1';3')G_2^c(2';4')\gamma_2(3',4';3,4)G_2^c(3;1)G_2^c(4;2) + G_1^c(1';1)G_1^c(2';2)\,. \tag{7.12}$$

Due to the diagonality of G_c in all indices, as discussed in the previous section, all symmetries of the full two-particle Green's function directly carry over to the two-particle vertex γ_2.

To simplify notation and make connection with the existing literature [59, 98, 99, 109, 110], we will, in the remainder of this thesis, refer to the two-particle vertex as Γ instead of γ_2. This is not to be confused with the effective action $\Gamma[\bar{\phi},\phi]$.

As in the case of the self-energy, we start form the local U(1) symmetry of the pseudo-fermions, which induces a bi-locality of the Green's function, which leads to the expansion

$$\Gamma(1',2';1,2) = \Gamma_{=,i_1i_2}(1',2';1,2)\delta_{i_1'i_1}\delta_{i_2'i_2} - \Gamma_{\times,i_1i_2}(1',2';1,2)\delta_{i_1'i_2}\delta_{i_2'i_1}\,. \tag{7.13}$$

$\Gamma_=$ and $\Gamma_\times$ have been defined as the parts of the vertex i eq. (7.13), where the first and second incoming and outgoing indices separately are located at the same real space site or are interchanged, respectively. Clearly, from the antisymmetry of the vertex in its arguments, the relation

$$\Gamma_{\times,i_1i_2}(1',2';1,2) = \Gamma_{=,i_2i_1}(1',2';2,1)\,, \tag{7.14}$$

holds.

Employing the space group symmetries of the lattice, we are able to project back one of the site indices the vertices depend on onto a single reference site, rendering the vertex only dependent on the difference vector of sites i_1 and i_2. We, however, only note this fact, but refrain from explicitly introducing it into our notation, as it would complicate the notation of the flow equations in the following.

As a next step, that does not involve the frequency arguments of the vertex functions, we expand the spin dependence of the vertex in terms of Pauli matrices. This leads to

$$\Gamma_{=,i_1i_2}(1',2';1,2) = \Gamma^{\nu'\nu}_{i_1i_2}(\omega_{1'},\omega_{2'};\omega_1,\omega_2)\sigma^{\nu'}_{\mu_{1'}\mu_1}\sigma^{\nu}_{\mu_{2'}\mu_2} \tag{7.15}$$

with a similar expansion for $\Gamma_{\times,i_1i_2}$. Summation over ν', ν is implied. In the special case of a Heisenberg Hamiltonian, which is spin-rotation invariant, this relation can be further simplified to

$$\Gamma_{=,i_1i_2}(1',2';1,2) = \Gamma_{\mathrm{s},i_1i_2}(\omega_{1'},\omega_{2'};\omega_1,\omega_2)\sigma^{\nu}_{\mu_{1'}\mu_1}\sigma^{\nu}_{\mu_{2'}\mu_2} + \Gamma_{\mathrm{d},i_1i_2}(\omega_{1'},\omega_{2'};\omega_1,\omega_2)\delta_{\mu_{1'}\mu_1}\delta_{\mu_{2'}\mu_2}\,, \tag{7.16}$$

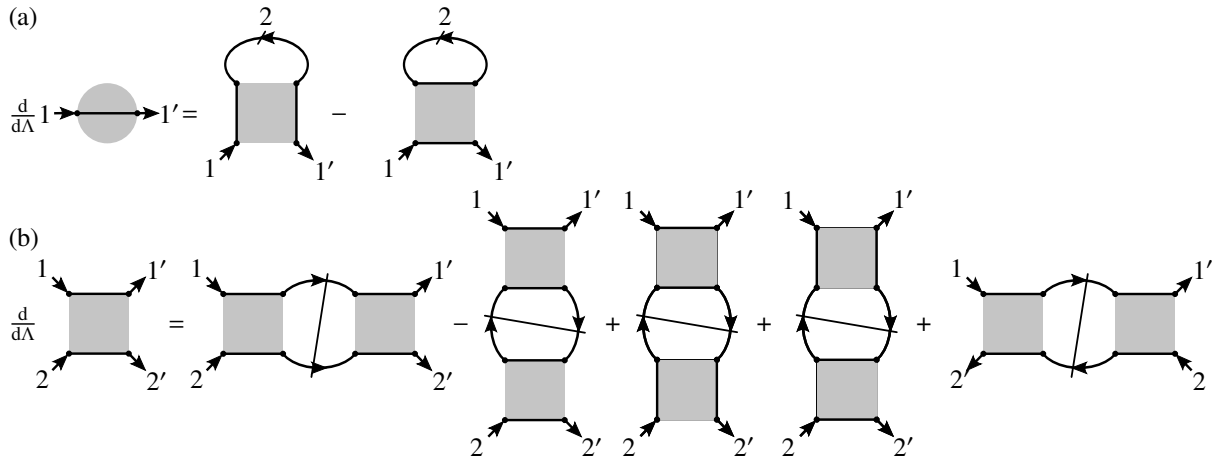

Figure 7.1: Diagrammatic representation of the multi-local PFFRG flow equations of the (a) self-energy Σ (circle, eq. (7.18)) and (b) two-particle vertex $\Gamma_=$ (gray square, eq. (7.19)). Along solid lines of the vertices, the site index remains constant. The arrows represent full Green's functions G^Λ, while slashed arrows are single scale propagators S^Λ. A slash crossing two propagators denotes a sum of the two possibilities of replacing one propagator by a single scale one. Along solid lines the lattice site index remains constant.

introducing the spin- and density vertex Γ_s and Γ_d, respectively.

The last symmetry we want to invoke to simplify the two-particle vertex is a combination of the two particle hole symmetries listed in Table 5.2, followed by a time-reversal transform, hermitian conjugation and another time-reversal operation. This involved sequence of symmetry transforms is necessary to achieve the relation

$$\Gamma^{\nu'\nu}_{i_1 i_2} = \xi(\nu')\xi(\nu)\left(\Gamma^{\nu'\nu}_{i_1 i_2}\right)^*, \tag{7.17}$$

extremely simplifying the analytic structure of the components of the vertex functions. In particular, this means, that both spin and density vertex Γ_s and Γ_d are purely real.

7.3 Multi-local flow equations

As an intermediate step, we present the multilocal flow equations, obtained by inserting the bilocal parametrization of the two-particle vertex, eq. (7.13) into the scale derivative of the one-particle vertex eq. (6.41) and two-particle vertex eq. (6.43), respectively. Keeping in mind the locality of the self-energy, we find

$$\frac{\mathrm{d}}{\mathrm{d}\Lambda}\Sigma^\Lambda(1';1) = \sum_2 \left(\Gamma^\Lambda_{\times,i_1 i_1}(1',2;1,2) - \sum_j \Gamma^\Lambda_{=,i_1 j}(1',2;1,2)\right) S^\Lambda(2,2) \tag{7.18}$$

for the self-energy and

$$\begin{aligned}\Gamma^{\Lambda}_{=,i_1i_2}(1',2';1,2) = \sum_{3,4} \big[&\Gamma^{\Lambda}_{=,i_1i_2}(1',2';3,4)\Gamma^{\Lambda}_{=,i_1i_2}(3,4;1,2) \\ &- \sum_j \Gamma^{\Lambda}_{=,i_1j}(1',4;1,3)\Gamma^{\Lambda}_{=,ji_2}(3,2';4,2) - (3 \leftrightarrow 4) \\ &+ \Gamma^{\Lambda}_{=,i_1i_2}(1',4;1,3)\Gamma^{\Lambda}_{\times,i_2i_2}(3,2';4,2) + (3 \leftrightarrow 4) \\ &+ \Gamma^{\Lambda}_{\times,i_1i_1}(1',4;1,3)\Gamma^{\Lambda}_{=,i_1i_2}(3,2';4,2) + (3 \leftrightarrow 4) \\ &+ \Gamma^{\Lambda}_{=,i_1i_2}(2',4;1,3)\Gamma^{\Lambda}_{=,i_1i_2}(3,1';4,2) + (3 \leftrightarrow 4)\big] \\ &\times G^{\Lambda}(3,3)S^{\Lambda}_{\mathrm{kat}}(4,4)\end{aligned} \tag{7.19}$$

for the two-particle vertex. Note, that we have already neglected the three-particle vertex terms and performed the Katanin substitution in these flow equations. Furthermore, we have explicitly incorporated the diagonality of the full and single-scale propagator in all their arguments.

Using eq. (7.14), we can replace $\Gamma_\times$ by $\Gamma_=$, fully decoupling the two (equivalent) components of the vertex. In Figure 7.1 we give a diagrammatic representation of the multilocal flow equations.

Comparing eq. (7.19) to eq. (6.43), there are a few notable features. Firstly, all but the second line in eq. (7.19) do not involve a site summation, rendering these terms completely local, in the sense, that at most two combinations of site indices appear in these terms. Secondly, the t-channel diagram contained in eq. (6.43) splits into three contributions: The second line in eq. (7.19) represents an RPA-like contribution, which involves a site summation. As this is the only term mixing correlations between different lattice sites, we can expect it to be pivotal in the formation of long-range order, a notion we will put on more solid grounds in Section 7.10.1. The third and fourth lines in eq. (7.19), we dub them, due to their appearance in Figure 7.1, chalice diagrams, originate in the intermixing of $\Gamma_\times$ and $\Gamma_=$ in the parametrization.

The flow of the self-energy, eq. (7.18), also splits into two contributions, with the first term resembling a purely local Fock-style diagram, while the second term is a Hartree contribution, which again involves a sum over the lattice.

7.4 Conventional frequency parametrization

In this section, we will discuss the frequency parametrization originally introduced in Reference [98], which will be used in all on-loop calculations in this thesis.

7.4.1 Parametrization of the two-particle vertex

Up to now, we have not utilized most symmetry relations shown in Table 5.2, as these involve the frequency arguments of the vertex function. To find a suitable parametrization of those, we first invoke time-translation invariance, dictating a conservation of Matsubara frequency, meaning

$$\Gamma^{\nu'\nu}_{i_1i_2}(\omega_{1'},\omega_{2'};\omega_1,\omega_2) = \Gamma^{\nu'\nu}_{i_1i_2}(\omega_{1'},\omega_{2'};\omega_1,\omega_2)\delta_{\omega_{1'}+\omega_{2'}-\omega_1-\omega_2}. \tag{7.20}$$

$\Gamma^{\nu' \nu}_{i_1 i_2}(s,t,u) = \xi(\nu')\xi(\nu)\Gamma^{\nu' \nu}_{i_1 i_2}(s,-t,u)$	(TR ∘ H)
$\Gamma^{\nu' \nu}_{i_1 i_2}(s,t,u) = \xi(\nu')\xi(\nu)\Gamma^{\nu \nu'}_{i_2 i_1}(s,t,-u)$	(X ∘ TR ∘ H)
$\Gamma^{\nu' \nu}_{i_1 i_2}(s,t,u) = \Gamma^{\nu \nu'}_{i_2 i_1}(-s,t,u)$	(X ∘ TR ∘ H ∘ PH1 ∘ PH2)
$\Gamma^{\nu' \nu}_{i_1 i_2}(s,t,u) = -\xi(\nu)\Gamma^{\nu' \nu}_{i_1 i_2}(u,t,s)$	(PH2)

Table 7.1: Symmetry relations of the two-particle vertex functions for pseudo-fermion Hamiltonians expanded in terms of Pauli matrices in transfer frequency parametrization. The labels specify the combinations of physical symmetries to realize the described relations. TR denotes time-reversal, H hermitian conjugation, X crossing symmetry in both incoming and outgoing particles and PH1/2 is a particle-hole transformation for particle 1/2.

Therefore, we can constrain ourselves to a parametrization in terms of three frequencies, for which we choose the transfer frequencies

$$\begin{aligned} s &= \omega_{1'} + \omega_{2'} \\ t &= \omega_{1'} - \omega_1 \\ u &= \omega_{1'} - \omega_2, \end{aligned} \tag{7.21}$$

which correspond to the three possible frequency transfers within the two-particle vertex.

Combining time-reversal and hermitian symmetry transforms (TR ∘ H) on top of this parametrization, we find

$$\Gamma^{\nu' \nu}_{i_1 i_2}(s,t,u) = \xi(\nu')\xi(\nu)\Gamma^{\nu' \nu}_{i_1 i_2}(s,-t,u)\,, \tag{7.22}$$

dictating (anti-)symmetry of the vertex components in the t frequency. Augmenting this relation with a crossing symmetry transformation in both arguments[2] (X ∘ TR ∘ H), we find a similar relation

$$\Gamma^{\nu' \nu}_{i_1 i_2}(s,t,u) = \xi(\nu')\xi(\nu)\Gamma^{\nu \nu'}_{i_2 i_1}(s,t,-u)\,, \tag{7.23}$$

for the symmetry in the u frequency. Note, that both site and spin indices are swapped here.

The analogous relation for the remaining transfer frequency s is more involved, necessitating a combination of both particle-hole transformations, time-reversal, hermitian conjugation and crossing symmetry, but directly leads to

$$\Gamma^{\nu' \nu}_{i_1 i_2}(s,t,u) = \Gamma^{\nu \nu'}_{i_2 i_1}(-s,t,u)\,. \tag{7.24}$$

As a last symmetry, we invoke a particle-hole transformation for the second arguments (PH2), which leads to a possibility of exchanging s and u

$$\Gamma^{\nu' \nu}_{i_1 i_2}(s,t,u) = -\xi(\nu)\Gamma^{\nu' \nu}_{i_1 i_2}(u,t,s). \tag{7.25}$$

We summarize these symmetries in Table 7.1. Altogether, Equations (7.22), (7.23), and (7.24) imply, that the frequency content of the vertex can be mapped to only the positive Matsubara axis for all three transfer frequencies. Additionally, it suffices to restrict the vertex to $s \geq u$ due to the exchange symmetry between the two frequencies given in eq. (7.25). In the special case of Heisenberg Hamiltonians, these relations imply, that both Γ_s and Γ_d are symmetric in all three transfer frequencies, with Γ_s being also symmetric under $s \leftrightarrow u$, while Γ_d is antisymmetric under this transformation.

[2] Due to the bilocal parametrization eq. (7.13) of the vertex, a crossing symmetry in only incoming or outgoing arguments is not present anymore.

7.4.2 Parametrized flow equations

At this point, we have all the necessary ingredients to formulate the fully parametrized PFFRG flow equations. To connect to existing literature, however, let us introduce some simplifying notation.

Taking advantage of the self-energy $\Sigma(\omega)$ defined in eq. (7.11) being purely imaginary by defining the real quantity

$$\gamma(\omega) = \mathrm{i}\Sigma(\omega). \tag{7.26}$$

Please note, that γ is not to be confused with the full one-particle vertex γ_1, but indeed $\gamma = -\mathrm{i}\gamma_1$. We furthermore will focus on Heisenberg systems, while the full flow equations for general spin systems can be found in References [59] and [111].

Combining this with the self-energy flow eq. (7.18), using eq. (7.14) to express $\Gamma_\times$ by $\Gamma_=$, and substituting the latter's parametrization in spin space, eq. (7.16), as well as using the transfer frequencies introduced in eq. (7.21), we find

$$\begin{aligned}\frac{\mathrm{d}}{\mathrm{d}\Lambda}\gamma^\Lambda(\omega) = \int \mathrm{d}\omega' \Big\{ & 3\Gamma_{\mathrm{s},i_1 i_1}(\omega+\omega', \omega-\omega', 0) \\ & + \Gamma_{\mathrm{d},i_1 i_1}(\omega+\omega', \omega-\omega', 0) \\ & - \sum_{i_2} 2\Gamma_{\mathrm{d},i_1 i_2}(\omega+\omega', 0, \omega-\omega') \Big\} \frac{\frac{\partial}{\partial\Lambda} R(\omega', \Lambda)}{\omega' + \gamma(\omega')},\end{aligned} \tag{7.27}$$

where we have also substituted the explicit form of the single-scale propagator following from Equations (7.10), (6.30), and (6.42), which involves introducing the FRG regulator R, which has the general properties given in eq. (6.31). Its explicit form we will discuss in Section 7.6. Furthermore, we have taken the zero temperature limit $T \to 0$, for which PFFRG is usually formulated, rendering the Matsubara frequencies we are dealing with continuous rather than discrete as for finite T. Therefore, all Matsubara sums $\frac{1}{\beta}\sum$ have to be replaces by the appropriate frequency integral $\frac{1}{2\pi}\int$, while at the same time $\beta \to 1/2\pi$.

Going to zero temperature has several advantages. Firstly, the continuous frequency axis does allow for arbitrary transformations of the integration variable, which would for finite temperature lead to an intermixing of fermionic and bosonic Matsubara frequencies. This leads to analytical difficulties solving the Matsubara sums using standard techniques mapping them to complex integrals, where the integrand has poles *either* at the bosonic *or* fermionic Matsubara frequencies. Secondly, the RG scale Λ acts as a regulator similarly to a temperature T by suppressing low-frequency degrees of freedom[3]. Having two of these regulating energy scales, i.e. Λ and T, in the description of the system would lead to ambiguities in the interpretation of effects at phase transition scales: one could not easily disentangle if lowering temperature or cutoff has caused the transition.

The same substitutions can also be performed for the two-particle vertex flow eq. (7.19). As the resulting equations are quite lengthy, we give them in appendix A. Let us here note, that we perform a split of the vertex derivative into the respective diagrammatic channels, according to

$$\frac{\mathrm{d}}{\mathrm{d}\Lambda}\Gamma^\Lambda = \dot{g}^{\mathrm{s}} + \dot{g}^{\mathrm{t}} + \dot{g}^{\mathrm{u}}. \tag{7.28}$$

[3] As we will see in Section 7.10.1, for the right choice of regulator, there is even an exact mean-field relation between Λ and T at large spin length $S \to \infty$.

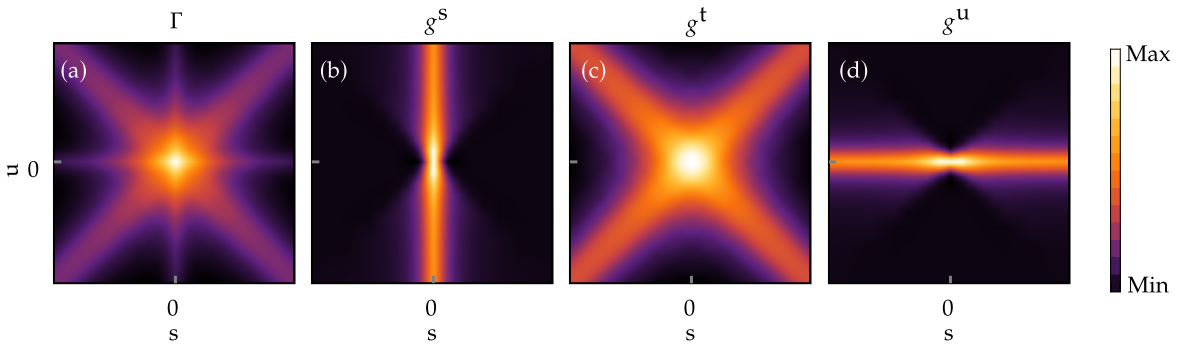

Figure 7.2: (a) A full representative spin-vertex Γ shown in the $t = 0$ plane, showing characteristic double-cross structure. Its decomposition in the (b) s-, (c) t- and (d) u-channel contributions reveals the origin of the structure in the different channels. Due to this structure, the asymptotics are not well-defined in the transfer frequency parametrization, necessitating a natural parametrization per channel.

Here $\dot{g}^{\mathrm{c}}$ describes the c-channel contributions ($\mathrm{c} = \mathrm{s}, \mathrm{t}, \mathrm{u}$) to the derivative. These correspond to the diagrammatic channels described in Section 6.4.3 and are distinguished in this parametrization by the fact, that the corresponding transfer frequency enters the propagator bubble

$$P^{\Lambda}(\omega, c+\omega) = S^{\Lambda}_{\mathrm{kat}}(\omega) G^{\Lambda}(c+\omega), \tag{7.29}$$

i.e. the respective contributions are two-particle reducible in the corresponding transfer frequency c, i.e. can be separated by cutting two propagator lines in a diagram involving c, which amounts to removing the bubble function eq. (7.29) and the correspoding frequency integration over ω. With g^{c} we denote the part of the full vertex generated by the derivatives $\dot{g}^{\mathrm{c}}$.

7.5 Asymptotic frequency parametrization

The parametrization of vertex functions in terms of transfer frequencies introduced in the previous section has been used for PFFRG calculations since the method has been established in Reference [98]. Despite its success in applications to both models [30–32, 98, 112–126] and real materials [33–35, 127–135], it is not the most natural way to express the vertex functions.

As established in References [136] and [137], the full vertex function displays a characteristic behavior, where it exhibits most of its structure around several lines: a cross-like feature parallel to two frequency axes, for the third transfer frequency fixed, overlaid by another one, rotated 45° with respect to the first one, as shown in Figure 7.2(a) for a representative PFFRG vertex. This in particular means, that there are no well-defined limits for taking any of the transfer frequencies to infinity, due to the diagonal structure. In particular $\lim_{c\to\infty} \Gamma(s,t,u) = 0$ for any one of the transfer frequencies $c = s/t/u$ separately, does not hold, but for simplicity is usually assumed in numerical calculations using this parametrization. The assumption is still justified, as the propagators will suppress the respective contributions when integrating the flow equations.

As laid out in Reference [136], this structure can be understood by the nature of the three diagrammatic channels. As each channel g^{c} is reducible in the transfer frequency c, this enters the internal propagator bubble, leading to an asymptotic behavior $\lim_{c\to\infty} g^{\mathrm{c}}(s,t,u) = 0$. This in turn means, that the other two contributions do not necessarily show this behavior, which calls for tracking the contributions of each channel separately during the RG flow. Indeed,

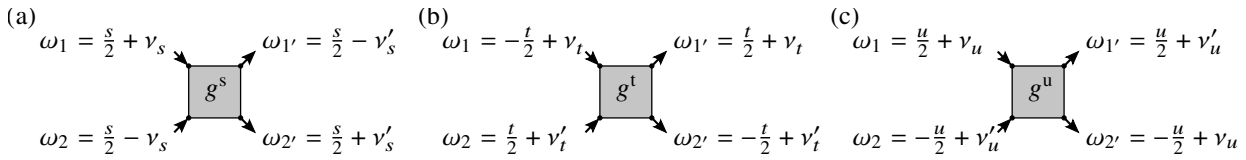

Figure 7.3: Natural frequency parametrization as used in the asymptotic parametrization scheme. The diagrammatic s-, t-, and u-channels have well-defined asymptotic in the corresponding bosonic transfer frequency $s/t/u$, as well as the respective fermionic frequencies ν and ν'. The shift by half the transfer frequency allows for a simpler implementation of symmetries.

$g^{\mathrm{s},\nu'\nu}_{i_1 i_2}(s,\nu_s,\nu'_s) = g^{\mathrm{s},\nu\nu'}_{i_2 i_1}(-s,\nu_s,\nu'_s)$	(X ∘ TR ∘ H ∘ PH1 ∘ PH2)
$g^{\mathrm{s},\nu'\nu}_{i_1 i_2}(s,\nu_s,\nu'_s) = -\xi(\nu')g^{\mathrm{u},\nu\nu'}_{i_2 i_1}(s,-\nu_s,\nu'_s)$	(PH2 ∘ X)
$g^{\mathrm{s},\nu'\nu}_{i_1 i_2}(s,\nu_s,\nu'_s) = -\xi(\nu)g^{\mathrm{u},\nu'\nu}_{i_1 i_2}(s,\nu_s,-\nu'_s)$	(PH2)
$g^{\mathrm{s},\nu'\nu}_{i_1 i_2}(s,\nu_s,\nu'_s) = g^{\mathrm{s},\nu\nu'}_{i_2 i_1}(s,\nu'_s,\nu_s)$	(X ∘ TR ∘ H)
$g^{\mathrm{t},\nu'\nu}_{i_1 i_2}(t,\nu_t,\nu'_t) = \xi(\nu')\xi(\nu)g^{\mathrm{t},\nu'\nu}_{i_1 i_2}(-t,\nu_t,\nu'_t)$	(TR ∘ H)
$g^{\mathrm{t},\nu'\nu}_{i_1 i_2}(t,\nu_t,\nu'_t) = -\xi(\nu')g^{\mathrm{t},\nu'\nu}_{i_1 i_2}(t,-\nu_t,\nu'_t)$	(PH1)
$g^{\mathrm{t},\nu'\nu}_{i_1 i_2}(t,\nu_t,\nu'_t) = -\xi(\nu)g^{\mathrm{t},\nu'\nu}_{i_1 i_2}(t,\nu_t,-\nu'_t)$	(PH2)
$g^{\mathrm{t},\nu'\nu}_{i_1 i_2}(t,\nu_t,\nu'_t) = g^{\mathrm{t},\nu\nu'}_{i_2 i_1}(t,\nu'_t,\nu_t)$	(X ∘ TR ∘ H)
$g^{\mathrm{u},\nu'\nu}_{i_1 i_2}(u,\nu_u,\nu'_u) = \xi(\nu')\xi(\nu)g^{\mathrm{u},\nu\nu'}_{i_2 i_1}(-u,\nu_u,\nu'_u)$	(X ∘ TR ∘ H)
$g^{\mathrm{u},\nu'\nu}_{i_1 i_2}(u,\nu_u,\nu'_u) = -\xi(\nu)g^{\mathrm{s},\nu\nu'}_{i_2 i_1}(u,-\nu_u,\nu'_u)$	(X ∘ PH2)
$g^{\mathrm{u},\nu'\nu}_{i_1 i_2}(u,\nu_u,\nu'_u) = -\xi(\nu)g^{\mathrm{s},\nu'\nu}_{i_1 i_2}(u,\nu_u,-\nu'_u)$	(PH2)
$g^{\mathrm{u},\nu'\nu}_{i_1 i_2}(u,\nu_u,\nu'_u) = g^{\mathrm{u},\nu\nu'}_{i_2 i_1}(u,\nu'_u,\nu_u)$	(TR ∘ H)

Table 7.2: Symmetry relations of the two-particle vertex functions for pseudo-fermion Hamiltonians expanded in terms of Pauli matrices in the natural frequency parametrization for the s-, t- and u-channels respectively. The labels specify the combinations of physical symmetries to realize the described relations. TR denotes time-reversal, H hermitian conjugation, X crossing symmetry in both incoming and outgoing particles and PH1/2 is a particle-hole transformation for particle 1/2.

implementing this scheme, we find that the full vertex structurally decomposes into contributions, each displaying only one specific part of the cross-structure, cf. Figure 7.2(b)-(d). To capture the corresponding asymptotics efficiently, we introduce a natural frequency parametrization for each of the channels, consisting of the respective bosonic transfer frequency c, as well as mixed bosonic-fermionic frequencies ν_c and ν'_c, given by

$$s = \omega_1 + \omega_2 = \omega_{1'} + \omega_{2'} \qquad \nu_s = (\omega_1 - \omega_2)/2 \qquad \nu'_s = (\omega_{2'} - \omega_{1'})/2 \tag{7.30}$$

$$t = \omega_{1'} - \omega_1 = \omega_2 - \omega_{2'} \qquad \nu_t = (\omega_1 + \omega_{1'})/2 \qquad \nu'_t = (\omega_2 + \omega_{2'})/2 \tag{7.31}$$

$$u = \omega_1 - \omega_{2'} = \omega_{1'} - \omega_2 \qquad \nu_u = (\omega_1 + \omega_{2'})/2 \qquad \nu'_u = (\omega_{1'} + \omega_2)/2. \tag{7.32}$$

For readability, we will in the following refer to $\nu^{(\prime)}$ as fermionic frequencies, because the mixed character will not be important for our discussions.

This choice differs from the prescription in References [136] and [137], where purely fermionic frequencies are used in addition to the transfer ones, by a shift of each fermionic frequency by half the transfer frequency. This more symmetric choice, illustrated in Figure 7.3, leads to simpler symmetry relations, as the cross-structures in the vertex are shifted to the frequency space origin. For a finite temperature implementation, which we are however not using,

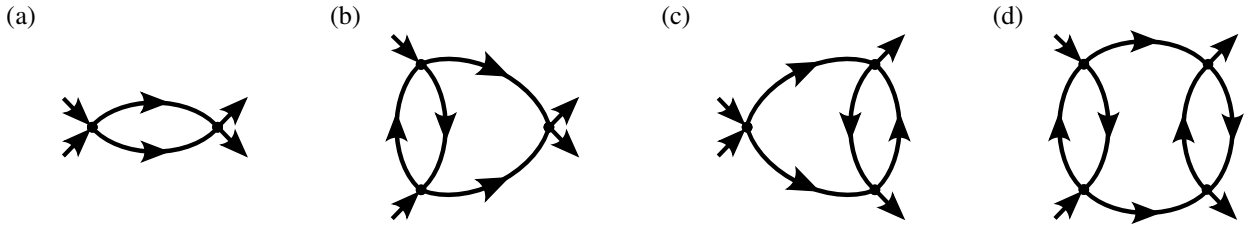

Figure 7.4: Exemplary diagrammatic contributions to the s-channel kernel functions. (a) K_1^{s} diagram, where all external legs couple to the bare vertex (black dot). (b) and (c) are K_2^{s} and $\bar{K}_2^{\mathrm{s}}$ contributions, respectively, as the ν_s or ν'_s dependencies enter the additional loops. These are dubbed fish-eye diagrams. The nested three-loop diagram (d) contributes to the K_3^{s} kernel.

this choice would complicate calculations, as $\nu^{(\prime)}$ do neither represent bosonic, nor fermionic Matsubara frequencies, but a mixture of both.

The actual symmetries of the channels can be obtained from the general relations for the two-particle vertex given in Table 5.2, similarly to the procedure in the transfer frequency parametrization. The resulting symmetries are summarized in Table 7.2. Most noteworthy, the t-channel decouples from the other two, while s- and u-channels are coupled by inverting the fermionic frequencies. In total, the symmetries listed allow us to reduce the domain of every channel individually to only positive frequencies on all axes with $\nu \geq \nu'$.

Analyzing the diagrammatic structure contained in a c-reducible channel further, we find, that this part of the vertex can further be decomposed into asymptotic classes, according to the number of external frequency arguments, that enter the internal loop integrations [136, 137], leading to

$$\dot{g}^{\mathrm{c}}(c, \nu_c, \nu'_c) = K_1^{\mathrm{c}}(c) + K_2^{\mathrm{c}}(c, \nu_c) + \bar{K}_2^{\mathrm{c}}(c, \nu'_c) + K_3^{\mathrm{c}}(c, \nu_c, \nu'_c). \tag{7.33}$$

Here the kernel functions K_i capture certain asymptotic limits of the full vertex derivative, as they vanish for taking any of their respective frequency arguments to infinity. The index i labels the number of external frequency dependencies of the kernels. In Figure 7.4 we illustrate diagrammatic contributions to the K_1, K_2 and K_3 classes. Note, that, although the FRG flow only contains single loop diagrams on the right-hand side, the multi-loop structure of the latter two asymptotic classes is generated when iterating the flow equations.

To see this explicitly, we expand the right-hand side of the flow at a scale $\Lambda_0 - \mathrm{d}\Lambda$ in terms of the infinitesimal deviation $\mathrm{d}\Lambda$ from the initial scale $\Lambda_0 \to \infty$. To focus on the Λ dependence, we here drop all frequency arguments, turning to a symbolic notation for the asymptotic classes

$$\dot{g}^{\mathrm{c},\Lambda} = \left[\Gamma^{\Lambda} \circ \frac{\mathrm{d}}{\mathrm{d}\Lambda}\left(G^{\Lambda} \times G^{\Lambda}\right) \circ \Gamma^{\Lambda}\right]_{\mathrm{c}}, \tag{7.34}$$

where the internal frequency and real space summations according to the respective channel c are implied. The expansion in $\mathrm{d}\Lambda$ in this notation reads

$$\dot{g}^{\mathrm{c}',\Lambda_0-\mathrm{d}\Lambda} = \left[\Gamma^{\Lambda_0} \circ \frac{\mathrm{d}}{\mathrm{d}\Lambda}\left(G^{\Lambda} \times G^{\Lambda}\right)\Big|_{\Lambda_0-\mathrm{d}\Lambda} \circ \Gamma^{\Lambda_0}\right]_{\mathrm{c}} \tag{7.35}$$

$$+ \left[\left(-\mathrm{d}\Lambda \sum_{c'} \dot{g}^{\mathrm{c}',\Lambda_0}\right) \circ \frac{\mathrm{d}}{\mathrm{d}\Lambda}\left(G^{\Lambda} \times G^{\Lambda}\right)\Big|_{\Lambda_0-\mathrm{d}\Lambda} \circ \Gamma^{\Lambda_0}\right]_{\mathrm{c}} \tag{7.36}$$

$$+\left[\Gamma^{\Lambda_0}\circ\frac{\mathrm{d}}{\mathrm{d}\Lambda}\left(G^{\Lambda}\times G^{\Lambda}\right)\Big|_{\Lambda_0-\mathrm{d}\Lambda}\circ\left(-\mathrm{d}\Lambda\sum_{c'}\dot{g}^{c',\Lambda_0}\right)\right]_{\mathrm{c}} \tag{7.37}$$

$$+\left[\left(-\mathrm{d}\Lambda\sum_{c'}\dot{g}^{c',\Lambda_0}\right)\circ\frac{\mathrm{d}}{\mathrm{d}\Lambda}\left(G^{\Lambda}\times G^{\Lambda}\right)\Big|_{\Lambda_0-\mathrm{d}\Lambda}\circ\left(-\mathrm{d}\Lambda\sum_{c'}\dot{g}^{c',\Lambda_0}\right)\right]_{\mathrm{c}}+O\left(\mathrm{d}\Lambda^2\right). \tag{7.38}$$

As Γ^{Λ_0} is frequency independent, the first term in this expansion, eq. (7.35), will be independent of the fermionic frequencies, but only depend on the transfer frequency, that enters the propagators, cf. appendix A. The diagram in Figure 7.4(a) is part of this contribution. The vertex derivative at the scale Λ, by virtue of this contribution, acquires a dependence on the respective transfer frequency ω_c of the different channels. The second contribution, eq. (7.36), therefore will carry a dependence on ν_c, which enters into the transfer frequency $\omega_{c'}$ for $c' \neq c$, these contributions are therefore of K_2 type, with a representative diagram shown in Figure 7.4(b). For the same reason, the third term, eq. (7.37), will contribute to the $\bar{K}_2$ class, with an exemplary diagrammatic contribution drawn in Figure 7.4(c). The last term, we consider here, eq. (7.38), is quadratic in $\mathrm{d}\Lambda$ and features two insertions of $\dot{g}^{\Lambda_0}$. AS argued before, this will lead to a dependence on both ν_c and $\nu_{c'}$, rendering these contributions K_3-type. We again give an example of a corresponding diagram in Figure 7.4(d).

The symmetries of the Kernel functions can be deduced from the ones given in Table 7.2 by setting the appropriate frequencies to infinity. We would like to emphasize, that, due to the symmetry under exchange of the bosonic frequencies, K_2 and $\bar{K}_2$ are equivalent for pseudo-fermionic systems.

We present the full flow equations in this asymptotic frequency parametrization in appendix B due to their length. Please note, that, for the right-hand side, the full set of frequencies in all channels has to be stated there, as the full vertex enters, rather than just a single asymptotic component, leading to an intermixing of these.

7.6 Choice of regulator

So far, we have not specified the regulator function R used to implement the RG flow. In FRG literature, a plethora of implementations of R have been used. In the context of itinerant fermions, a simple cutoff in reciprocal space, separating high and low energy degrees of freedom, has been utilized [101], but also a rescaling of the interactions [138] or temperature itself [84, 91] have been utilized to implement the renormalization flow.

For PFFRG, however, being formulated in real space at zero temperature, a cutoff in frequency space is the most natural way to introduce the RG scale Λ. We will discuss here two different implementations. Firstly, the sharp step regulator used since the first implementation of PFFRG [98] and secondly a smoothened version of this recently introduced by us [139, 140].

7.6.1 Step regulator

The easiest way to separate high- and low-energy degrees of freedom is by introducing a step-like regulator of the form

$$R(\omega,\Lambda)=\theta(|\omega|-\Lambda), \tag{7.39}$$

in frequency space, where θ denotes the Heaviside step function

$$\theta(x)=\begin{cases}0 & x<0\\ 1 & x\geq 1,\end{cases} \tag{7.40}$$

which trivially fulfills the limiting conditions on a regulator function given in eq. (6.31).

The bare propagator of a pseudo-fermionic system using this cutoff scheme reads

$$\mathrm{i}G_0^\Lambda(\omega) = \frac{\theta(|\omega'| - \Lambda)}{\omega}, \tag{7.41}$$

from which we immediately find the full propagator using Dyson's equation eq. (7.10) to be

$$\mathrm{i}G^\Lambda(\omega) = \frac{\theta(|\omega'| - \Lambda)}{\omega + \gamma^\Lambda(\omega)}. \tag{7.42}$$

At first glance, the discontinuity in the regulator function renders the single-scale propagator S^Λ as introduced in eq. (6.42) ill-defined: The scale derivative of the regulator $\frac{\partial}{\partial\Lambda}\theta(|\omega'|-\Lambda) = -\delta(|\omega'|-\Lambda)$ is the Dirac delta-distribution, which features the peak right at the discontinuity of the step functions in the denominator of eq. (6.42). This leads at first glance leads to an ambiguity, as the value of the step function at this point is not uniquely defined.

Invoking the representation of the Heaviside function as a limit of a regularized family of smooth functions $\theta(x) = \lim_{\epsilon\to 0}\theta_\epsilon(x)$, one can prove Morris' Lemma [141] consistently defining such products:

$$\lim_{\epsilon\to 0}\delta_\epsilon(x) f(\theta_\epsilon(x)) = \delta(x)\int_0^1 \mathrm{d}t\, f(t), \tag{7.43}$$

where f is a continuous function and the regularized delta function is defined by $\delta_\epsilon(x) = \frac{\partial}{\partial x}\theta_\epsilon(x)$.

Invoking this lemma, we find the single-scale propagator to be

$$\mathrm{i}S^\Lambda(\omega) = \frac{\delta(|\omega'| - \Lambda)}{\omega + \gamma^\Lambda(\omega)}, \tag{7.44}$$

which *a posteriori* accounts for its name: the single-scale propagator in this formulation filters out exactly the frequency corresponding to the RG scale Λ by the means of the Dirac-delta distribution. As we will see in Section 7.10.1, this form of S allows for a direct connection between the RG sclae Λ and an effective temperature T via the relation $T = \frac{\pi}{2}\Lambda$. Moreover, the appearance of the Dirac delta extremely simplifies the bubble integrations on the right-hand side of the FRG equations, as it analytically replaces these by a finite summation.

This advantage, however, is gone, once we employ the Katanin-substitution eq. (6.45), as the Katanin-substituted single-scale propagator

$$S^\Lambda_{\mathrm{kat}} = -\frac{\mathrm{d}}{\mathrm{d}\Lambda}G^\Lambda = S^\Lambda - \left(G^\Lambda\right)^2\frac{\mathrm{d}}{\mathrm{d}\Lambda}\Sigma^\Lambda \tag{7.45}$$

does not contain the delta-peak in its second term and therefore a frequency integration is necessary anyway.

Furthermore, due to the non-analyticity of the regulator, the frequency dependence of the vertex functions shows characteristic kinks at Λ dependent positions, which in a numerical implementation leads to an oscillating behavior of the RG flow, see e.g. Reference [98].

7.6.2 Smoothened frequency cutoff

To circumvent these numerical problems, in more recent implementations of PFFRG, especially the one of the multi-loop scheme, which will be introduced in Chapter 8, we employ a smoothened version of the step cutoff, given

by

$$R(\omega, \Lambda) = 1 - \mathrm{e}^{-\frac{\omega^2}{\Lambda^2}}, \tag{7.46}$$

which smears out the step at $|\omega| = \Lambda$ over a width of Λ. This regulator is similar to the so-called Ω-flow used in itinerant fermion FRG [142], in the sense, that in eq. (7.46) the suppression of the low-frequency region is done in a Gaussian shape, while in the Ω-flow, this is done using a Lorentzian.

The bare propagator for the smooth cutoff is given by

$$\mathrm{i}G_0^\Lambda(\omega) = \frac{1 - \mathrm{e}^{-\frac{\omega^2}{\Lambda^2}}}{\omega}, \tag{7.47}$$

and, consequently, the full propagator reads

$$\mathrm{i}G^\Lambda(\omega) = \frac{1 - \mathrm{e}^{-\frac{\omega^2}{\Lambda^2}}}{\omega + \gamma^\Lambda(\omega)}. \tag{7.48}$$

As no discontinuities are present in this function, we can directly use eq. (6.42) to obtain the single scale propagator

$$\mathrm{i}S^\Lambda(\omega) = \frac{2\mathrm{e}^{-\frac{\omega^2}{\Lambda^2}}}{(\omega + \gamma^\Lambda(\omega))^2}\frac{\omega^3}{\Lambda^3}, \tag{7.49}$$

which is, as in the sharp cutoff case, features two peaks located symmetrically around $\omega = 0$, but at a frequency $\omega_p < \Lambda$, whereas we have $\omega_p = \Lambda$ in the sharp case.

7.7 Susceptibilities

The PFFRG formalism we have laid out in the previous sections implicitly assumed, that no symmetries present in the original Hamiltonian are spontaneously broken during the RG flow. While this is a good assumption in spin liquid phases, which are exactly defined by the lack of such a breaking, magnetically long-range ordered states naturally will break lattice symmetries. This will lead to an instability of the RG flow below a certain critical scale Λ_c, usually in the form of a divergence or kink, as the formalism below this scale can no longer faithfully track the physical content of the model.

While flow into such phases is in principle possible in FRG by introducing an order parameter field, which becomes finite approaching Λ_c [100], we refrain from implementing such a scheme. As the form of the order parameter is specific to the exact way symmetries are spontaneously broken, one would have to anticipate an ordering pattern to *a priori* implement the suitable field. This, however, would introduce a bias in the PFFRG method, which is up to now not present, as we have not assumed any symmetry breaking whatsoever.

As an alternate route to access the ordering tendencies, we calculate the static spin-spin real-space correlators

$$\chi_{ij}^{\alpha\beta,\Lambda}(\omega = 0) = \int_0^\infty \mathrm{d}\tau \left\langle T_\tau S_i^\alpha(\tau) S_j^\beta(0) \right\rangle \tag{7.50}$$

during the flow. For Heisenberg systems, only the $\alpha = \beta$ components are non-vanishing and all equal, therefore we will in this case use $\chi_{ij}^\Lambda(\omega = 0) = \chi_{ij}^{zz,\Lambda}(\omega = 0)$ as a shorthand.

A long-range ordering tendency will be signalled by an instability in the flow of these correlators. At this RG scale, the maximum of the static susceptibility

$$\chi(\boldsymbol{k}) = \frac{1}{N}\sum_{i,j} \mathrm{e}^{\mathrm{i}\boldsymbol{k}\cdot(\boldsymbol{r}_i-\boldsymbol{r}_j)}\chi^{\Lambda}_{ij}(\mathrm{i}\omega=0) \tag{7.51}$$

characterizes the magnetic long-range order the system would realize.

Using the relations between full and connected Green's functions eq. (6.21) as well as the tree expansion of the latter given in eq. (6.29), we can express this quantity in terms of one-particle Green's functions and the two-particle vertex as

$$\begin{aligned}\chi^{\alpha\beta,\Lambda}_{ij}(\omega) = &-\frac{1}{2}\frac{1}{2\pi}\int \mathrm{d}\omega' G^{\Lambda}(\omega')G^{\Lambda}(\omega'+\omega)\delta_{ij}\\ &-\frac{1}{4}\left(\frac{1}{2\pi}\right)\iint \mathrm{d}\omega'\mathrm{d}\omega'' G^{\Lambda}(\omega')G^{\Lambda}(\omega'+\omega)G^{\Lambda}(\omega'')G^{\Lambda}(\omega''+\omega)\\ &\times\sum_{\mu_{1'},\mu_{2'},\mu_1,\mu_2}\Gamma^{\Lambda}(i,\omega'+\omega,\mu_{1'},j,\omega'',\mu_{2'};i,\omega',\mu_1,j,\omega''+\omega,\mu_2)\sigma^{\alpha}_{\mu_1\mu_{1'}}\sigma^{\alpha}_{\mu_2\mu_{2'}}.\end{aligned} \tag{7.52}$$

Although we in principle can calculate the susceptibility for all Matsubara frequencies $\mathrm{i}\omega$, we here focus on the static limit $\omega \to 0$, as this is the only real Matsubara frequency. In principle, the frequency dependence of χ would be interesting to explore due to it being measurable using inelastic neutron scattering, from the PFFRG formalism presented here, we, however, only obtain it along the imaginary frequency axis. Although an analytical continuation to the real frequency axis is possible [143], it is well-known, that for any approximate numerical data, as we would have to use as a starting point after solving the RG flow numerically, is inherently unstable [144].

7.8 Initial conditions

As the last ingredient to complete our discussion of the PFFRG method, we have to specify the initial conditions for both the self-energy and the two-particle vertex. For a general fermionic problem, we already have stated these in Equations (6.47) and (6.48), but we want to specify to the specific parametrizations tailored towards pseudo-fermionic Hamiltonians developed in this chapter.

From eq. (6.47) we trivially find that the self-energy has to vanish at the beginning of the flow, meaning

$$\gamma^{\Lambda\to\infty}(\omega) = 0. \tag{7.53}$$

To connect the initial condition for the two-particle vertex eq. (6.48), we first have to rewrite the pseudo-fermion Hamiltonian eq. (5.15) into the antisymmetrized form used in eq. (6.10). We find

$$H = \frac{1}{2}\frac{1}{2}\frac{1}{4}\sum_{\substack{i_{1'},i_{2'}\\ i_1,i_2\\ \mu_{1'},\mu_{2'}\\ \mu_1,\mu_2}}\left(J_{i_{1'}i_{2'}}\boldsymbol{\sigma}_{\mu_{1'}\mu_1}\cdot\boldsymbol{\sigma}_{\mu_{2'}\mu_2}\delta_{i_{1'}i_1}\delta_{i_{2'}i_2} - J_{i_{1'}i_{2'}}\boldsymbol{\sigma}_{\mu_{1'}\mu_1}\cdot\boldsymbol{\sigma}_{\mu_{2'}\mu_2}\delta_{i_{1'}i_2}\delta_{i_{2'}i_1}\right)c^{\dagger}_{i_{1'}\mu_{1'}}c^{\dagger}_{i_{2'}\mu_{2'}}c_{i_2\mu_2}c_{i_1\mu_1}, \tag{7.54}$$

where we got an additional factor ½ from reintroducing the double-counting of interactions not present in eq. (5.15) and another factor ½ from antisymmetrization[4].

[4]The combinatorial factor for antisymmetrization actually would be 2! = 4, but all terms appear twice, thus only 2 remains.

Therefore, combining Equations (6.48), (7.14), and (7.16), we find for the spin- and density vertex [98]

$$\Gamma^{\Lambda\to\infty}_{\mathrm{s},i_1i_2} = \frac{J_{i_1i_2}}{4} \tag{7.55}$$

$$\Gamma^{\Lambda\to\infty}_{\mathrm{d},i_1i_2} = 0. \tag{7.56}$$

7.9 Single occupation constraint

So far, we have not discussed the implementation of the single occupation constraint per site eq. (5.4). As shown in Section 5.5, the introduction of an SU(2) gauge field will enforce its fulfillment, as this consequently acts as a Lagrange multiplier. In FRG, however, the treatment of such a non-Abelian field is far from trivial [145]. It is also not clear, how different approximation and truncation schemes would influence the ability of the gauge field to enforce the constraint. Hence, we refrain from implementing such an approach in our current work.

A second approach, that has been put forward by Popov and Fedotov in Reference [146], is to include an imaginary chemical potential

$$\mu_{\mathrm{PPV}} = -\mathrm{i}\frac{\pi T}{2} \tag{7.57}$$

in the Hamiltonian via the replacement

$$H \to H_{\mathrm{PPV}} = H - \mu_{\mathrm{ppv}} \sum_{i,\mu} c^\dagger_{i\mu} c_{i\mu}\,. \tag{7.58}$$

Although spoiling the hermiticity of the Hamiltonian, expectation values calculated with respect to H_{PPV} and considering the full Hilbert space of the pseudo-fermions, i.e. including the unphysical states, will be identical to the same expectation values obtained using H constrained to only the half-filled states [146, 147]. This is true for any physical operator, i.e. one vanishing in the unphysical sector. As explicated in Reference [99], this is due to a cancellation of the contributions from the non- and doubly occupied sectors in the partition sum.

PFFRG as we have set up here, is formulated in the $T \to 0$ limit. In this case, formally also $\mu_{\mathrm{PPV}} \to 0$, but this limit not necessarily commutes with the calculation of thermal averages involving H_{PPV}, as the cancellation can only occur for any finite T. With the pseudo-fermionic Hamiltonian eq. (5.15) being particle-hole symmetric, a vanishing chemical potential, however, amounts to half-filling. This implies, that the constraint, in this case, will be fulfilled on average, instead of exactly.

Previous PFFRG studies have found, that, at low temperatures, this averaged fulfillment already leads to the physically correct results when compared to an exact implementation of the Popov-Fedotov scheme [99, 145]. Therefore, we will in this thesis resort to the average projection scheme.

We can rationalize these findings along the lines of References [99] and [59]: The Hamiltonian by itself respects the constraint in the sense, that it does not induce transitions from the physical half-filled to unphysical empty or doubly occupied states. Therefore, all contributions to the partition sum stemming from this sector have to be thermally activated. Starting now from a system at exactly half-filling at every site, a fluctuation into the unphysical sector will amount to creating a doubly occupied site and an empty one at the same time. As these both feature a total spin $S = 0$, their energetic contribution in the Hamiltonian vanishes, effectively removing the sites from the system. In generic spin systems, however, the binding energy of a site is negative, thus this fluctuation will lead to an energetically higher state. For small enough temperature, such an excited state cannot be thermally activated, strongly suppressing the respective contribution to the thermal average.

7.10 Exact limits

Closing our discussion of the PFFRG formalism, we will outline two of its extensions, both leading to exact limits: the generalization to arbitrary spin-length S, rendering the formalism exact in the classical $s \to \infty$ limit, and the extension from SU(2) to SU(N) spins, which gives also an exact analytical solution in the $N \to \infty$ limit.

7.10.1 Large-S limit

So far, we have considered only the $S = 1/2$ case of spin. Having in mind applications of the Heisenberg model to real materials, it however would be beneficial to also be able to treat higher values of S. To this end, we have to extend the fermionic representation of spin operators (5.2) to a higher spin representation of SU(2) generators. The most straightforward way to achieve this would be to generalize the Pauli matrices $\sigma^\alpha/2$ to their higher spin counterparts, i.e. traceless hermitian $(2S+1) \times (2S+1)$ matrices σ_S^μ fulfilling the su(2)-algebra

$$[\sigma_S^\alpha, \sigma_S^\beta] = i\epsilon_{\alpha\beta\gamma}\sigma_S^\gamma. \tag{7.59}$$

This leads to a pseudo-fermionic representation

$$S_i^\alpha = \frac{1}{2} \sum_{\mu,\nu=-2S}^{2S} c_{i\mu}^\dagger \sigma_{S,\mu\nu}^\alpha c_{i\nu}, \tag{7.60}$$

where we have introduced $2S+1$ fermions per lattice point i. For this to be a faithful representation of SU(2), the number of fermions has also in this case to be restricted to one, i.e. the constraint

$$\sum_{\alpha=-2S}^{2S} c_{i\alpha}^\dagger c_{i\alpha} = 1. \tag{7.61}$$

has to be fulfilled. This $1/(2S+1)$ filling is not easily achieved in an average projection scheme, as it is not *a priori* known what the value of the chemical potential has to be. An exact implementation would be possible using imaginary chemical potentials at finite temperatures, which is however not possible in a $T = 0$ scheme [147].

As an alternative route, in Reference [148] it has been put forward to instead introduce $2S$ replicas of spin $S = 1/2$ fermions per site, expressing a spin-S at site i as

$$\boldsymbol{S}_i = \sum_{\kappa=1}^{2S} \boldsymbol{S}_{i,\kappa}, \tag{7.62}$$

with κ enumerating the different replicas. Form this, we can deduce a pseudo-fermionic representation of the spin-operator

$$\boldsymbol{S}_i^\alpha = \frac{1}{2} \sum_{\kappa,\mu,\nu} c_{\mu\kappa}^\dagger \sigma_{\mu\nu}^\alpha c_{\nu\kappa}, \tag{7.63}$$

now subject to the constraint, that at each lattice point, the system has to be at half-filling and additionally, the total spin length must be maximized at each point individually. Similarly to the Popov-Fedotov scheme, this can be achieved using imaginary valued chemical potential [147], but we again will resort to an average projection scheme to implement half-filling.

From the spin addition rules, apart from the maximum spin length states with total spin S, there also exist states with a smaller effective spin, the minimum possible spin length being $S = 0$ for $2S$ even and $S = 1/2$ in the case $2S$

being odd. To minimize the contributions of these states to the partition sum, we can add a level-repulsion term [148]

$$H_{\mathrm{LR}} = -A \sum_i \left(\sum_{\kappa=1}^{2S} \boldsymbol{S}_{i,\kappa} \right)^2 \tag{7.64}$$

to the Hamiltonian. For positive $A < 0$, this will energetically favor the case, where the spin replicas line up to form effective spin S, while gapping out the sectors with smaller spin. It has however been shown, that such a term usually is not needed in practical calculations, as the spin replicas already tend to form the largest spin length multiplets [148]. An alternative point of view is to interpret A in eq. (7.64) as a Lagrange multiplier implementing maximum total spin length in the field theory.

Flow equations at arbitrary S

From the definition of the spin S pseudo-fermions in eq. (7.63), we can readily derive the modifications necessary to the flow equations in order to treat arbitrary spin length S.

Firstly, we note, that in eq. (7.63) every site index i is accompanied by an additional flavor index κ. As the U(1) gauge symmetry of the pseudo-fermions (cf. Section 5.2) acts on every replica of the $S = 1/2$ fermions separately, we find a locality not only in the site index, as discussed in Section 5.4.6, but also for the flavor index.

Secondly, considering the initial conditions of the vertex in Equations (7.55) and (7.56), we see, that these are agnostic of the flavor index. Combined with the flavor index locality, this leads to the vertex function staying completely independent of the flavor index during the flow. Therefore, any summation over flavor indices is trivially carried out, contributing a factor of $2S$ in the flow equations, wherever there is an internal site summation, due to the intimate connection between site and flavor indices discussed above. This effect is most easily shown in the multi-local form of the flow equations discussed in Section 7.3. Generalizing to arbitrary spin S, Equations (7.18) and (7.19) are modified to become

$$\frac{\mathrm{d}}{\mathrm{d}\Lambda} \Sigma^\Lambda(1';1) = \sum_2 \left(\Gamma^\Lambda_{\times,i_1 i_1}(1',2';1,2) - 2S \sum_j \Gamma^\Lambda_{=,i_1 j}(1',2';1,2) \right) S^\Lambda(2,2) \tag{7.65}$$

for the self-energy and

$$\begin{aligned}
\frac{\mathrm{d}}{\mathrm{d}\Lambda} \Gamma^\Lambda_{=,i_1 i_2}(1',2';1,2) = \sum_{3',4',3,4} \Big[& \Gamma^\Lambda_{=,i_1 i_2}(1',2';3,4)\Gamma^\Lambda_{=,i_1 i_2}(3',4';1,2) \\
& - 2S \sum_j \Gamma^\Lambda_{=,i_1 j}(1',4';1,3)\Gamma^\Lambda_{=,j i_2}(3',2';4,2) - (3' \leftrightarrow 4', 3 \leftrightarrow 4) \\
& + \Gamma^\Lambda_{=,i_1 i_2}(1',4';1,3)\Gamma^\Lambda_{\times,i_2 i_2}(3',2';4,2) + (3' \leftrightarrow 4', 3 \leftrightarrow 4) \\
& + \Gamma^\Lambda_{\times,i_1 i_1}(1',4';1,3)\Gamma^\Lambda_{=,i_1 i_2}(3',2';4,2) + (3' \leftrightarrow 4', 3 \leftrightarrow 4) \\
& + \Gamma^\Lambda_{=,i_1 i_2}(2',4';1,3)\Gamma^\Lambda_{=,i_1 i_2}(3',1';4,2) + (3' \leftrightarrow 4', 3 \leftrightarrow 4) \Big] \\
& \times G^\Lambda(3,3') S^\Lambda_{\mathrm{kat}}(4,4')
\end{aligned} \tag{7.66}$$

for the two-particle vertex.

As one can see, in the limit $S \to \infty$, the leading contribution to the vertex function is the RPA-like t-channel diagram. As this contains a non-local summation over the lattice, it is, therefore, the natural candidate to induce quasi-classical long-range ordering, which is confirmed by this construction.

Mean-field temperature conversion

The limit outlined above limit simplifies the flow equations enough to allow for an analytical solution of the two-particle vertex. As we can see from eq. (7.66), the only term surviving in the $S \to \infty$ limit is the non-local t-channel contribution. Therefore, the initially frequency independent vertex can only acquire a structure in the t transfer frequency. For simpler notation, let us define

$$\tilde{\Gamma}^{s/d,\Lambda}_{ij}(t) = \frac{1}{2S}\Gamma^{s/d,\Lambda}_{ij}(s,t,u), \tag{7.67}$$

which remains finite in the $S \to \infty$ limit due to the rescaling with $2S$. Using this notation, the simplified flow equation for the density vertex, derived from eq. (A.6) reads

$$\tilde{\Gamma}^{d,\Lambda}_{i_1 i_2}(t) = \frac{1}{\pi}\int \mathrm{d}\omega \sum_j \tilde{\Gamma}^{d,\Lambda}_{i_1 j}(t)\tilde{\Gamma}^{d,\Lambda}_{j i_2}(t)\left(S^{\Lambda}_{\mathrm{kat}}(\omega)G^{\Lambda}(\omega+t) + S^{\Lambda}_{\mathrm{kat}}(\omega+t)G^{\Lambda}(\omega)\right), \tag{7.68}$$

which shows, that the density vertex decouples from the spin component in this limit. Due to its vanishing initial condition $\tilde{\Gamma}^{d,\Lambda\to\infty} = 0$, the density vertex therefore will not be generated in the RG flow.

The same holds for the self-energy, which in the $S \to \infty$ limit only couples to the density part of the vertex according to

$$\frac{\mathrm{d}}{\mathrm{d}\Lambda}\gamma(\omega) = -\frac{1}{\pi}\int \mathrm{d}\omega \sum_j \tilde{\Gamma}^{d,\Lambda}_{i_1 j}(0)S^{\Lambda}(\omega), \tag{7.69}$$

which is the $S \to \infty$ limit of eq. (7.27).

This extremely simplifies the flow of the remaining spin component of the two-particle vertex, as due to the vanishing self-energy and its derivative the propagators assume a simple form. Resorting to the step-like cutoff, the flow of the spin vertex given in eq. (A.3) reduces to

$$\tilde{\Gamma}^{s,\Lambda}_{i_1 i_2}(t) = \frac{1}{\pi}\int \mathrm{d}\omega \sum_j \tilde{\Gamma}^{s,\Lambda}_{i_1 j}(t)\tilde{\Gamma}^{s,\Lambda}_{j i_2}(t)\left(\frac{\delta(|\omega|-\Lambda)}{\omega}\frac{\theta(|\omega+t|-\Lambda)}{\omega+t} + \frac{\delta(|\omega+t|-\Lambda)}{\omega+t}\frac{\theta(|\omega|-\Lambda)}{\omega}\right), \tag{7.70}$$

which allows for an analytic solution of the frequency integration. Additionally, introducing a Fourier transform of the spatial dependence of the vertex to simplify the lattice sum, the flow equation reads

$$\tilde{\Gamma}^{s,\Lambda}(\boldsymbol{k},t) = \frac{2}{\pi\Lambda(\Lambda+t)}\tilde{\Gamma}^{s,\Lambda}(\boldsymbol{k},t)^2, \tag{7.71}$$

which is amenable to an analytic solution [149]. If there is more than one point in the lattice's basis, $\tilde{\Gamma}$ is to be understood as a matrix in sublattice space and the square as the according product. The analytic solution to eq. (7.71) is given by

$$\tilde{\Gamma}^{s,\Lambda}(\boldsymbol{k},t) = \frac{J(\boldsymbol{k})/4}{1+\frac{J(\boldsymbol{k})}{2\pi\Lambda}\ln\left(1+\frac{t}{\Lambda}\right)}. \tag{7.72}$$

Examining the analytic structure of this solution, we find, that it has a leading divergence for $t = 0$ at

$$\Lambda_c = -\frac{\min_{\boldsymbol{k}} J(\boldsymbol{k})}{2\pi}, \tag{7.73}$$

in other words, the spin vertex diverges at the wave-vector, where the Fourier transform of the initial interaction is most negative. In case of a multi-site basis, the minimum in eq. (7.73) has to be taken over the eigenvalues of the matrix valued Fourier transform in sublattice space.

We can now compare these results to our findings in Chapter 3: In accordance with our findings in the Luttinger-Tisza eigenvalue problem, eq. (3.9), the location of the minimal eigenvalue of the interaction matrix determines the Luttinger-Tisza ordering vector $\boldsymbol{q}_{\mathrm{LT}}$. Therefore, the $S \to \infty$ limit of PFFRG is exact in the sense, that it produces the same ordering tendencies as the Luttinger-Tisza method [148].

Connecting further to our discussions of the classical O($N \to \infty$) mean-field in Section 3.3.3, we can even make a connection between the critical scale Λ_c determined here and the critical temperature determined by the mean-field calculation. Specializing to the case $N = 3$ in the mean-field result, relevant for three-dimensional spin operators, and rescaling energies by $S(S+1)$ to reinclude the spin-length, the mean-field critical temperature is given by $T^c_{\mathrm{MF}} = -S(S+1)/3 \min(\Lambda^\alpha(\boldsymbol{q}))$. Comparing to eq. (7.73), we find the linear connection

$$T^c = \frac{2\pi S(S+1)}{3}\Lambda_c \tag{7.74}$$

between critical temperature and renormalization scale. The above outlined derivation holds only in the classical $S \to \infty$ limit of PFFRG right at the phase transition temperature. Assuming, however, that the transition into an ordered phase at smaller spin values, even in the extreme case $S = 1/2$, can be well described by a suitable classical mean-field state, the conversion is also valid for finite spin lengths and has been successfully used in literature [31, 34, 125, 134] and remarkable agreement between temperature and scale dependence has been found even for larger scales $\Lambda > \Lambda_c$ [30].

7.10.2 Large-N limit

The second case, where PFFRG becomes exact is, in contrast to the classical $S \to \infty$ limit, the extreme quantum limit. This is achieved by promoting the SU(2) symmetry group of spins to SU(N). Although the generalization of spins in this sense is not unique and several implementations with possibly different ground-state properties exist [150], these details do not matter for the general intention of the approach. By enlarging the symmetry group of the spin operators, the relevance of quantum fluctuations is significantly enhanced, rendering them dominant in the $N \to \infty$ limit.

The approach we show here was introduced in References [149] and [151] and our discussion will follow their presentation. In contrast to the arbitrary S generalization of PFFRG, as discussed in the previous section, for arbitrary N we can follow the intuitive path of promoting the spin operators directly to a higher symmetry class. To this end, we introduce the generators T^α of SU(N) in the fundamental representation of this group, with $\alpha \in 1, 2, \ldots, N^2 - 1$. They are $N \times N$ hermitian, traceless matrices characterized by the $\mathfrak{su}(N)$ Lie-algebra

$$\left[T^\alpha, T^\beta\right] = \mathrm{i} \sum_{\gamma=1}^{N^2-1} f_{\alpha\beta\gamma} T^\gamma, \tag{7.75}$$

where f are the structure factors of the group. The generalized spin operators can then be decomposed into N flavors of pseudo-fermions according to

$$S^\alpha = \sum_{\mu,\nu=1}^{N} c^\dagger_\mu T^\alpha_{\mu\nu} c_\nu, \tag{7.76}$$

in accordance with the SU(2) case[5] in eq. (5.2). For this mapping to be faithful, we now have to introduce the modified half-filling constraint

$$\sum_{\mu=1}^{N} c_\mu^\dagger c_\mu = \frac{N}{2}, \tag{7.77}$$

which immediately constraints the generalization to even N. As for the SU(2) case, this will only be implemented on average, as again defects in the spin structure should be energetically gapped out, similarly to what we have discussed in Section 7.9.

Employing a parametrization in terms of spin and density like vertex components

$$\Gamma_{=,i_1 i_2}(1',2';1,2) = \Gamma_{\mathrm{s},i_1 i_2}(\omega_{1'},\omega_{2'};\omega_1,\omega_2) T^\alpha_{\mu_{1'}\mu_1} T^\alpha_{\mu_{2'}\mu_2} + \Gamma_{\mathrm{d},i_1 i_2}(\omega_{1'},\omega_{2'};\omega_1,\omega_2)\delta_{\mu_{1'}\mu_1}\delta_{\mu_{2'}\mu_2}, \tag{7.78}$$

we immediately see, that the general structure of the flow equations will remain unchanged by the generalization, which amounts to a mere change of prefactors. As we will not need the explicit equations for the remainder of this thesis, we refer to literature for the corresponding parametrization of the SU(N) PFFRG flow, which can be found in References [30] and [59].

The main outcome we mention here is the result for $N \to \infty$: In this limit, the only contribution to the two-particle vertex is the u-channel diagram of the spin vertex, which does not generate non-local terms. Thus, the susceptibility will remain finite throughout the whole RG flow, while the vertex itself will diverge, signaling a transition into an ordered, but not magnetically ordered, phase [149]. This reproduces the analytical mean-field results for $N \to \infty$, which are exact in this limit. Furthermore, the relation between critical scale and mean-field critical temperature, eq. (7.74), found in the $S \to \infty$ limit is also reproduced in the $N \to \infty limit$. This instills confidence in the validity of the conversion factor also away from the extreme classical and quantum limits.

The Katanin truncation is a vital ingredient in making this connection, *a posteriori* rationalizing the necessity to include these corrections to obtain magnetically disordered ground-states. In summary, PFFRG is exact in both the classical large-S and extreme quantum large-N limits, instilling confidence in the unbiasedness of the method.

The SU(N) generalization breaks the symmetry between s- and u-channel we have found in eq. (7.25) not only for $N \to \infty$, but also for any finite $N > 2$. We can easily understand this fact by considering the origin of this connection: being rooted in the SU(2) gauge symmetry of the pseudo-fermion mapping, the symmetry naturally will no longer be present in the SU(N) generalization of the fermions. While this enlarged symmetry group at first is only introduced regarding the physical spin-SU(2), due to its inherent connection with the pseudo-fermion mapping, the change will also destroy the SU(2) gauge structure of the mapping. Please note, that this fact was not fully appreciated in the original publication Reference [149] introducing finite N calculations, where this symmetry, although broken in the analytical formulation, was still implemented in the numerical code, producing wrong results. To the best of our knowledge, this, however, was not rectified in literature to date.

[5] Please note, that in the context of the large N generalization the factor ½ in eq. (5.2) is absorbed into the definition of the generators T^α.

CHAPTER 8

Multi-Loop extension to PFFRG

The implementation of PFFRG introduced in the previous chapter, although proven in many applications, suffers from the approximations inherent to its formulation. Specifically, the necessity to truncate the flow equations after the two-particle vertex effectively eliminates all correlations in the physical system involving three or more spins. This, however, is an uncontrolled approximation, as there exists no estimate for the impact of such terms. Chiral spin liquids [152], e.g., are characterized by a non-vanishing expectation value of the spin chirality $\langle \boldsymbol{S}_1 \cdot (\boldsymbol{S}_2 \times \boldsymbol{S}_3) \rangle$ [33], which – by definition – can only be captured through the three-particle vertex. Additionally, the full FRG flow should be independent of the specific regulator function chosen, as long as it fulfills the general boundary conditions given in eq. (6.31) [101]. Unfortunately, this is only true for the full FRG flow and will be spoiled by truncation of the equations [153].

To partially remedy these shortcomings, in this chapter we will discuss a way to consistently include parts of the m-particle vertex flows for $m > 2$, which are constructible using self-energy and two-particle vertices only. Due to two-particle reducibility of the FRG equations, these higher-particle vertex contributions will in turn be made up of the two-particle reducible subset of diagrams representing them. This class of diagrams, we end up with, is known as parquet-type [154].

The general formalism we adopt here has been laid out in References [155], [153], and [156], where the flow equations have been derived from the self-consistency equations of the parquet formalism, namely the Schwinger-Dyson and Bethe-Salpeter equations. It turns out, that the resulting formalism naturally extends the one-loop structure of the FRG flow by including orders on the right-hand side [156]. In the context of the one-band Hubbard model, multi-loop FRG has been shown to significantly improve the quantitative outcome of FRG to be on par with other state-of-the-art numerical methods [81, 90].

Concerning the notion of loop-order, we have to distinguish two different scenarios this term is used in: Firstly, the diagrammatic content of the vertex function Γ, which solves the FRG flow already has a loop multi-loop structure introduced by the flow equations even without including the corrections we will discuss. The loop order we are concerned with, however, is the one of the right-hand side of the FRG flow equations. In the standard formulation, cf. eq. (6.43), there is only one loop present, while the corrections we derived in this section will feature multiple overlapping ones.

Concerning PFFRG, first steps have been taken in Reference [157] to include such corrections up to two-loop level into the flow. This was done in an iterative manner based on an implementation of the scheme for itinerant fermions introduced in Reference [158]. This two-loop PFFRG is indeed part of the formalism we present in the following, which therefore can be seen as a natural extension to higher loop orders.

As a first step, we will go back to the Katanin truncation to show, that by virtue of the corresponding substitution, what we consider one-loop PFFRG actually contains two-loop contributions. Starting from the Katanin-truncated

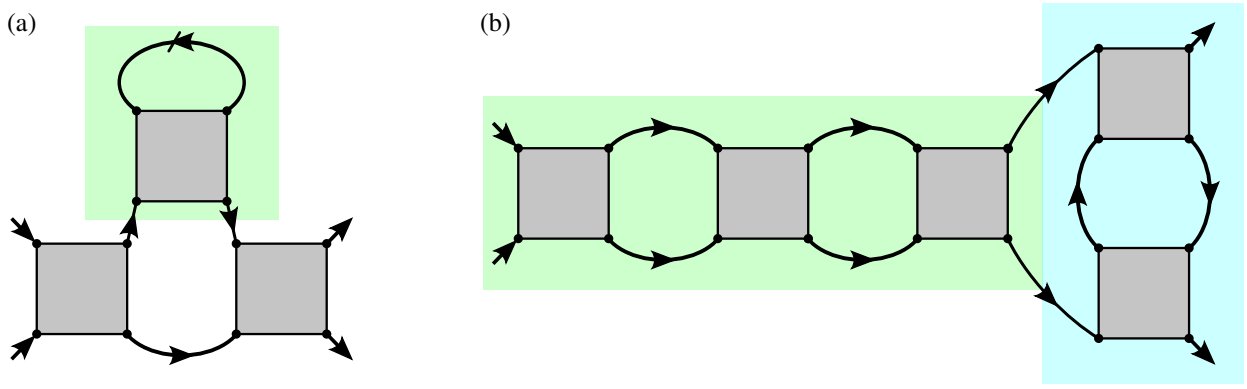

Figure 8.1: (a) Exemplary contribution from the Katanin substitution, where the self-energy derivative (green box) is inserted in the s-channel contribution. (b) Partial ladder diagram already included in the two-particle vertex by virtue of the flow. Here a s-channel ladder (green box) is connected to a t-channel contribution.

flow equations, we will outline a derivation of the multi-loop FRG for general models purely starting from the flow equations. This means, we do not have to invoke the self-consistent parquet equations at any point, to construct our multi-loop flow, but can rely on a self-contained derivation in the context of FRG. To the best of our knowledge, this direct connection has not been drawn in the literature to date.

Finally, we will discuss the caveats of implementing the multi-loop equations in a PFFRG context, which mostly are rooted in the parametrizations introduced in Chapter 7 and the corresponding symmetries.

8.1 Katanin truncation as partial two-loop

The Katanin truncation is widely employed in standard PFFRG calculations, as it restores the balance between classical ordering tendencies from the $S \to \infty$ limit, cf. Section 7.10.1 and quantum fluctuations, as distilled in the $N \to \infty$ limit, cf. Section 7.10.2 . While the former is already exact without invoking Katanin[1], the exactness of the latter limit explicitly requires the replacement

$$S^{\Lambda}(\omega) \to S^{\Lambda}_{\mathrm{kat}}(\omega) = -\frac{\mathrm{d}}{\mathrm{d}\Lambda} G^{\Lambda}(\omega) \tag{8.1}$$

to capture the right physics. This also explains, why without invoking eq. (8.1), magnetic long-range order is found even in systems known to avoid such a transition due to quantum fluctuations, such as the nearest-neighbor Heisenberg antiferromagnet on the Kagome lattice [59].

To better understand the structure introduce by the substitution prescribed in eq. (8.1), let us first state, that the additional terms introduced

$$S^{\Lambda}_{\mathrm{kat}}(\omega) - S^{\Lambda}(\omega) = -\frac{\mathrm{d}}{\mathrm{d}\Lambda} G^{\Lambda} + \frac{\mathrm{d}}{\mathrm{d}\Lambda} G^{\Lambda}\Big|_{\gamma^{\Lambda}=\mathrm{const.}} = -\mathrm{i}\left(G^{\Lambda}\right)^2 \frac{\mathrm{d}}{\mathrm{d}\Lambda}\gamma^{\Lambda} \tag{8.2}$$

are proportional to the scale-derivative of the self-energy. This quantity already recasts as a diagram containing a loop integration, cf. eq. (7.27), therefore inserting it into the FRG flow equations, which as well have a one-loop structure, will yield a contribution containing two nested loops, as shown in Figure 8.1(a). The structure of the two loops, however, a vastly different: In the self-energy derivative being a single-particle quantity constructed from a

[1] The additional contributions from the Katanin-substitution exactly vanish in the $S \to \infty$ limit.

two-particle vertex, naturally, the loop only consists of one propagator joining one incoming and outgoing leg of the same two-particle vertex. In contrast, the loop from the two-particle vertex flow equation connects two vertices Γ by virtue of two separate propagators, each carrying different frequency arguments. These are chosen, such that their sum is the transfer frequency of the two-particle reducible channel the respective diagram is part of.

This justifies the notion found in literature, that the Katanin substituted flow, even though there are two loop integrations present, is still considered to have a one-loop structure [139, 140, 153, 155–157]. In accordance with this naming scheme, in the following discussion of multi-loop FRG, by referring to loop order we always mean the number of two-propagator loops, as found in the flow of the two-particle vertex, included in the scheme.

We want to highlight an additional crucial feature of the Katanin substitution: It is only performed in the two-particle vertex flow, while the equation for the self-energy derivative is left unaltered [106]. We will find the reason for this seemingly inconsistent prescription in the discussion of the full multiloop expansion in Section 8.2.4.

8.2 Derivation of Multi-loop corrections from general flow-equations

In literature, the first steps to include higher loop orders in the FRG flow was taken in References [159] and [160] by explicitly calculating two-loop corrections to the two-particle vertex flow originating from the hitherto neglected three-particle vertex, cf. Section 6.5. The practical implementation was tremendously simplified by the realization by Eberlein in Reference [158]: These two-loop contributions can either be recast into a sum of the Katanin contributions discussed in the previous Section 8.1 or into additional diagrams featuring overlapping loops, which can be obtained by reinserting one-loop results into the flow equations.

Kugler *et al.*have extended this structure in References [155], [153], and [156], however from a completely different point of view: Starting from the self-consistent parquet equations for the self-energy and two-particle vertex, they derive multi-loop flow equations by introducing the RG regulator function as prescribed in eq. (6.30) and subsequently differentiating the self-consistency with respect to the scale Λ. The standard Katanin-substituted FRG equations in this approach are recovered in a one-loop approximation.

While a completely valid construction, in a FRG context, employing the parquet equations as an external input seems out-of-place, as they do not immediately connect to the flow equations. Therefore, our following derivation of the multi-loop corrections is based solely on the diagrammatic FRG formalism we have developed in Chapter 6. We will see, that the resulting equations are the same as the ones derived from the parquet equations, rendering both approaches equivalent.

8.2.1 Loop structure, cutting lines and reducibility

As a prerequisite for our derivation, we first have to fix the exact meaning of a few technical terms we have intuitively used so far in the context of a diagrammatic representation of the FRG. In particular, we have to put the notion of a loop belonging to the transfer frequency channel c, as well as cutting a line in diagrams and the resultant reducibility of diagrams on more solid grounds.

We have introduced in Section 7.5 a shorthand notation for the c-channel ($c = s/t/u$) loop in eq. (7.34). To arrive at a better understanding of the frequency structure of this quantity, consider a slightly expanded expression, based on the general flow equation eq. (6.43), inserting the asymptotic frequency parametrization introduced in Section 7.5,

but explicitly refraining from using the multilocality of the pseudo-fermion vertex[2]

$$\left[\Gamma^\Lambda \circ \frac{\mathrm{d}}{\mathrm{d}\Lambda}\left(G^\Lambda \times G^\Lambda\right) \circ \Gamma^\Lambda\right]_{\mathrm{c}} (c, \nu_c, \nu_c') = C_{\mathrm{c}} \int \mathrm{d}\omega\, \Gamma^\Lambda(c, \nu_c, \omega) \frac{\mathrm{d}}{\mathrm{d}\Lambda}\left[G^\Lambda\left(\omega + \frac{c}{2}\right) \times G^\Lambda\left(\omega - \frac{c}{2}\right)\right] \Gamma^\Lambda(c, \omega, \nu_c'), \tag{8.3}$$

where we have only given the frequency arguments of the vertex functions in the natural parametrization of the vertex. The corresponding conversions can be found in the flow equations in appendix B. Lattice and spin sums are implied and the constant C_{c} denotes all channel specific prefactors.

From eq. (8.3) it becomes immediately clear, what is meant by a c-channel loop contribution: The loop integration variable ω in the propagators is accompanied by the respective transfer frequency c, which is referred to c "flowing through the loop". Note, that the fermionic frequencies $\nu^{(\prime)}$, in contrast, do not enter the loop integration.

Cutting a line in diagrammatic language now means removing one of the (possibly differentiated) propagators G in eq. (8.3). As this still leaves one one-particle Green's function, which depends on the loop frequency, the graph representing eq. (8.3) remains connected by this cut, rendering it one-particle irreducible. On the other hand, cutting both propagator lines, ω is no longer part of the argument of any G, meaning that as part of the cutting we have to additionally remove the integral at this point, and eq. (8.3) factorizes into two-particle vertices. This is equivalent to the graph being disconnected, rendering the channels two-particle reducible.

As a last comment on the analytical structure of eq. (8.3), we want to note, that although we have given the frequency dependence of the full vertex in terms of the respective natural frequencies of a channel c, Γ, in fact, is made up of contributions from all channels according to

$$\Gamma = R + \sum_{c'} g^{c'}, \tag{8.4}$$

where the remainder term R denotes all two-particle irreducible contributions[3] to Γ. This means, that for the contributions from channels $c' \neq c$, a conversion from the asymptotic frequencies of channel c to the ones of c' has to be performed, which intermixes bosonic and fermionic frequencies, as explicitly stated in appendix B.

8.2.2 Diagrammatic content of the two-particle vertex in Katanin-truncation

As we will extend the standard one-loop flow in the following, let us first discuss, which diagrams are already included in the standard one-loop flow equation

$$\frac{\mathrm{d}}{\mathrm{d}\Lambda}\Gamma = \sum_c \left[\Gamma^\Lambda \circ \frac{\mathrm{d}}{\mathrm{d}\Lambda}\left(G^\Lambda \times G^\Lambda\right) \circ \Gamma^\Lambda\right]_{\mathrm{c}} \tag{8.5}$$

and what this implies for the vertex Γ, that solves eq. (8.5). In Section 7.5 we have argued, that during the flow equation implies, that starting from the bare vertex at $\Lambda_0 \to \infty$, a structure of coupled two-particle bubbles is formed, cf. the expansion of the flow in eq. (7.38). We can view this as a repeated reinsertion of the (integrated) right-hand side of eq. (8.5) into itself for successive infinitesimal scale steps $\mathrm{d}\Lambda$. This means, that in particular all partial ladder diagrams in a specific channel, i.e. diagrams, in which multiple of the same c-channel reducible bubbles are chained together, possibly connecting to a part of different reducibility, are included in the flow. Such a diagram featuring a partial s-ladder is shown in Figure 8.1(b). Therefore, the solution of the standard flow equations already has a multi-loop structure.

[2] This choice of parametrization broadens the application of our derivation, rendering it in principle also valid for itinerant fermionic systems, where the frequency arguments are extended to become full 4-momenta.

[3] In the truncated formulation of FRG, R is just the bare vertex $\Gamma^{\Lambda\to\infty}$.

What we will consider in the following, however, is not the diagrammatic structure of the vertex Γ itself, but its derivative given in the flow equations. From eq. (8.5) we immediately find, that even having the structure of the vertex function in mind, the differentiated loop still is the outermost one, i.e. it is not nested. Therefore, all corrections to eq. (8.5) we will derive have to feature the differentiated loop as a nested one.

8.2.3 Multi-loop flow of the two-particle vertex

We now can start our derivation of the multi-loop flow of the two-particle vertex. To this end we rewrite the symbolic form of the Katanin-truncated flow equation, given in eq. (7.34), as

$$\begin{aligned}\frac{\mathrm{d}}{\mathrm{d}\Lambda}\Gamma^{\Lambda} &= \sum_{c}\left[\Gamma^{\Lambda}\circ\frac{\mathrm{d}}{\mathrm{d}\Lambda}\left(G^{\Lambda}\times G^{\Lambda}\right)\circ\Gamma^{\Lambda}\right]_{\mathrm{c}} \\ &= \frac{\mathrm{d}}{\mathrm{d}\Lambda}\sum_{c}\left[\Gamma^{\Lambda}\circ\left(G^{\Lambda}\times G^{\Lambda}\right)\circ\Gamma^{\Lambda}\right]_{\mathrm{c}} - \sum_{c}\left[\frac{\mathrm{d}\Gamma^{\Lambda}}{\mathrm{d}\Lambda}\circ\left(G^{\Lambda}\times G^{\Lambda}\right)\circ\Gamma^{\Lambda}\right]_{\mathrm{c}} - \sum_{c}\left[\Gamma^{\Lambda}\circ\left(G^{\Lambda}\times G^{\Lambda}\right)\circ\frac{\mathrm{d}\Gamma^{\Lambda}}{\mathrm{d}\Lambda}\right]_{\mathrm{c}}.\end{aligned} \tag{8.6}$$

Upon integration with respect to the flow parameter from the initial scale $\Lambda_0 \to \infty$ to some lower Λ, we find

$$\begin{aligned}\Gamma^{\Lambda} = \Gamma^{\Lambda_0} &+ \sum_{c}\left[\Gamma^{\Lambda}\circ\left(G^{\Lambda}\times G^{\Lambda}\right)\circ\Gamma^{\Lambda}\right]_{\mathrm{c}} - \int_{\Lambda_0}^{\Lambda}\mathrm{d}\Lambda'\sum_{c}\left[\frac{\mathrm{d}\Gamma^{\Lambda'}}{\mathrm{d}\Lambda'}\circ\left(G^{\Lambda'}\times G^{\Lambda'}\right)\circ\Gamma^{\Lambda'}\right]_{\mathrm{c}} \\ &- \int_{\Lambda_0}^{\Lambda}\mathrm{d}\Lambda'\sum_{c}\left[\Gamma^{\Lambda'}\circ\left(G^{\Lambda'}\times G^{\Lambda'}\right)\circ\frac{\mathrm{d}\Gamma^{\Lambda'}}{\mathrm{d}\Lambda'}\right]_{\mathrm{c}}.\end{aligned} \tag{8.7}$$

A crucial observation now is, that the second term on the right-hand side of eq. (8.7) is of order $O\left(\Gamma^2\right)$, whereas the last two terms, containing derivatives of the vertex, are $O\left(\Gamma^3\right)$. These originate from completing the scale derivative in eq. (8.6). As they prevent the right-hand side of the flow equation from being a total scale derivative, we can view the integral terms in eq. (8.7) as manifestations of the Katanin truncation. Therefore, to reinclude at least part of the discarded three-particle vertex contributions and find a self-consistent flow-equation on two-particle vertex level, we discard these integral terms, leading to

$$\Gamma^{\Lambda} = \Gamma^{\Lambda_0} + \sum_{c}\left[\Gamma^{\Lambda}\circ\left(G^{\Lambda}\times G^{\Lambda}\right)\circ\Gamma^{\Lambda}\right]_{\mathrm{c}} - \text{o.c.}, \tag{8.8}$$

where we have already anticipated, that this formulation will overcount contributions to the flow by including diagrams, which cannot be derived from three-particle vertex contributions, by subtracting o.c..

Differentiating eq. (8.8) with respect to the RG scale Λ, we find the corresponding flow-equation

$$\begin{aligned}\frac{\mathrm{d}}{\mathrm{d}\Lambda}\Gamma^{\Lambda} = \sum_{c}\left[\Gamma^{\Lambda}\circ\frac{\mathrm{d}}{\mathrm{d}\Lambda}\left(G^{\Lambda}\times G^{\Lambda}\right)\circ\Gamma^{\Lambda}\right]_{\mathrm{c}} &+ \sum_{c}\left[\frac{\mathrm{d}\Gamma^{\Lambda}}{\mathrm{d}\Lambda}\circ\left(G^{\Lambda}\times G^{\Lambda}\right)\circ\Gamma^{\Lambda}\right]_{\mathrm{c}} \\ &+ \sum_{c}\left[\Gamma^{\Lambda}\circ\left(G^{\Lambda}\times G^{\Lambda}\right)\circ\frac{\mathrm{d}\Gamma^{\Lambda}}{\mathrm{d}\Lambda}\right]_{\mathrm{c}} - \text{o.c.},\end{aligned} \tag{8.9}$$

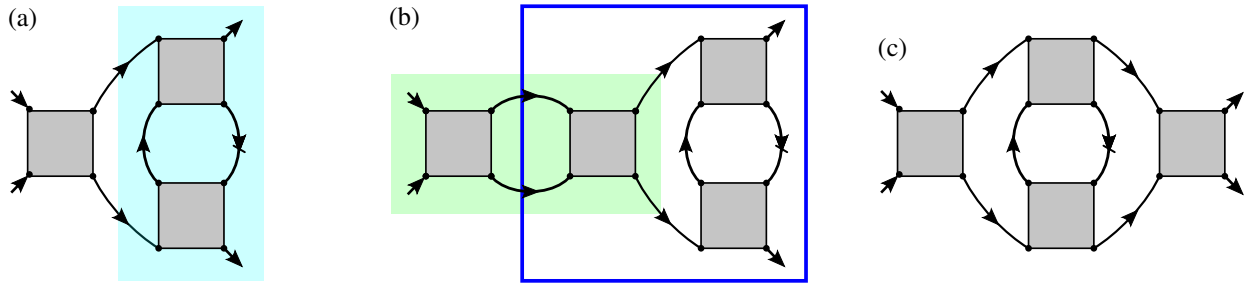

Figure 8.2: Exemplary diagrammatic content of the multi-loop expansion of the two-particle vertex Γ. (a) Two-loop diagram resulting from the insertion of a one-loop s-channel contribution (blue box) into the right vertex of a s-channel diagram. (b) Example of a three-loop diagram not to include in multi-loop, obtained by inserting the $\ell = 2$ contribution form (a) (blue box) into the right vertex of the s-channel. The partial ladder (green box) is already included in the two-particle vertex by virtue of the flow equations, meaning this diagrammatic contribution is already included in (a). (c) Contribution to the central part, where the right insertion (a) is inserted into the left vertex of the s-channel, leading to a nested structure not included before.

i.e. we now have found an implicit differential equation for the two-particle vertex Γ. In an attempt to solve eq. (8.9), we resort to a fixed point iteration: starting from $\frac{\mathrm{d}}{\mathrm{d}\Lambda}\Gamma^{\Lambda,(0)} = 0$ we apply the right-hand side of the implicit equation repeatedly to find the iterated approximations

$$\begin{aligned}\frac{\mathrm{d}}{\mathrm{d}\Lambda}\Gamma^{\Lambda,(n+1)} = &\sum_c \left[\Gamma^\Lambda \circ \frac{\mathrm{d}}{\mathrm{d}\Lambda}\left(G^\Lambda \times G^\Lambda\right) \circ \Gamma^\Lambda\right]_c + \sum_c \left[\frac{\mathrm{d}}{\mathrm{d}\Lambda}\Gamma^{\Lambda,(n)} \circ \left(G^\Lambda \times G^\Lambda\right) \circ \Gamma^\Lambda\right]_c \\ &+ \sum_c \left[\Gamma^\Lambda \circ \left(G^\Lambda \times G^\Lambda\right) \circ \frac{\mathrm{d}}{\mathrm{d}\Lambda}\Gamma^{\Lambda,(n)}\right]_c - \text{o.c.}\,,\end{aligned} \tag{8.10}$$

converging to the final solution. This scheme is not guaranteed to converge, however, as we will see in Sections 11.3 and 12, numerical results show the validity of this approach.

As we can see,

$$\frac{\mathrm{d}}{\mathrm{d}\Lambda}\Gamma^{\Lambda,(1)} = \sum_c \left[\Gamma^\Lambda \circ \frac{\mathrm{d}}{\mathrm{d}\Lambda}\left(G^\Lambda \times G^\Lambda\right) \circ \Gamma^\Lambda\right]_c \tag{8.11}$$

exactly reproduces the (over-counting free) one-loop FRG result. Due to the insertion of the vertex from iteration n into the loops to obtain iteration $n+1$, all diagrams newly generated in this step will be of loop-order $\ell = n+1$. As these diagrams are topologically different for each ℓ, they cannot cancel each other, i.e. the overcounting has to be addressed at each loop order separately. This motivates to define the ℓ-loop contributions

$$\frac{\mathrm{d}}{\mathrm{d}\Lambda}\Gamma^{\Lambda,\ell} = \frac{\mathrm{d}}{\mathrm{d}\Lambda}\Gamma^{\Lambda,(\ell)} - \frac{\mathrm{d}}{\mathrm{d}\Lambda}\Gamma^{\Lambda,(\ell-1)}\,, \tag{8.12}$$

with

$$\frac{\mathrm{d}}{\mathrm{d}\Lambda}\Gamma^{\Lambda,\ell=1} = \sum_c \left[\Gamma^\Lambda \circ \frac{\mathrm{d}}{\mathrm{d}\Lambda}\left(G^\Lambda \times G^\Lambda\right) \circ \Gamma^\Lambda\right]_c \tag{8.13}$$

$$\frac{\mathrm{d}}{\mathrm{d}\Lambda}\Gamma^{\Lambda,\ell>1} = \sum_c \left[\frac{\mathrm{d}}{\mathrm{d}\Lambda}\Gamma^{\Lambda,\ell-1} \circ \left(G^\Lambda \times G^\Lambda\right) \circ \Gamma^\Lambda\right]_c + \sum_c \left[\Gamma^\Lambda \circ \left(G^\Lambda \times G^\Lambda\right) \circ \frac{\mathrm{d}}{\mathrm{d}\Lambda}\Gamma^{\Lambda,\ell-1}\right]_c - \text{o.c.}\,. \tag{8.14}$$

Equations (8.13) and (8.14) clearly define an iterative scheme in the spirit of the two-loop corrections derived in References [158] and [157]. To close the derivation, we just have to address the issue of overcounting still present in eq. (8.14). Referring to the untruncated flow equation for the two-article vertex, eq. (6.43), clearly all $\ell \geq 2$

contributions to the flow have to be part of the three-particle vertex, where two external legs are connected by a single-scale propagator S. By definition, the three-particle vertex is one-particle irreducible, meaning eq. (8.14) can only include terms, which are one-particle irreducible *after* cutting the single scale propagator contained in the diagrams. This in turn means for $\ell = 2$, that any insertion of terms of loop order $\ell = 1$ in eq. (8.14) have to be performed such that the single-scale propagator is contained in a nested loop. By this, we mean, that the loop variable of the outer loop has to flow through the loop of the insertion. Following our discussions in Section 8.2.1, this implies, that the outer loop frequency has to enter the transfer frequency of the respective channels of the insertion of loop-order $\ell = 1$, cf. eq. (8.3). From the same expression, we can deduce, that this excludes all insertions of a channel c into a diagram of the same channel, as then the integration variable would enter the fermionic frequency of the insertion. Therefore, we have to restrict insertion in a way, that only complementary channels are to be inserted to calculate the $\ell = 2$ contributions. As an illustration, we show one of the resulting diagrams in Figure 8.2(a).

The same rule applies for higher loop orders, but for a different reason. If we were to insert a c-channel term of loop order $\ell - 1$ into the c-reducible diagram, we would generate a contribution, that features a partial ladder structure. As we have discussed in Section 8.2.2, the two-particle vertex already contains all partial ladders, i.e. we can absorb the partial ladder, leading to an $\ell - 1$-loop diagram already summed up. We illustrate this in Figure 8.2(b) using a partial s-channel ladder. Therefore, a self-insertion of channels is also not possible for $\ell \geq 3$.

Here, however, we find one exception: for $\ell \geq 3$, there is the possibility to insert $\ell - 1$ diagrams of the same channel, such that the propagator bubble is connected to the $\ell - 2$ insertion, leading again to a nested loop structure, cf. Figure 8.2(c). This means, that we have to insert the c-channel $\ell - 1$ contribution, where the $\ell - 2$ insertion has been performed in the right vertex or vice versa. This term has been coined the central part in literature [153, 155, 156].

In total, we can summarize our findings by rewriting eq. (8.14) as

$$\frac{\mathrm{d}}{\mathrm{d}\Lambda}\Gamma^{\Lambda,\ell>1} = \sum_c \left(\dot{g}_{\mathrm{L}}^{c,\Lambda,\ell} + \dot{g}_{\mathrm{C}}^{c,\Lambda,\ell} + \dot{g}_{\mathrm{R}}^{c,\Lambda,\ell}\right), \tag{8.15}$$

where the left (L), right (R) and central (C) part of the channels are defined by

$$\dot{g}_{\mathrm{L}}^{c,\Lambda,\ell>1} = \left[\sum_{c'\neq c} \dot{g}^{c',\Lambda,\ell-1} \circ \left(G^\Lambda \times G^\Lambda\right) \circ \Gamma^\Lambda\right]_c \tag{8.16}$$

$$\dot{g}_{\mathrm{R}}^{c,\Lambda,\ell>1} = \left[\Gamma^\Lambda \circ \left(G^\Lambda \times G^\Lambda\right) \circ \sum_{c'\neq c} \dot{g}^{c',\Lambda,\ell-1}\right]_c \tag{8.17}$$

$$\dot{g}_{\mathrm{C}}^{c,\Lambda,\ell>2} = \dot{g}_{\mathrm{L}}^{c,\Lambda,\ell} = \left[\dot{g}_{\mathrm{R}}^{c,\Lambda,\ell-1} \circ \left(G^\Lambda \times G^\Lambda\right) \circ \Gamma^\Lambda\right]_c = \left[\Gamma^\Lambda \circ \left(G^\Lambda \times G^\Lambda\right) \circ \dot{g}_{\mathrm{L}}^{c,\Lambda,\ell-1}\right]_c. \tag{8.18}$$

where the full channel at loop order ℓ is defined by

$$\dot{g}^{c,\Lambda,\ell} = \dot{g}_{\mathrm{L}}^{c,\Lambda,\ell} + \dot{g}_{\mathrm{C}}^{c,\Lambda,\ell} + \dot{g}_{\mathrm{R}}^{c,\Lambda,\ell} \tag{8.19}$$

and the central part is vanishing for $\ell = 2$. The iterative structure of the flow equations given here exactly reproduces the results from the derivation based on the parquet equations [153, 155, 156].

8.2.4 Multi-loop flow of the self-energy

Having found the higher loop corrections to the two-particle vertex flow, we now also have to consider the changes these corrections induce in the flow of the self-energy, as given in eq. (6.41). We will arrive there considering a similar fix-point iteration as in the previous section. To this end, we rewrite eq. (6.41), using, that the one-particle vertex is, up to a sign, the self-energy, in the symbolic form

$$\frac{\mathrm{d}}{\mathrm{d}\Lambda}\Sigma^{\Lambda} = -\left[\Gamma^{\Lambda} \circ S^{\Lambda}\right]. \tag{8.20}$$

In a similar fashion to eq. (8.6), we now distill a total derivative out of eq. (8.20) by using the definition of the single-scale propagator, eq. (6.42). We find

$$\frac{\mathrm{d}}{\mathrm{d}\Lambda}\Sigma^{\Lambda} = \frac{\mathrm{d}}{\mathrm{d}\Lambda}\left[\Gamma^{\Lambda} \circ G^{\Lambda}\right] - \left[\frac{\mathrm{d}\Gamma^{\Lambda}}{\mathrm{d}\Lambda} \circ G^{\Lambda}\right] + \left[\Gamma^{\Lambda} \circ \left(G^{\Lambda} \times \frac{\mathrm{d}\Sigma^{\Lambda}}{\mathrm{d}\Lambda} \times G^{\Lambda}\right)\right] \tag{8.21}$$

and upon integration with respect to the scale

$$\Sigma^{\Lambda} = \Sigma^{\Lambda_0} + \left[\Gamma^{\Lambda} \circ G^{\Lambda}\right] - \int_{\Lambda_0}^{\Lambda} \left[\frac{\mathrm{d}\Gamma^{\Lambda}}{\mathrm{d}\Lambda} \circ G^{\Lambda}\right] - \int_{\Lambda_0}^{\Lambda} \left[\Gamma^{\Lambda} \circ \left(G^{\Lambda} \times \frac{\mathrm{d}\Sigma^{\Lambda}}{\mathrm{d}\Lambda} \times G^{\Lambda}\right)\right]. \tag{8.22}$$

This is the one-particle equivalent to the integrated two-particle flow given in eq. (8.7). Similar to the argument we have given there, the integral terms in eq. (8.22) are realizations of the approximation introduced by truncating the hierarchy of flow equations using the Katanin substitution. We therefore go the same route as for the two-particle vertex and neglect these terms to alleviate shortcomings of the formulation, leading to the improved expression

$$\Sigma^{\Lambda} = \Sigma^{\Lambda_0} + \left[\Gamma^{\Lambda} \circ G^{\Lambda}\right] - \text{o.c.}, \tag{8.23}$$

where we again have anticipated an overcounting of diagrams. Upon differentiation with respect to Λ, we again find the improved flow equation

$$\frac{\mathrm{d}}{\mathrm{d}\Lambda}\Sigma^{\Lambda} = -\left[\Gamma^{\Lambda} \circ S^{\Lambda}\right] + \left[\frac{\mathrm{d}\Gamma^{\Lambda}}{\mathrm{d}\Lambda} \circ G^{\Lambda}\right] - \left[\Gamma^{\Lambda} \circ \left(G^{\Lambda} \times \frac{\mathrm{d}\Sigma^{\Lambda}}{\mathrm{d}\Lambda} \times G^{\Lambda}\right)\right] - \text{o.c.}. \tag{8.24}$$

The first term in eq. (8.24) now is nothing else than the standard self-energy derivative we have used earlier, while the second term introduces corrections generated by multi-loop contributions to the vertex-derivative. The third term again renders eq. (8.24) an implicit differential equation, which necessitates another fixed point iteration.

Before we, however, turn to implementing this, let us first consider, which diagrams to actually include in the flow, to avoid the overcounting. We start with the second term in eq. (8.24), which introduces contributions stemming from the three-particle vertex. Here we have to take care to not include diagrams, that can already be generated by the first term. Our observation now is, that in the two-particle vertex, no diagrams are included, where a propagator connects a two-particle vertex to itself, cf. Equations (8.16), (8.17), and (8.18), but all other fully connected ones. Therefore, the first term in eq. (8.24) captures all possibilities, building multi-loop contributions in which all undifferentiated propagators are connected to pairwise different vertices. What is left for the second term now is to sum up contributions, in which the propagator G can connect two legs of the same vertex, meaning we have to restrict the insertions done there to t-channel corrections.

Furthermore, as already outlined in Section 8.2.2, we cannot form partial ladders to avoid overcounting, as they are already included in the two-particle vertex. We, therefore, have to restrict the insertions to terms, where the outermost loop structure is fully nested, which exactly is the case in the central part of the vertex corrections given by eq. (8.18). Therefore, the second term has to be restricted to only feature $\dot{g}_{\mathrm{C}}^{\mathrm{t},\Lambda,\ell}$ contributions to the self-energy. Having performed the full multi-loop summation, these terms are readily available, meaning no additional computations are necessary.

To be consistent at this level of loop order, we now have to reinsert the contributions from the second term into the third term in eq. (8.24). This then concludes the full self-energy correction in the first step of the fixed point iteration of eq. (8.24), at which level the self-energy derivative now is given by

$$\frac{\mathrm{d}}{\mathrm{d}\Lambda}\Sigma^{\Lambda} = \dot{\Sigma}_{\mathrm{Std}}^{\Lambda} + \dot{\Sigma}_{\mathrm{t}}^{\Lambda} + \dot{\Sigma}_{\bar{\mathrm{t}}}^{\Lambda} \tag{8.25}$$

where the three terms are given by

$$\dot{\Sigma}_{\mathrm{Std}}^{\Lambda} = -\left[\Gamma^{\Lambda} \circ S^{\Lambda}\right] \tag{8.26}$$

$$\dot{\Sigma}_{\mathrm{t}}^{\Lambda} = \left[\sum_{\ell} \dot{g}_{\mathrm{C}}^{\mathrm{t},\Lambda,\ell} \circ G^{\Lambda}\right] \tag{8.27}$$

$$\dot{\Sigma}_{\bar{\mathrm{t}}}^{\Lambda} = -\left[\Gamma^{\Lambda} \circ \left(G^{\Lambda} \times \dot{\Sigma}_{\mathrm{t}}^{\Lambda} \times G^{\Lambda}\right)\right]. \tag{8.28}$$

As the multi-loop corrections to the vertex depend, by virtue of the Katanin substitution, on the self-energy derivative, the fixed point iteration has to be performed by recalculating the two-particle vertex derivatives with eq. (8.25) to find the completely self-consistent limit [153]. If, the corrections given by $\dot{\Sigma}_{\mathrm{t}}^{\Lambda}$ and $\dot{\Sigma}_{\bar{\mathrm{t}}}^{\Lambda}$ turn out to be small, however, a one-shot scheme, calculating eq. (8.25) only once without reaching self-consistency, will be a good approximation.

We want to highlight a special feature of the multi-loop corrections given in eq. (8.25): As both contributions not captured by the standard flow depend on the central part of the multi-loop vertex flow, this, in turn, means, that up to $\ell = 2$-loop order, the standard self-energy flow fully captures all diagrammatic contributions. This *a posteriori* justifies, that the Katanin substitution is only performed in the two-particle vertex flow, while leaving the self-energy flow equation unchanged.

8.3 Peculiarities of PFFRG

The multi-loop corrections given in eq. (8.15) and eq. (8.25) have been derived without referring to any of the parametrization specifically implemented for pseudo-fermionic systems. While the multi-loop corrections can be straightforwardly implemented by plugging the explicit parametrization of the two-particle vertex into the multi-loop equations, we want here to give a simple recipe to generalize the flow given in Sections A and B to arbitrary loop orders.

Analogous to the prescription in eq. (8.15), ℓ-loop multi-loop corrections for the self-energy flow for the parametrized two-particle vertex are obtained by inserting the $(\ell-1)$-loop terms of complementary channels into the flow equations. For the s- and u-channels, this can be done straightforwardly, for the t-channel, we have to pay special attention. The non-local term involving the lattice sum does not need any treatment, the chalice diagrams, however, are different: As can be seen from eq. (7.19), the local vertex in these contributions originates from $\Gamma_{\times}$, which is mapped to $\Gamma_{=}$ using crossing symmetry eq. (7.14). This exchanges the meaning of t and u transfer frequencies, meaning the external

transfer frequency now flows through the other channel, as can be seen in the explicit frequency parametrization given in eq. (B.3). As the insertions have to be done such that the loop integration enters the transfer frequency of the insertion, we have to substitute the complementary channels to the u channel for this vertex. Similarly, in the flow of the self-energy, the local terms in eq. (B.1) originate from $\Gamma_\times$, meaning there the central part of the u-channel, instead of the t-channel has to be inserted.

The last caveat concerns the implementation of symmetries on the level of $\dot{g}^{\mathrm{c}}_{\mathrm{L}}$, $\dot{g}^{\mathrm{c}}_{\mathrm{C}}$ and $\dot{g}^{\mathrm{c}}_{\mathrm{R}}$. While the central part exhibits the full symmetries given in Table 7.2, care has to be taken considering the exchange in ν and ν'. As this amounts to exchanging the role of left and right vertices, this symmetry additionally maps left and right parts onto each other.

CHAPTER 9

Numerical implementation of PFFRG

The solution of the PFFRG flow is analytically only possible in very few limiting cases, such as the large-S (cf. Section 7.10.1) and large-N (cf. Section 7.10.2) limits we have discussed before. In the physically relevant SU(2) case with finite spin-length, however, the highly coupled structure of the PFFRG equations prevents any analytical attempt to find a closed solution. Therefore, we have to resort to numerical methods to obtain an approximate solution to the flow equations.

Historically, most numerical codes used in this context employed the algorithmic structure introduced in the first PFFRG works in References [98] and [99], in particular employing the step regulator introduced in Section 7.6.1 and the conventional frequency parametrization in terms of transfer frequencies, cf. Section 7.4. In this section, we will discuss the steps taken to render the flow equations amenable to numerical integration in what we dub the "conventional implementation" of PFFRG. All one-loop results presented in this thesis have been obtained employing these algorithms. There is also an open-source codebase available, which exactly implements the scheme we have used for our calculation in Reference [161].

Through the development of the multi-loop scheme describe in Chapter 8, however, it became clear, that it is imperative to utilize more advanced algorithms to control numerical errors. This is especially important, as due to the iterative nature of the multi-loop corrections, numerical errors will grow significantly by reinserting numerical derivatives into the diagrams. From an analytical point of view, to amend the numerical improvements, we employ the asymptotic frequency parametrization introduced in Section 7.5 in conjunction with the smoothened frequency cutoff described in Section 7.6.2. In addition, we describe in the following the more advanced algorithms implemented in the `PFFRGSolver.jl` open-source package we have developed in this thesis [129, 162], which we dub "improved implementation".

9.1 Lattice symmetries

Before diving into the numerical details of the implementation, let us first discuss the practical implementation of the lattice underlying the spin system. Considering the spatial dependence of the flow equations given in Equations (7.18) and (7.19) in conjunction with the lattice space group symmetries, which carry over to the vertex functions, as discussed in Section 5.4.4, we firstly realize, that the vertex only depends on the displacement $\boldsymbol{r}_i - \boldsymbol{r}_j$ between two lattice points.

To efficiently parametrize this dependence and to make the, in principle infinite, lattice numerically tractable, we construct a finite-size lattice in real space, centered around one lattice point we treat as the reference. This is done up to a maximum distance $d_{\max}$, such that $d(\boldsymbol{r}_i, \boldsymbol{r}_j) \leq d_{\max}$ for all j, with d being a suitable length measure in real space. For d several measures have been used, including the Euclidean norm of the distance vector [140] and a norm

counting the minimum number of nearest neighbor connections in the lattice connecting $\boldsymbol{r}_i$and $\boldsymbol{r}_j$ [30, 129], which all agree qualitatively in the physics found. We then allow only vertex functions, that have a spatial extent within this lattice, to obtain finite values. This amounts to the physical approximation of allowing only a finite correlation length to be taken on within the calculations, which is limited by the lattice size. This is in contrast to a true finite-size calculation, as we still employ translational symmetry, but only limit the correlation length to be taken on.

Utilizing further the symmetries of the lattice, we identify an irreducible wedge of lattice points in real space, which are mutually symmetry inequivalent. By definition, all other points can be mapped onto this part of the lattice employing a combination of point group symmetries. This symmetry reduced set then can be linearly indexed, rendering the actual implementation of the flow equations independent of the geometry.

To be able to carry out the lattice sum contained in the t-channel contribution, we also have to define how to handle these non-local terms in the flow equations. As we have limited the spatial extent of the vertex function, out of the terms $\Gamma_{i_1 j}\Gamma_{j i_2}$ in eq. (7.19), only the ones with $d(\boldsymbol{r}_{i_1}, \boldsymbol{r}_j) \leq d_{\max}$ and at the same time $d(\boldsymbol{r}_j, \boldsymbol{r}_{i_1}) \leq d_{\max}$ contribute. It is now convenient to tabulate the pairs $(i_1 j, j i_2)$ for which this is the case for all $i_1 i_2$ combinations within the irreducible wedge at the beginning of the flow to construct what we call the overlap matrix. At the same time, using lattice symmetries, we map the connection $j i_2$ back to the irreducible wedge, such that we find an equivalent connection $i_1 i_2^*$ originating from the reference point i_1. The lattice sum during the flow then only runs over these pairs of spatial vertex components. Converting both $i_1 j$ and $i_1 i_2^*$ to the linear index defined within the irreducible lattice again removes the specific lattice dependence, allowing the further implementation to be lattice agnostic.

9.2 Frequency discretization

In the $T \to 0$ formulation of PFFRG, both the self-energy and the two-particle vertex acquire a continuous dependence on one and three frequencies, respectively. Symmetries imply, that we can resort to only considering positive frequency components in all frequencies for both conventional and asymptotic parametrization schemes. Nevertheless, a numerical treatment of continuous functions always necessitates a discretization of their continuous domain, introducing a frequency mesh.

The frequency integration on the right-hand side implies, that values of the vertex not coinciding with the discrete mesh points are needed in the flow calculation. To extract vertex values at an arbitrary point (ω, ν, ν') in three-dimensional frequency space, we use a multilinear interpolation scheme

$$
\begin{aligned}
\Gamma(\omega,\nu,\nu') = \big[&\Gamma(\omega_{i_<},\nu_{i_<},\nu'_{i_<})(\omega_{i_>}-\omega)(\nu_{i_>}-\nu)(\nu'_{i_>}-\nu')+\\
&\Gamma(\omega_{i_<},\nu_{i_<},\nu'_{i_>})(\omega_{i_>}-\omega)(\nu_{i_>}-\nu)(\nu'-\nu'_{i_<})+\\
&\Gamma(\omega_{i_<},\nu_{i_>},\nu'_{i_<})(\omega_{i_>}-\omega)(\nu-\nu_{i_<})(\nu'_{i_>}-\nu')+\\
&\Gamma(\omega_{i_<},\nu_{i_>},\nu'_{i_>})(\omega_{i_>}-\omega)(\nu-\nu_{i_<})(\nu'-\nu'_{i_<})+\\
&\Gamma(\omega_{i_>},\nu_{i_<},\nu'_{i_<})(\omega-\omega_{i_<})(\nu_{i_>}-\nu)(\nu'_{i_>}-\nu')+\\
&\Gamma(\omega_{i_>},\nu_{i_<},\nu'_{i_>})(\omega-\omega_{i_<})(\nu_{i_>}-\nu)(\nu'-\nu'_{i_<})+\\
&\Gamma(\omega_{i_>},\nu_{i_>},\nu'_{i_<})(\omega-\omega_{i_<})(\nu-\nu_{i_<})(\nu'_{i_>}-\nu')+\\
&\Gamma(\omega_{i_>},\nu_{i_>},\nu'_{i_>})(\omega-\omega_{i_<})(\nu-\nu_{i_<})(\nu'-\nu'_{i_<})\big]\\
&\times\frac{1}{(\omega_{i_>}-\omega_{i_<})(\nu_{i_>}-\nu_{i_<})(\nu'_{i_>}-\nu'_{i_<})},
\end{aligned}
\tag{9.1}
$$

where the indices $i_>(i_<)$ indicate the nearest larger (smaller) frequency in the grid on the respective frequency axis. This scheme is used for the full vertex in the transfer frequency parametrization or for the three different diagrammatic channels in the asymptotic frequency parametrization separately. The asymptotic parts of the vertex function in the latter as well as the self-energy are interpolated using the two- and one-dimensional analogs of this interpolation scheme.

9.2.1 Frequency discretization in the conventional implementation

In the conventional scheme, where the parametrization in terms of transfer frequencies is used, traditionally, one frequency mesh is chosen for all transfer frequency axes and the self-energy. It is built up from logarithmically spaced discrete points, being denser towards the origin of the axis. The intent of this construction is to resolve the richer structure of the vertex functions around zero frequency, while at the same time being able to capture the behavior of the large frequency tails of the vertex. If one of the frequencies exceeds the upper limit of the discrete frequencies, the vertex value is set to zero.

This approach has proven itself in various applications, in particular in combination with *ab initio* data to explain real material properties [30, 33–35, 131, 134]. It however has several shortcomings regarding numerical accuracy. Firstly, the vertex functions do not necessarily vanish in the limit of a single large transfer frequency. As we have seen in Section 7.5, this is only true for the three diagrammatic channels in their respective transfer frequency, but not for the sum of the three comprising the full vertex. From literature, this inaccuracy, however, seems to be not important at one-loop level, as the physical results fit experiments.

The second shortcoming, in contrast, is more severe: As the frequency mesh is chosen at the beginning of the flow, it remains the same for all RG scales Λ. Due to the scale dependence of the regulator function in the propagators, however, the location of features, i.e. extrema and roots of the vertex function along the frequency axes, will change and be proportional to the specific scale Λ. This means, that a static mesh will never be able to capture all features of the vertex at every scale. As the density of the mesh increases towards the origin, resolution at the important locations will increase with decreasing Λ, such that the inaccuracies only occur at high scale, where the vertex still is relatively small meaning that a one-loop scheme still will be sufficiently accurate. As for the inclusion of higher loops, the right-hand side of the flow has to be reinserted into diagrams, these inaccuracies will multiply, rendering a static mesh inadequate for such an application.

A third numerical problem originates in the interplay of the sharp cut-off employed in the conventional scheme combined with the static mesh. Every time the scale Λ crosses a discrete frequency ω_i, new contributions for this frequency point will become finite in the frequency integrals, which were suppressed by the regulator before. This leads to a discontinuity in the flow of the vertex at the corresponding frequency, to which the RG dynamics reacts with an overcompensation in the flow, leading to oscillating behavior, which is most pronounced at low Λ.

9.2.2 Frequency discretization in the improved implementation

In the improved implementation, we ameliorate the shortcomings of the previously described scheme in multiple ways. On an analytical level, we switch from the conventional to the asymptotic frequency parametrization, cf. Section 7.4. This allows to fully capture the behavior for both large transfer frequencies and also large fermionic frequencies in all channels independently.

In the practical implementation, we do not use the Kernel functions K defined in eq. (7.33), as in this formulation calculating the value of a single channel at a specific frequency point amounts to the interpolation and subsequent

summation of all kernel functions. To reduce this computational overhead, we define new functions Q according to

$$Q_3^{\mathrm{c}}(c, \nu_c, \nu_c') = \dot{g}^{\mathrm{c}}(c, \nu_c, \nu_c') \tag{9.2}$$

$$Q_2^{\mathrm{c}}(c, \nu_c) = \lim_{|\nu_c'|\to\infty} \dot{g}^{\mathrm{c}}(c, \nu_c, \nu_c') \tag{9.3}$$

$$\bar{Q}_2^{\mathrm{c}}(c, \nu_c') = \lim_{|\nu_c|\to\infty} \dot{g}^{\mathrm{c}}(c, \nu_c, \nu_c') \tag{9.4}$$

$$Q_1^{\mathrm{c}}(c) = \lim_{|\nu_c|,|\nu_c'|\to\infty} \dot{g}^{\mathrm{c}}(c, \nu_c, \nu_c'). \tag{9.5}$$

In an evaluation of the vertex, we then only have to interpolate Q_3^{c} within its domain of definition, while resorting to the according asymptotics if one or both of the fermionic arguments of the vertex exceed the frequency mesh.

These new functions can be related to the kernel functions according to

$$Q_3^{\mathrm{c}}(c, \nu_c, \nu_c') = K_1^{\mathrm{c}}(c) + K_2^{\mathrm{c}}(c, \nu_c) + \bar{K}_2^{\mathrm{c}}(c, \nu_c') + K_3^{\mathrm{c}}(c, \nu_c, \nu_c') \tag{9.6}$$

$$Q_2^{\mathrm{c}}(c, \nu_c) = K_1^{\mathrm{c}}(c) + K_2^{\mathrm{c}}(c, \nu_c) \tag{9.7}$$

$$\bar{Q}_2^{\mathrm{c}}(c, \nu_c') = K_1^{\mathrm{c}}(c) + \bar{K}_2^{\mathrm{c}}(c, \nu_c') \tag{9.8}$$

$$Q_1^{\mathrm{c}}(c) = K_1^{\mathrm{c}}(c). \tag{9.9}$$

The asymptotic behavior we extract by numerically setting the according frequency arguments to a practically infinite value. The numerical advantage of the Q functions defined here, however, comes at a price: in the parametrization using the kernels K, the frequency discretization on all axes for all asymptotic classes, i.e. K_1, K_2, $\bar{K}_2$ and K_3 can be chosen independently, such that the numerically cheaper to calculate K_1 class can be augmented by a higher resolution mesh. Using the sum of these kernels in form of the Qs defined above, we do not have this choice anymore. Although one would naively expect, that the same split can be done for the limiting functions, i.e. Q_1, Q_2, $\bar{Q}_2$ and Q_3, in a real implementation, this will lead to interpolation artifacts at the boundaries of the frequency mesh, which lead to unphysical errors in the flow. The reduced accuracy in the kernel functions with lower frequency degrees of freedom, however, turned out to not alter the accuracy of the calculation as a whole, cf. Reference [163].

Therefore, the only split we introduce in the frequency meshes is to allow for different meshes for the bosonic and fermionic axes, with the latter being the same for both ν and ν'. The reason for this is the symmetry under exchange of ν and ν', as discussed in Section 7.5. We also allow the t-channel contributions to be defined on a different set of meshes than the s- and u-channel, with the latter utilizing the same discretization, again due to the symmetry between both under exchange of the two fermionic arguments. This split in the diagrammatic channels turns out to be crucial for tracking the interplay between magnetic ordering tendencies in the t channel and paramagnetic behavior stemming from the s- and u-channels at low RG scale Λ. Additionally, spin- and density-part of the vertex are allowed to be defined on possibly different meshes, as their frequency content qualitatively differs. Including another separate mesh for the self-energy, the improved implementation, therefore, utilizes nine different frequency meshes.

We also change the nature of the meshes themselves compared to the conventional implementation. The logarithmical increase of the mesh spacing is only used for frequencies larger than a bound ω_b, up to which we employ a linear mesh spacing. This allows to more accurately resolve the structure of the vertex around the origin in frequency space, while still resolving the high-frequency behavior of the functions.

The linear part consists of 40% of the frequencies per axis, while the remainder is put into the logarithmic tail. The bound ω_b between these, as well as the maximum frequency ω_m, both needed to fully define the mesh, are adjusted during the flow to best fit the actual frequency structure of the vertex. After each step in the RG flow, we scan both

bosonic and fermionic axes in all channels and subsequently adjust ω_b and ω_m to resolve the main extrema of the vertex along these axes appropriately. For details, we refer to References [139] and [162].

This dynamical adjustment of the frequencies, in conjunction with the implementation of the smooth frequency cutoff, removes the unphysical oscillations from the flow.

9.3 Frequency integration

With the frequency discretization defined, a quadrature rule has to be put in place to solve the frequency integrals over vertices and bubbles on the right-hand side of the flow equations. In the conventional implementation, this was realized using a trapezoidal rule, where the integration points coincide with the mesh points.

This fixed quadrature rule is highly inaccurate and misses structures of the integrand away from the integration origin and therefore is highly dependent on the exact way the integration variable is shifted in an implementation. Analyzing the way the flow equations in conventional parametrization, given in appendix A, are parametrized in frequency space, we can trace back the success of this quadrature rule to the structure of the bubble function P. From the definition in eq. (7.29), we see, that it has two (regulated) poles, the one from the Katanin substituted single-scale propagator S_{kat} and the other one from the full propagator G. The former, however, is stronger peaked than the latter, and additionally the frequency integrals are shifted, such that the single-scale pole is located at $\omega = 0$, meaning, that the quadrature rule accurately captures at least the dominant contribution of the propagator bubble.

In a multi-loop scheme, however, the single-scale propagator is replaced by a full one, rendering both contributions equal. To efficiently capture the richer frequency structure in this case, adaptive integration routines are called for to control the numerical error. In the improved implementation, we use an adaptive trapezoidal rule augmented by a Richardson extrapolation. Tho this end we divide the integration interval into four regions, $[-100(\Lambda+\omega/2), -2(\Lambda+\omega/2)]$, $[-2(\Lambda+\omega/2), 0]$, $[0, 2(\Lambda+\omega/2)]$, and $[2(\Lambda+\omega/2), 100(\Lambda+\omega/2)]$, where ω represents the bosonic transfer frequency to enter the bubble integration. The outer limits are meant as numerical approximations to the infinite integration range, while the additional division points aid the adaptive integration routine in accurately resolving the structure of the bubble function, as they are located near the zeros of the latter. The four intervals are further subdivided into 30 intervals each, with a linear distribution of division points for the inner two and a logarithmical one for the outer intervals. Finally, on each of these subintervals the adaptive trapezoidal rule is used, further subdividing these till a set relative and absolute error, computed from the change between two divisions, is reached.

9.4 Differential equation solver

As last step in the numerical implementation, an algorithm for the integration of the ordinary differential equation comprising the RG flow has to be chosen. In the conventional scheme, an Euler stepper was chosen, where the flow was updated according to

$$\Gamma^{\Lambda+\mathrm{d}\Lambda} = \Gamma^{\Lambda} + \mathrm{d}\Lambda \frac{\mathrm{d}}{\mathrm{d}\Lambda}\Gamma^{\Lambda}, \tag{9.10}$$

and analogously for the self-energy. The step-size $\mathrm{d}\Lambda$ in these schemes is chosen proportional to the current scale Λ, typically with $\mathrm{d}\Lambda = 1 - 5\% \cdot \Lambda$. This accounts for the fact, that at high RG scales the change in the vertex is small, allowing for larger steps, while at lower Λ care has to be taken to not miss a breakdown of the flow. The main advantage of the Euler scheme is, that it does not put any requirements on the smoothness of the right-hand side of the flow equations, allowing also to integrate the flow utilizing the step regulator, which leads to a non-differentiable (with respect to Λ) right-hand side.

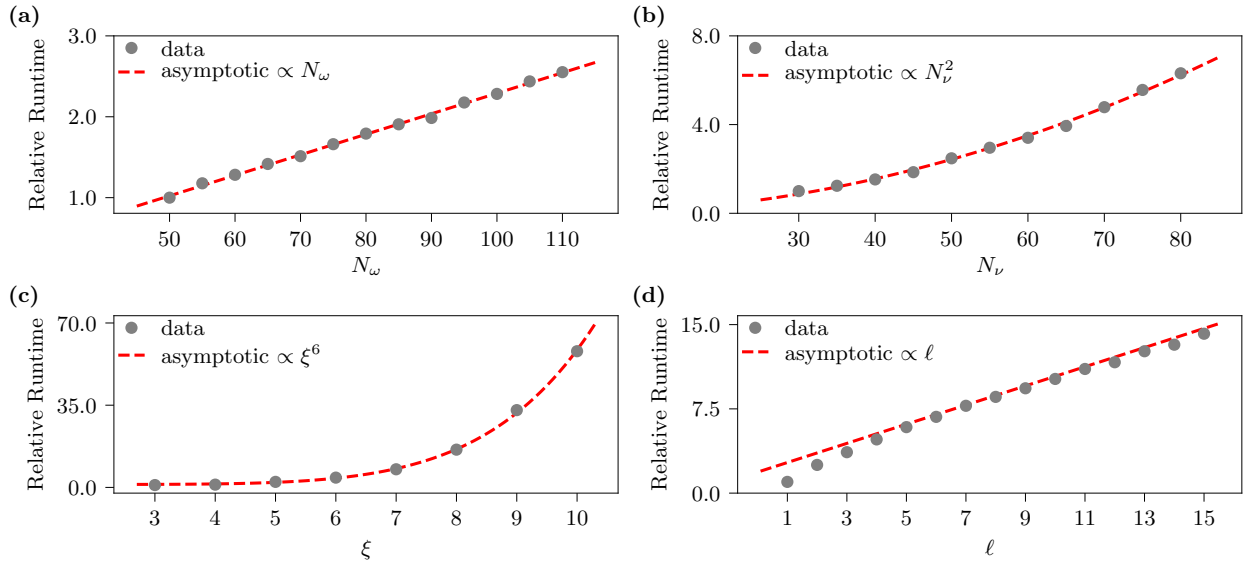

Figure 9.1: Median computational runtime of 60 samples of a single calculation of the right-hand side of the flow equation for $\Lambda/J = 1$ relative to the runtime of the fastest computation in each series. Calculations start from a parquet solution to make the code integrate over non-trivial frequency structures. The numerical parameters for all plots are fixed to $N_\omega = 50$, $N_\nu = 30$, $\xi = 4$ and $\ell = 1$, if not varied. The asymptotic behavior expected analytically is achieved in all cases (dashed red lines).

Introducing the smooth regulator in the improved implementation, however, allows employing more advanced algorithms, which depend on the smoothness of the derivative function. We resort to a third-order Bogacki-Shampine method [164], which adapts the step width in Λ according to the current absolute and relative errors. This allows for a more efficient calculation of the flow, as in numerically less demanding regions of Λ, larger steps will automatically be taken, while in the harder to solve parts, especially close to a flow breakdown, the step size will be decreased. We have found this integrator to be a good compromise between accuracy and efficiency [165].

9.5 Initial conditions

In the conventional implementation, the initial vertex was set according to Equations (7.55) and (7.56) at a scale $\Lambda \sim 100 \cdot J$, where j is a measure for the interaction strength. This is a valid numerical approximation for $\Lambda \to \infty$. For multi-loop calculations, which reproduce the parquet approximation, another route can be taken, which we optionally can use in the improved implementation: We set ourselves to a smaller scale Λ, where the regularized parquet equations are still easily solvable using a fixed point iteration and start the flow from the resulting vertex and self-energy.

9.6 Run-time scaling

The dominant contribution to the numerical runtime is given by the evaluation of the deriviatives of the two-particle vertex, as given in Sections A and B. The self-energy derivative, in comparison, is negligible. Analyzing the flow equations, we find, that the asymptotic complexity is given by

$$O\left(N_\mathrm{L}^2 \times N_\omega N_\nu^2 \times \ell\right), \tag{9.11}$$

where N_L is the number of symmetry reduced lattice sites, N_ω (N_ν) the number of bosonic (fermionic) frequencies, and ℓ denotes the number of loops. In d spatial dimensions, the number of sites is expected to follow a $O(d_\mathrm{max}^d)$ dependence, with d_max the maximal correlation length considered, cf. Section 9.1.

In our implementation in `PFFRGSolver.jl`, we indeed reach these asymptotic scaling limits, as shown in Figure 9.1. Here we show the median runtime for 60 evaluations of the right-hand side of the flow equations. The expected linear and quadratic behavior in the number of both bosonic and fermionic frequencies, respectively, is achieved for the whole range of parameters tested. Slight deviations, as we find here, are to be expected due to adaptive integration and the numerical parallelization employed. Similarly, the power-law in the maximal correlation length d_max is achieved for the whole parameter range. The linear scaling in the number of loops only sets in at $\ell = 5$, while we find a steeper slope for smaller ℓ. This behavior we attribute to the fact, that due to the successively diminishing contributions from higher and higher loops, the adaptive frequency integration converges faster. Therefore, the initial overhead with of twice (thrice) the number of integrals to be computed, compared to $\ell = 1$ for two (three) loop contributions diminishes, and the analytically expected linear scaling in ℓ is recovered.

III

Phase-diagrams of frustrated three-dimensional lattices

scrheadingsIn this part, we analyze the phase diagrams of Heisenberg models on the three-dimensional body-centered cubic, Pyrochlore, and simple cubic lattices, unveiling a plethora of different ordered phases as well as quantum spin liquid candidates.

The contents of this part of the thesis are partially included in References [32], [31], and [139].

CHAPTER 10

Body-Centered Cubic Lattice up to third-nearest-neighbor interactions

scrheadingsIn the two-dimensional (2D) square-lattice, it has been established, that classical spiral orders, comprising the ground state of any Bravais lattice (cf. Section 3.2), give way to extended quantum spin liquid phases in parameter-space upon inclusion of quantum fluctuations [126, 166, 167]. Taking this insight as a guiding principle, we will investigate the phase diagram of the body-centered cubic (BCC) lattice with couplings up to third-nearest-neighbors. It is a natural extension of the two-dimensional square lattice in three dimensions in the sense, that it is bipartite, i.e. it can be decomposed into two interpenetrating simple cubic lattices, as shown in Figure 10.1, when keeping only second-nearest neighbor interactions. This is similarly true for the square lattice, which decomposes into two square lattices, and can host both Nèel and stripe ordered phases [168].

The corresponding magnetic Hamiltonian is given by

$$\hat{H} = J_1 \sum_{\langle i,j\rangle_1} \hat{\boldsymbol{S}}_i \cdot \hat{\boldsymbol{S}}_j + J_2 \sum_{\langle i,j\rangle_2} \hat{\boldsymbol{S}}_i \cdot \hat{\boldsymbol{S}}_j + J_3 \sum_{\langle i,j\rangle_3} \hat{\boldsymbol{S}}_i \cdot \hat{\boldsymbol{S}}_j, \tag{10.1}$$

where we denote sums over nearest, second-nearest and third-nearest neighbors by $\langle i,j\rangle_1$, $\langle i,j\rangle_2$ and $\langle i,j\rangle_3$, respectively. The coupling structure is illustrated together with the lattice in Figure 10.1. As there is no a priori restriction on the couplings, we will consider both ferromagnetic (FM) ($J_i < 0$) and antiferromagnetic (AF) (J_i>0) values for J_1, J_2 as well as J_3.

10.1 Classical Phase diagram

The BCC lattice being a Bravais lattice allows us to employ the Luttinger-Tisza method to determine its exact classical phase diagram. To this end, we need the Fourier transform of the considered interactions, given by

$$\begin{aligned} J(\mathbf{k}) = \; & 8J_1 \cos\left(\frac{k_x}{2}\right)\cos\left(\frac{k_y}{2}\right)\cos\left(\frac{k_z}{2}\right) \\ & +2J_2\left(\cos(k_x)+\cos(k_y)+\cos(k_z)\right) \\ & +4J_3\left(\cos(k_x)\cos(k_y)+\cos(k_y)\cos(k_z)+\cos(k_x)\cos(k_z)\right). \end{aligned} \tag{10.2}$$

The classical ground-state for a given set of couplings can subsequently be found by minimizing eq. (10.2) with respect to the wave-vector $\boldsymbol{k}$ and employing the general form of a Luttinger-Tisza spiral state given in eq. (3.13).

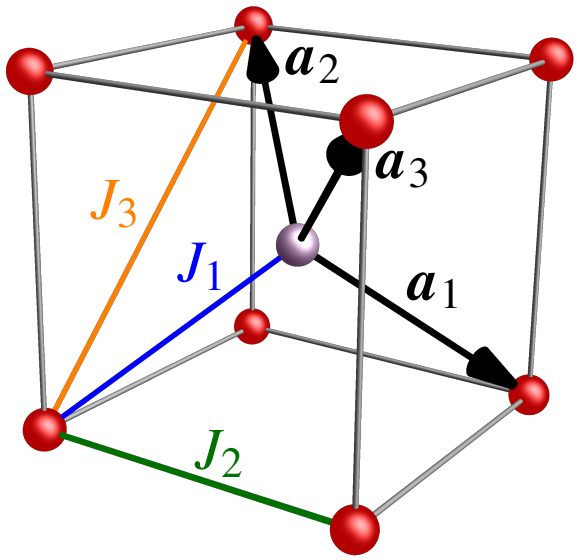

Figure 10.1: Cubic unit cell of the BCC lattice together with its lattice vectors $\boldsymbol{a}_1 = a(\frac{1}{2}, \frac{1}{2}, -\frac{1}{2})$, $\boldsymbol{a}_2 = a(-\frac{1}{2}, \frac{1}{2}, \frac{1}{2})$, and $\boldsymbol{a}_3 = a(\frac{1}{2}, -\frac{1}{2}, \frac{1}{2})$ with lattice constant a. Exemplary exchange paths corresponding to nearest neighbor (NN) (J_1), next-to-nearest neighbor (NNN) (J_2), and next-to-next-to-nearest neighbor (NNNN) (J_3) Heisenberg coupling are shown, as defined in the model Hamiltonian eq. (10.1). The BCC lattice decomposes into two interpenetrating simple cubic lattices, shown in red and purple, respectively, which are offset by the Bravais vectors $\boldsymbol{a}_1$, $\boldsymbol{a}_2$ and $\boldsymbol{a}_3$, rendering the BCC bipartite.

Before discussing the effects of quantum fluctuations in the $S = 1/2$-limit, we first present the classical magnetic phase diagram of the J_1–J_2–J_3 Heisenberg model on the BCC lattice. The phase diagrams, shown in Figure 10.2(a) and (c) host in total six distinct incommensurate spiral orders, three each for FM and AF nearest-neighbor coupling, respectively. In addition, four commensurate orders are observed. In Figure 10.3 we illustrate the different real space configurations found in parameter space, which we further outline in the following, placing them in the corresponding phase diagrams.

10.1.1 Ferromagnetic J_1

The classical phase diagram in the J_1–J_2–J_3 parameter space with FM J_1 is shown in Fig. 10.2(a). Starting with both FM J_1 and J_2 we trivially find a FM ground state (see Figure 10.3(a)). The inclusion of a moderate AF J_3 coupling up to a critical value $J_3^c = \frac{1}{4}(|J_1| + |J_2|)$ does not destabilize the FM state. At this value a phase transition into an incommensurate spiral phase (Figure 10.3(e)) takes place. The corresponding ordering vector is of the form $\boldsymbol{q} = (q, 0, 0)$ with q given in Table 10.1, evolving smoothly from the FM value of $q = 0$, establishing the second order nature of the transition. As in this state spins are only spiraling when moving in one cardinal direction in real space, but are FM ordered in the other two, we call this a 1D spiral state. Its ordering vector is 3-fold degenerate within the first BZ due to cubic symmetry. However, the spiral state spontaneously breaks this symmetry, as a superposition of spirals with different incommensurate wave vectors would violate the strong spin length constraint, which means the 1D spiral has to be governed by only *one* of these symmetry equivalent vectors. Hence, the degeneracy is only a discrete one. This 1D spiral structure is stabilized purely by a FM J_2 interaction and subsequently, along the line $J_2 = 0$, there is a 1st order phase transition to another incommensurate spiral whose wave vector is $\boldsymbol{q} = (q, q, 0)$ with q given in Table 10.1 and therefore dubbed 2D spiral (see Figure 10.3(f) for an illustration). Similar to the 1D

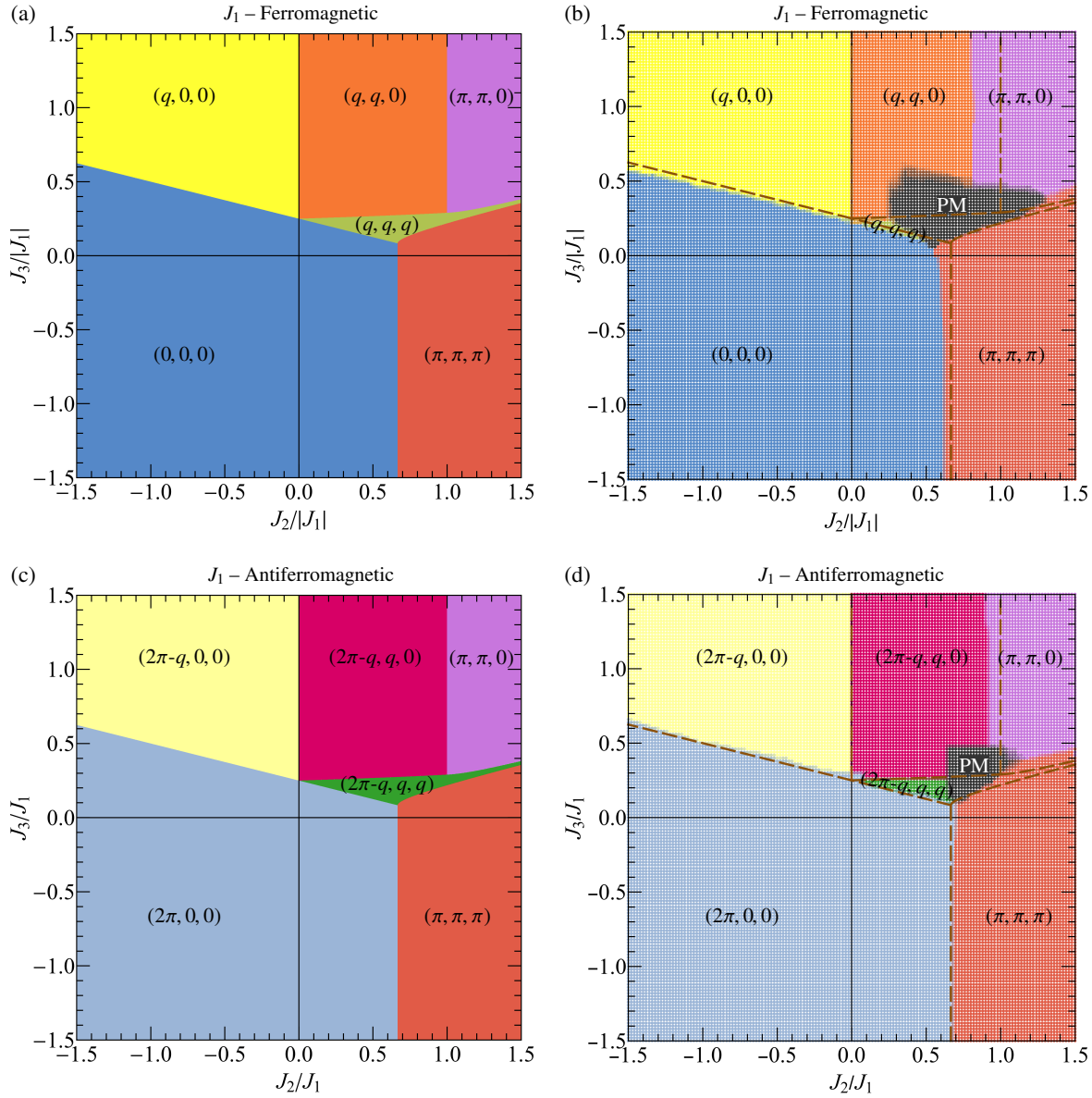

Figure 10.2: Classical and $S = 1/2$ quantum phase diagrams of the Heisenberg model up to third-nearest neighbor on the BCC lattice for (a) and (b) FM and (c) and (d) AF nearest-neighbor coupling J_1. Solid (dashed) phase boundaries mark first (second) order phase transitions. In the (b) and (d), we overlay the classical phase boundaries to visualize the impact of quantum fluctuations on the phase diagram. Figure reproduced from Reference [32].

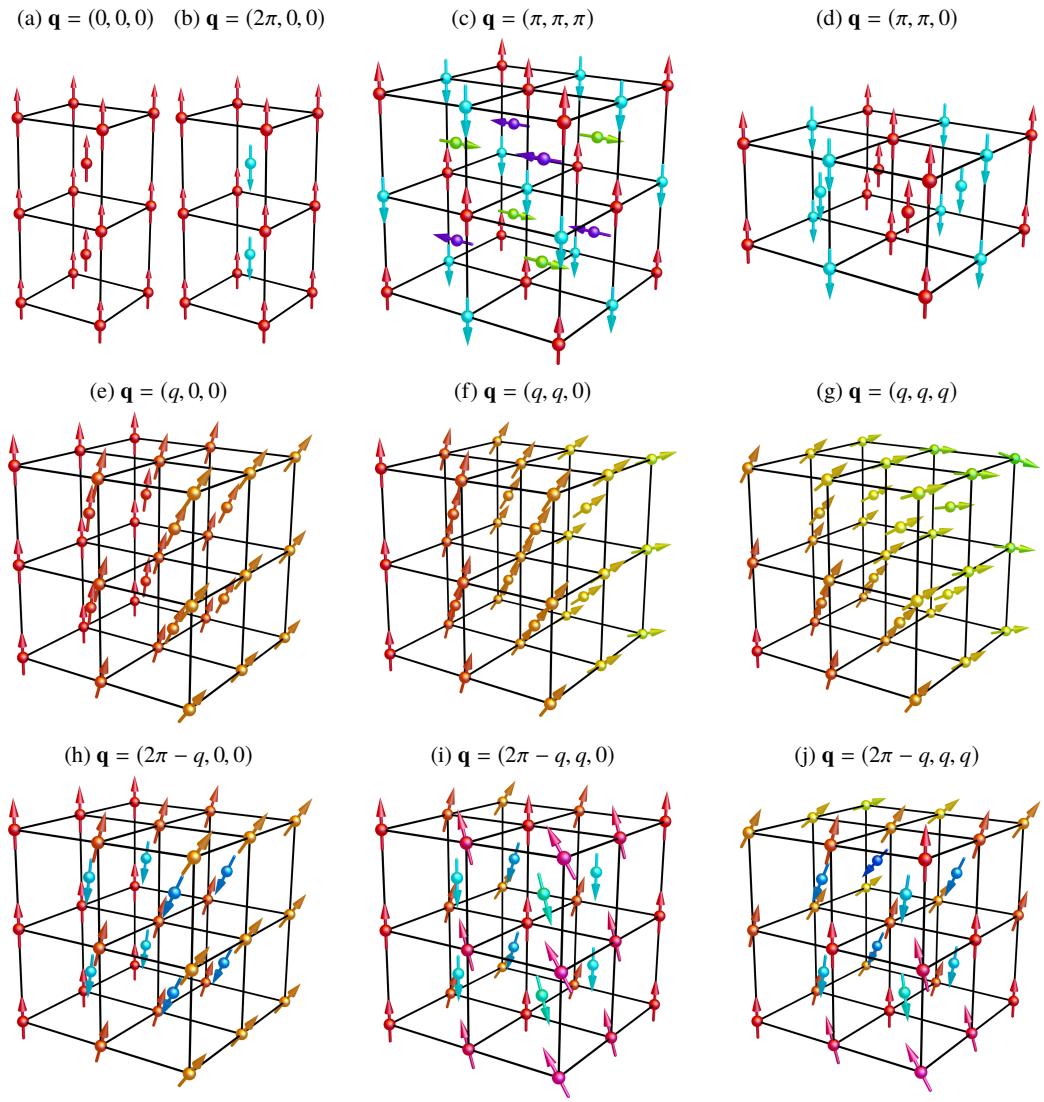

Figure 10.3: Classical spin configurations found in the phase diagram of the Heisenberg model on the BCC lattice up to third-nearest neighbor couplings. Due to global rotational symmetry, the global orientation of the spins and chiralities for the spiral states are not determined by the model. The (a) ferromagnet and (b) Nèel antiferromagnet are the simplest, collinear states found. The latter can be viewed as two interpenetrating FM simple cubic lattices located at each other's body centers, which are oriented antiparallel to each other. The (π, π, π) stripe AF (c) can similarly be decomposed into interpenetrating Nèel-ordered simple cubic lattices, which can be freely rotated with respect to each other. We choose a relative rotation by $\pi/2$ for this illustration. The $(\pi, \pi, 0)$ planar antiferromagnet is built from FM 110-type planes of spins, AF aligned to neighboring planes. The remaining spiral phases come in pairs corresponding to FM and AF J_1. In the $(q, 0, 0)$ one-dimensional (1D) spiral (e), spins are rotating when moving along one cardinal direction, but are FM ordered in the two remaining directions. For AF J_1 the corresponding $(2\pi - q, 0, 0)$ 1D spiral (h) is the same configuration, but with flipped spins at the body center. In the $(q, q, 0)$ 2D spiral (f) rotation is present along two cardinal directions, with the same period for both. This leads to FM ordered $\{110\}$-planes parallel to the remaining direction. In the corresponding $(2\pi - q, q, 0)$ 2D spiral (i) the same spiraling in two cardinal directions is found, but again with flipped spins on the body centers. This results in opposite chiralities of the spirals in the two directions, which is fixed by the Heisenberg model, in contrast to the global direction of spiraling. The (q, q, q) three-dimensional (3D) spiral (j) features the same spiraling behavior in all three directions, leading to FM ordered $\{111\}$-planes. The $(2\pi - q, q, q)$ state for AF J_1 again has a different chirality along one particular spatial direction ad flipped spins on the body centers, which leads to FM $\{-111\}$-planes. Figure reproduced from Reference [32].

Ordering vector ($\boldsymbol{q}$)	Component q	Degeneracy	Energy $\frac{E}{NS^2}$
$(q,0,0)$ $(2\pi-q,0,0)$	$2\cos^{-1}\left(\frac{\lvert J_1\rvert}{J_2+4J_3}\right)$	3–fold	$J_2-2J_3-\frac{2(J_1)^2}{J_2+4J_3}$
$(q,q,0)$ $(2\pi-q,q,0)$	$\cos^{-1}\left(\frac{\lvert J_1\rvert-J_2-2J_3}{2J_3}\right)$	6–fold 12–fold	$-J_2-2J_3-\frac{(-\lvert J_1\rvert+J_2)^2}{2J_3}$
(q,q,q) $(2\pi-q,q,q)$	$2\cos^{-1}\left(\frac{\lvert J_1\rvert+\sqrt{u}}{16J_3}\right)$	4–fold 12–fold	$-\frac{(J_1)^2(u+16J_3(4J_3+J_2))+\lvert J_1\rvert u^{\frac{3}{2}}+384(J_2)^2(J_3)^2}{1024(J_3)^3}$ $u=(J_1)^2+32J_3(4J_3-J_2)$
$(0,0,0)$ $(2\pi,0,0)$		1–fold	$-4\lvert J_1\rvert+3J_2+6J_3$
$(\pi,\pi,0)$		3–fold	$-J_2-2J_3$
(π,π,π)		1–fold	$-3J_2+6J_3$

Table 10.1: Ordering vectors of the spiral orders in the classical J_1–J_2–J_3 Heisenberg model on the BCC lattice. The degeneracy in the first Brillouin zone (BZ) up to inversion in reciprocal space, as well as the energy per spin in the corresponding ground-state is additionally given.

spiral, no superpostions of the six symmetry equivalent $(q,q,0)$-type wave vectors[1] are possible without violating the spin length constraint, leading again to a spontaneous symmetry broken single-$\boldsymbol{q}$ state with discrete degeneracy. Upon increasing J_2 for sufficiently large J_3 (the analytical expression for this phase boundary is given in Table 10.2), the value of q continuously evolves towards π. At the line $J_2/|J_1| = 1$ and above a critical $J_3^c/|J_1| \approx 0.29$, a 2nd order phase transition to a planar AF order with $\boldsymbol{q} = (\pi,\pi,0)$, illustrated in Figure 10.3(d), takes place. In contrast to the incommensurate previously discussed, this ordering vector is commensurate, as it is half of a reciprocal lattice vector, i.e., $2\boldsymbol{q} \cong \boldsymbol{0}$. This special condition allows the ground state to be composed of all six symmetry equivalent ordering vectors, namely, $(\pi,\pi,0)$, $(\pi,0,\pi)$, $(0,\pi,\pi)$, $(\pi,-\pi,0)$, $(-\pi,0,\pi)$, and $(0,-\pi,\pi)$[169]. For all six vectors the relation $\sin(\boldsymbol{q}\cdot\boldsymbol{R}_i)=0$ holds at every lattice site. Therefore, the general ground state can be written as

$$\begin{aligned}\boldsymbol{S}_i = S\{&\boldsymbol{a}\cos[(\pi,\pi,0)\cdot\boldsymbol{R}_i]+\boldsymbol{b}\cos[(\pi,0,\pi)\cdot\boldsymbol{R}_i]+\boldsymbol{c}\cos[(0,\pi,\pi)\cdot\boldsymbol{R}_i]\\&+\boldsymbol{d}\cos[(\pi,-\pi,0)\cdot\boldsymbol{R}_i]+\boldsymbol{e}\cos[(-\pi,0,\pi)\cdot\boldsymbol{R}_i]+\boldsymbol{f}\cos[(0,-\pi,\pi)\cdot\boldsymbol{R}_i]\}\end{aligned} \tag{10.3}$$

with

$$\begin{aligned}\boldsymbol{a}^2+\boldsymbol{b}^2+\boldsymbol{c}^2+\boldsymbol{d}^2+\boldsymbol{e}^2+\boldsymbol{f}^2&=1\\ \boldsymbol{a}\cdot\boldsymbol{b}+\boldsymbol{d}\cdot\boldsymbol{e}=\boldsymbol{a}\cdot\boldsymbol{c}+\boldsymbol{d}\cdot\boldsymbol{f}=\boldsymbol{a}\cdot\boldsymbol{e}+\boldsymbol{b}\cdot\boldsymbol{d}=\boldsymbol{a}\cdot\boldsymbol{f}+\boldsymbol{c}\cdot\boldsymbol{d}&=0\\ \boldsymbol{b}\cdot\boldsymbol{c}+\boldsymbol{e}\cdot\boldsymbol{f}=\boldsymbol{c}\cdot\boldsymbol{e}+\boldsymbol{b}\cdot\boldsymbol{f}=\boldsymbol{b}\cdot\boldsymbol{e}+\boldsymbol{a}\cdot\boldsymbol{d}+\boldsymbol{c}\cdot\boldsymbol{f}&=0\end{aligned} \tag{10.4}$$

[1] By symmetry equivalent vectors, we only consider the ones not related by inversion, as these will always be present in any spin structure. The remaining six vectors therefore are $(q,q,0)$, $(-q,q,0)$,$(q,0,q)$,$(q,0,-1)$,$(0,q,q)$, and $(0,q,-q)$.

Phase I	Phase II	Equation for the phase boundary	Transition Type
$(0,0,0)$ $(2\pi,0,0)$	$(q,0,0)$ $(2\pi-q,0,0)$	$J_2 = \lvert J_1\rvert - 4J_3$	2nd Order
$(0,0,0)$ $(2\pi,0,0)$	(q,q,q) $(2\pi-q,q,q)$	$J_2 = \lvert J_1\rvert - 4J_3$	2nd Order
$(0,0,0)$ $(2\pi,0,0)$	(π,π,π)	$J_2 = \frac{2}{3}\lvert J_1\rvert$	1st Order
$(q,0,0)$ $(2\pi-q,0,0)$	$(q,q,0)$ $(2\pi-q,q,0)$	$J_2 = 0$	1st Order
$(q,q,0)$ $(2\pi-q,q,0)$	$(\pi,\pi,0)$	$J_2 = \lvert J_1\rvert$	2nd Order
$(q,q,0)$ $(2\pi-q,q,0)$	(q,q,q) $(2\pi-q,q,q)$	$J_2 = \frac{56\lvert J_1\rvert(J_3)^2-11(J_1)^2J_3-32(J_3)^3-\sqrt{\lvert J_1\rvert(J_3)^2(5\lvert J_1\rvert-16J_3)^3}}{8(J_3)^2}$	1st Order
(q,q,q) $(2\pi-q,q,q)$	$(\pi,\pi,0)$	$J_2 = \frac{(J_1)^4+4416(J_1)^2(J_3)^2+((J_1)^2+48(J_3)^2)\sqrt[3]{u}+(u)^{2/3}+36864(J_3)^4}{108J_3\sqrt[3]{u}}$	1st Order
(q,q,q) $(2\pi-q,q,q)$	(π,π,π)	$J_2 = \frac{(J_1)^2+144(J_3)^2}{36J_3}$	1st Order

where $u = (J_1)^6 - 10872(J_1)^4(J_3)^2 - 2709504(J_1)^2(J_3)^4 + 7077888(J_3)^6 + 108\sqrt{3}J_3\sqrt{-(J_1)^2\left(12(J_3)^2-(J_1)^2\right)\left(512(J_3)^2-(J_1)^2\right)^3}$

Table 10.2: Analytical phase boundaries between the respective Phase I and Phase II in the classical phase diagram of the J_1–J_2–J_3 Heisenberg model on the BCC lattice. The corresponding order of the phase transition is additionally given.

where $\boldsymbol{a}$, $\boldsymbol{b}$, $\boldsymbol{c}$, $\boldsymbol{d}$, $\boldsymbol{e}$, $\boldsymbol{f}$ are arbitrary vectors constrained by eq. (10.4), which normalizes the spin length at each site. These six vectors have in total 18 continuous degrees of freedom. As they are subject to 8 constraints and two additional degrees of freedom are accounted for by the global spin rotation invariance of the Heisenberg model, the planar AF order has a *continuous* 8-dimensional ground state manifold. This is in contrast to the other classical magnetic orders in the J_1–J_2–J_3 parameter space which feature only an n-fold *discrete* degeneracy due to them being defined by incommensurate ordering vectors, where n depends on the exact phase. The respective degeneracies are given in Table 10.1. A similar enhancement for the available degrees of freedom is also found for the stripe AF phase on the square lattice [170] and other cubic lattice systems [171].

Keeping AF J_2 and decreasing J_3, the interplay between these couplings stabilizes an incommensurate $\boldsymbol{q} = (q,q,q)$ 3D spiral (see Figure 10.3(g)) in a sliver of parameter space, which again, due to incommensurability of the ordering vector, spontaneously breaks lattice symmetry and is described by only *one* of the 4 degenerate wave vectors of (q,q,q)-type. At the phase boundaries to the FM phase, we find a continuous 2nd order phase transition, whereas

the transition into the $(q, q, 0)$ and $(\pi, \pi, 0)$ states is of 1st order. For even lower AF J_3, we find that in the region $J_2/|J_1| > 2/3$ the collinear stripe order (see Figure 10.3(c)) with wave vector $\boldsymbol{q} = (\pi, \pi, \pi)$ is stabilized. In this state the BCC lattice can be decomposed into two interpenetrating simple cubic lattices, each being Nèel ordered. For any spin on a given sublattice, all its nearest-neighbor spins are located on the other sublattice and subsequently their sum vanishes. Hence, the energy of the stripe ordered state is independent of the relative spin orientation on the two sublattices [172], which is thus not determined within the J_1–J_2–J_3 Heisenberg model. As the ordering vector of this state is located at the corners of the first BZ, it is non-degenerate. Changing the sign of J_3 to FM only enhances the stability of the state, as all third-nearest neighbors of a given spin are second-nearest ones on the respective simple cubic sublattice and therefore FM ordered. Thus, this state occupies the entire parameter space for $J_2/|J_1| > 2/3$ and FM J_3. Due to the independence of the stripe order's energy from J_1, the phase value of the boundary between the FM and the stripe collinear order is determined solely by the coordination numbers of nearest-neighbors (z_1) and second-nearest neighbors (z_2) of the BCC lattice and therefore given by $J_2/|J_1| = z_1/2z_2 = 2/3$.

10.1.2 Antiferromagnetic J_1

Changing J_1 from FM to AF, the phase boundaries and orders of phase transitions in the J_2–J_3 parameter space do not change, as shown in the corresponding phase diagram Figure 10.2(c) and analytical expressions in Table 10.2. To understand this behavior, one should view the BCC lattice as two interpenetrating simple cubic lattices, located at the body centers of each other. In this geometry, J_2 and J_3 couple sites within the same sublattices, whereas J_1 is an inter-sublattice coupling. Therefore, a sign change in J_1 can be compensated by flipping the spins on only one of the sublattices, which leaves J_2 and J_3 couplings unaffected. This does not shift the phase boundaries, however, the spin flips are reflected by a shift of ordering vectors $\boldsymbol{q} \rightarrow (2\pi, 2\pi, 2\pi) - \boldsymbol{q}$ in reciprocal space. Folding back the resulting wave-vector into the first BZ, this transformation is equivalent to shifting any, but only, *one* of the wave vector components $q \rightarrow 2\pi - q$. As a result, the Nèel AF (Figure 10.3(b)) with wave vector $\boldsymbol{q} = (2\pi, 0, 0)$ [2] replaces the FM phase. Similarly, the incommensurate spirals are shifted: the 1D spiral is now controlled by a wave vector of the form $\boldsymbol{q} = (2\pi - q, 0, 0)$, shown in Figure 10.3(h), where q and ground state degeneracy are the same as for the FM 1D spiral. Along the same lines, the 2D spiral wave vector is modified for AF J_1 as $\boldsymbol{q} = (2\pi - q, q, 0)$, which is now 12–fold degenerate, whereas its FM counterpart only possesses 6–fold degeneracy. Nevertheless, as this ordering vector is still incommensurate, only *one* of these wave vectors is present in any given ground state. Upon increasing J_2, the 2D spiral evolves continuously into the planar AF, which remains unchanged compared to the case with FM J_1. The 3D spiral's incommensurate wave vector for FM J_1 is given by $\boldsymbol{q} = (2\pi - q, q, q)$, also extending the degeneracy to 12–fold in contrast to the 6–fold one for FM nearest-neighbor coupling. The final phase in the J_2–J_3 parameter space, the stripe AF with $\boldsymbol{q} = (\pi, \pi, \pi)$ remains unchanged when inverting the sign of J_1.

A complete overview of the analytical expressions for the ordering vectors governing the different spiral phases on the BCC, depicted in Figure 10.3, together with the degeneracy of the phases, is given in Table 10.1. Additionally, analytical expressions for the phase boundaries and the corresponding orders of the phase transition can be found in Table 10.2.

[2] The Nèel AF state is also specified by the ordering vector $\boldsymbol{q} = (2\pi, 2\pi, 2\pi)$ in literature, which is equivalent to $\boldsymbol{q} = (2\pi, 0, 0)$ after folding back to the first BZ.

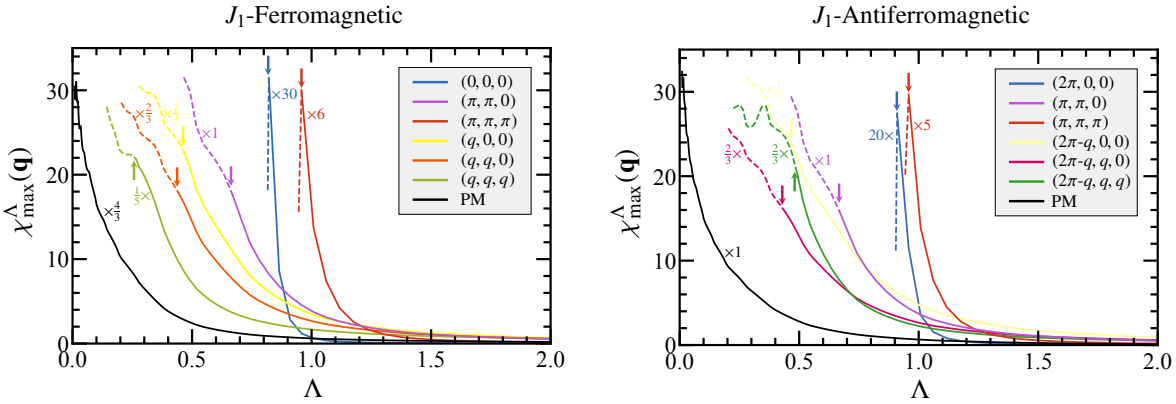

Figure 10.4: Representative RG flows at the maxima of the magnetic susceptibility in reciprocal space for the phases in Figure 10.2(b) and (d). The flows are given for the couplings $(J_2/|J_1|, J_3/|J_1|) = (0, 0)$ (FM order), $(1.5, 1)$ for $(\pi, \pi, 0)$ order, $(1.5, 0)$ for (π, π, π)-order, $(-0.5, 1)$ (1D spiral), $(0.5, 1)$ (2D spiral), $(0.26, 0.2)$ (3D spiral) and $(0.8, 0.3)$ for the paramagnet, each for FM (left panel) and AF (right panel) J_1. The transition from solid to dashed lines marks an instability of the flow, signalling the onset of long-range magnetic order, whereas a smooth flow for $\Lambda \to 0$ indicates paramagnetism. Figure reproduced form Reference [32].

10.2 Quantum Phase diagram

To investigate the changes to the classical phase diagram upon inclusion of quantum fluctuations, we employ one-loop pseudo-fermion functional renormalization group (PFFRG) in the sharp regulator scheme. As one-loop calculations already are usually sufficient to capture the correct phase boundaries [139, 157], and we find, that two-loop corrections do not significantly change the ordering tendencies in the vicinity of the phase boundaries[3], we reserve to employ two-loop calculations only for a select set of parameter points to more correctly calculate ordering temperatures, which we will present in Section 10.3.

Comparing the so-obtained quantum phase diagrams shown in Figure 10.2(b) and Figure 10.2(d) to their classical counterparts, we first of all find, that *all* orders of the classical phase diagram are also found in the quantum version and additionally no new long-range magnetic orders are stabilized in the $S = 1/2$ limit. In Fig. 10.4, we show the representative renormalization group (RG) flows for all the quantum phases and present their momentum resolved susceptibility profiles in Figures 10.5 and 10.6.

The most striking effect of quantum fluctuations for $S = 1/2$, however, is the appearance of a PM phase for both FM and AF J_1, which occupies an extended region in both J_2–J_3 parameter spaces. Its extent is larger for FM J_1 than in the AF case and in both regimes occupies a substantial portion of parameter space, where we classically find 2D and 3D spirals, as well as, to a smaller extend, also takes over the domain of classical the planar AF with ordering vector $\boldsymbol{q} = (\pi, \pi, 0)$. The Nèel order present for AF J_1 withstands the effect of quantum fluctuations, whereas the classical FM phase is destabilized and partially taken over by a paramagnetic regime. In contrast, the $\boldsymbol{q} = (\pi, \pi, \pi)$ stripe AF present classically for both FM and AF nearest-neighbor couplings is not destabilized at all by quantum fluctuations, meaning that the paramagnetic phase does not eat into to classical stripe ordered phase at all. The momentum resolved susceptibility profiles taken deep within the paramagnetic phase, as shown in Figure 10.7, show remnants of the underlying classical correlations, i.e. in the shown cases the 3D (q, q, q)- and $(2\pi - q, q, q)$-orders for FM and AF J_1 respectively. The paramagnetic phase, therefore, can be viewed as the classical state, molten down by quantum fluctuations.

[3] In the case of $S = 1/2$, for FM J_1, the maximal shift of the critical scale is $\approx 4\%$ of $|J_1|$, while for AF J_1 it is $\approx 2\%$ of J_1.

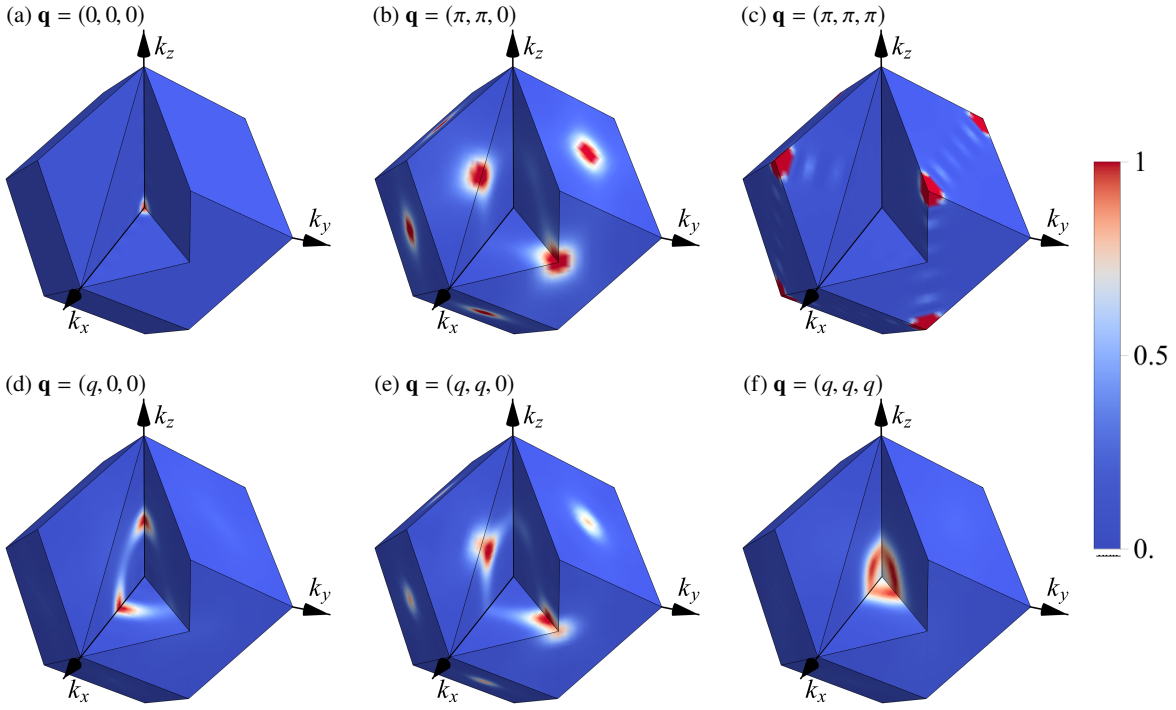

Figure 10.5: Normalized susceptibility profiles in the first BZ of the BCC lattice for the Heisenberg model with FM J_1 for the magnetically ordered states. The susceptibilities are plotted for the couplings used in Figure 10.4 at the cutoff values indicated by arrows in the left panel of this figure. Figure reproduced from [32].

In the following, we investigate in more detail, the effects of quantum fluctuations for $S = 1/2$ on the different magnetically ordered phases.

Starting with the $\boldsymbol{q} = (\pi, \pi, \pi)$ stripe AF, we find, that quantum fluctuations shift its phase boundaries severely. For J_2 sufficiently large, for both J_1 FM and AF, it completely replaces the 3D spiral present in the classical phase diagram and also cuts into the region in the J_2–J_3, where the $\boldsymbol{q} = (\pi, \pi, 0)$ planar AF exists, leading in turn to a phase boundary between the two AF states not present in the classical phase diagram. The finding, that stripe AF is favored over a planar AF is similar to the situation on the square lattice, where the (π, π) AF wins over $(\pi, 0)$ state [170].

For the second phase boundary between stripe order and FM/ Nèel AF, we find a strong dependence on the sign of J_1. For AF nearest-neighbor coupling, the transition between Nèel AF and the stripe order is shifted towards slightly larger J_2, similar to the analogous phase boundary in the simple cubic lattice [125]. In contrast to the simple cubic and also the square lattice, however, we find no paramagnetic phase between FM/Nèel and the stripe order, which agrees with previous findings in the J_1–J_2-model [168, 173–178]. In Table 10.3 we compare the phase boundaries for $J_3 = 0$ obtained in these studies with the one obtained by PFFRG, which shows excellent agreement with both exact diagonalization and the couple-cluster method. The fundamentally different behavior of FM and Nèel state with respect to quantum fluctuations can be understood by the fact, that the FM state is an eigenstate of the Heisenberg Hamiltonian, which will therefore not alter its ground state energy. As outlined in Section 1, the AF orders, in contrast, are strongly affected and their ground state energies are lowered [179, 180]. This gives both a reason for why the FM to stripe AF phase boundary is shifted towards smaller J_2 and also, that the shift from the classical value $J_2^c/|J_1| = 2/3$ is larger for FM J_1 than for AF (see Figure 10.2(b) and (d)).

Similar to this finding, the boundary between FM/Nèel state and the spiral orders behaves differently depending on the sign of J_1. For FM J_1 both 1D and 3D spirals take over regions in the J_2–J_3 plane, where classically FM order

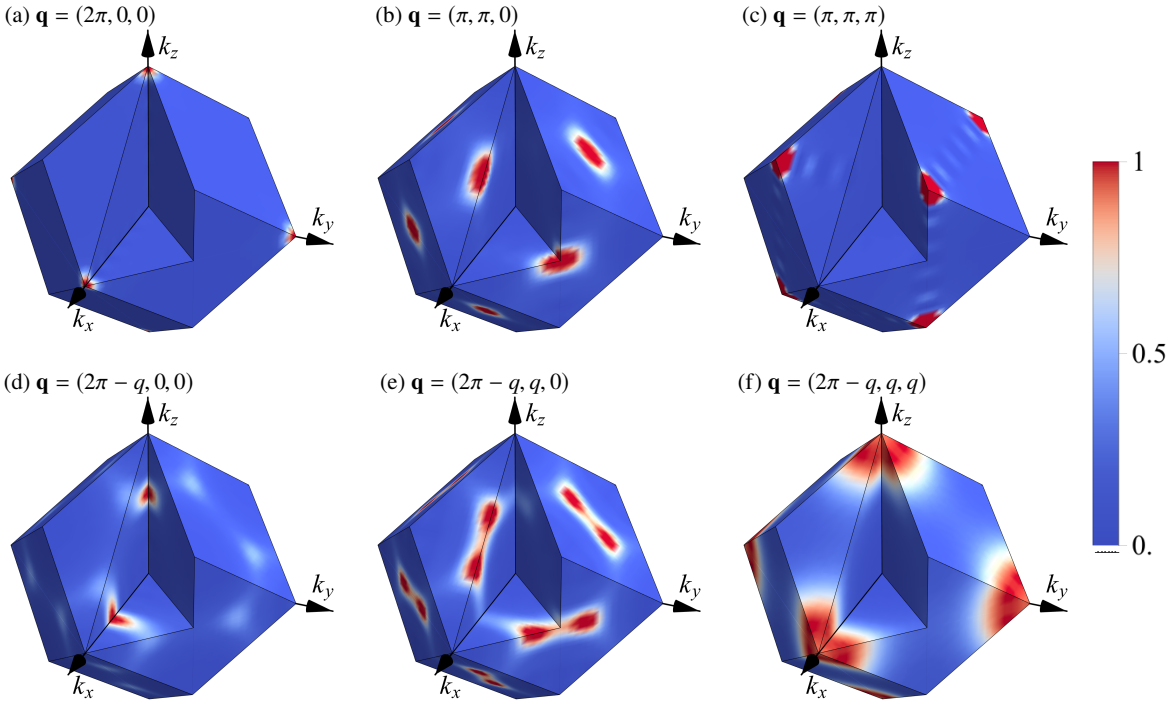

Figure 10.6: Normalized susceptibility profiles in the first BZ of the BCC lattice for the Heisenberg model with AF J_1 for the magnetically ordered states. The susceptibilities are plotted for the couplings used in Figure 10.4 at the Λ values indicated by arrows in the right panel of this figure. Figure reproduced from Reference [32].

is located, similar to the shift in the boundary between FM and stripe order. In total, this means that the FM ordered regime shrinks under quantum fluctuations compared to its classical extent, as expected from the above-mentioned eigenstate argument. In contrast, for AF J_1, the Nèel state takes over parts of the classical 1D, 2D and 3D spiral phases, but the shifts in phase boundaries are not as pronounced as in the FM J_1 case. The domain of Nèel order, therefore, is enhanced by quantum fluctuations.

Shifting focus to the phase boundary between 2D spiral and the planar AF, we find another significant shift by quantum fluctuations. The classical value of $J_2/|J_1| = 1$ is lowered for both FM as well as AF J_1, which implies a stabilization of the planar AF by quantum fluctuations. This can be explained by the *continuous* 8–dimensional degeneracy of the classical planar AF, as discussed in Section 10.1, in contrast to the 6–and 12–fold *discrete* degeneracies of the 2D spirals for J_1 FM and AF, respectively. Therefore, quantum fluctuations are more pronounced on top of the planar AF, compared to the 2D spirals. The difference in degeneracy for the two cases of J_1 can also account for the fact, that for FM J_1 the phase boundary is significantly shifted to $J_2/|J_1| \approx 0.82$, whereas for AF J_1 the shift is smaller and the phase boundary is located at $J_2/|J_1| \approx 0.93$.

The remaining phase boundaries, namely the one between 1D and 2D spirals and the one between 2D and 3D spirals remain insensitive to quantum fluctuations.

Within the incommensurate spiral phases, we find quantum effects to shift the values of the ordering wave vectors. As can be seen in Figure 10.8, for the 1D spiral the shift is such, that both for FM and AF J_1 the ordering vector is shifted towards the Nèel ordering vector $\boldsymbol{q} = (2\pi, 0, 0)$, with the effect being, at fixed J_2 more pronounced for smaller J_3 and appearing to decrease with increasing value of third-nearest neighbor coupling. This shift is in accordance with the stabilization of the Nèel and destabilization of the FM state reflected in the phase boundary changes. Keeping J_3 fixed (see Figure 10.8(c)), the wave vector shift towards the Nèel one increases with increasing FM J_2 for FM J_1,

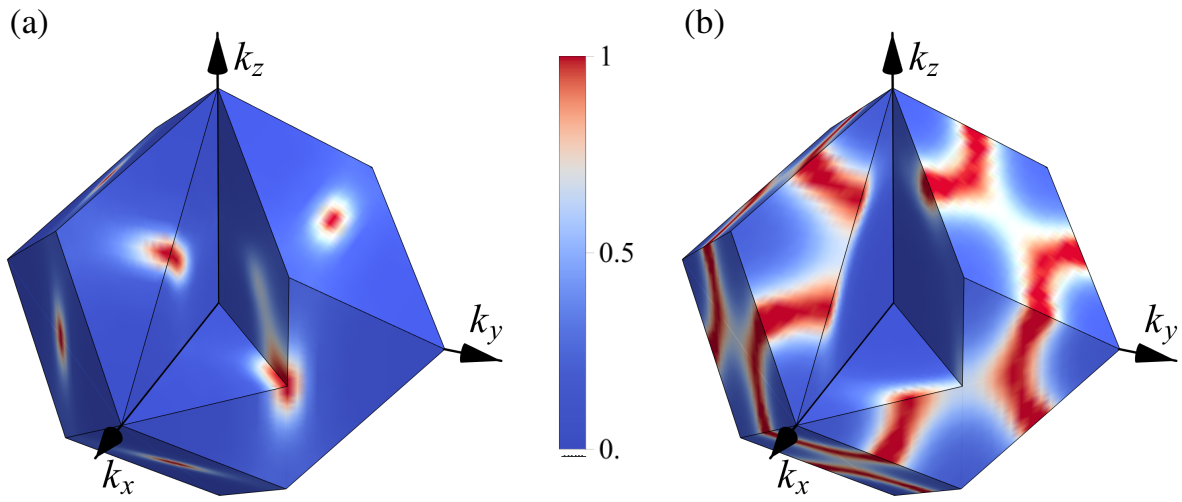

Figure 10.7: Normalized paramagnetic susceptibility profiles for $\Lambda \to 0$, i.e. the lowest simulated Λ at $(J_2/|J_1|, J_3/|J_1|) = (0.8, 0.3)$ for (a) FM J_1 and (b) AF J_1 for the spin-1/2 BCC Heisenberg model. Note, that the peaks are softer than the corresponding ones in the ordered states. Figure reproduced from Reference [32].

which is counterintuitive, as one would expect a FM interaction to favor the ferromagnetically ordered state. For AF J_1 this tendency is reversed, as there the shift towards the Nèel ordering vector decreases and is almost negligible for large enough J_2. Turning to the 2D spiral phase, we find, that for FM J_1, the ordering vector is shifted towards planar AF order, the absolute value of the shift again decreasing with increasing J_3, as shown in Figure 10.8(b). With respect to J_2 for fixed J_3, this shift is essentially constant (Figure 10.8(c)). Both findings result in a shift of the planar AF phase boundary towards smaller J_2. In the case of AF J_1, however, we find, that the wave vectors are shifted towards the $\boldsymbol{q} = (2\pi, 0, 0)$ Nèel ordering vector, with a shift that is essentially constant with respect to J_2 and J_3. We do not discuss the 3D spiral, as its extent in parameter space is too small to draw reasonable conclusions.

10.3 Nèel and Curie temperatures

The Nèel temperature (T_N) of an AF order, as well as the Curie temperature (T_C) for a FM one can serve as a measure thermodynamic measure of frustration in a magnetic system. In the absence of frustration, these can be computed by (numerically) exact quantum Monte Carlo, i.e. on the BCC lattice in the region $J_2 \leq 0$ for $J_3 = 0$. If one, however, adds frustration, there are only approximate methods available. As already realized early one, one-loop PFFRG in the step-cutoff formulation is not converged with respect to ordering temperatures, when compared to its ability to determine phase boundaries [157]. Therefore, we calculate ordering temperatures in both one- and two-loop formalism, to compare the ordering temperature estimates with the ones obtained from high-temperature expansion and Green's function methods, as well as QMC for the pure nearest-neighbor model.

Classically, the nearest neighbor model has equal Curie and Nèel temperatures $T_C^{\text{class}}/|J_1| = T_N^{\text{class}}/|J_1| = 1.54$ [185], but the finite spin Heisenberg model is known to have $T_N > T_C$ for nonfrustrating interactions on bipartite lattices, such as the BCC [183]. The difference between T_N and T_C of about 9% found in QMC [32] (see Table 10.4) is also reproduced by two-loop PFFRG, but slightly overestimated by one-loop calculations, where we find a difference of $\sim 12\%$. Both formulations, however, overestimate both critical temperatures slightly. However, going from one- to two-loop results, the errors in ordering temperature approximately halve. One therefore could expect higher accuracy

	Phase I	Phase II	Method	$J_2^c/\lvert J_1\rvert$
J_1–FM	$(0,0,0)$	(π,π,π)	PFFRG	0.56(2)
			Exact Diagonalization [32]	0.568
			Coupled Cluster Method [32]	0.579
			Rotation-invariant Green's function method [173]	0.68
			Random phase approximation [174]	0.6799
J_1–AF	$(2\pi,0,0)$	(π,π,π)	PFFRG	0.70(2)
			Coupled Cluster Method [175]	0.704
			Exact Diagonalization [168]	0.7
			Non-linear spin-wave theory [176]	0.705
			Random phase approximation [177]	0.72
			Linked Cluster Series expansions [178]	0.705(5)

Table 10.3: The critical value $J_2^c/|J_1|$ for the pure J_1–J_2 Heisenberg model on the BCC lattice, marking the transition between FM Nèel and the stripe AF obtained from PFFRG and different methods for comparison.

for even higher loop-order calculations, which however are currently not possible in the step-cutoff scheme due to numerical problems concerning the non-analytical cutoff, as discussed in Section 7.6.

Adding a frustrating next-nearest neighbor interaction J_2, we find the ordering temperatures to monotonically decrease with increasing J_2, with a sharp drop close to the phase transition. From Table 10.4, we see from PFFRG, that $T_N > T_C$ is valid even in the presence of frustrating interactions, in agreement with high-temperature expansion [173, 178, 183, 184], but contradicting the results from Green's function approaches [173, 184]. As for the nearest-neighbor model, PFFRG overestimates the ordering temperatures compared to high-temperature expansion results, while two-loop PFFRG again gives mostly better agreement. This implies, that PFFRG in two-loop formulation is well suited for capturing relative behavior of ordering temperatures, but absolute values are still to be taken with error bars of a few percent.

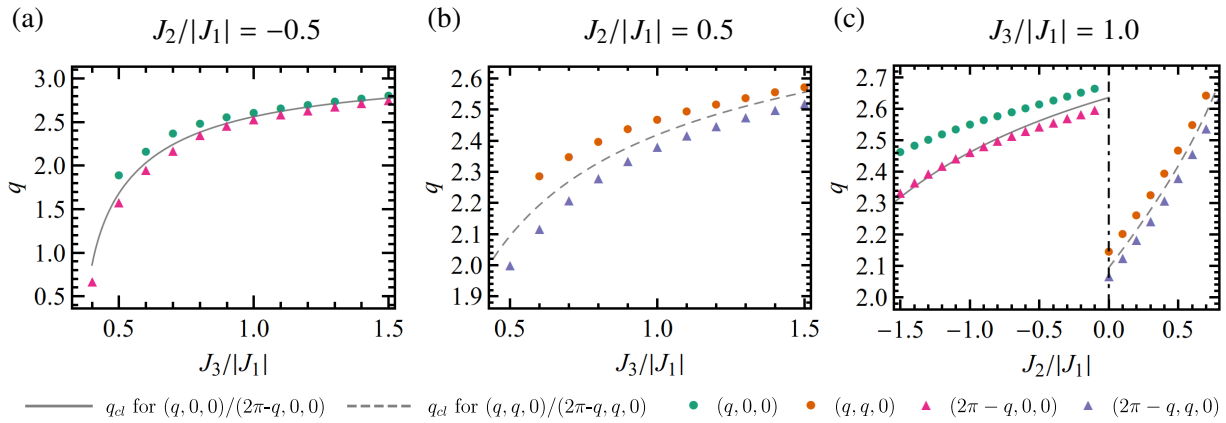

Figure 10.8: Variation of q for the incommensurate spiral phases $(q,0,0)$, $(q,q,0)$, $(2\pi-q,0,0)$, and $(2\pi-q,q,0)$ along three different cuts in the J_2–J_3 plane of the Heisenberg model on the BCC lattice. Circles (triangles) denote the case of FM (AF) J_1. The corresponding classical values are shown by gray lines. Figure reproduced from Reference [32].

	Method	$\frac{J_2}{\lvert J_1\rvert}=0$	$\frac{J_2}{\lvert J_1\rvert}=0.1$	$\frac{J_2}{\lvert J_1\rvert}=0.2$	$\frac{J_2}{\lvert J_1\rvert}=0.3$	$\frac{J_2}{\lvert J_1\rvert}=0.4$	$\frac{J_2}{\lvert J_1\rvert}=0.5$	$\frac{J_2}{\lvert J_1\rvert}=0.6$
J_1–FM	PFFRG (one loop)	1.45(1)	1.33(1)	1.18(1)	1.04(1)	0.88(1)	0.66(1)	
	PFFRG (two loop)	1.37(1)	1.26(3)	1.11(1)	0.97(1)	0.84(3)	0.62(1)	
	QMC [32]	1.260(1)						
	HTE [χ_u] [181–183]	1.2602(5)						
	HTE [χ_u^{quot}] [173]	1.253(8)	1.125(15)		1.06(32)			
	HTE [χ_u^{DA}] [173]	1.268(8)	1.16(3)		0.89(7)			
	HTE [$S(\boldsymbol{Q})$] [184]	1.273(8)	1.17(3)	1.09(10)	0.89(7)	0.72(11)	0.45(18)	
	GFA [173]	1.359	1.247	1.136	1.022	0.903	0.771	
J_1–AF	PFFRG (one loop)	1.63(1)	1.52(1)	1.36(1)	1.26(2)	1.10(1)	0.90(1)	0.71(1)
	PFFRG (two loop)	1.50(1)	1.42(1)	1.32(1)	1.16(1)	1.06(1)	0.89(1)	0.75(1)
	QMC [32]	1.377(2)						
	HTE [χ_s] [183]	1.376(4)						
	HTE [$S(\boldsymbol{Q})$] [184]	1.50(8)	1.36(10)	1.26(13)	1.09(13)	0.96(7)	0.75(6)	0.61(10)
	HTE [χ_s] [178]	1.38(2)	1.26(2)	1.13(1)	1.00(2)	0.86(2)	0.71(2)	0.57(3)
	GFA [184]	1.530	1.369	1.195	1.004	0.786	0.520	

Table 10.4: Critical temperatures $T_c/|J_1|$ of the $S = 1/2$ J_1–J_2 BCC Heisenberg model for various values of the frustrating AF J_2 coupling, obtained from different methods for both FM as well as AF J_1.

CHAPTER 11

J_1-J_2 Heisenberg model on the Pyrochlore lattice

Similar to the BCC , the Pyrochlore lattice can also be seen as a 3D generalization of a 2D lattice namely the Kagome. While the latter is built up as a net of corner-sharing triangles of lattice points, likewise the Pyrochlore lattice is built up from corner-sharing tetrahedra, as shown in Figure 11.1. Its underlying Bravais lattice is the FCC lattice, supplemented by a four-site basis, forming a single tetrahedron.

We here will focus on NN and NNN Heisenberg interactions on the Pyrochlore lattice, which we parametrize using a single angle θ, such that the Hamiltonian of the system is given by

$$\hat{H} = J_1 \sum_{\langle i,j\rangle_1} \hat{\boldsymbol{S}}_i \cdot \hat{\boldsymbol{S}}_j + J_2 \sum_{\langle i,j\rangle_2} \hat{\boldsymbol{S}}_i \cdot \hat{\boldsymbol{S}}_j \quad \text{with} \quad J_1 = J\cos(\theta) \quad \text{and} \quad J_2 = J\sin(\theta), \tag{11.1}$$

where J is a for the ground state irrelevant overall energy scale. We denote the sums over nearest and second-nearest $\langle i,j\rangle_1$ and $\langle i,j\rangle_2$, respectively.

Akin to its 2D counterpart, the Pyrochlore NNAF features an extensively degenerate classical ground state [186–189]. To understand this, let us introduce the total magnetization $\boldsymbol{M}_{\mathcal{T}}$ of the $\mathcal{T}$th tetrahedron

$$\boldsymbol{M}_{\mathcal{T}} = \sum_{\alpha=1}^{4} \boldsymbol{S}_{\mathcal{T},\alpha}, \tag{11.2}$$

whereby $\boldsymbol{S}_{\mathcal{T},\alpha}$ we label the αth spin on the $\mathcal{T}$th tetrahedron. Recasting the classical NN Heisenberg Hamiltonian eq. (2.5) on the Pyrochlore lattice, i.e. $J_2 = 0$, in terms of the $S \to \infty$ limit of eq. (11.2), we find, that it decomposes into a *disjoint* sum of the magnetizations on the tetrahedra

$$H = \frac{J_1}{2} \sum_{\mathcal{T}} \boldsymbol{M}_{\mathcal{T}}^2 + \text{const.} \tag{11.3}$$

This clearly is minimized if and only if all magnetizations vanish separately, i.e.

$$\boldsymbol{M}_{\mathcal{T}} = \boldsymbol{0} \quad \forall \mathcal{T}. \tag{11.4}$$

This set of constraints is commonly called ice rule, due to its similarity to the local order constraints found in water ice [190]. It can indeed be fulfilled on the whole lattice and leads to a countably infinite manifold of degenerate ground states, as can be seen from a "Maxwellian counting argument" [186, 187]. Considering a finite Pyrochlore lattice consisting of N_S spins, their number of degrees of freedom is $F = 2N_S$, as due to the strong spin length constraint eq. (2.6), only two of the three spin vector components are independent. Due to the ice-rule eq. (11.4), the number of constraints is $K = 3N_{\mathcal{T}}$, where $N_{\mathcal{T}}$ is the number of tetrahedra (one constraint for each of the components of the

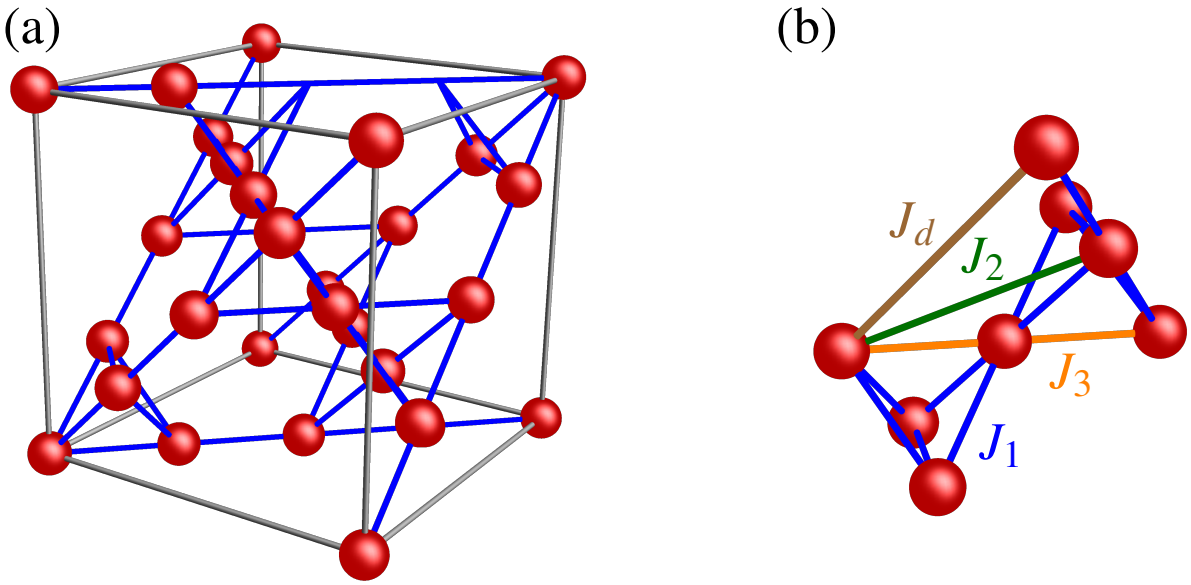

Figure 11.1: (a) Cubic unit cell of the Pyrochlore lattice containing 16 sites. All nearest-neighbor couplings (blue) within the cell are shown. (b) Corner sharing tetrahedra as the building block of the Pyrochlore lattice. The nearest neighbor couplings J_1 (blue) together with exemplary NNN J_2 (green) and the two symmetry inequivalent third-nearest neighbor interactions J_3 and J_d are shown. J_3 (orange) is the one crossing a NN site, while J_d (brown) does not and connects to an additional point not belonging to the two tetrahedra. The Bravais lattice of the Pyrochlore is a face-centered cubic (FCC) lattice with a four site unit cell, which comprises one of the tetrahedra.

magnetization). As for corner-sharing tetrahedra, each spin is part of two tetrahedra, we have $N_\mathcal{T} = N_s/2$. Therefore, the total dimensionality of the ground-state manifold is $D = F - K = 4N_\mathcal{T} - 3N_\mathcal{T} = N_\mathcal{T}$.

11.1 Classical phase diagram

The absence of magnetic long-range order at zero temperature in the classical Heisenberg NN AF on the Pyrochlore lattice means, that this cooperative paramagnetic state will be highly susceptible to any perturbations to that model, resulting in strong changes of magnetic and thermodynamic properties of the system, e.g. inducing long-range order. Already adding a NNN Heisenberg coupling J_2 to the classical NN model will stabilize an abundance of intricate magnetic orders, listed in Table 11.1, with the corresponding phase diagram shown in Figure 11.2. Part of these have already been investigated in References [191–194], while the full phase diagram of the J_1-J_2 parameter space was explored in Reference [38]. We will in the following recapitulate this already quite extensive knowledge about the classical phases of the classical J_1-J_2, but also add some corrections and amendments to the current picture of the phases drawn in literature.

Apart from the classical spin-liquid state for the antiferromagnetic pure nearest-neighbor model, we find seven different classical magnetic long-range orders in the J_1-J_2 phase diagram. Employing a Luttinger-Tisza analysis combined with iterative minimization on large systems consisting of 32×32×32 cubic unit cells, cf. Figure 11.1, which corresponds to 524 288 spins, we refine the analysis of the nature of the classical orders and the phase diagram originally presented in Reference [38]. There, a similar approach based on smaller systems of $4 \times 4 \times 4$ cubic unit cells (1024 sites) was used, which leads to more severe finite-size effects compared to our analysis, which we can attribute the main differences in our findings to. Additionally, we give the ordering vectors within the extended BZ in

State	Wave vector	Ordering	Classical domain	Quantum $S = 1/2$ domain
Paramagnet				$[345.6° \pm 1.8°, 12.6° \pm 1.8°]$
$\boldsymbol{k} = \mathbf{0}$	$2\pi(2,0,0)$	Coplanar	$(0°, 26.56°]$	$[12.6° \pm 1.8°, 26.56°]$
Planar Spiral	$2\pi(k,0,0)$	Coplanar	$[26.56°, 145.78°]$	$[26.56°, 151.74° \pm 0.36°]$
Double-Twist	$2\pi(\frac{3}{4}, \frac{3}{4}, 0)$	Noncoplanar	$[145.78°, 154.59°]$	$[151.74° \pm 0.36°, 160.83° \pm 0.09°]$
Multiply Modulated Spiral	$2\pi(\frac{3}{4}^*, \frac{1}{2}, \frac{1}{4}^*)$	Noncoplanar	$[154.59°, 158.37°]$	$[160.83° \pm 0.09°, 161.91° \pm 0.09°]$
Cuboctahedral Stack	$2\pi(\frac{1}{2}, \frac{1}{2}, \frac{1}{2})$	Noncoplanar	$[158.37°, 170.30°]$	$[161.91° \pm 0.09°, 171.27° \pm 0.27°]$
FM	$2\pi(0,0,0)$	Coplanar	$[170.30°, 312.53°]$	$[171.27° \pm 0.27°, 308.61° \pm 0.27°]$
Kawamura	$2\pi(\frac{5}{4}^*, \frac{5}{4}^*, 0)$	Noncoplanar	$[312.53°, 0°)$	$[308.61° \pm 0.27°, 345.6° \pm 1.8°]$

Table 11.1: Classically ordered phases featuring magnetic long-range order found in the J_1-J_2 Pyrochlore Heisenberg model. If the possible spin configurations corresponding to an order contain a subset of states which are coplanar, the phase is labeled as such. Asterisks (*) indicate slight incommensurate deviations within the phase away from the given rational values of the wave-vector components.

Table 11.1, in contrast to backfolded ones within the first BZ in Reference [38], as these are the ones that would be determined in neutron-scattering experiments. The detailed discussion of the classical case will facilitate the one of the quantum phase diagram in Section 11.2, as there we will find the same long-range ordered phases for both spin $S = 1/2$ and $S = 1$.

We start our discussion from the nearest-neighbor antiferromagnet, where the extensively degenerate ground state manifold is solely characterized by the zero spin sum rule on every tetrahedron given in eq. (11.4). In Reference [48], it was shown, that any infinitesimal perturbation of the nearest neighbor model by a second-nearest-neighbor interaction J_2 will reduce this manifold down to either an ordered state for FM J_2 or a nonextensive subset of ground states of the pure nearest-neighbor model in the AF case. In the latter case, the AF $J_2 > 0$ selects states out of the ice-rule manifold, in which spins within each of the four FCC sublattices of the Pyrochlore lattice assume FM order, from which the state is dubbed $\boldsymbol{k} = \mathbf{0}$. The ice-rule, however, is still preserved in this state, i.e. the four sublattices are not necessarily aligned parallel to each other, but align such, that the spin sum on a given tetrahedron remains zero. This leaves a subextensive manifold of degenerate ground states, which all are characterized by ordering wave-vectors at $\boldsymbol{k} = 2\pi(2,0,0)$ and symmetry-related points in the extended BZ. Such a state can be understood by realizing, that as long as the ice-rule is fulfilled on every tetrahedron, a second-nearest-neighbor interaction J_2 is equivalent to a third-nearest-neighbor interaction J_3 of opposite sign [193]. To illustrate this, consider the for spins $\boldsymbol{S}_1$, $\boldsymbol{S}_2$, $\boldsymbol{S}_3$ and $\boldsymbol{S}_4$ that constitute a single tetrahedron. According to the ice-rule we have

$$\sum_{i=1}^{4} \boldsymbol{S}_i = \mathbf{0}. \tag{11.5}$$

Considering only J_1 and J_2 couplings, the effective field due to this tetrahedron a spin neighboring $\boldsymbol{S}_1$ belonging to an adjacent tetrahedron will be subjected to is given by

$$\boldsymbol{B}_{\mathrm{eff},J_2} = J_1 \boldsymbol{S}_1 + J_2(\boldsymbol{S}_2 + \boldsymbol{S}_3). \tag{11.6}$$

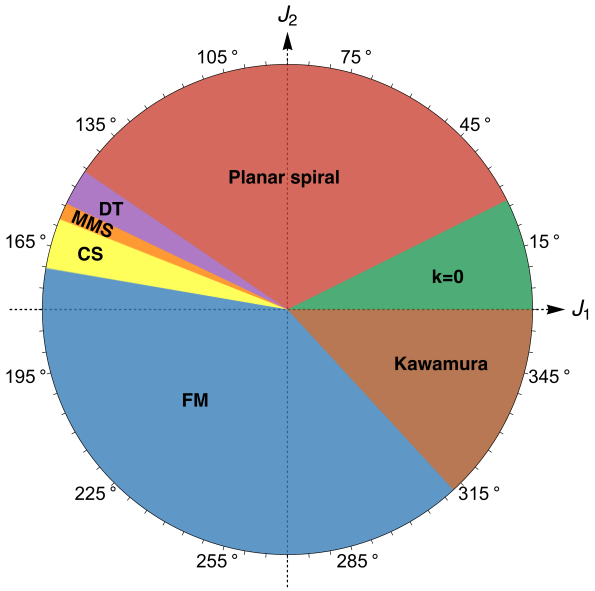

Figure 11.2: The classical phase diagram of the J_1-J_2 Heisenberg model on the Pyrochlore lattice. The couplings are parametrized as $J_1 = J\cos(\theta)$ and $J_2 = J\sin(\theta)$ with J an overall energy scale. See Table 11.1 for a description of the phases and the location of the phase boundaries. Figure reproduced from Reference [31].

Employing J_3 instead of J_2, we find

$$\begin{aligned} \boldsymbol{B}_{\text{eff},J_3} &= J_1\boldsymbol{S}_1 + J_3\boldsymbol{S}_4 \\ &= J_1\boldsymbol{S}_1 + J_3(-\boldsymbol{S}_1 - \boldsymbol{S}_2 - \boldsymbol{S}_3) \\ &= (J_1 - J_3)\boldsymbol{S}_1 - J_3(\boldsymbol{S}_2 + \boldsymbol{S}_3), \end{aligned} \tag{11.7}$$

where we have used eq. (11.5). Comparing Equations (11.6) and (11.7), J_3 is equivalent to J_2 of opposite sign, while at the same time renormalizing the NN interaction. J_3 now only mediates interactions within the same sublattice, so for AF J_2 the effective FM J_3 will select states with parallel spins on the sublattices form the NN ground state manifold.

The $\boldsymbol{k} = \boldsymbol{0}$ is an *exact* Luttinger-Tisza eigenstate with an energy per spin $E = -2J_1 - 4J_2$. The ferromagnetic correlations within the individual sublattices lead to the formation of subdominant peaks in the spin structure factor at *all* symmetry equivalent points of $2\pi(1,1,1)$-type at the edge of the extended BZ. The spectral weight of any given subdominant peak is one-eighth of the total spectral weight of the dominant ones at the $2\pi(2,0,0)$-type points. As the relative orientation of the sublattices is not completely fixed by the ice-rule, but three angular degrees of freedom are left, the exact distribution of spectral weight among the dominant peaks, and therefore the breaking of the cubic Pyrochlore symmetry, is not fixed by the interactions. Consequently, at $T = 0$, there is no *a priori* determination of the complete structure factor possible, however, for any finite temperature, there might be entropic effects selecting a unique ground state. In this case, one can use the relative spectral weight of the dominant peaks in the structure factor as a measure of the collinearity of the spins, with only a single peak being present corresponding to a completely collinear state.

Since the $\boldsymbol{k} = \boldsymbol{0}$ relies on the ice-rule still being valid on each tetrahedron, naturally it minimizes the energy only for AF $J_1 > 0$, as long as AF J_2 is sufficiently small for J_1 to be the dominant interaction. As every site has twice as many

second-nearest neighbors than nearest-neighbors, J_2 becomes the dominant interaction for $J_2 > {}^{J_1}/_2$, i.e. $\theta \gtrsim 26.56°$ in Figure 11.2. For larger J_2, the system transitions into *planar* spiral phase, governed by one of the symmetry-related $\boldsymbol{k} = 2\pi(k, 0, 0)$-type ordering wave vectors. Again, this is a Luttinger-Tisza eigenstate, allowing to extract

$$k = \frac{2}{\pi} \arccos\left[-\frac{J_1}{4J_2} - \frac{1}{2}\right] \tag{11.8}$$

as the exact wave vector. The energy per spin of the state is given by $E = -{}^{J_1^2}/_{2J_2} - 6J_2$. Compared to Reference [38], the wave vector differs by a factor of 2. This we trace back to the mapping of the state onto an equivalent spin-chain model [37] being carried out incorrectly.

The planar spiral phase also encompasses the pure second-nearest-neighbor AF with $J_1 = 0$, $J_2 = 1$, which features a 120° spiral on each of the FCC sublattices, which results in an overall ordering wave-vector $\boldsymbol{k} = 2\pi(4/3, 0, 0)$ in the extended BZ when taking into account the relative phases of the spirals on the different sublattices. In addition to the aforementioned dominant peaks at $\boldsymbol{k} = 2\pi(k, 0, 0)$-type wave-vectors, there exist additional subdominant peaks in the extended BZ at ordering wave-vectors of $\boldsymbol{k} = 2\pi(3 - k, 1, 1)$-type. Here, the k and $3 - k$ components in the dominant and subdominant ordering vectors, respectively, always appear in the same entry for both corresponding wave-vectors. The subdominant peaks carry a fixed ${}^1/_4$ of the spectral weight of the dominant ones and are a signature of the correlations within the FCC sublattices in the Pyrochlore lattice.

Beyond the pure second-nearest-neighbor point, the planar spiral phase is still stable for FM $J_1 < 0$, while keeping J_2 AF. Beyond the phase transition at $J_2/J_1 = -0.68$ ($\theta \approx 145.78°$), the ground state changes to the so-called double-twist (DT) state, a non-coplanar spin configuration first found on the frustrated octahedral lattice with antiferromagnetic interactions [37]. In this state, the spins form two different kinds of spirals in two distinct directions, but both being controlled by the same wave-vector.

The spin structure factor of this state is characterized by cubic symmetry breaking selecting two of the three reciprocal space planes. As the Heisenberg Hamiltonian does not determine this breaking, but it is spontaneously chosen when entering the phase, for definiteness, we consider the k_x-k_y and k_y-k_z planes in our discussion of the state. On both planes, peaks at pairs of $\boldsymbol{k} = 2\pi(3/4, 3/4, 0)$-type wave vectors are present. On the first plane, the k_x-k_y plane, these are $\boldsymbol{k} = 2\pi(3/4, 3/4, 0)$ and $\boldsymbol{k} = 2\pi(3/4, -3/4, 0)$, where the dominant peaks of the structure factor with identical spectral weight are located. In the second plane, the k_y-k_z plane, located at wave vectors $\boldsymbol{k} = 2\pi(0, 3/4, 3/4)$ and $\boldsymbol{k} = 2\pi(0, 3/4, -3/4)$, there are additional subdominant peaks with approximately 59 % of the spectral weight of the dominant ones. These pairs of wave vectors characterize the spiral ordering on the individual FCC sublattices. An approximate parametrization of the state is given in Reference [38]. Additionally, due to the relative angles between the spins on the sublattices, there appear subdominant peaks at $\boldsymbol{k} = 2\pi(5/4, 5/4, 0)$-type wave vectors, corresponding to the pairs of dominant peaks on the respective planes, i.e. k_x-k_y plane, we find subdominant peaks at $\boldsymbol{k} = 2\pi(5/4, 5/4, 0)$ and $\boldsymbol{k} = 2\pi(5/4, -5/4, 0)$ carrying approximately 29 % of the amplitude of the dominant peaks. In the k_y-k_z plane, where the subdominant $\boldsymbol{k} = 2\pi(3/4, 3/4, 0)$-type peaks are present, corresponding weaker peaks at wave vectors $\boldsymbol{k} = 2\pi(0, 5/4, 5/4)$ and $\boldsymbol{k} = 2\pi(0, 5/4, -5/4)$, which have approximately 13 % of the spectral weight of the most dominant ones in the k_x-k_y plane.

For even lower AF $J_2 > 0$ keeping FM $J_1 < 0$, at $J_2/J_1 = -0.475(5)$, i.e. $\theta \approx 154.59°$, we find a phase transition to a state, which closely resembles the *multiply modulated commensurate spiral* found in Reference [38], where the phase boundary is estimated to $J_2/J_1 \approx -0.43$. The state there is characterized by four dominant ordering vectors at commensurate $\boldsymbol{k} = 2\pi(3/4, 1/2, 1/4)$ type points in the extended BZ, which all have the $1/2$ component in the same direction in spin space. Additionally, subdominant wave-vectors of $\boldsymbol{k} = 2\pi(3/4, 0, -3/4)$ type are present, where the

zero component coincides with the $1/2$ direction in the dominant ordering vectors. This structure originates from a real space spin configuration, in which, moving along different directions in direct space, the spins trace out multiple spirals, characterized by the aforementioned wave-vectors.

The commensurability of the wave-vectors found in Reference [38], however, is only an artifact of sizeable finite-size effects in the simulations done there. By employing periodic boundary conditions on a system of $L \times L \times L$ cubic unit cells in the iterative minimization, the accessible wave-vectors are restricted to have components, which are integer multiples of $2\pi/L$. This in turn will lead to an observation of an almost commensurate wave vector as a peak at a commensurate position. Using $L = 32$ compared to $L = 5$ in Reference [38], we can resolve, that the dominant wave vectors are indeed incommensurate. At the phase boundary, we find $\boldsymbol{k} = 2\pi[0.81(2), 0.50(2), 0.19(2)]$ type wave-vectors, which, within the numerical resolution of $2\pi/32$ in the components in reciprocal space, upon lowering J_2 evolve continuously towards the commensurate values given above. The latter are assumed at the phase transition to the cuboctahedral stack (CS) state in Figure 11.2. In contrast to the dominant ones, the subdominant ordering vectors stay unchanged, only their relative spectral weight compared to the dominant peaks changes. Starting from approximately 26 % at the border to the DT state, it increases to approximately 32 % when reaching the phase boundary with the CS state. This means, although the way in which the state is built up from the wave-vectors does not change, the value of the dominant wave-vector is a function of J_2/J_1, which is also supported by a Luttinger-Tisza analysis. For the parameters considered here, we find, that there are minimal Luttinger-Tisza eigenvalues at incommensurate wave vectors close to the commensurate points given above. These Luttinger-Tisza states, however, do not fulfill the strong spin-length constraint (see Section 3.1), which necessitates the admixture of subdominant wave-vectors to be able to normalize the state. As the dominant wave vectors are incommensurable, we refer to this state as a multiply-modulated spiral (MMS).

Abovementioned phase transition from the MMS to the CS state, we find at $J_2/J_1 = -0.3965(5)$ ($\theta \approx 158.37°$). The latter can be best understood by viewing the Pyrochlore lattice as a stacking in [111] direction, consisting of alternating Kagome and triangular lattice layers. In this state, the spins of the triangular lattice point towards the eight corners of a cube, while the spins on the Kagome layers point towards the 12 edge midpoints of this same cube, resulting in a 12-sublattice magnetic ordering on these layers. This structure was already found on the Kagome lattice [46, 195], where it was viewed as the spins pointing towards the vertices of a cuboctahedron, inscribed to the cube considered here. Extending this picture to the 3D Pyrochlore, the spins on the triangular lattice layers point towards the middles of the eight triangular faces of the cuboctahedron. This state is inherently non-coplanar, but still a Luttinger-Tisza eigenstate. Its average energy per spin is given by $E = J_1(3/4 + \sqrt{6}/2)$, which is independent of J_2, as, within the cuboctahedral state, the second-nearest neighbor interactions on the Kagome layer sum to zero for all spins individually, whereas the NNN of the Kagome spins located in the triangular plane are perpendicular, meaning the interaction vanishes. Given that all NNN of triangular layer spins within the Kagome layers, their J_4 interactions vanish completely. For more details on this argument, cf. Reference [38].

The particular spin arrangement of the CS state is achieved by building up the configuration from any three of the four wave vectors of $\boldsymbol{k} = 2\pi(1/2, 1/2, 1/2)$ type, e.g., $\boldsymbol{k} = 2\pi(1/2, 1/2, 1/2)$, $\boldsymbol{k} = 2\pi(-1/2, 1/2, 1/2)$, and $\boldsymbol{k} = 2\pi(1/2, -1/2, 1/2)$, carrying identical spectral weight. The stacking direction is then the [111] direction parallel to the fourth, unused symmetry equivalent wave vector, in this case $\boldsymbol{k} = 2\pi(1/2, 1/2, -1/2)$. An analytical parametrization of this state is given in Reference [38]. Due to the relative orientation of the FCC sublattices, subdominant wave vectors of $\boldsymbol{k} = 2\pi(1/2, 1/2, 3/2)$ type, carrying approximately 18 % of the spectral weight of the dominant ones accompany each of the ordering vectors used to built up the state.

Due to the energetical independence of J_2 in the CS means, lowering AF J_2 even more only changes the energy of competing states, in particular, the FM ordered state. At $J_2/J_1 = (-3/8 + \sqrt{6}/12)$ ($\theta \approx 170.30°$), the FM state actually

supersedes the CS energetically. Apart from the dominant ordering vector at $\boldsymbol{k} = 2\pi(0,0,0)$, subdominant peaks at all the $\boldsymbol{k} = 2\pi(1,1,1)$-type wave-vectors in the extended BZ are present, which carry a quarter of the spectral weight of the dominant ferromagnetic peak. These signal, as for the $\boldsymbol{k} = \boldsymbol{0}$ state, the ferromagnetic correlations within the individual FCC sublattices of the Pyrochlore lattice.

The FM state, compared to the other states, occupies the largest extent in the phase diagram. Starting from moderate AF J_2 at the phase transition from the CS state, it trivially extends into the unfrustrated region, where both J_1 and J_2 are FM and even beyond the pure second-nearest neighbor FM: for FM $J_2 < 0$, the FM state proves to be robust even against moderately strong AF $J_1 > 0$.

Only at $J_2/J_1 \approx -1.09$ ($\theta \approx 312.53°$), the FM order is destroyed by the frustrated AF J_1 coupling, giving way to the Kawamura states, named after the group that investigated this family of states in depth [191]. It is characterized by dominant wave-vectors at almost commensurate $\boldsymbol{k} = (k,k,0)$-type points with $k \approx 2\pi(5/4)$ and additional subdominant ordering vectors at $k \approx 2\pi(3/4)$ carrying approximately 22 % of the spectral weight of the dominant vectors. Stronger subdominant peaks are additionally located at $\boldsymbol{k} \approx 2\pi(1,1/4,7/4)$-type vectors with approximately 55 % spectral weight. There are two classes of ground states, which either feature four or all of the six symmetry equivalent ordering vectors: The former state clearly breaks the cubic symmetry of the Pyrochlore lattice, again without *a priori* determination of the specific nature of this breaking from the Heisenberg Hamiltonian, while the latter state respects this symmetry. Both types of ground states have in common, that they realize a non-coplanar spin configuration by superposition of spirals controlled by the aforementioned wave vectors. They also approximately fulfill the zero spin sum constraint on the tetrahedra and therefore can be viewed as perturbed eigenstates of the J_1 antiferromagnet. From iterative minimization, we find k to evolve from $k \approx 2\pi(1.31)$ at the FM phase boundary towards $k = 2\pi(5/4)$ approaching the pure NNAF model.

11.2 Quantum Phase Diagram

Strong quantum fluctuations in a highly frustrated magnetic lattice like Pyrochlore at small spin S can have several effects on the phase diagram. Due to quantum corrections to the energy being strongly dependent on the underlying order, phase boundaries can be shifted or, within spiral phases, the wave vector corresponding to a given set of couplings can differ from its classical value. More severely, quantum effects can even lead to the stabilization of orders not present in the classical model, even to the extent of melting classical long-range orders completely, allowing room for a quantum paramagnetic phase.

On the Pyrochlore lattice, there is a natural candidate region in the $J_1 - J_2$-parameter space for the latter, namely in the vicinity of the classical spin liquid in the pure AFNN model. However, even for this point, its fate in the $S = 1/2$ limit is not fully settled. There have been indications from perturbative and mean-field approaches for an $SU(2)$-symmetric spin liquid [31, 196–202], but also chiral spin liquid states [203–205] and a variety of dimerized ground states [206–215] were proposed. Recent studies employing large scale unbiased numerical methods point towards a dimerized, inversion and rotation symmetry breaking ground state [117, 216, 217].

We defer the discussion of the pure NN point to Section 11.3, but will first answer the question, how stable a quantum paramagnet is against additional NNN interactions. Classically, as already discussed, even an infinitesimal addition of NNN interaction J_2 will induce long-range magnetic order [48]. However, due to quantum fluctuations, this selection may be prevented in the low spin S regime for AF or even FM J_2.

Mapping out the full $J_1 - J_2$ phase diagram using PFFRG for $S = 1/2$, $S = 1$ and $S = 3/2$, as shown in Figure 11.3, we find, that for both $S = 1/2$ and, more surprisingly, even for $S = 1$ a paramagnetic regime is found around the

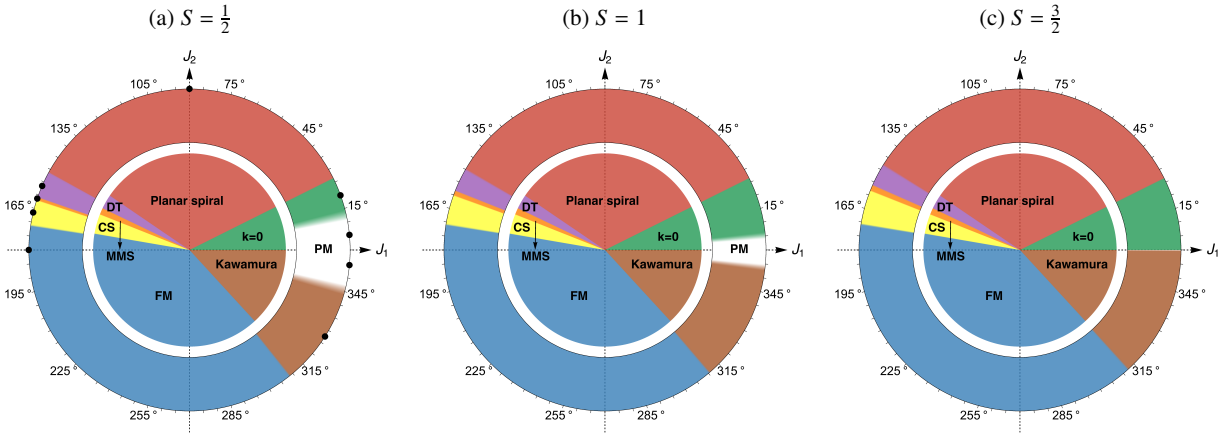

Figure 11.3: Quantum phase diagram (outer rings) of the J_1-J_2 Heisenberg model on the Pyrochlore lattice for increasing values of spin S. For comparison, the inner discs show the classical phase diagram. Apart from shifts in the phase boundaries, quantum effects stabilize an extended paramagnetic regime for $S = 1/2$ and $S = 1$. The black dots in (a) highlight parameter points, for which we show the susceptibility profiles in Figures 11.4 and 11.7, Figure reproduced from Reference [31].

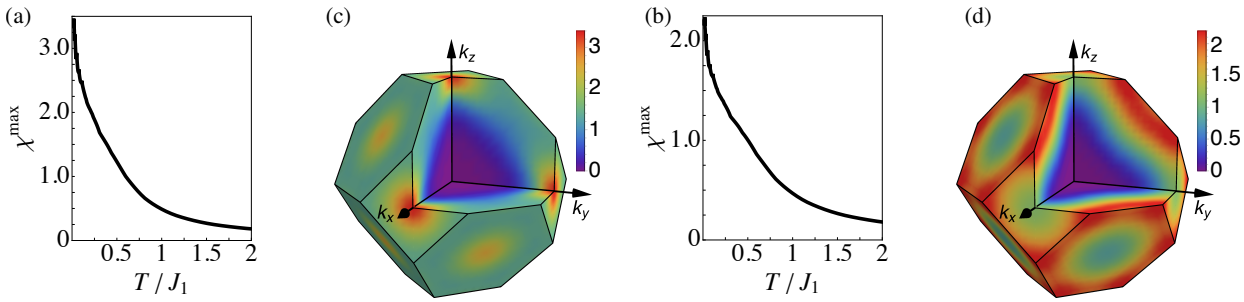

Figure 11.4: Representative RG flows (in units of $1/J$) in the paramagnetic regime for (a) $J_2/J_1 = 0.1$ and (b) $J_2/J_1 = -0.1$ with $J_1 > 0$, located by black circles in Figure 11.3(a). Their respective spin susceptibilities at the lowest T are shown in (c) and (d). Figure reproduced from Reference [31].

NNAF point. As shown in Figure 11.3(a), the paramagnet melts a significant slice of parameter space around $J_2 = 0$, classically occupied by $\boldsymbol{k} = \boldsymbol{0}$ and Kawamura orders for AF $J_2 > 0$ and FM $J_2 < 0$ respectively. The same is true for $S = 1$, however the span of the paramagnetic phase is found to be halved from $-0.25(3) \leqslant J_2/J_1 \leqslant 0.22(3)$ for $S = 1/2$ to $-0.11(2) \leqslant J_2/J_1 \leqslant 0.09(2)$, which is still non-negligible.

Representative RG flows for $S = 1/2$ in Figure 11.4 (a) and (b) for antiferromagnetic and ferromagnetic J_2 (J_1 being AF), respectively, display a monotonically increasing smooth behavior down to the smallest RG scale simulated, indicating the absence of long-range order. The corresponding spin susceptibilities in reciprocal space in the extended BZ (Figure 11.4 (c) and (d)) support this finding, as there are no sharp maxima present. Such incipient Bragg peaks would indicate the onset of magnetic long-range order. Instead, the spectral weight is smeared out by quantum fluctuations, but still resembling a molten version of the underlying classical ground state. For AF J_2, the susceptibility, as shown in Figure 11.4(c), features maxima at $\boldsymbol{k} = 2\pi(2, 0, 0)$ (and symmetry-related points), in correspondence with the dominant Bragg peaks of the classical $\boldsymbol{k} = \boldsymbol{0}$ order found in this coupling regime.

For FM J_2, the parent classical state in the paramagnetic region is the Kawamura order, with dominant and subdominant Bragg peaks at $\boldsymbol{k} \approx 2\pi(5/4, 5/4, 0)$ and $\boldsymbol{k} \approx 2\pi(3/4, 3/4, 0)$ (and symmetry-related points). Melting the corresponding ordered susceptibility shown in Figure 11.7(h) via quantum fluctuations gives rise to smeared, almost

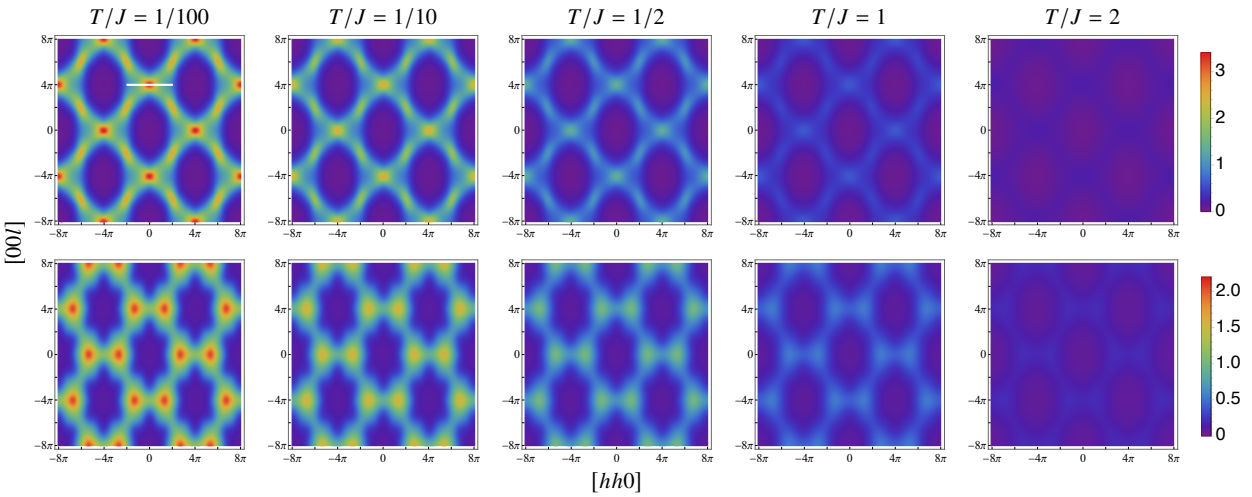

Figure 11.5: Temperature evolution of the spin susceptibility in the $[hhl]$ plane for paramagnetic states on the Pyrochlore lattice. Top row is evaluated for AF $J_2 = 0.1$, bottom row at FM $J_2 = -0.1$, both for $J_1 > 0$.

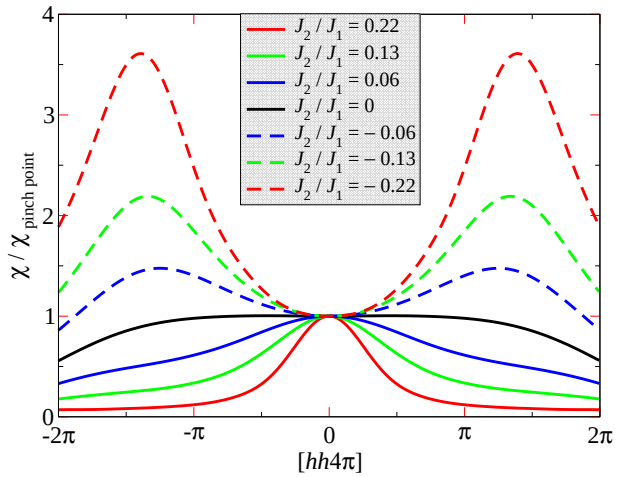

Figure 11.6: Susceptibility cuts along the $[hh4\pi]$ line (white line in Figure 11.5) for different values of J_2 in the paramagnetic regime at $T/J = 1/100$ showing the spectral shift when changing the sign of J_2. Figure reproduced from Reference [31].

homogenous ringlike features on the hexagonal surfaces of the BZ, see Figure 11.4(d). The corresponding $[hhl]$ plane susceptibility profiles for both cases of J_2 are shown in Figure 11.5. We find, that the NNN coupling modifies the paramagnetic susceptibility substantially. For AF NNN coupling $J_2 > 0$, the maximum of the susceptibility lies at $\boldsymbol{k} = 2\pi(2,0,0)$, the location of the so-called pinch point in the NNAF model, in accordance with the behavior of the classical model [218]. At this point, the classical susceptibility is non-differentiable with a discontinuity in $[00l]$ direction, while being constant on the perpendicular $[hh4\pi]$ line, leading to a pinched shape of the structure factor, resembling a bow-tie in total. In contrast, for FM $J_2 < 0$, the pinch point susceptibility is suppressed in favor of a hexagonal cluster pattern in the $[hhl]$ plane, also similar to the classical limit [218].

To better illustrate this redistribution of spectral weight, in Figure 11.6 we plot a 1D cut along the white line in Figure 11.5 of the susceptibility normalized to the pinch point, i.e. $\chi/\chi_{\text{pinch point}}$ with $\chi_{\text{pinch point}} = \chi(0,0,4\pi)$ at $T/J = 1/100$. Here we clearly see the enhancement of the pinch point weight at $\boldsymbol{k} = 2\pi(2,0,0)$ for increasing AF J_2, while for $J_2 < 0$, the maxima of the susceptibility move away from these points due to the shift of spectral

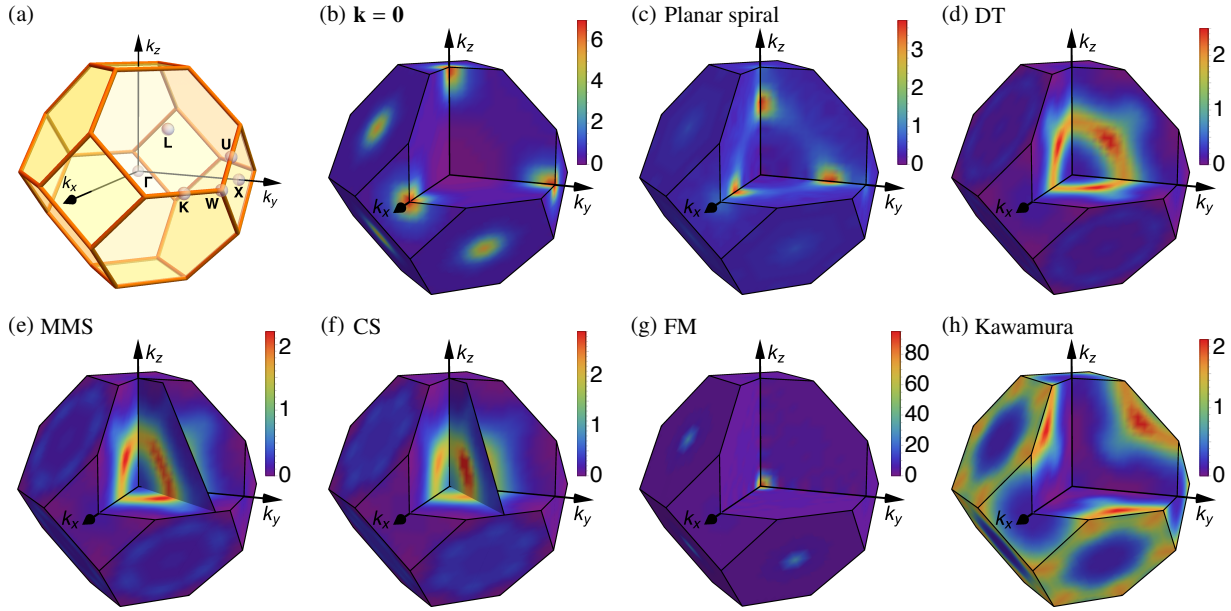

Figure 11.7: (a) Extended BZ of the Pyrochlore lattice, a truncated octahedron, with the high symmetry points labeled. (b)-(h) Reciprocal space plots of the magnetic susceptibilities (in units of $1/J$) for the different magnetic orders found in the $S = 1/2$ phase diagram for representative points marked by black dots in Figure 11.3(a). Figure reproduced from Reference [31].

weight towards the Kawamura state wave vectors. Increasing temperature, the general susceptibility profile of the paramagnetic states appears to be robust up to temperatures of the order of the coupling $T/J \sim 1$, as seen in Figure 11.5. Starting from that temperature, the profile starts to smear out, with the disordered state giving way to a high-temperature paramagnet.

Increasing spin length from $S = 1/2$ to $S = 1$, the qualitative results for the quantum paramagnet discussed above do not change, but only quantitative differences are found, most notably the smaller extent of the paramagnetic phase. Apart from that, the entire discussion for $S = 1/2$ also holds true for the $S = 1$ case.

Moving away from the paramagnetic regime, we now turn to the magnetically long-range ordered part of the low-spin J_1-J_2 phase diagram. Comparing the classical and quantum phases in 11.3, we find, that all classical magnetic orders are also found in the low-spin regime of the Pyrochlore model, and, more importantly, *no new* long-range orders are stabilized by quantum effects. The latter is in contrast to, e.g. the square lattice Heisenberg model, where additional commensurate phases are stabilized [166]. Starting from the region, where both J_1 and J_2 are AF, we find, that the span of the $\boldsymbol{k} = \mathbf{0}$ phase is substantially shrunk in the $S = 1/2$ case (see Table 11.1 for exact boundaries), due to its melting into the extended paramagnetic phase around the NN point, which, to a lesser extent, is also true for spin $S = 1$. The onset of $\boldsymbol{k} = \mathbf{0}$ magnetic long-range order is indicated by a clear instability in the RG flow of the susceptibility for a representative point in the middle of the phase at $J_2/J_1 = 0.36$, as marked in Figure 11.3(a). From the position of the breakdown, indicated by an arrow in Figure 11.8(a), we find a Nèel temperature $T_c/J \approx 0.39(2)$. Furthermore, the corresponding spin susceptibility profile at the instability in Figure 11.7(b) shows clear dominant incipient Bragg peaks at the X point, i.e., $\boldsymbol{k} = 2\pi(2, 0, 0)$, and all symmetry-related points. The expected subdominant peaks at the L points ($\boldsymbol{k} = 2\pi(1, 1, 1)$ and symmetry-related) are also clearly resolved. While in principle both thermal and quantum fluctuations, which could select a specific (non-)coplanar ground state out of the subextensive manifold of $\boldsymbol{k} = \mathbf{0}$ states, are captured in the PFFRG [33], the RG flow will not spontaneously break any lattice symmetry. Therefore, all symmetry-related Bragg peaks show the same density, which however cannot be taken as an indicator

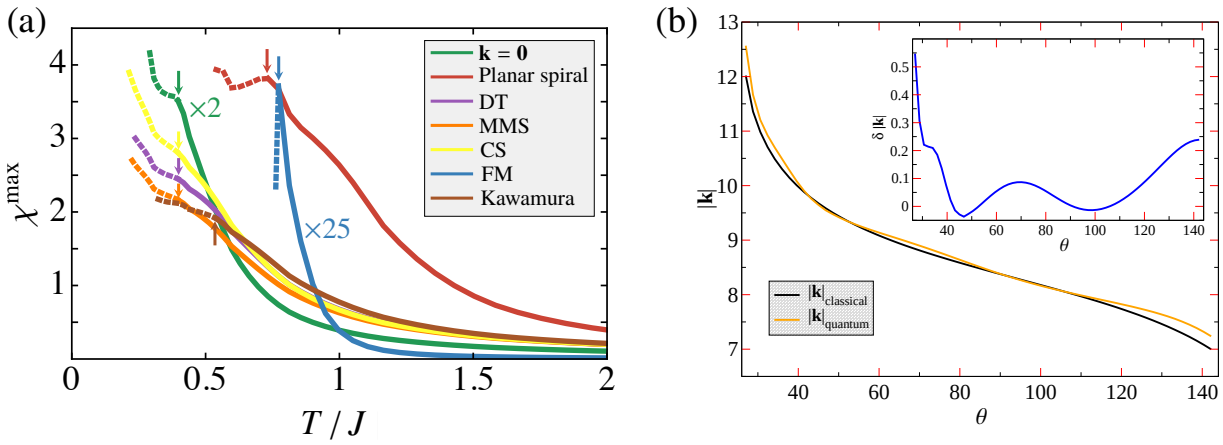

Figure 11.8: (a) Representative susceptibility RG flows at the ordering wave vectors for the seven long-range ordered phases of the $S = 1/2$ model. The corresponding parameter points are marked by black dots in Figure 11.3(a). Arrows mark the position of an instability of the flow, indicating the onset of long-range magnetic order. (b) Evolution of the ordering wave vectors of classical and quantum planar spiral phase with varying NN coupling strength parametrized by $\theta = \arctan(J_2/J_1)$. The inset shows the deviation $\delta|\boldsymbol{k}| = |\boldsymbol{k}_{\text{quantum}}| - |\boldsymbol{k}_{\text{classical}}|$ of quantum from the classical value. Figure reproduced from Reference [31].

of a non-collinear state. Indeed, as discussed in sec. 11.1, classically, the collinear $\boldsymbol{k} = \boldsymbol{0}$ state is selected by thermal fluctuations [193], and quantum fluctuations are likely to select the same state [219].

As in the classical case, we find the phase transition from the $\boldsymbol{k} = \boldsymbol{0}$ to the incommensurate planar spiral order at $J_2/J_1 = 1/2$. From the RGflow deep in the spiral phase ($J_2 = J_1$, marked by a black disk in Figure 11.3(a)), as shown in Figure 11.8(a), shows an onset of magnetic long-range order at $c/J \approx 0.73(3)$ signalled by a flow instability. In the susceptibility profile at the breakdown in Figure 11.7(c) the expected incommensurate Bragg peak is found. However, the quantum model differs in two ways from the classical one in this phase. Firstly, quantum fluctuations stabilize the planar spiral relative to the DT phase, extending the planar spiral phase in parameter space compared to its classical boundaries. The transition between the two states is shifted from $J_2/J_1 \approx -0.68$ to $J_2/J_1 \approx -0.537(6)$ in the $S = 1/2$ model, cf. Figure 11.3(a) and Table 11.1, implying a significant stabilization of the planar spiral by quantum fluctuations.

Secondly, we find, that the spiral wave vector in the quantum case is shifted compared to its classical counterpart, an effect already known on the cubic lattice [220]. In Figure 11.8(b), we find, that both quantum $\boldsymbol{k}_{\text{quantum}}$ and classical $\boldsymbol{k}_{\text{classical}}$ ordering vectors evolve monotonically decreasing throughout the planar spiral phase, starting from the boundary with the $\boldsymbol{k} = \boldsymbol{0}$ phase towards the DT order. The deviation $\delta|\boldsymbol{k}| \equiv |\boldsymbol{k}_{\text{quantum}}| - |\boldsymbol{k}_{\text{classical}}|$, in contrast, shows a nonmonotonical behavior over the same parameter range hosting planar order, as seen in the inset of Figure 11.8(b). For the most part of the phase, however, we find quantum fluctuations to *increase* the value of the wave-vector, shifting the character of the order towards antiferromagnetism. The maximum shift $\delta|\boldsymbol{k}|$ of approximately 4% of the classical wave vector value is found at the boundary to $\boldsymbol{k}$=$\boldsymbol{0}$ order at $\theta \approx 26\,57^\circ$.

The DT magnetic order takes over from the planar spiral at $J_2/J_1 = -0.537(6)$, with a representative RG flow of the dominant wave vector evaluated at $J_2/J_1 \approx -0.43$ (marked by a black disk in Figure 11.3(a)) shows an instability around $T_c/J \approx 0.39(2)$. The spin susceptibility profile (Figure 11.7(d)) clearly shows the dominant Bragg peaks for this state at $\boldsymbol{k} = 2\pi(3/4, 3/4, 0)$-type wave vectors, but also the subdominant peaks at $\boldsymbol{k} = 2\pi(5/4, 5/4, 0)$ and symmetry-related points are clearly resolved. The extent of the DT phase in the J_1-J_2 space in the $S = 1/2$ case is similar to the classical one, however its boundaries are shifted, with the planar spiral eating away some of its classical extend, while DT, in turn, takes over parameter space classically occupied by MMS and CS orders.

Method	Pyrochlore	Simple cubic	$T_c^{\text{Pyro}}/T_c^{\text{SC}}$	Pyrochlore	Simple cubic	$T_c^{\text{Pyro}}/T_c^{\text{SC}}$
PFFRG	0.77(4)	0.90(4)	0.86			
QMC/CMC	0.7182(3) [221]	0.839(1) [222, 223]	0.86	1.316 95(2) [224]	1.443 [185, 225]	0.91
HTE (Padé)	0.724–0.754 [221]	0.827 [226]	0.88	1.316–1.396 [221]	1.438 [226]	0.92
RGM	0.778 [221]	0.926 [221]	0.84	1.172 [221]	1.330 [221]	0.88
RPA	0.872 [227]	0.989 [228]	0.88			
MFA [a]	3/2	3/2	1	2	2	1

Table 11.2: The ordering (Curie) temperatures for the $S = 1/2$ nearest-neighbor quantum Heisenberg ferromagnet (in units $T_c/|J_1|$) (columns 2 and 3) and its corresponding classical ($S \to \infty$) model (in units of $T_c/[|J_1|S(S+1)]$) (columns 5 and 6) on the Pyrochlore (Pyro) and simple cubic (SC)lattices as obtained by PFFRG and compared with estimates obtained from quantum Monte Carlo (QMC), classical Monte Carlo (CMC), high-temperature expansion (HTE), rotation-invariant Green's function method (RGM), and random-phase-approximation (RPA). The fact that $T_c^{\text{pyro}}/T_c^{\text{SC}} < 1$ can be attributed to finite-temperature frustration effects [221]. We also quote the result in the mean-field approximation (MFA), which is insensitive to the difference between the Pyrochlore and simple-cubic lattice, since it depends only on the coordination number.

[a] We adopt the convention of single-counting of bonds in eq. (11.1), and thus employ the formula $T_c/|J_1| = \frac{1}{3}zS(S+1)$, where z is the coordination number.

The transition from DT to MMS order is for $S = 1/2$ found at $J_2/J_1 = -0.347(2)$, placing the phase completely in the classical domain of MMS order. Its extent is also severely reduced to about one-third of the classical phase, confining the phase to a small slice in the phase diagram Figure 11.3(a). The susceptibility profile, taken at the point $J_2/J_1 \approx -0.335$ marked therein, shown in Figure 11.7(e) shows Bragg peaks at incommensurate wave vectors, as in the classical model, which are, however, shifted compared to their classical values. The profile is shown at the Nèel temperature $T_c/J = 0.39(2)$, where the RG flow of the susceptibility at the dominant wave vector shows an instability (see Figure 11.8(a)).

The MMS phase extends down to $J_2/J_1 = -0.326(2)$, where a transition to CS order takes place. For $S = 1/2$ its extent is comparable to the classical one, but shifted partially into the classically FM phase region. Its dominant Bragg peak is located on the line connecting Γ and L point in reciprocal space, as can be seen in Figure 11.7(f) for $J_2/J_1 = -0.24$, but substantially smeared out in reciprocal space due to quantum fluctuations. Additionally, the instability in the corresponding RG flow (Figure 11.8(a)) is extremely weak. Both these facts hint at a certain "weakness" of the CS order, analogous to the cuboctahedral orders on the Kagome lattice with longer-ranged Heisenberg interactions [46, 195], which also display only feeble, i.e. not well pronounced, instabilities in their RG flow [123, 131].

Lowering AF J_2 even further, the now dominant FM J_1 takes over, driving a transition at $J_2/J_1 = -0.153(5)$ into the ferromagnetically ordered phase. As the FM state, being an exact eigenstate of the Hamiltonian, is not affected by quantum fluctuations, these can make the CS order favorable over the FM one, by lowering this state's energy. That this indeed is the case is signaled by the shift of the phase boundary between these two states into the classically FM domain. This had been predicted before [126, 179] and was also the case in the BCC lattice, see Section 10.2. For the pure NNFM $J_2 = 0$, the RG flow of the susceptibility in Figure 11.8(a) shows a clear instability at the critical (Curie) temperature $T_c/|J_1| = 0.77(4)$, which compares well with the Quantum Monte Carlo value of $T_c/|J_1| = 0.718$ [221] within two error bars. In Table 11.2 we compare this value with additional methods, showing a similarly good agreement. Furthermore, the Curie temperatures on the simple cubic lattice are given, which, as the Pyrochlore lattice, has a coordination number $z = 6$, but, due to being a Bravais lattice, is bipartite. The Curie temperature, both

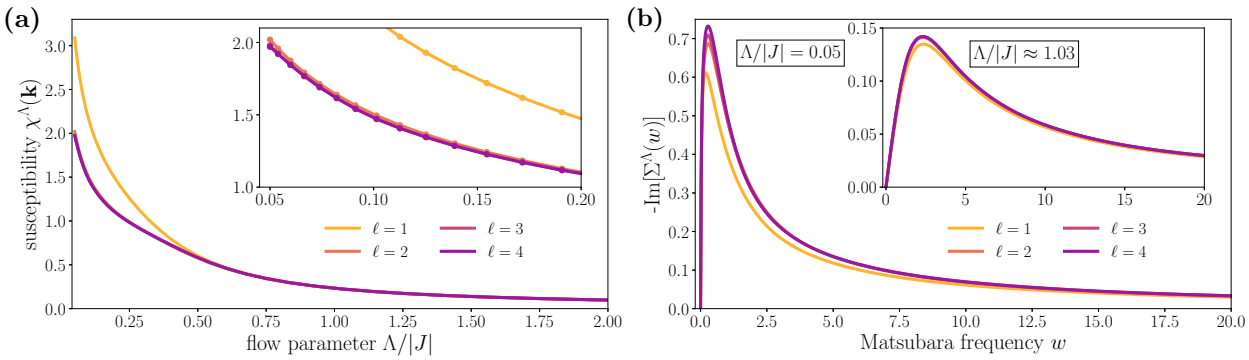

Figure 11.9: (a) Susceptibility flows for the Pyrochlore NNAF at the momentum with carrying the largest spectral weight for loop orders $\ell = 1$ through $\ell = 4$, showing rapid convergence and significant reduction of the susceptibility. (b) Self-energy evolution with increasing loop order, showing excellent convergence for high scales $\Lambda \sim |J|$, while convergence especially around the maximum is worse in terms of height and location of the peak for small $\Lambda/|J|$, indicating slower convergence on the vertex level in line with the findings in Reference [140]. Figure reproduced from Reference [139].

in the classical and extreme quantum $S = 1/2$, is always lower for the Pyrochlore than the simple cubic lattice, which can be attributed to *finite temperature* frustration effects [173, 221, 226, 229, 230].

Apart from the dominant Bragg peak at the Γ point, the spin susceptibility in Figure 11.7(g) clearly shows the subdominant peaks at the L points, which are due to the sublattice structure of the Pyrochlore lattice. Naturally, the FM phase spans from its boundary at $J_2/J_1 = -0.153(5)$ throughout the whole quadrant of the phase diagram, where both J_1 and J_2 are FM and, as in the classical case, is stable against quite sizeable AF J_1 for FM J_2. From PFFRG we find the phase boundary between FM and Kawamura order at $J_2/J_1 \approxeq -1.09$, slightly lower compared to the classical value, which we again attribute to the lack of energy corrections due to quantum fluctuations in the FM phase.

The dominant wave vector within the Kawamura phase is found to vary slightly throughout the phase, but remains close to $2\pi(5/4, 5/4, 0)$. At $J_2/J_1 = -0.634$, as marked by a black disk in Figure 11.3(a), the RG flow shown in Figure 11.8(a), shows a very weak signature of an instability around $c/J = 0.54(2)$. The susceptibility at this point, Figure 11.7(h), also shows a significant smearing of the dominant and subdominant Bragg peaks, both signaling a weak order prone to being destabilized by further range interactions, as we will discuss in Chapter 14.

Increasing the spin length to $S = 1$, the quantum phase diagram remains qualitatively similar to $S = 1/2$, see Figure 11.3(a) and (b), only showing quantitative differences such as shifts in the phase boundaries and precise location of ordering vectors in reciprocal space, but the qualitative discussion remains unchanged. Increasing S further, the quantum phase diagram evolves towards the classical one, with $S = 3/2$ already only showing marginal differences in Figure 11.3(c), most notably the absence of a paramagnetic phase.

11.3 Nearest-neighbor antiferromagnet in multi-loop

As already explicated in Section 11.1, the ground state of the $S = 1/2$ NNAF on the Pyrochlore lattice is still a highly debated problem. Latest simulations employing the density matrix renormalization group point towards a state, in which inversion symmetry is spontaneously broken [216]. At the same time both unconstrained many-variable variational Monte Carlo [217] and PFFRG [117] point towards a state with not only inversion but also C_3 rotational symmetry breaking[1].

[1] In Reference [117] a sole breaking of C_3 rotations, while leaving inversion symmetry intact, is also supported by the data.

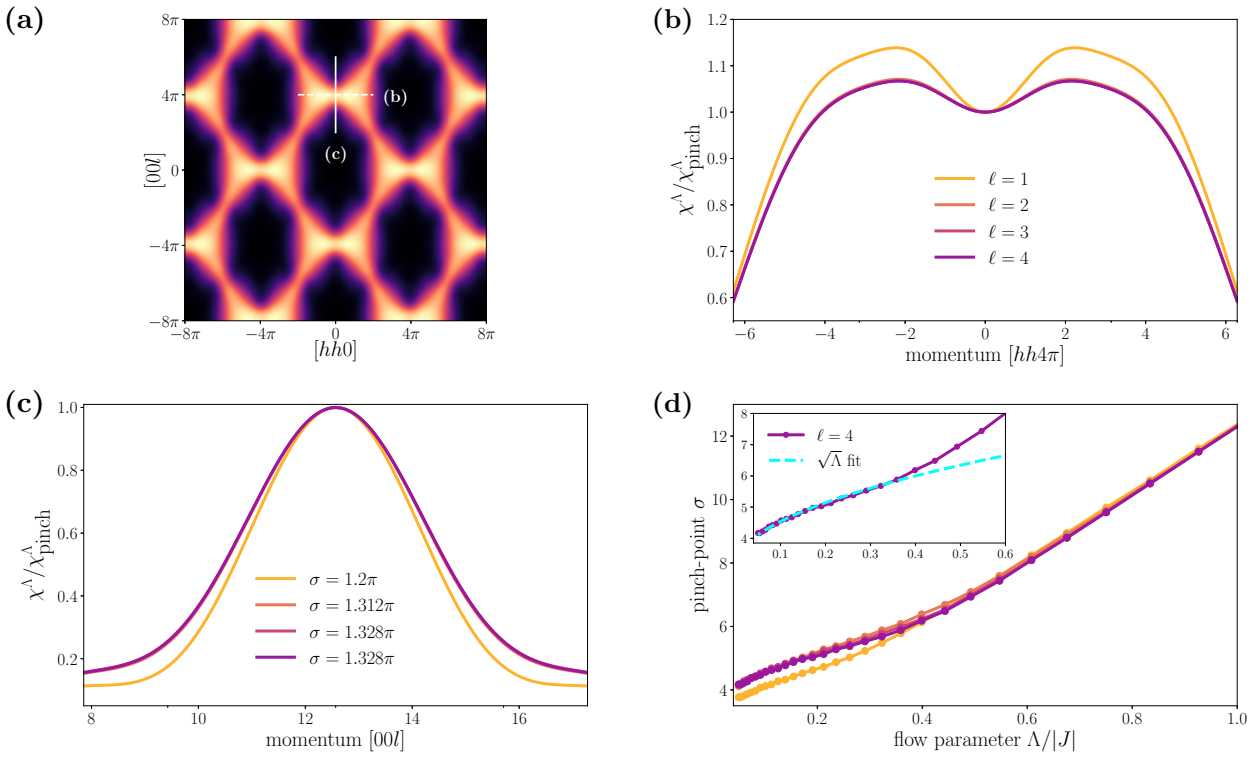

Figure 11.10: (a) Susceptibility profile at $\Lambda = 0.05|J|$ in the $[hhl]$ plane for $\ell = 4$, showing the characteristic bowtie pattern of the Pyrochlore NNAF. (b) Cut along the bowtie in the $[hh4\pi]$ direction as indicated by the dashed horizontal line in (a). (c) Line profile perpendicular to the bowtie along the $[00l]$ direction as indicated by the solid vertical line in (a) with the respective full-width-at-half-maximum σ, which increases with inclusion of higher loops, signifying enhanced quantum fluctuations. (d) Flow of σ for different loop orders. The inset shows σ (for $\ell = 4$) at small values of $\Lambda/|J|$ following a $\sqrt{\Lambda}$ behavior, as found in the classical limit [52], while being linear for large Λ. Figure reproduced from Reference [139].

In PFFRG calculations, a symmetry breaking tendency has to explicitly be included and can subsequently be probed for by tracking the response of the RG flow to this breaking [31, 117]. This procedure, however, can only probe for predefined symmetry breaking patterns, thus spoiling the unbiased nature of PFFRG. Using the symmetry respecting formulation we cannot distinguish these paramagnetic phases from each other, but at least at $\ell = 1$ loop level, a smooth flow of the susceptibility was found throughout the whole BZ, indicating a paramagnetic behavior even in the symmetric case [31].

Employing multi-loop PFFRG, we find, that this result is robust with respect to the inclusion of higher loop corrections. From the RG flows of the susceptibility shown in Figure 11.9(a), we find, that firstly already at $\ell = 4$ loop convergence for the flow is reached, but also the RG flows are smooth down to the lowest simulated scale Λ, providing strong evidence for a quantum paramagnet even under inclusion of higher loop corrections. On the level of the self-energy, the loop-convergence is dependent on the renormalization scale Λ, with convergence becoming harder to achieve for small scales (see Figure 11.9(a)), which was also found in Reference [140]. The susceptibility profile in this phase is distinctly characterized by a bowtie pattern [52] in the $[hhl]$ plane in reciprocal space, which develops sharp singularities at $\boldsymbol{k} = 2\pi(0, 0, 2)$, called pinch points, in the $T = 0$ limit of the classical model. These features directly reflect dipolar spin correlations in this paramagnetic phase [231, 232], direct evidence of a cooperative paramagnetic Coulomb phase [233], which has been argued to arise from the ice-rule eq. (11.4) for the classical NNAF [52, 186, 187].

Due to quantum fluctuations, it is impossible for the $S = 1/2$ to feature vanishing variance of the magnetization on every tetrahedron. Therefore, the ice-rule will be violated by spin fluctuations, smearing out the pinch points, rounding off their sharp peaks, as seen in Figure 11.10(a) at the $\boldsymbol{k} = 2\pi(0, 0, 2)$ and symmetry-related points. The finite width of the pinch point perpendicular to the bowtie then serves as a measure for the net magnetization on the tetrahedra, i.e. the violation of the ice-rule [31, 196, 198, 201, 206, 234–236]. In Figure 11.10(c) we show the relevant cuts along the $h = 0$ line (vertical white line in Figure 11.10(a)) for multiple loop orders. Here we find, that the width of the pinch point, given as the full-width-at-half-maximum σ increases with increasing loop order ℓ, converging at $\sigma = 1.328\pi$ for $\ell = 4$. This suggests, that the inclusion of higher loops in the PFFRG flow *enhances* the effect quantum fluctuations in the Pyrochlore Heisenberg AF. Tracking σ over the flow, as shown in Figure 11.10(d), reveals a monotonical reduction of σ when lowering Λ, serving as an effective temperature. At lowest Λ, we remarkably find σ to obey a $\sqrt{\Lambda}$ behavior, as found in the classical model [52].

Taking cuts along the bowties, i.e. perpendicular to the so far discussed direction (horizontal white line in Figure 11.10(a)), we find, that the maxima in the susceptibility are located symmetrically to the pinch points, but not right at these points. This finding is in agreement with Reference [196], but has to be contrasted to recent finite-temperature matrix product state studies, which locate the maxima of the equal time structure factor at the pinch points at $\boldsymbol{k} = (0, 0, \pm 4\pi)$ [216, 236]. These however suffer from the fact, that most geometries considered there do not preserve the lattice symmetries, rendering their thermodynamically extrapolated result unreliable. Rotation-invariant Green's function method [201] and diagrammatic Monte Carlo simulations [198] find an essentially constant intensity across the bowtie, adding a third scenario to the list of possible intensity distributions. All these different patterns likely correspond to different spin liquid mean-field ansätze [237], rendering it even more important to accurately resolve the susceptibility in reciprocal space accurately, to unambiguously identify the nature of the ground state of the Pyrochlore NNAF. This, in turn, also shows the relevance of the multi-loop corrections to PFFRG which have been shown here to quantitatively change the spectral distribution of the susceptibility.

J_1-J_3 Heisenberg model on the simple cubic lattice in multi-loop

In Section 11.3 we have established, that in the disordered NNAF on the Pyrochlore lattice the multi-loop corrections to PFFRG enhance the effects of quantum fluctuations, leading to quantitative changes in the susceptibility profile, most notably a smearing of the pinch points. This specific case, although promising rich physics due to the absence of long-range order in its ground state, can however not answer, how multi-loop corrections will affect the PFFRG flow within ordered phases. As a test bed to probe for this influence, we consider the simplest geometry for a 3D quantum magnet, the $S = 1/2$ Heisenberg model on the simple cubic lattice. In addition to AF NN interaction $J_1 > 0$, we include a NNN coupling J_3 as shown in Figure 12.1.

As long as J_3 similarly is taken to be AF, the lattice remains unfrustrated and bipartite, i.e. can be decomposed into two simple cubic lattices, which are coupled by AF interactions. These are sufficient conditions for the ground state to realize a Néel order, in which neighboring spins are aligned antiparallel. A FM J_3, on the other hand, parametrically frustrates the nearest-neighbor model, leading in the classical $S \to \infty$ to a phase transition from staggered Néel towards collinear order at $J_3/J_1 = -0.25$.

This, on one hand, enables us to compare to quantum Monte-Carlo (QMC) simulations in the unfrustrated regime, which have found relatively large ordering temperatures of $T_c/|J| \sim 1$ [125, 238] with $|J| = (J_1^2 + J_3^2)^{1/2}$, a fact already reproduced at one-loop level in PFFRG [125]. In the frustrated regime, QMC calculations are not feasible due to a sign problem, which would to exponentially long computation times to find reliable results. PFFRG on the other hand, is still applicable, allowing us to probe for the effects of quantum fluctuations on the position of the phase boundary.

Focussing on the $J_3 = 0$ point first we show the influence of varying loop orders on the susceptibility flow in Figure 12.2(a). At one loop level, we find a divergence at $\Lambda_c/|J| \approx 0.86$[1], with the real space correlations at this point (see Figure 12.2(b)) clearly indicating antiferromagnetic Néel order, in line with the findings in References [238] and [125]. Including higher loop orders into the flow, this picture changes, and only a slight shoulder replaces the divergence in the susceptibility flow for loop level $\ell > 1$ up to $\ell = 6$, but still in close vicinity to the $\ell = 1$ divergence. Additionally, a convergence in loop order is not possible below $\Lambda_c/|J| \approx 0.85$, where also numerical errors in the differential equation solver were growing relatively large.

We attribute this lack of loop convergence to the onset of long-range magnetic order. Indeed, a complete convergence at finite loop order would be surprising, when interpreting multi-loop PFFRG form the view of a large-S extension, as discussed in Section 7.10.1. On $\ell = 1$ level, as shown in eq. (7.66), the leading contributions in a large-S expansion

[1] A conversion to Temperature using the mean-field argument outlined in Section 7.10.1 is not valid here, as for multi-loop calculations a smooth cutoff is used, invalidating the conversion factor of $\pi/2$.

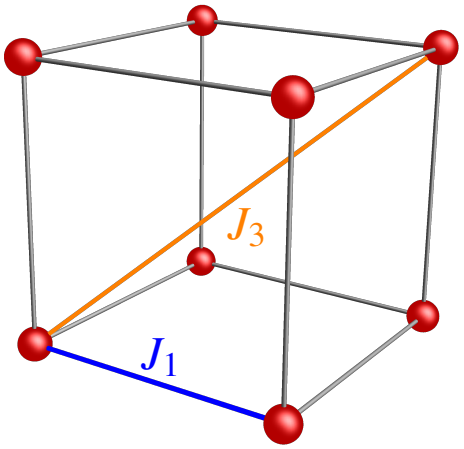

Figure 12.1: Unit cell of the simple cubic Bravais lattice. The NN (J_1, blue) and NNN (J_3,orange) couplings are shown by exemplary exchange paths. For AF J_1, AF(FM) J_3 is parametrically unfrustrated (frustrated).

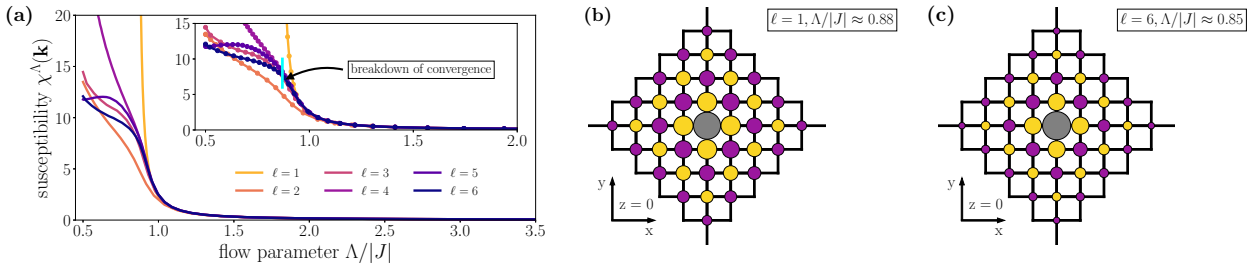

Figure 12.2: (a) The susceptibility flow for the NNAF at the ordering wave-vector $\boldsymbol{k} = (\pi, \pi, \pi)$ displays a divergence at $\ell = 1$ loop level, which is rounded off for $\ell > 1$. Here onset of order is marked by a failure of loop convergence at $\Lambda/|J| \approx 0.85$ (point, where deviation between $\ell = 5$ and $\ell = 6$ exceeds 5%). Real space correlations in the $z = 0$ plane at the point of flow breakdown for (b) $\ell = 1$ and (c) $\ell = 6$ normalized to the reference site in gray. Purple/Yellow indicate positive/negative correlations, clearly showing Néel order. Figure reproduced from Reference [139].

are constituted by the RPA diagram in the t-channel, being of $O(1)$, while all other $\ell = 1$ terms are subleading with $O(1/S)$.

Constructing the multi-loop extension according to the iterative scheme devised in Chapter 8, additional $O(1/S)$ terms are obtained when inserting the $\ell = 1$ t-channel terms into subleading $O(1/S)$ s- and u-channel diagrams and vice versa. All other terms in the $\ell = 2$ expansion lead to $O(1/S^2)$ terms as subleading $\ell = 1$ contributions from the s- and u-channel as well as the chalice diagrams of the t-channel are inserted back into these subleading diagrams, but of another channel.

Additional $O(1/S)$ terms are subsequently generated for $\ell = 3$ by inserting the leading $\ell = 2$ t-channel terms in the central part contribution to the t-channel. This completes this order of $1/S$, as these terms have to be inserted back into subleading diagrams in $\ell = 4$ and higher. Additionally, further subleading terms are generated from the remaining diagrams at $\ell = 3$.

As the $S \to \infty$ limit is exact already for $\ell = 1$[110, 148], all multi-loop contributions have to subleading in $1/S$ consequently vanish in the classical limit. At finite S, however, the corrections from multi-loop constitute an incomplete $1/S$ expansion, where every loop level adds additional subleading terms in the large-S expansion, but, as can be seen from $O(1/S^2)$ terms for $\ell = 2$ and $\ell = 3$, any given loop level truncation will only capture an incomplete

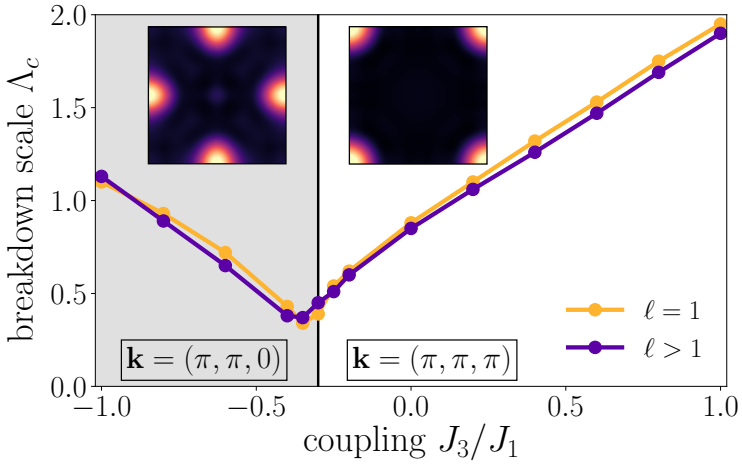

Figure 12.3: J_1-J_3 phase diagram and critical scales Λ_c on the simple cubic lattice from one- and multi-loop ($\ell \leq 6$) PFFRG. The quantum phase transition at $J_3/J_1 = -0.3$ (black line) from the $\boldsymbol{k} = (\pi, \pi, \pi)$ Néel to the $\boldsymbol{k} = (\pi, \pi, 0)$ collinear order is shifted compared to its classical value $J_3/J_1 = -0.25$. Insets show the respective susceptibilities for $k_z = \pi$. The breakdown scales Λ_c, though slightly shifted for higher loops, qualitatively show consistent behavior, with a suppression of Λ_c around the phase transition. Figure reproduced from Reference [139].

set of diagrams of a given order in $1/S$, rendering this expansion inherently inconsistent. This is in contrast to the findings of multi-loop functional renormalization group (FRG) for itinerant systems, where due to the perturbative nature of the coupling strength [91, 239], loop order is equivalent to an expansion in terms of this small parameter, rendering it controlled even at a finite loop truncation [81, 90]. A similar argument holds for the $1/N$ expansion for a SU(N) generalization of the spins discussed in Section 7.10.2, with the u-channel being the leading contribution in this case, swapping its role with the t-channel in the large S case.

Therefore, there are only two limits of the multi-loop expansion, that can be regarded as physically consistent and relevant: Firstly, the case $\ell = 1$, which includes the relevant leading contributions for both magnetic ordering and disordering tendencies to faithfully reproduce the large-S and large-N limits. The consistency is guaranteed by means of the Katanin substitution implemented in the $\ell = 1$ calculations. Secondly, the fully converged case for some $\ell > \ell_{\text{conv}}$, where the multi-loop corrections to PFFRG have converged and reproduce a solution to the parquet equations. The loop level ℓ_{conv}, where this happens, can however turn out to be infinite, i.e. multi-loop fails to converge.

Considering, that in the Pyrochlore case in Section 11.3, loop convergence we found to be reached already at $\ell = 5$, even at RG scales Λ, which are an order of magnitude smaller than $\Lambda_c/|J| \approx 0.85$ found here, the lack of loop-convergence cannot be attributed to a methodological or numerical deficiency. We, therefore, conclude, that in the magnetically ordered case, the large contributions from the t-channel found already in the $\ell = 1$ case, spoil loop convergence around the ordering scale.

We, therefore, regard this failure of loop convergence as an indicator for the onset of long-range magnetic order in the multi-loop calculations. The correlations computed at a scale $\Lambda \gtrsim \Lambda_c$, shown in Figure 12.2(c), are still indicative of a Néel order, but decay faster with distance than the one in the $\ell = 1$ case (cf. Figure 12.2(b)).

Having established the lack of loop convergence as an indicator for long-range magnetic order, we now turn to finite J_3, obtaining a coarsely scanned phase diagram for both AF $J_3 > 0$ and FM $J_3 < 0$, shown in Figure 12.3. The breakdown scales Λ_c defined for $\ell = 1$ by the point at which the flow shows a divergence, as well as $\ell > 1$, where multi-loop seizes to converge, show a qualitatively similar behavior, with the multi-loop critical scales, for the most

part, being lowered with respect to $\ell = 1$. Around the phase transition from the (π, π, π) ordered Néel phase to the collinear order, characterized by wave vector $(\pi, \pi, 0)$, which we locate for spin $S = 1/2$ at $J_3/J_1 = -0.3$, we find a suppression of Λ_c, which we attribute to the competition of the two phases.

The only light shift of phase boundary from the classical value of $J_3/J_1 = -0.25$ in the classical to $J_3/J_1 = -0.3$ in the quantum model indicates, that quantum fluctuations have little influence on the nature of the ordered states in this model. At the same time, the excellent agreement between one- and multi-loop PFFRG in both critical scales Λ_c and phase boundary means, that higher loop corrections to the ordered phases, at least in this mildly frustrated model, are almost negligible. This instills confidence in the analysis of magnetic systems using one-loop PFFRG in literature [30–32, 34, 35, 98, 99, 111–123, 125, 127–135, 143, 148, 151, 157, 240–242].

IV

Magnetic ordering and its absence in real material systems

In this part, we study the spiral spin liquid in the diamond lattice compound $MnSc_2S_4$ and the gearwheel spin liquid in the Pyrochlore material $Lu_2Mo_2O_5N_2$.

The contents of this part of the thesis are partially included in References [134] and [33].

CHAPTER 13

Spiral spin liquid in $MnSc_2S_4$

In quantum spin liquids, as introduced in Section 1, the combination of frustration, both geometric and parametric, and quantum fluctuations in the extreme limit of spins with small quantum number prevents the spins from assuming a long-range order.

This, however, is not the only path to achieving a spin liquid behavior. There is a second class of disordered systems, dubbed classical spin liquids, in which even in the large spin limit $S \to \infty$ no long-range order is assumed [188, 189, 243, 244]. Here the suppression of order is not by a fluctuation mechanism of the single spins, but due to an extensive energetical degeneracy of the classical ground states. This allows the system to collectively fluctuate through these configurations, which justifies the notion of a classical liquid behavior. We have already discussed an example for such a classically degenerate system in form of the nearest neighbor (NN)antiferromagnetic (AF) on the Pyrochlore lattice in Chapter 11, where the ice-rule as the sole constraint on the ground state still leaves an extensively degenerate ground state manifold in energy space for the classical model [186, 187, 190].

The existence of an ice-rule, however, is not a necessary condition to realize a classical spin liquid. The interplay of geometry of a lattice and special arrangements of frustrating interactions can as well introduce a macroscopic degeneracy of ground states, which are not connected by a common constraint.

This is for example realized on the three-dimensional (3D) diamond lattice, illustrated in Figure 13.1, a bipartite lattice, constructed from the face-centered cubic (FCC) Bravais vectors, where every lattice point is decorated by a two-site basis. This construction allows an exact solvability of the classical Heisenberg model on this lattice, as discussed in Section 3.2 Including NN and NNN interactions J_1 and J_2 on this arrangement of spins and tuning ourselves to the region, where $\frac{J_2}{|J_1|} > 1/8$ while taking $J_2 < 0$ to be AF[1], we find exactly such a degenerate ground-state manifold [30, 243, 245, 246]. In this regime, the possible ground states occupy a closed surface in reciprocal states, with each of these wave vectors $\boldsymbol{q}$ corresponding to a distinct spiral configuration governed by this vector. This allows the system to collectively move through these degenerate manifold of coplanar spiral-states, which is the reason, this state is dubbed a *spiral spin liquid*. Note, that a similar spiral spin liquid state is found on the two-dimensional (2D) Honeycomb lattice [148, 247, 248].

Relying on a fine-tuning of the interactions, spiral spin liquid states are in general very susceptible to perturbations. Adding additional interactions, e.g. NNN couplings J_3 to the J_1-J_2 spiral liquid, will select a specific spiral configuration, therefore forcing the system into long-range magnetic order. The same can happen by entropic effects, where thermal fluctuations select a specific ground state in an *order-by-disorder* mechanism [249] and thus lift the degeneracy. Indeed, for the diamond lattice spiral spin liquid, a series of phase transitions between different ordered states is found for increasing $\frac{J_2}{|J_1|} > 1/8$ [243]. Similarly, quantum fluctuations for large, but finite, spin have been found to select an ordered state [30]. Both effects destroy the spiral spin liquid, however, when increasing temperature

[1] The sign of J_1 is not important in the J_1-J_2 model, as the change of sign can be undone by flipping all spins on one of the sublattices.

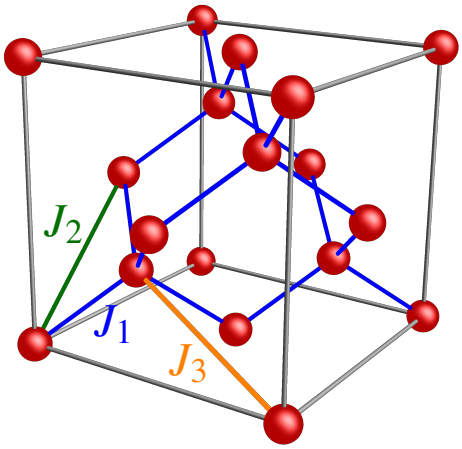

Figure 13.1: Cubic unit cell of the diamond lattice with NN couplings J_1 (blue) within the unit cell, and exemplary next-to-nearest neighbor (NNN) (J_2, green), and next-to-next-to-nearest neighbor (NNNN) couplings (J_3, orange).

above the transition into an ordered state, there may survive an approximate version of the spiral spin liquid state, as order-by-disorder selection is not yet energetically active.

There remarkably exists a material, which shows approximate spiral spin liquid behavior, the A-site spinel $MnSc_2S_4$ [244, 250–254]. In this compound, Mn^{2+} ions form a diamond lattice of spin $S = 5/2$ spins. This large spin moment in turn implies, that quantum fluctuations should be strongly suppressed, meaning the system will behave quasi-classically. Indeed, in its paramagnetic phase above the ordering temperature $T_c \approx 2.3$K [244, 250, 252–254], but well below the Curie-Weiß temperature $|\Theta_{\mathrm{CW}}| = 23$K [250], neutron scattering experiments 2.9K directly show a surface structure in the scattering profile, which is reminiscent of the spiral spin liquid [244].

13.1 Model and classical analysis

Comparing the experimental radius of the spiral surface, in Reference [243], the ration of NN to NNN coupling has been estimated to be $\frac{J_2}{|J_1|} = 0.85$ with J_1 being ferromagnetic (FM). The classical model, however, does not capture the selection of $\mathbf{q} \sim 2\pi(0.75, 0.75, 0)$ magnetic long-range order in experimental data below the transition, but rather predicts a selection of momenta at incommensurate wave-vectors off the high-symmetry $(hh0)$-line [243]. The selected wave-vectors are already visible above the magnetic ordering temperature in the form of higher intensities in the structure factor [244, 252, 254].

In Reference [33], this discrepancy was resolved using *ab initio* density functional theory (DFT) calculations, which reveal a significant presence of NNNN coupling J_3. Here, as a best fit reproducing the experimentally determined Curie-Weis temperature, $J_1 = -0.378$K, $J_2 = 0.621$K and $J_3 = 0.217$ were determined, with the next longer range coupling J_4 being two orders of magnitude smaller than J_3. This gives relative coupling strengths $\frac{J_2}{|J_1|} = 1.64$ and $\frac{J_3}{|J_1|} = 0.57$, substantially larger than proposed in previous studies [243, 245]. This can be explained by the ambiguity of using fitting methods when dealing with competing interactions [33].

Treating the model completely classically for a moment, using the Luttinger-Tisza method, which is exact for a diamond lattice, we first set $J_3 = 0$ to get a better understanding for the effect of the DFT couplings. This pure J_1-J_2 model exhibits a spiral surface, shown in Figure 13.2(a), which crosses the boundary as illustrated in Figure 13.2(b). Compared to the one for the fitted $\frac{J_2}{|J_1|} = 0.85$, it has a slightly larger diameter. Tracking the size of the surface in

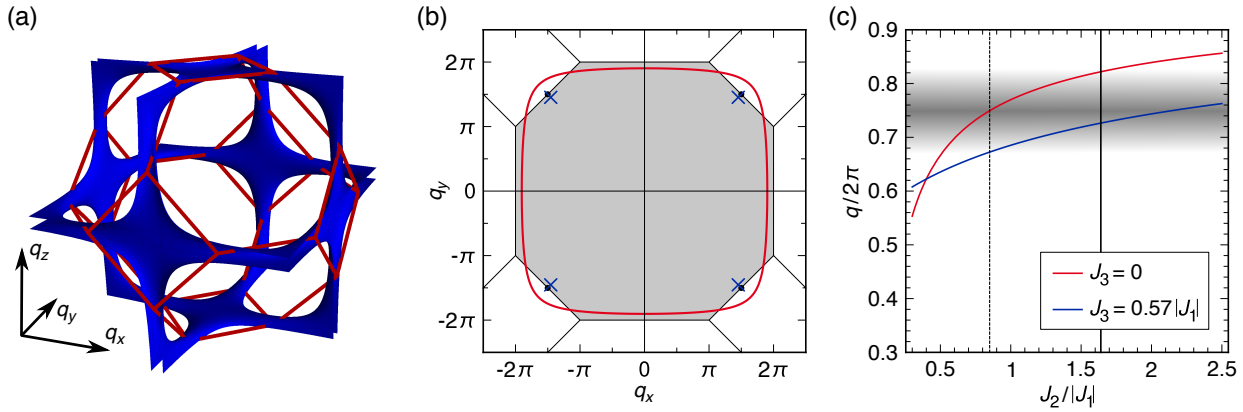

Figure 13.2: (a) Spiral surface of the classical spiral spin liquid on the diamond lattice for $J_2/|J_1| = 1.64$ and $J_3 = 0$ shown in the extended Brillouin zone (BZ). All wave-vectors on this surface form a energetically degenerate manifold of spiral ground states of the model. (b) q_x-q_y cut of this surface shown in red reaching into higher BZs indicated in black. Blue crosses mark the positions of ordering vectors selected by adding NNNN coupling $J_3/|J_1| = 0.57$, black dots the experimentally measured order of $MnSc_2S_4$ at $\boldsymbol{q} \sim 2\pi(0.75, 0.75, 0)$. (c) Size of the spiral surface for $J_3 = 0$ (red) and position of the ordering vector for $J_3/|J_1| = 0.57$ (blue). The shaded area marks the position and width of the experimental Bragg peak at $\boldsymbol{q} \sim 2\pi(0.75, 0.75, 0)$ [244]. Vertical lines indicate the coupling rations of NNN $J_2/|J_1| = 0.85$ from Reference [243] and $J_2/|J_1| = 1.64$ from Reference [33]. Figure reproduced from Reference [33].

Figure 13.2(c), it only increases moderately between $\frac{J_2}{|J_1|} = 0.85$ and $\frac{J_2}{|J_1|} = 1.64$, but still the DFT couplings seem to overestimate its size, even when taking into account experimental uncertainties in the form of Bragg peak widths (see Figure 13.2(c)).

The inclusion of J_3, however, drastically changes this picture: already including infinitesimal AF J_3 selects a $\boldsymbol{q} = (q, q, 0)$ wave vector from the degenerate manifold. Increasing J_3 shifts this vector towards smaller values of q. For the *ab initio* value of $J_3/|J_1| = 0.57$, the Bragg peak is found at ordering vector $\mathbf{q} = 2\pi(0.73, 0.73, 0)$, which is in good agreement with the experimentally measured position. A shift of this wave-vector towards the close by commensurate position found in experiment can be explained by lock-in effects rooted in weak anisotropic magnetic effects possibly present in the real material, which however are not captured by the Heisenberg model. These lead to a modification of the ground state structure to become commensurate with the underlying lattice [245].

13.2 PFFRG results

Having a classical understanding of the model and the importance of the J_3 coupling, we now add thermal and quantum fluctuations via pseudo-fermion functional renormalization group (PFFRG) to determine their role in destabilizing the spiral spin liquid. To this end, we use the analogy between temperature and cutoff discussed in Section 7.10.1, generalized to arbitrary spin S. The corresponding conversion between temperature T and cutoff Λ is then given by [125, 148]

$$\frac{T}{J} = \left(\frac{2\pi S(S+1)}{3}\right)\frac{\Lambda}{J}. \tag{13.1}$$

As in the classical case, we start from the pure NN limit $\frac{J_2}{|J_1|} = 1.64$ and $J_3 = 0$, where we classically find an intact spiral surface. As shown in Figure 13.3(a)-(e), for large temperatures, i.e. renormalization group (RG) cut-offs Λ, the spiral surface is still intact even under inclusion of fluctuations, with both its shape and size hardly changing as a function of temperature, as indicated by the location of the maximal susceptibility along the $(q, q, 0)$ line shown in

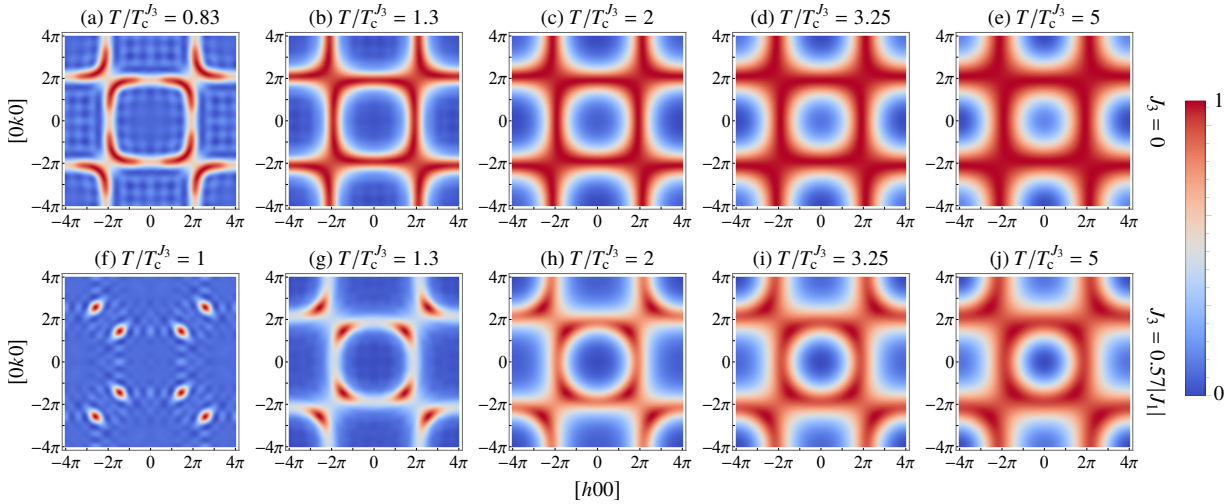

Figure 13.3: Temperature evolution of the susceptibility profiles in the q_x-q_y plane for the pure J_1-J_2 model with $J_2/|J_1| = 1.64$ (top row) and including additional $J_3/|J_1| = 0.57$ (bottom row). Temperatures are given in units of the ordering temperature $T_c^{J_3}$ of the full J_1-J_2-J_3 Hamiltonian including $J_3/|J_1| = 0.57$. For both models and all temperatures the susceptibilities have been normalized to lie in the range from 0 to 1 separately to highlight the prominent features of susceptibilities. The cut along the radial $(q, q, 0)$ direction for profiles is shown in Figure 13.8. For both models the profile changes from a magnetic long-range order selecting $(q, q, 0)$-type points to a closed spiral surface upon increasing temperature, which subsequently smears out giving way to correlations of a high temperature paramagnet. Figure reproduced from Reference [33].

Figure 13.4. Its sharpness, however, as captured by the full-width-at-half-maximum of the susceptibility along this line, significantly increases at lower temperatures. At the critical scale $\Lambda_c^0 = 0.83(1)|J_1|$, we find the surface to split up into segments around the $(q, q, 0)$-type points. The susceptibility along these segments is almost constant, with only a very weak selection of the aforementioned points. Due to the lack of J_3 couplings, the value of q as shown in Figure 13.4(a) is significantly larger than the experimental value of $q/(2\pi) = 0.75$, as expected form our findings in the classical model. The quantum model also does not noticeably shift the location of the surface, compared to its classical location. To quantify the intactness of the spiral surface, we use the ratio of the maximum susceptibility along the $(q, q, 0)$ and $(q, 0, 0)$ directions, shown in Figure 13.5. We find it to approach unity, i.e. a fully restored surface, already at around $\Lambda \approx 2\Lambda_c^0$, which means the spiral spin liquid is rapidly recovered.

Adding $\frac{J_3}{|J_1|} = 0.57$ has a pronounced effect on the selection of the $(q, q, 0)$ state. The susceptibility peaks at $\mathbf{q} = 2\pi(0.719, 0.719, 0)$ visible in Figure 13.3(f) are way more pronounced than for the pure J_1-J_2 model, cf. Figure 13.5, and also shifted slightly towards the Γ point compared to their classical location at $\mathbf{q} = 2\pi(0.727, 0.727, 0)$. The critical scale in turn is higher at $\Lambda_c^{J_3} = 0.99(1)|J_1|$, which means the addition of J_3 interactions reduces the frustration of the model. Furthermore, the restoration of the spiral surface with increasing temperature happens more slowly for full model, compared to $J_3 = 0$ (see Figure 13.5), which is a general trend when gradually varying the strength of the J_3 coupling, as seen in Figures 13.6 and 13.7.

From the ratios of maximal susceptibilities along the $(q, q, 0)$ and $(q, 0, 0)$ direction in Figure 13.5, we see, that at the magnetic ordering transition, the selection of the $(q, q, 0)$ ordering vector is quite pronounced with a diverging ratio. This slowly approaches unity as expected for a spiral spin liquid upon increasing temperature. Indeed, we find a reappearance of the surface at $\Lambda \approx 3\Lambda_c^{J_3}$ in a smooth crossover, as shown in Figure 13.3. The width of this surface, shown in the inset of Figure 13.5, although increasing with temperature, generally is lowered by the inclusion of J_3, implying, that the ordering in the system is more concentrated around the spiral surface compared to $J_3 = 0$, i.e. the spiral spin liquid is well-defined and "intact" for the full model.

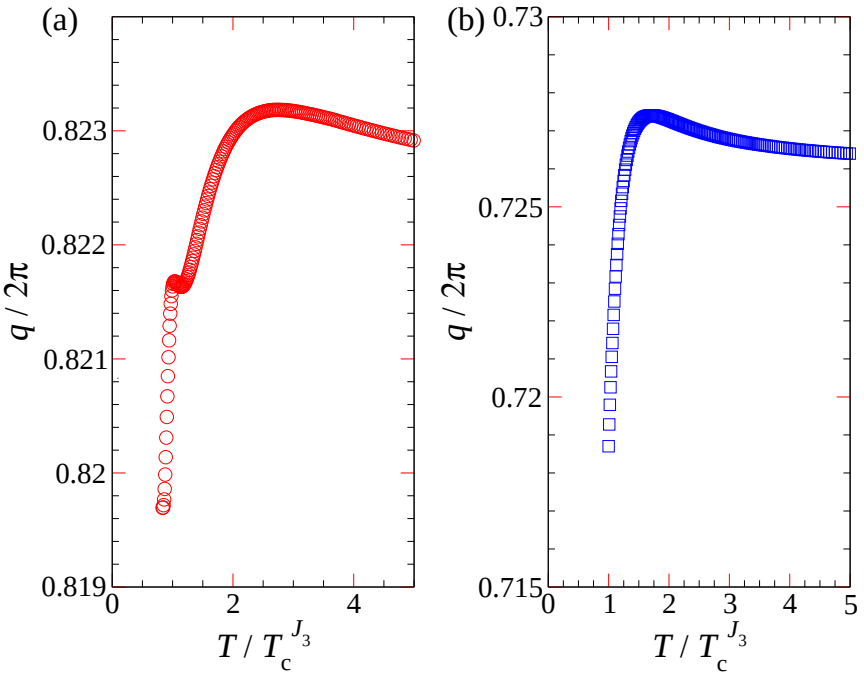

Figure 13.4: Temperature dependence of the peak position along the $(q, q, 0)$ radial direction for the Hamiltonian with $\frac{J_2}{|J_1|} = 1.64$ and (a) $J_3 = 0$ and (b) $J_3 = 0.57|J_1|$. Figure reproduced from Reference [33].

Upon increasing temperature, the spiral surface smears out further when approaching the high-temperature paramagnetic state. The corresponding crossover is reached, when the width of the spiral surface reaches its distance to the one in the neighboring BZ, i.e. the gap between the two maxima approximately located at $2\pi(0.75, 0.75, 0)$ and $2\pi(1.25, 1.25, 0)$ is gapped. Then the individual spiral surfaces are no longer discernible and the spiral spin liquid becomes unstable. For the pure J_1-J_2 model we find this to happen at about $T_{\text{crossover}} \approx 3T_c^{J_3}$, while the inclusion of $J_3 = 0.57|J_1|$ stabilizes the spiral surfaces to even higher temperature $T_{\text{crossover}} \approx 5T_c^{J_3}$. This behavior is illustrated in Figure 13.8.

In total, we summarize the approximate phase diagram as follows: For $T/T_c^{J_3} \leqslant 1$ the model is long-range spiral ordered, with the order melting down in the range $1 < T/T_c^{J_3} \lesssim 3$. Although the susceptibility still is concentrated around the wave-vectors of the long-range order for lower temperature, but the same does not emerge. With increasing temperature, the system's susceptibility develops towards the spiral surface, which is established in the temperature interval $3 \lesssim T/T_c^{J_3} \lesssim 5$. In this regime, the spectral weight of the susceptibility is uniformly distributed along the spiral surfaces, which are clearly discernible. The system, therefore, realizes a stable spiral spin liquid. As the critical temperature of $MnSc_2S_4$ is $T_c = 2\,3\text{K}$, these temperature regimes all lie well below the Curie-Weiss temperature $|\Theta_{\text{CW}}| = 23\text{K}$. This means our calculations confirm the existence of a spiral spin liquid in this material in the temperature range between three and five times the ordering temperature. For high temperatures $T/T_c^{J_3} \gtrsim 5$ the spiral surfaces merge, destabilizing the spiral spin liquid towards a high-temperature paramagnetic phase.

To further assess the relevance of both the DFT model and our calculations for $MnSc_2S_4$, we compared the calculated susceptibility at $\Lambda = 1.33\Lambda_c^{J_3}$ to the experimentally measured spin-structure factor at the corresponding temperature $T = 2\,9\text{K} = 1.33T_c$ from Reference [244]. To make this comparison meaningful, we have to include the magnetic form factor of the Mn^{2+} magnetic moments [255]. This $|\boldsymbol{q}|$ dependent modulation function is due to the extended orbital structure of ions, which influences the neutron scattering, in contrast to the assumption of point-like moments for all

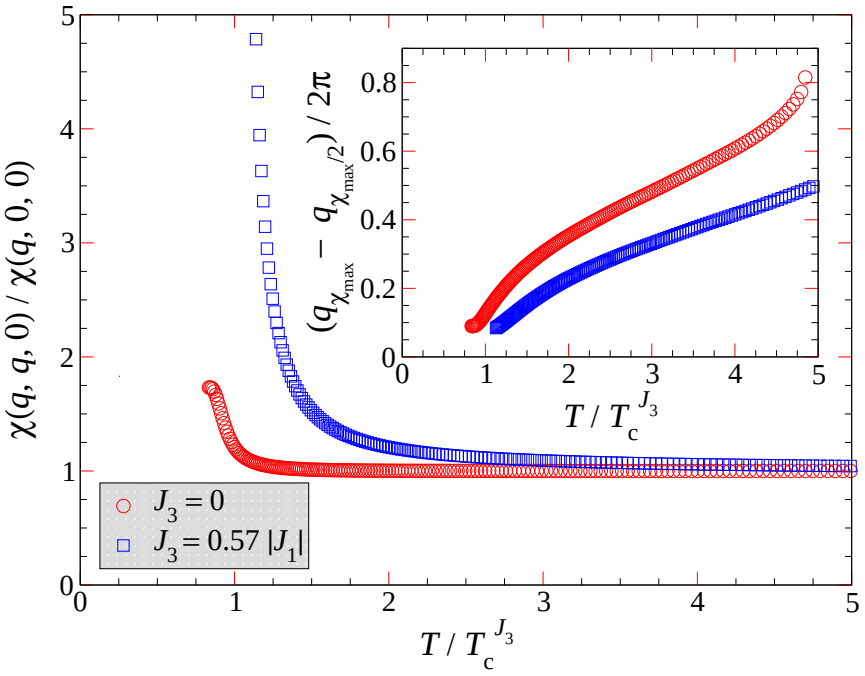

Figure 13.5: Ratio $\chi(q,q,0)/\chi(q,0,0)$ of the susceptibility maxima along the $(q,q,0)$ and $(q,0,0)$ over temperature T, used as a measure of the intactness o the spiral spin liquid, with a value of unity indicating an undisturbed spiral surface. Inset: Temperature dependence of the full-width-at-half-maximum of the susceptibility along the $(q,q,0)$ direction in reciprocal space. Figure reproduced from Reference [33].

presented PFFRG results. It is given by a sum of Gaussians tabulated in Reference [255]. Modulating the calculated susceptibility profile with this factor dampens the spectral weight with increasing $|\boldsymbol{q}|$, as shown in Figure 13.9. As it becomes apparent there, the experimental neutron scattering profile is well reproduced by the PFFRG data, in particular the spiral selection, which is pronounced Modulating the calculated susceptibility profile with this factor dampens the spectral weight with increasing $|\boldsymbol{q}|$, as shown in Figure 13.9. As it becomes apparent there, the experimental neutron scattering profile is well reproduced by the PFFRG data, in particular the spiral selection, which is pronounced at this temperature, as well as the incipient spiral surface already visible.

13.3 Further considerations

We have shown, that the inclusion of sizeable $J_3/|J_1| = 0.57$ in the model Hamiltonian for $MnSc_2S_4$, as predicted by DFT [33], is essential to reproduce the experimental neutron scattering data for this material close to the ordering temperature. Upon increasing the temperature, however, thermal fluctuations restore an approximate spiral spin liquid, which actually is stabilized by the J_3 coupling, as it is found to reduce the width of the spiral surface, allowing it to exist over an even larger temperature range than in a pure J_1-J_2 model.

The Heisenberg Hamiltonian we consider, being rotationally symmetric, does not determine the spiral plane with respect to the lattice orientation. Including small anisotropic interactions like dipolar couplings, expected to exist in a real material [244, 245], may lift this degeneracy. However, they are estimated to have a strength of only a few percent relative to the NN coupling [244], rendering them only relevant close to the phase transition towards magnetic order.

In contrast, below the critical point, such couplings may explain the observed ordering process involving multiple intermediate phases, such as sinusoidal collinear, incommensurate, and helical spin orders [244]. We however cannot probe for these with PFFRG, as currently we are not able to flow into symmetry broken phases.

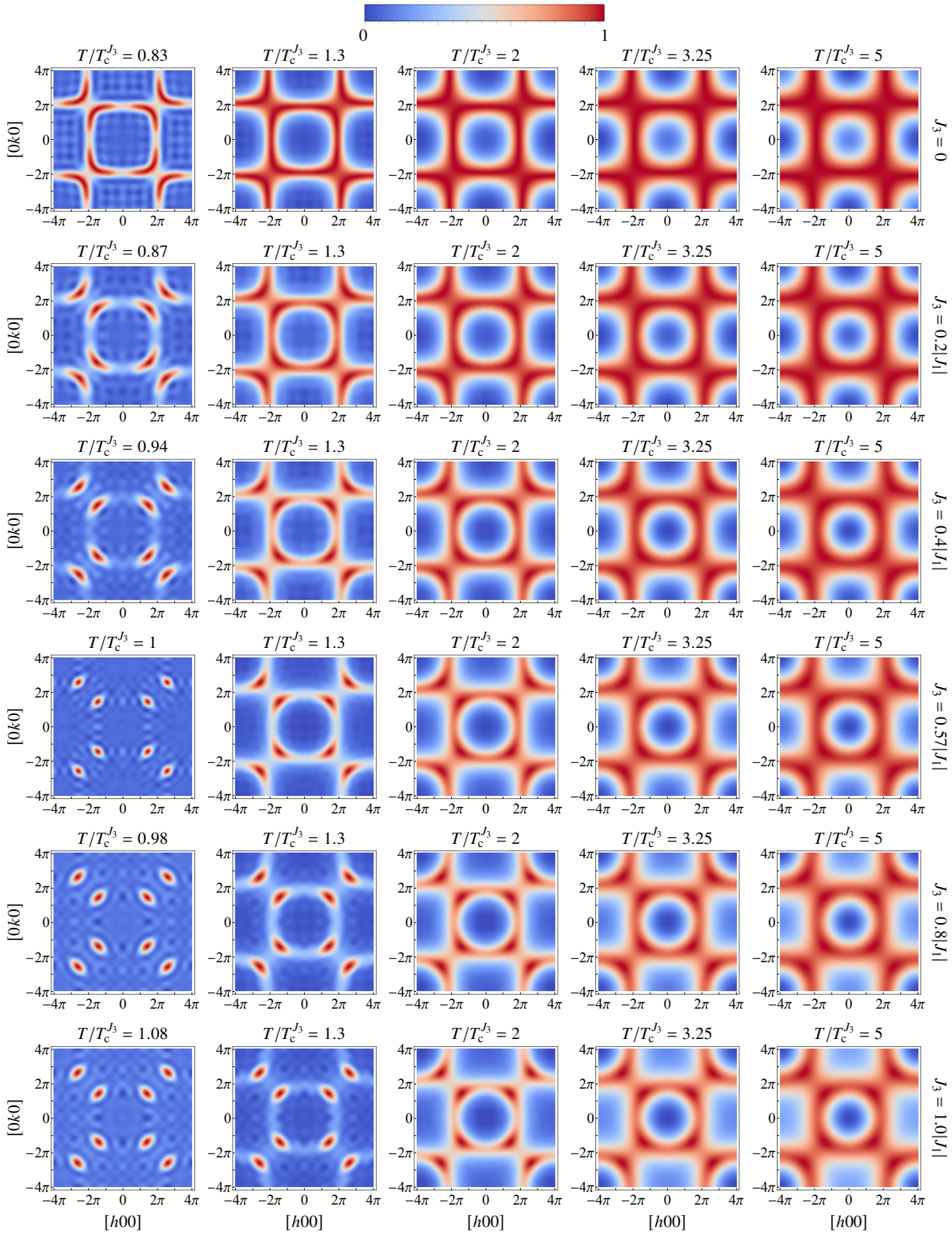

Figure 13.6: Temperature evolution of the spin susceptibility of the diamond model Hamiltonian with fixed ratio $J_2/|J_1| = 1.64$ plotted in the q_x-q_y-plane. Different rows correspond to different ratios of $J_3/|J_1|$, with $J_3/|J_1| = 0.57$ being the DFT model parameter for $MnSc_2S_4$. Temperatures are measured with respect to the critical temperature $T_c^{J_3}$ of this model. Each panel has to be rescaled to have susceptibility values lying between 0 and 1 to highlight the relevant features. Figure reproduced from Reference [33].

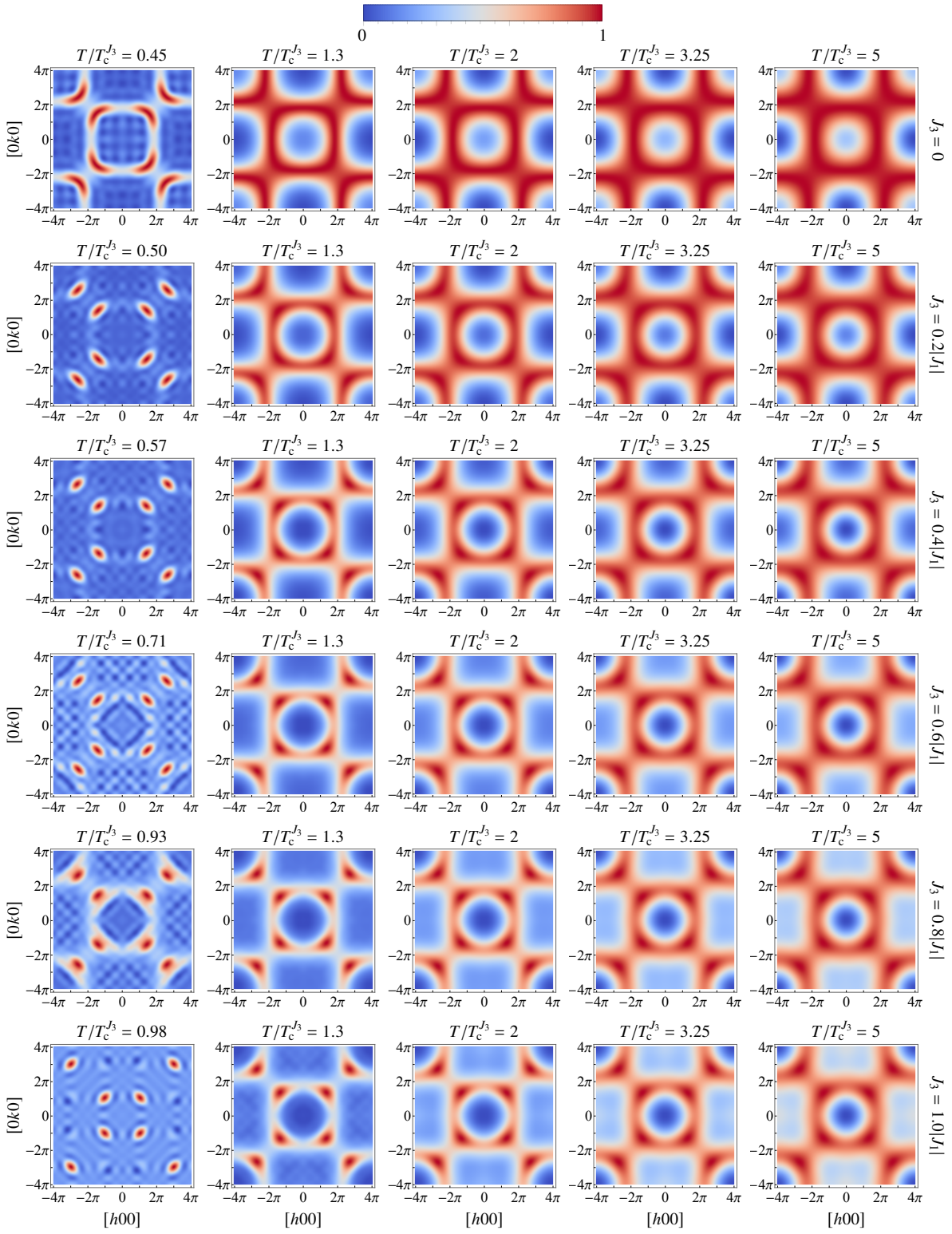

Figure 13.7: Temperature evolution of the spin susceptibility of the diamond model Hamiltonian with fixed ratio $J_2/|J_1| = 0.85$ plotted in the q_x-q_y-plane. Different rows correspond to different ratios of $J_3/|J_1|$, with $J_3/|J_1| = 0$ corresponding to the estimation of model parameters from the radius of the spiral surface for $MnSc_2S_4$ performed in Reference [243]. Temperatures are measured with respect to the critical temperature $T_c^{J_3}$ of the DFT model Hamiltonian for this material with $J_2/|J_1| = 1.64$ and $J_3/|J_1| = 0.57$. Each panel has to be rescaled to have susceptibility values lying between 0 and 1 to highlight the relevant features. Figure reproduced from Reference [33].

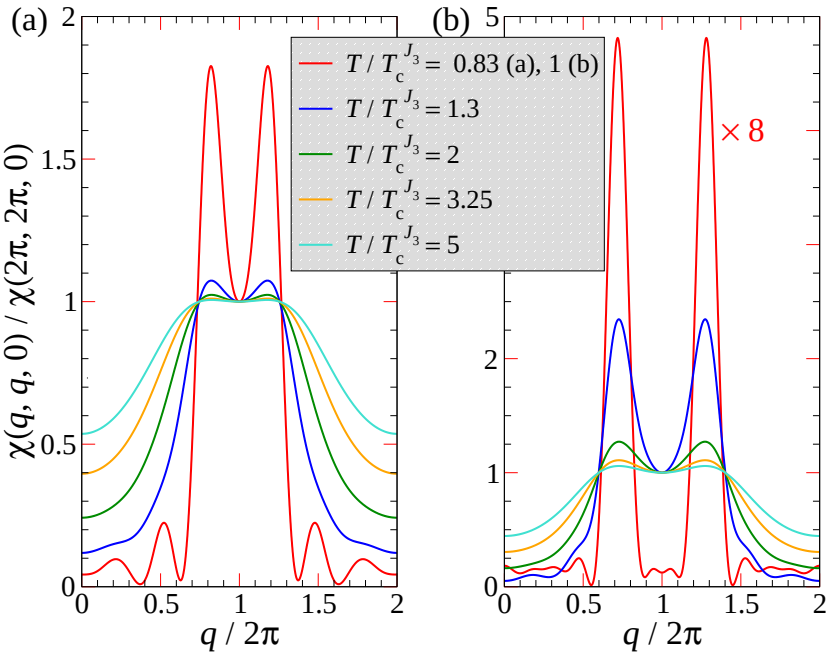

Figure 13.8: Radial $(q, q, 0)$ cut through the susceptibilities at different temperatures for the diamond Hamiltonian with $J_2/|J_1| = 1.64$ and (a) $J_3 = 0$ and (b) $J_3 = 0.57|J_1|$. Figure reproduced from Reference [33].

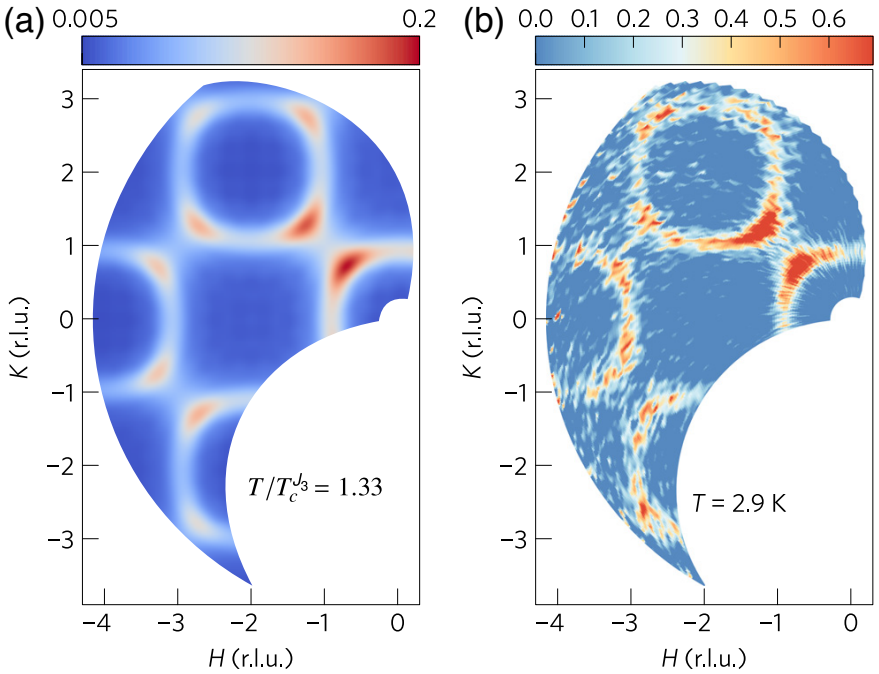

Figure 13.9: Comparison of (a) the spin structure factor calculated from PFFRG modulated wit the magnetic structure factor of Mn^{2+} taken from Reference [255] and (b) measured structure factor from neutron scattering, reproduced from Reference [244] in the q_x-q_y plane for $T/T_c^{J_3} = 1.33$ and $T = 2.9$K, respectively. Susceptibilities are calculated in units of $1/|J_1|$, experimental data given in arbitrary units. Figure reproduced from Reference [33].

CHAPTER 14

Gearwheel spin liquid in $Lu_2Mo_2O_5N_2$

The Pyrochlore lattice is not only a model system hosting a multitude of ordered, and, most notably, extended quantum paramagnetic phases, as discussed in length in Chapter 11, but also is realized in a plethora of real materials. Most prominently, in so-called *B*-site spinel systems, whit chemical composition AB_2X_4, the B ions occupy a Pyrochlore lattice and can be magnetic, while A is a non-magnetic metal ion and X is either Oxygen or Sulfur [48, 256, 257]. But also other materials feature such a magnetic sublattice [196, 258–265]. However, most of these materials either display a spin freezing akin to spin-glass or develop long-range magnetic order at low temperatures [134, 265].

A notable exception to this observation is the Molybdenum-based Pyrochlore Heisenberg antiferromagnet $Lu_2Mo_2O_5N_2$. In this compound, the Mo^{5+} ions are arranged in a Pyrochlore lattice and carry spin $S = 1/2$ moments, see Figure 14.1(a) for the lattice structure. Experimentally, it does neither show magnetic long-range order nor any signs of other ordering tendencies down to $T^* \approx 0.5$K [263]. This is in stark contrast to its measured Curie-Weiss temperature of $\Theta_{CW} = -121(1)$K [263], which provides evidence for the strongly frustrated nature of the spin interactions in this material.

Taking into account only leading AF NN interaction, one could place the material in the phase diagram Figure 11.3 discussed in Section 11.2. *Ab initio* calculations of Reference [134], however, have shown, that one of the two symmetry-inequivalent NNNN interactions is non-negligible, at 23% of the nearest-neighbor interaction strength. Basing our investigations on the model Hamiltonian

$$\hat{H} = J_1 \sum_{\langle i,j\rangle_1} \hat{\mathbf{S}}_i \cdot \hat{\mathbf{S}}_j + J_2 \sum_{\langle i,j\rangle_2} \hat{\mathbf{S}}_i \cdot \hat{\mathbf{S}}_j + J_3 \sum_{\langle i,j\rangle_3} \hat{\mathbf{S}}_i \cdot \hat{\mathbf{S}}_j + J_d \sum_{\langle i,j\rangle_d} \hat{\mathbf{S}}_i \cdot \hat{\mathbf{S}}_j, \tag{14.1}$$

of Reference [134], where we distinguish the two inequivalent NNNN couplings J_3, which connects two magnetic sites with one additional one in between, and J_d, which crosses an empty Hexagon in the Kagome structure of a [111] cut of the Pyrochlore lattice, see Figure 14.1(b). The relative coupling strength was determined to be $J_2/J_1 = 0.008$, $J_3/J_1 = 0.23$ and $J_d/J_1 = -0.078$. As $J_1 > 0$ is AF, so are J_2 and J_3, while the subleading $J_d < 0$ is a FM interaction.

To determine the influence of the sizeable longer-range interactions on the state, which would be on J_1-J_2 only level a quantum paramagnet, as shown in Section 11.2, we first carry out a classical investigation of the model Hamiltonian eq. (14.1), discussing also the influence of possible additional Dzyaloshinsky-Moriya interactions, which are not diagonal in spin-space. Afterwards, we turn towards the quantum case, employing a PFFRG analysis. The results of both approaches are summarized in Figure 14.2

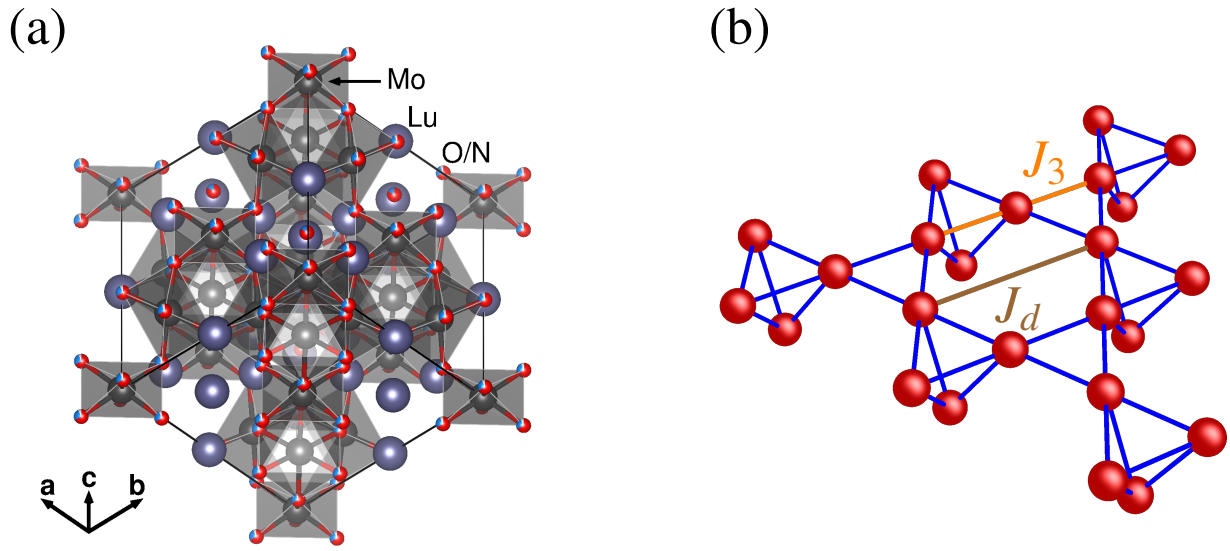

Figure 14.1: (a) Crystal structure of $Lu_2Mo_2O_5N_2$. (b) Slab of the Pyrochlore lattice formed by the Mo^{5+} ions, cut in the [111] plane. The NNNN coupling J_d crosses an empty hexagon in the Kagome lattice formed in this layer, while J_3 with the same length has another ion in between. Figure (a) reproduced from Reference [134].

14.1 Classical limit

As the Pyrochlore lattice features a four-site unit cell, the Luttinger-Tisza method will generically only allow to determine an approximate classical ground state. Therefore, we supplement, as in Section 11.1, our analysis with an iterative minimization calculation.

Using the equivalence of Luttinger-Tisza calculations to the O($N \to \infty$) limit of classical spins discussed in Section 3.3.3, we first investigate the susceptibility in this limit defined by eq. (3.23). It diverges at a critical Néel temperature of $T_N/J_1 \approx 0.625$ at the ordering wave vector $\boldsymbol{k}_{\mathrm{LT}} = 2\pi(1.305, 1.305, 0)$, as marked by an arrow in the full susceptibility profile in Figure 14.2(e), and all symmetry-related points in reciprocal space. This signals the transition from the high-temperature paramagnetic phase into a long-range ordered state.

To confirm the relevance of this approximate susceptibility, we perform an iterative minimization of the classical energy as outlined in 4, where we can take into account the strong spin length constraint $|\mathbf{S}_i|^2 = S^2$ exactly and also allow for spontaneous breaking of the lattice symmetries.

For the ground state of the classical model, using this technique, we find a noncoplanar triple-$\boldsymbol{k}$ structure, which is the superposition of three different spirals. Each of these is controlled by a different incommensurate $\boldsymbol{k}_{\mathrm{o}} = (q, q, 0)$-type wave-vector with $q/2\pi = 1.312$, which is in good agreement with $\boldsymbol{k}_{\mathrm{LT}}$.

Examining the configuration closer, we find, that the spin sum on each tetrahedron is not completely zero, but the energy deviation from the zero spin case is only a few percent of J_1, rendering it energetically insignificant. This implies, that an approximate equivalence between AF J_3 and FM J_2, along the lines discussed in Section 11.1 still holds, which explains the similarities of the state found here to the Kawamura states found in the J_1-J_2 only model, see Section 11.1.

The full susceptibility profile from iterative minimization is shown in Figure 14.2(f). As finite-size effects in conjunction with periodic boundary conditions leads to a splitting of Bragg peaks, the data here is shown after applying a Gaussian smoothing over the peaks. The line cuts through these peaks, shown in Figure 14.2(g) reveal, that there is a breaking of the cubic symmetry inherent to this state: The Bragg peaks n the k_x-k_y and k_x-k_z planes

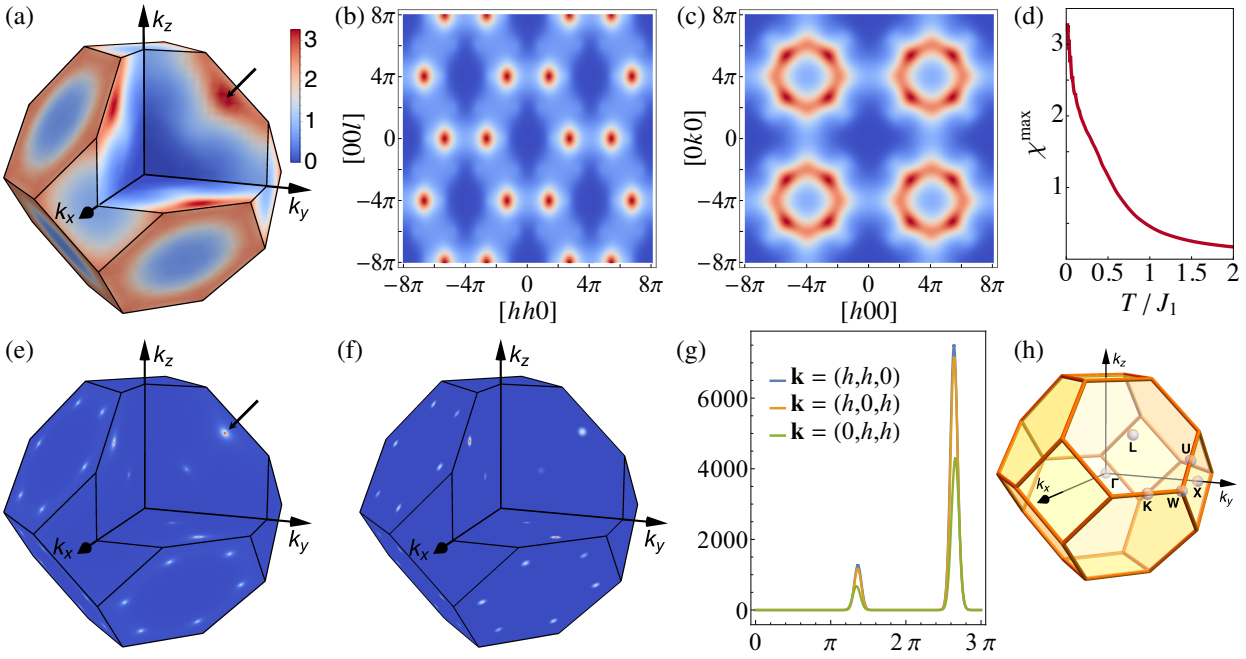

Figure 14.2: Classical and quantum susceptibilities for the model Hamiltonian eq. (14.1) for $Lu_2Mo_2O_5N_2$. The magnetic susceptibility at $T = |\Theta_{CW}|/100$ as obtained from PFFRG for $S = 1/2$ is shown in (a) the fullBZ, (b) the $[hhl]$ plane, where its maxima form hexagonal clusters and (c) the $[hko]$ plane, featuring a characteristic gearwheel pattern. The RG flow of the dominant susceptibility (d) shows no signs of magnetic long-range order. The PFFRG susceptibility can be viewed as an molten version of the classical one obtained from an (e) $O(N \to \infty)$ and (f) iterative minimization calculation, showing distinct Bragg peaks. The (g) cuts through (f) reveal a breaking of the cubic lattice symmetry. (h) BZ of the Pyrochlore lattice, a truncated octahedron, showing the location of high-symmetry points. Figure reproduced from Reference [134].

are of only slightly different height, but roughly twice as high as the one in the k_y-k_z plane. If this feature carries over to the $S = 1/2$ case, it could give rise to a nematic spin liquid [124, 126].

Moreover, the classical magnetic order we find here, is not invariant under a time-reversal operation $\boldsymbol{S} \to -\boldsymbol{S}$, i.e. this cannot be done by a global SO(3) rotation of the spins. This is characteristic of a *chiral* spin configuration, which consequently features a finite scalar spin chirality $\sim \mathbf{S}_i \cdot (\boldsymbol{S}_j \times \boldsymbol{S}_k)$, in this case i, j and k denote three arbitrary positions on any given tetrahedron of the Pyrochlore lattice. This opens up the possibility to carry over to a possible quantum spin liquid phase for the $S = 1/2$ model [203, 204, 266], which would be the first realization of such in a three-dimensional insulator.

To round up our classical discussion, we want to study the influence of a symmetry allowed Dzyaloshinsky-Moriya interaction term of the form $\mathbf{D}_{ij} \cdot (\hat{\mathbf{S}}_i \times \hat{\mathbf{S}}_j)$ [267] off-diagonal in spin space on top of the Heisenberg model Hamiltonian eq. (14.1). The so-called Moriya rules [268] determine that there are only two types of this interaction in the Pyrochlore lattice, dubbed "direct" or "indirect" [269, 270]. The *ab initio* calculations of Reference [134] determine its strength to be of the order of $\sim 0.08{-}0.1 J_1$. However, including such an interaction up to 10% into our minimization calculations, we do not find a significant alteration of the state determined by the pure Heisenberg model eq. (14.1). More precisely, we do not find a shift of the Bragg peak positions within the reciprocal space resolution given by the size of the considered real space lattice and observe only a minor redistribution of weight between the Bragg peaks. This leads us to the conclusion, that the Heisenberg Hamiltonian given in eq. (14.1) already is an adequate description of the system.

14.2 Quantum ground state

To determine the fate of the classical triple-$\boldsymbol{k}$ ground state in the quantum limit of $S = 1/2$ spins relevant for $Lu_2Mo_2O_5N_2$, we employ one-loop PFFRG. The RG flow of the maximal susceptibility in reciprocal space, shown in Figure 14.2(d) shows no sign of divergencies or instabilities down to $T \to 0$, signaling the absence of long-range order in the $S = 1/2$ model, in agreement with measurements on $Lu_2Mo_2O_5N_2$ [263]. The full three-dimensional profile at the lowest simulated temperature $T = |\Theta_{CW}|/100 = 1\,21\text{K}$ is shown in Figure 14.2(a). At this point, which is two orders of magnitude below the Curie-Weiss temperature Θ_{CW}, we find a smeared out spectral weight around the edges of the Brillouin zone, which features slight enhancement at the W points. This interestingly is akin to the spectral eight distribution of the spin liquid state of the $S = 1/2$ AF on the 2D Kagome lattice [25, 123, 271]. Moving away from the boundary of the BZ, we find soft maxima at an incommensurate wave vector $\boldsymbol{k}_Q = 2\pi(1.296, 1.296, 0)$ and symmetry-related points, marked by an arrow in Figure 14.2(a). For a better overview over the momentum structure of the susceptibility, let us turn to the $[hhl]$ plane, as shown in Figure 14.2(b). Here we find, that the spectral weight forms hexagonal clusters [272] with the symmetry-related $\boldsymbol{k}_Q$-points as corners, akin to the spectral distribution experimentally found in $ZnCr_2O_4$ [273]. At the same time, the spectral weight at the pinch-points of the NNAF on the Pyrochlore at $\boldsymbol{k}_{\text{Pinch}} = 2\pi(2, 0, 0)$ and symmetry-related points is strongly suppressed. Following the classical analysis of Reference [218], this redistribution in the susceptibility is due to the non-vanishing NNNN couplings in the model Hamiltonian eq. (14.1) for $Lu_2Mo_2O_5N_2$.

In the $[hk0]$ plane, the diffuse susceptibility profile resembles an arrangement of "gearwheels", which we dub the spin liquid state following Reference [274]. Comparing the classical susceptibility profile in Figure 14.2(e) to the quantum version Figure 14.2(a), one can view the latter as a molten version of the former. Quantum fluctuations diffuse the dominant Bragg peaks at $\boldsymbol{k}_{\text{o}}$ to form the gearwheel structure, with the susceptibility maxima at $\boldsymbol{k}_Q$ being remnants of the classical peaks. Also, the whitish "teeth" of the gearwheels visible in Figure 14.2(c) can be viewed as originating from this melting. The subdominant peaks in the classical model on the hexagonal faces of the Brillouin zone likewise smear out and form uniform rings.

The PFFRG cannot probe for scalar spin chiralities discussed in Section 14.1 due to the absence of six-particle vertices in the RG flow, which would be needed to calculate a three-spin quantity. Therefore, to probe for the possibility of a chiral spin liquid in $Lu_2Mo_2O_5N_2$, a variational Monte Carlo analysis together with a projective symmetry group classification of chiral spin liquids on the Pyrochlore lattice would be called for [275, 276].

CHAPTER 15

Conclusion

In this thesis, we have set out to develop and methodologically as well as pedagogically refine a toolset applicable to the analysis of quantum magnetism on three-dimensional lattices. In Part I, we have discussed the classical $S \to \infty$ limit of spins as an intuitively accessible foundation for the subsequent analysis of quantum spin systems. As an approximate approach to determining the ground state of such classical micromagnetic models, we have introduced the Luttinger-Tisza method. We have discussed the cases, in which the method becomes exact and introduced a connection to the classical large N mean-field not drawn in literature before, which allowed us to extract physically meaningful results even in the realm, where Luttinger-Tisza is only approximately valid. For the determination of the true ground state of such systems, we have additionally introduced the iterative minimization technique.

In Part II we have introduced our main approach to quantum spin systems, the pseudo-fermion functional renormalization group (PFFRG) method. After reviewing the general properties of the pseudo-fermion mapping of spin operators and its consequences for Green's functions, we have laid out the derivation of the functional renormalization group (FRG) for general fermionic models. Combining those two aspects, we arrive at the PFFRG in Chapter 7, which was originally introduced by Reuther [98, 99]. We have both pedagogically reviewed the conventional parametrization of the vertex functions tailored towards pseudo-fermion systems and improved upon it by introducing the natural frequency into the realm of PFFRG. In particular, our scheme possesses well-defined asymptotic behavior at large frequencies, in contrast to the transfer-frequency formulation in previous works. This fact can be used to improve the numerical accuracy in an implementation of the PFFRGflow equations.

In Chapter 8 we then introduced our second important methodological development, the introduction of multi-loop corrections to the PFFRG flow. We give a derivation of the flow equations solely starting from the approximations applied to the standard one-loop flow, which complements the discussion based on the Parquet approximation found in literature [153, 155, 156] and outlined the caveats when applying the corrections to PFFRG.

The following Chapter 9 we devoted to sketching the conventional numerical implementation of PFFRG, commented on its shortcomings and our improvements on that, employing state-of-the-art numerical algorithms. This development has culminated in the open-source package `PFFRGSolver.jl` [129, 162], which has been developed in the course of this thesis in cooperation with Dominik Kiese [139, 162]. It aims at rendering the numerical implementation of multi-loop PFFRG, as developed in this work, accessible to a broader audience, sparing future researchers the overhead of implementing a suitable numerical codebase from scratch.

In Part III of this thesis, we have finally applied the techniques developed in the previous chapters to physical model systems. On the body-centered cubic (BCC) lattice, we establish on analytical grounds the complete magnetic phase diagram up to third-nearest neighbor Heisenberg interactions. Using PFFRG we found, that quantum fluctuations both shift phase boundaries compared to the classical model and, most importantly, destabilize the orders found for $S \to \infty$ in an extended parametric regime. This quantum paramagnetic phase is a candidate region or quantum spin liquid

behavior. In the Pyrochlore Heisenberg model, we also established the classical phase diagram for interactions up to second-nearest neighbors, reproducing and improving upon earlier studies of this model, which, however, only got published as a preprint [38]. Here, we find a plethora of magnetically ordered states, which all survive upon inclusion of quantum fluctuations. Additionally, as in the BCC lattice, in a finite region around the classically disordered nearest-neighbor antiferromagnet, classical order gives way to a quantum paramagnetic regime putatively hosting spin liquid physics. Most notably, this region is also present for increased spin length $S = 1$. The aforementioned NNAFwas chosen as a testbed to check the influence of the multi-loop corrections to PFFRGin a disordered ground state. We show, that in this state lacking magnetic long-range order, loop convergence is achieved already for a moderate number of loops and discuss the quantitative effects of the corrections. As a second test case, we use the J_1-J_3 simple cubic model to also discuss the loop corrections in ordered phases and find, that an ordered is signaled by a lack of loop convergence rather than a divergence in the flow at higher loop orders, which we explain on the grounds of the $1/S$ expansion nature of the multi-loop corrections. The qualitatively unchanged results upon including higher loops instill confidence in the one-loop calculations used in literature.

In the final Part IV we turned our focus towards *ab initio* models for the magnetic interactions in real materials. We showed, that the spiral spin surface found in the diamond lattice compound $MnSc_2S_4$ for temperatures above the ordering transition can be explained on microscopic grounds employing a Heisenberg model up to third-nearest neighbor interactions. Using PFFRG we extracted the temperature evolution of the spiral surface and demonstrate excellent agreement between the calculated structure factor and neutron scattering data. The second material we considered, $Lu_2Mo_2O_5N_2$, features a magnetic Pyrochlore lattice and is known to not exhibit order down to low temperatures. From PFFRG we find a spin-liquid structure factor, which resembles a gearwheel. We showed, that this pattern can be viewed as a melted version of the classical parent order for the considered model up to third-nearest neighbor interactions.

In summary, we have demonstrated, that PFFRG is capable of determining the ground-state properties of three-dimensional quantum magnets on a variety of lattice geometries. We have improved the method by alleviating some of its inherent approximations and provided a state-of-the-art open-source implementation of the corresponding numerical implementation, which recently has been proven to be on par with independent implementations [163].

Outlook

Despite these methodological advances already implemented in this thesis, there still is room for improvement of the method. On a purely numerical front, there is potential for more efficient algorithms to be employed. In the light of our recent benchmark calculations comparing differential equation solvers in the context of itinerant fermion FRG in Reference [165], showing potential for significant run-time gain, a similar study for PFFRG is called for. Additionally, the adaptive frequency integration, although a major improvement over previous implementations, could be replaced by a more efficient algorithm based on the known analytical structure of the interpolating functions making up the integrands. We sketch this idea in appendix D, but leave its implementation as a future endeavor.

On an analytical level, the implementation of PFFRG could benefit from a reformulation akin to the truncated unity FRG for itinerant fermions [277]. In this context, the momentum dependence of the vertex is expressed in terms of form factors connected to the lattice symmetries. It turns out, that convergence in this expansion is rapid, such that only a low number of form factors has to be kept, dramatically decreasing the numerical effort [90]. Although there are no inherent lattice symmetries in frequency space, an expansion of these dependencies in terms of suitable basis functions is still rapidly converging, promising a numerical speedup [278]. We propose an expansion as outlined in

appendix E, relying on polynomials suitably mapped to reproduce the right asymptotic behavior. Due to its numerical advantages, we propose Chebyshev polynomials as a suitable choice for the basis functions.

Another route that is called for is to access the real frequency axes in the susceptibilities. This would immediately allow for comparisons with inelastic neutron scattering data at finite energy transfer corresponding to the frequency ω of the susceptibility. While a numerical analytic continuation of the Matsubara-frequency resolved susceptibility data is in principle possible [143], such a procedure is known to be numerically unstable [144]. As an alternative approach, reformulation of the whole PFFRG formalism in terms of the Keldysh technique [279] would allow immediate access to real frequencies. Although this approach has been designed with non-equilibrium processes in mind, taking the thermal equilibrium limit is possible. An implementation in the context of low-dimensional itinerant fermions has been demonstrated [280–282], but it remains to be seen, if an implementation for PFFRG will be feasible in a suitable high frequency resolution. First steps have recently been taken in that direction in Reference [283].

Broadening the scope, the lately introduced pseudo-Majorana FRG for spin systems [284, 285] offers a complementary approach to PFFRG, as it is applicable at finite temperatures. Our multi-loop formalism developed in this thesis is in principle also applicable to this approach, allowing for a more accurate determination of finite-temperature properties of spin systems.

Application-wise, there is still a plethora of open questions to be tackled in the realm of frustrated magnetism. As one example, there is the physics of the Pyrochlore lattice for a line in parameter space, where due to macroscopic degeneracies the classical model does not order at zero temperature, leading to half-moon patterns in the structure factor [286], which is possibly relevant for the spin-liquid candidate $NaCNi_2F_7$ [235]. To fully explore this problem, a generalization of the multi-loop implementation to include off-diagonal interactions in spin-space is probably needed. Although we have derived all the necessary ingredients to do so in this thesis, mainly the symmetries of the vertex functions away from the Heisenberg limit, an implementation still is lacking.

A second model system to be investigated is the XXZ-model on the Pyrochlore lattice, again calling for implementation of off-diagonal interactions. For this model, phase diagrams from approximate methods show a rich variety of exotic phases, such as a U(1) spin liquid, nematic, and spin ice phases [287]. A PFFRG perspective on this problem would introduce an unbiased view on the whole phase diagram from a singular approach.

An extension of the `PFFRGSolver.jl` to allow for these more general models will open up the way to exploring more phase diagrams and real materials realizing quantum magnetism in three dimensions.

V

Appendices

Appendix A

Flow equations in conventional parametrization

A.1 Selfenergy flow

$$\begin{aligned}\frac{\mathrm{d}}{\mathrm{d}\Lambda}\gamma^{\Lambda}(\omega) = \int \mathrm{d}\omega' \Big\{ & 3\Gamma_{\mathrm{s},i_1 i_1}(\omega+\omega', \omega-\omega', 0) \\ & + \Gamma_{\mathrm{d},i_1 i_1}(\omega+\omega', \omega-\omega', 0) \\ & - \sum_{i_2} 2\Gamma_{\mathrm{d},i_1 i_2}(\omega+\omega', 0, \omega-\omega') \Big\} \frac{\frac{\partial}{\partial\Lambda} R(\omega', \Lambda)}{\omega' + \gamma(\omega')}\end{aligned} \tag{A.1}$$

A.2 Spin vertex flow

A.2.1 s-channel

$$\begin{aligned}\dot{g}^{\mathrm{s}}_{si_1i_2}(s,t,u) = \frac{1}{2\pi}\int \mathrm{d}\omega \Big\{ & \\ & -2\Gamma_{\mathrm{s},i_1i_2}\left(s, -\frac{s-t-u}{2}-\omega, \frac{s+t+u}{2}+\omega\right)\Gamma_{\mathrm{s},i_1i_2}\left(s, \frac{s+t-u}{2}+\omega, \frac{s-t+u}{2}+\omega\right) \\ & +\Gamma_{\mathrm{s},i_1i_2}\left(s, -\frac{s-t-u}{2}-\omega, \frac{s+t+u}{2}+\omega\right)\Gamma_{\mathrm{d},i_1i_2}\left(s, \frac{s+t-u}{2}+\omega, \frac{s-t+u}{2}+\omega\right) \\ & +\Gamma_{\mathrm{d},i_1i_2}\left(s, -\frac{s-t-u}{2}-\omega, \frac{s+t+u}{2}+\omega\right)\Gamma_{\mathrm{s},i_1i_2}\left(s, \frac{s+t-u}{2}+\omega, \frac{s-t+u}{2}+\omega\right) \\ & -2\Gamma_{\mathrm{s},i_1i_2}\left(s, \frac{s+t+u}{2}+\omega, -\frac{s-t-u}{2}-\omega\right)\Gamma_{\mathrm{s},i_1i_2}\left(s, -\frac{s-t+u}{2}-\omega, -\frac{s+t-u}{2}-\omega\right) \\ & +\Gamma_{\mathrm{s},i_1i_2}\left(s, \frac{s+t+u}{2}+\omega, -\frac{s-t-u}{2}-\omega\right)\Gamma_{\mathrm{d},i_1i_2}\left(s, -\frac{s-t+u}{2}-\omega, -\frac{s+t-u}{2}-\omega\right) \\ & +\Gamma_{\mathrm{d},i_1i_2}\left(s, \frac{s+t+u}{2}+\omega, -\frac{s-t-u}{2}-\omega\right)\Gamma_{\mathrm{s},i_1i_2}\left(s, -\frac{s-t+u}{2}-\omega, -\frac{s+t-u}{2}-\omega\right) \\ & \Big\} P(\omega, s+\omega)\end{aligned} \tag{A.2}$$

A.2.2 t-channel

$$
\begin{aligned}
\dot{g}^{\mathrm{t}}_{si_1i_2}(s,t,u) = \frac{1}{2\pi}\int \mathrm{d}\omega \Big\{ & \\
& 2\sum_j \Gamma_{s,i_1 j}\left(\frac{s+t+u}{2}+\omega, t, \frac{s-t+u}{2}-\omega\right)\Gamma_{s,ji_2}\left(\frac{s+t-u}{2}+\omega, t, -\frac{s-t-u}{2}+\omega\right) \\
& 2\sum_j \Gamma_{s,i_1 j}\left(\frac{s-t+u}{2}-\omega, t, \frac{s+t+u}{2}+\omega\right)\Gamma_{s,ji_2}\left(\frac{s-t-u}{2}-\omega, t, -\frac{s+t-u}{2}-\omega\right) \\
& +\Gamma_{s,i_1i_2}\left(\frac{s+t+u}{2}+\omega, t, \frac{s-t+u}{2}-\omega\right)\Gamma_{s,i_2i_2}\left(\frac{s+t-u}{2}+\omega, -\frac{s-t-u}{2}+\omega, t\right) \\
& -\Gamma_{s,i_1i_2}\left(\frac{s+t+u}{2}+\omega, t, \frac{s-t+u}{2}-\omega\right)\Gamma_{\mathrm{d},i_2i_2}\left(\frac{s+t-u}{2}+\omega, -\frac{s-t-u}{2}+\omega, t\right) \\
& +\Gamma_{s,i_1i_2}\left(\frac{s-t+u}{2}-\omega, t, \frac{s+t+u}{2}+\omega\right)\Gamma_{s,i_2i_2}\left(\frac{s-t-u}{2}-\omega, -\frac{s+t-u}{2}-\omega, t\right) \\
& -\Gamma_{s,i_1i_2}\left(\frac{s-t+u}{2}-\omega, t, \frac{s+t+u}{2}+\omega\right)\Gamma_{\mathrm{d},i_2i_2}\left(\frac{s-t-u}{2}-\omega, -\frac{s+t-u}{2}-\omega, t\right) \\
& +\Gamma_{s,i_1i_1}\left(\frac{s+t+u}{2}+\omega, \frac{s-t+u}{2}-\omega, t\right)\Gamma_{s,i_1i_2}\left(\frac{s+t-u}{2}+\omega, t, -\frac{s-t-u}{2}+\omega\right) \\
& -\Gamma_{\mathrm{d},i_1i_1}\left(\frac{s+t+u}{2}+\omega, \frac{s-t+u}{2}-\omega, t\right)\Gamma_{s,i_1i_2}\left(\frac{s+t-u}{2}+\omega, t, -\frac{s-t-u}{2}+\omega\right) \\
& +\Gamma_{s,i_1i_1}\left(\frac{s-t+u}{2}-\omega, \frac{s+t+u}{2}+\omega, t\right)\Gamma_{s,i_1i_2}\left(\frac{s-t-u}{2}-\omega, t, -\frac{s+t-u}{2}-\omega\right) \\
& -\Gamma_{\mathrm{d},i_1i_1}\left(\frac{s-t+u}{2}-\omega, \frac{s+t+u}{2}+\omega, t\right)\Gamma_{s,i_1i_2}\left(\frac{s-t-u}{2}-\omega, t, -\frac{s+t-u}{2}-\omega\right) \\
& \Big\} P(\omega, t+\omega)
\end{aligned}
\tag{A.3}
$$

A.2.3 u-channel

$$
\begin{aligned}
\dot{g}^{\mathrm{u}}_{si_1i_2}(s,t,u) = \frac{1}{2\pi}\int \mathrm{d}\omega \Big\{ & \\
& -2\Gamma_{s,i_1i_2}\left(\frac{s-t-u}{2}-\omega, -\frac{s-t+u}{2}-\omega, u\right)\Gamma_{s,i_1i_2}\left(\frac{s+t-u}{2}-\omega, \frac{s+t+u}{2}+\omega, u\right) \\
& -\Gamma_{s,i_1i_2}\left(\frac{s-t-u}{2}-\omega, -\frac{s-t+u}{2}-\omega, u\right)\Gamma_{\mathrm{d},i_1i_2}\left(\frac{s+t-u}{2}-\omega, \frac{s+t+u}{2}+\omega, u\right) \\
& -\Gamma_{\mathrm{d},i_1i_2}\left(\frac{s-t-u}{2}-\omega, -\frac{s-t+u}{2}-\omega, u\right)\Gamma_{s,i_1i_2}\left(\frac{s+t-u}{2}-\omega, \frac{s+t+u}{2}+\omega, u\right) \\
& -2\Gamma_{s,i_1i_2}\left(\frac{s-t+u}{2}+\omega, -\frac{s-t-u}{2}+\omega, u\right)\Gamma_{s,i_1i_2}\left(\frac{s+t+u}{2}+\omega, \frac{s+t-u}{2}-\omega, u\right) \\
& -\Gamma_{s,i_1i_2}\left(\frac{s-t+u}{2}+\omega, -\frac{s-t-u}{2}+\omega, u\right)\Gamma_{\mathrm{d},i_1i_2}\left(\frac{s+t+u}{2}+\omega, \frac{s+t-u}{2}-\omega, u\right) \\
& -\Gamma_{\mathrm{d},i_1i_2}\left(\frac{s-t+u}{2}+\omega, -\frac{s-t-u}{2}+\omega, u\right)\Gamma_{s,i_1i_2}\left(\frac{s+t+u}{2}+\omega, \frac{s+t-u}{2}-\omega, u\right) \\
& \Big\} P(\omega, u+\omega)
\end{aligned}
\tag{A.4}
$$

A.3 Density vertex flow

A.3.1 s-channel

$$\begin{aligned}\dot{g}^{\mathrm{s}}_{\mathrm{d}i_1i_2}(s,t,u) = \frac{1}{2\pi}\int \mathrm{d}\omega \Big\{ & \\ & 3\Gamma_{\mathrm{s},i_1i_2}\left(s,-\frac{s-t-u}{2}-\omega,\frac{s+t+u}{2}+\omega\right)\Gamma_{\mathrm{s},i_1i_2}\left(s,\frac{s+t-u}{2}+\omega,\frac{s-t+u}{2}+\omega\right) \\ & +\Gamma_{\mathrm{d},i_1i_2}\left(s,-\frac{s-t-u}{2}-\omega,\frac{s+t+u}{2}+\omega\right)\Gamma_{\mathrm{d},i_1i_2}\left(s,\frac{s+t-u}{2}+\omega,\frac{s-t+u}{2}+\omega\right) \\ & 3\Gamma_{\mathrm{s},i_1i_2}\left(s,\frac{s+t+u}{2}+\omega,-\frac{s-t-u}{2}-\omega\right)\Gamma_{\mathrm{s},i_1i_2}\left(s,-\frac{s-t+u}{2}-\omega,-\frac{s+t-u}{2}-\omega\right) \\ & +\Gamma_{\mathrm{d},i_1i_2}\left(s,\frac{s+t+u}{2}+\omega,-\frac{s-t-u}{2}-\omega\right)\Gamma_{\mathrm{d},i_1i_2}\left(s,-\frac{s-t+u}{2}-\omega,-\frac{s+t-u}{2}-\omega\right) \\ & \Big\} P(\omega,s+\omega)\end{aligned} \tag{A.5}$$

A.3.2 t-channel

$$\begin{aligned}\dot{g}^{\mathrm{t}}_{\mathrm{d}i_1i_2}(s,t,u) = \frac{1}{2\pi}\int \mathrm{d}\omega \Big\{ & \\ & 2\sum_j \Gamma_{\mathrm{d},i_1j}\left(\frac{s+t+u}{2}+\omega,t,\frac{s-t+u}{2}-\omega\right)\Gamma_{\mathrm{d},ji_2}\left(\frac{s+t-u}{2}+\omega,t,-\frac{s-t-u}{2}+\omega\right) \\ & +2\sum_j \Gamma_{\mathrm{d},i_1j}\left(\frac{s-t+u}{2}-\omega,t,\frac{s+t+u}{2}+\omega\right)\Gamma_{\mathrm{d},ji_2}\left(\frac{s-t-u}{2}-\omega,t,-\frac{s+t-u}{2}-\omega\right) \\ & -3\Gamma_{\mathrm{d},i_1i_2}\left(\frac{s+t+u}{2}+\omega,t,\frac{s-t+u}{2}-\omega\right)\Gamma_{\mathrm{s},i_2i_2}\left(\frac{s+t-u}{2}+\omega,-\frac{s-t-u}{2}+\omega,t\right) \\ & -\Gamma_{\mathrm{d},i_1i_2}\left(\frac{s+t+u}{2}+\omega,t,\frac{s-t+u}{2}-\omega\right)\Gamma_{\mathrm{d},i_2i_2}\left(\frac{s+t-u}{2}+\omega,-\frac{s-t-u}{2}+\omega,t\right) \\ & -3\Gamma_{\mathrm{d},i_1i_2}\left(\frac{s-t+u}{2}-\omega,t,\frac{s+t+u}{2}+\omega\right)\Gamma_{\mathrm{s},i_2i_2}\left(\frac{s-t-u}{2}-\omega,-\frac{s+t-u}{2}-\omega,t\right) \\ & -\Gamma_{\mathrm{d},i_1i_2}\left(\frac{s-t+u}{2}-\omega,t,\frac{s+t+u}{2}+\omega\right)\Gamma_{\mathrm{d},i_2i_2}\left(\frac{s-t-u}{2}-\omega,-\frac{s+t-u}{2}-\omega,t\right) \\ & -3\Gamma_{\mathrm{s},i_1i_1}\left(\frac{s+t+u}{2}+\omega,\frac{s-t+u}{2}-\omega,t\right)\Gamma_{\mathrm{s},i_1i_2}\left(\frac{s+t-u}{2}+\omega,t,-\frac{s-t-u}{2}+\omega\right) \\ & -\Gamma_{\mathrm{d},i_1i_1}\left(\frac{s+t+u}{2}+\omega,\frac{s-t+u}{2}-\omega,t\right)\Gamma_{\mathrm{s},i_1i_2}\left(\frac{s+t-u}{2}+\omega,t,-\frac{s-t-u}{2}+\omega\right) \\ & -3\Gamma_{\mathrm{d},i_1i_1}\left(\frac{s-t+u}{2}-\omega,\frac{s+t+u}{2}+\omega,t\right)\Gamma_{\mathrm{s},i_1i_2}\left(\frac{s-t-u}{2}-\omega,t,-\frac{s+t-u}{2}-\omega\right) \\ & -\Gamma_{\mathrm{d},i_1i_1}\left(\frac{s-t+u}{2}-\omega,\frac{s+t+u}{2}+\omega,t\right)\Gamma_{\mathrm{d},i_1i_2}\left(\frac{s-t-u}{2}-\omega,t,-\frac{s+t-u}{2}-\omega\right) \\ & \Big\} P(\omega,t+\omega)\end{aligned} \tag{A.6}$$

A.3.3 u-channel

$$
\begin{aligned}
\dot{g}^{\mathrm{u}}_{\mathrm{s}i_1i_2}(s,t,u) = \frac{1}{2\pi}\int \mathrm{d}\omega \Big\{ & \\
& -3\Gamma_{\mathrm{s},i_1i_2}\left(\frac{s-t-u}{2}-\omega,-\frac{s-t+u}{2}-\omega,u\right)\Gamma_{\mathrm{s},i_1i_2}\left(\frac{s+t-u}{2}-\omega,\frac{s+t+u}{2}+\omega,u\right) \\
& -\Gamma_{\mathrm{d},i_1i_2}\left(\frac{s-t-u}{2}-\omega,-\frac{s-t+u}{2}-\omega,u\right)\Gamma_{\mathrm{d},i_1i_2}\left(\frac{s+t-u}{2}-\omega,\frac{s+t+u}{2}+\omega,u\right) \\
& -3\Gamma_{\mathrm{s},i_1i_2}\left(\frac{s-t+u}{2}+\omega,-\frac{s-t-u}{2}+\omega,u\right)\Gamma_{\mathrm{s},i_1i_2}\left(\frac{s+t+u}{2}+\omega,\frac{s+t-u}{2}-\omega,u\right) \\
& -\Gamma_{\mathrm{d},i_1i_2}\left(\frac{s-t+u}{2}+\omega,-\frac{s-t-u}{2}+\omega,u\right)\Gamma_{\mathrm{d},i_1i_2}\left(\frac{s+t+u}{2}+\omega,\frac{s+t-u}{2}-\omega,u\right) \\
& \Big\} P(\omega,u+\omega)
\end{aligned}
\tag{A.7}
$$

A.4 Susceptibility

$$
\begin{aligned}
\chi_{i_1i_2}(\nu) = & -\frac{1}{4\pi}\int \mathrm{d}\omega G(\omega)G(\omega+\nu) \\
& -\frac{1}{8\pi^2}\int \mathrm{d}\omega \int \mathrm{d}\omega' G(\omega)G(\omega+\nu)G(\omega')G(\omega'+\nu) \\
& \left(2\Gamma_{\mathrm{s},i_1i_2}\left(\omega+\omega'+\nu,\nu,\omega-\omega'\right)\right. \\
& +\Gamma_{\mathrm{s},i_1i_2}\left(\omega+\omega'+\nu,\omega-\omega',\nu\right)\delta_{i_1i_2} \\
& \left.-\Gamma_{\mathrm{d},i_1i_2}\left(\omega+\omega'+\nu,\omega-\omega',\nu\right)\delta_{i_1i_2}\right)
\end{aligned}
\tag{A.8}
$$

Flow equations in asymptotic parametrization

B.1 Selfenergy flow

$$\begin{aligned}\frac{\mathrm{d}}{\mathrm{d}\Lambda}\gamma(\omega) = \int \mathrm{d}\omega' \Bigg\{ & 3\Gamma_{si_1i_1}\begin{pmatrix} s=\omega+\omega' & \nu_s=\omega'/2-\omega/2 & \nu'_s=\omega'/2-\omega/2 \\ t=\omega-\omega' & \nu_t=\omega'/2+\omega/2 & \nu'_t=\omega'/2+\omega/2 \\ u=0 & \nu_u=\omega' & \nu'_u=\omega \end{pmatrix} \\ & + \Gamma_{\mathrm{d}i_1i_1}\begin{pmatrix} s=\omega+\omega' & \nu_s=\omega'/2-\omega/2 & \nu'_s=\omega'/2-\omega/2 \\ t=\omega-\omega' & \nu_t=\omega'/2+\omega/2 & \nu'_t=\omega'/2+\omega/2 \\ u=0 & \nu_u=\omega' & \nu'_u=\omega \end{pmatrix} \\ & - \sum_{i_2} 2\Gamma_{\mathrm{d}i_1i_2}\begin{pmatrix} s=\omega+\omega' & \nu_s=\omega/2-\omega'/2 & \nu'_s=\omega'/2-\omega/2 \\ t=0 & \nu_t=\omega & \nu'_t=\omega' \\ u=\omega-\omega' & \nu_u=\omega/2+\omega'/2 & \nu'_u=\omega/2+\omega'/2 \end{pmatrix} \Bigg\} \frac{\frac{\partial}{\partial\Lambda}R(\omega',\Lambda)}{\omega'+\gamma(\omega')}\end{aligned} \tag{B.1}$$

B.2 Spinvertex Flow

B.2.1 s-channel

$$
\begin{aligned}
\dot{g}^{\mathrm{s}}_{\mathrm{s}i_1i_2}\left(s,\nu_s,\nu'_s\right) = \frac{1}{2\pi}\int \mathrm{d}\omega \Bigg\{ & \\
& -2\Gamma_{\mathrm{s}i_1i_2}\begin{pmatrix} s=s & \nu_s=\nu_s & \nu'_s=-\omega \\ t=\omega-\nu_s & \nu_t=(s+\omega+\nu_s)/2 & \nu'_t=(s-\nu_s-\omega)/2 \\ u=\omega+\nu_s & \nu_u=(s+\nu_s-w)/2 & \nu'_u=(s-\nu_s+\omega)/2 \end{pmatrix}\times \\
& \times\Gamma_{\mathrm{s}i_1i_2}\begin{pmatrix} s=s & \nu_s=\omega & \nu'_s=\nu'_s \\ t=-\nu'_s-\omega & \nu_t=(s+\omega-\nu'_s)/2 & \nu'_t=(s-\omega+\nu'_s)/2 \\ u=-\nu'_s+\omega & \nu_u=(s+w+\nu'_s)/2 & \nu'_u=(s-\omega-\nu'_s)/2 \end{pmatrix} \\
& +\Gamma_{\mathrm{d}i_1i_2}\begin{pmatrix} s=s & \nu_s=\nu_s & \nu'_s=-\omega \\ t=\omega-\nu_s & \nu_t=(s+\omega+\nu_s)/2 & \nu'_t=(s-\nu_s-\omega)/2 \\ u=\omega+\nu_s & \nu_u=(s+\nu_s-w)/2 & \nu'_u=(s-\nu_s+\omega)/2 \end{pmatrix}\times \\
& \times\Gamma_{\mathrm{s}i_1i_2}\begin{pmatrix} s=s & \nu_s=\omega & \nu'_s=\nu'_s \\ t=-\nu'_s-\omega & \nu_t=(s+\omega-\nu'_s)/2 & \nu'_t=(s-\omega+\nu'_s)/2 \\ u=-\nu'_s+\omega & \nu_u=(s+w+\nu'_s)/2 & \nu'_u=(s-\omega-\nu'_s)/2 \end{pmatrix} \\
& +\Gamma_{\mathrm{s}i_1i_2}\begin{pmatrix} s=s & \nu_s=\nu_s & \nu'_s=-\omega \\ t=\omega-\nu_s & \nu_t=(s+\omega+\nu_s)/2 & \nu'_t=(s-\nu_s-\omega)/2 \\ u=\omega+\nu_s & \nu_u=(s+\nu_s-w)/2 & \nu'_u=(s-\nu_s+\omega)/2 \end{pmatrix}\times \\
& \times\Gamma_{\mathrm{d}i_1i_2}\begin{pmatrix} s=s & \nu_s=\omega & \nu'_s=\nu'_s \\ t=-\nu'_s-\omega & \nu_t=(s+\omega-\nu'_s)/2 & \nu'_t=(s-\omega+\nu'_s)/2 \\ u=-\nu'_s+\omega & \nu_u=(s+w+\nu'_s)/2 & \nu'_u=(s-\omega-\nu'_s)/2 \end{pmatrix} \\
& \Bigg\}\left(P(\frac{s}{2}+\omega,\frac{s}{2}-\omega)+P(\frac{s}{2}-\omega,\frac{s}{2}+\omega)\right)
\end{aligned}
\tag{B.2}
$$

B.2.2 t-channel

$$
\begin{aligned}
\dot{g}^{\mathrm{t}}_{\mathrm{s}i_1i_2}\left(t,\nu_t,\nu'_t\right) = \frac{1}{2\pi}\int \mathrm{d}\omega \Bigg\{ & -2\sum_j \Gamma_{\mathrm{s}i_1j}\begin{pmatrix} s=\nu_t+\omega & \nu_s=(\nu_t-t-\omega)/2 & \nu'_s=(\omega-\nu_t-t)/2 \\ t=t & \nu_t=\nu_t & \nu'_t=\omega \\ u=-\omega+\nu_t & \nu_u=(w+\nu_t-t)/2 & \nu'_u=(w+t+\nu_t)/2 \end{pmatrix}\times \\
& \times\Gamma_{\mathrm{s}ji_2}\begin{pmatrix} s=\nu'_t+\omega & \nu_s=(\omega-t-\nu'_t)/2 & \nu'_s=(\nu'_t-t-\omega)/2 \\ t=t & \nu_t=\omega & \nu'_t=\nu'_t \\ u=-\nu'_t+\omega & \nu_u=(\nu'_t-t+\omega)/2 & \nu'_u=(t+\omega+\nu'_t)/2) \end{pmatrix}
\end{aligned}
$$

$$
\begin{aligned}
&-\Gamma_{si_1i_2}\begin{pmatrix} s=\nu_t+\omega & \nu_s=(\nu_t-t-\omega)/2 & \nu'_s=(\omega-t-\nu_t)/2 \\ t=t & \nu_t=\nu_t & \nu'_t=\omega \\ u=-\omega+\nu_t & \nu_u=(\omega-t+\nu_t)/2 & \nu'_u=(t+\nu_t+\omega)/2 \end{pmatrix}\times \\
&\times\Gamma_{si_2i_2}\begin{pmatrix} s=\nu'_t+\omega & \nu_s=(\nu'_t+t-\omega)/2 & \nu'_s=(\nu'_t-t-\omega)/2 \\ t=w-\nu'_t & \nu_t=(\nu'_t+t+\omega)/2 & \nu'_t=(\nu'_t-t+\omega)/2 \\ u=t & \nu_u=\nu'_t & \nu'_u=\omega \end{pmatrix} \\
&+\Gamma_{si_1i_2}\begin{pmatrix} s=\nu_t+\omega & \nu_s=(\nu_t-t-\omega)/2 & \nu'_s=(\omega-t-\nu_t)/2 \\ t=t & \nu_t=\nu_t & \nu'_t=\omega \\ u=-\omega+\nu_t & \nu_u=(\omega-t+\nu_t)/2 & \nu'_u=(t+\nu_t+\omega)/2 \end{pmatrix}\times \\
&\times\Gamma_{di_2i_2}\begin{pmatrix} s=\nu'_t+\omega & \nu_s=(\nu'_t+t-\omega)/2 & \nu'_s=(\nu'_t-t-\omega)/2 \\ t=w-\nu'_t & \nu_t=(\nu'_t+t+\omega)/2 & \nu'_t=(\nu'_t-t+\omega)/2 \\ u=t & \nu_u=\nu'_t & \nu'_u=\omega \end{pmatrix} \qquad \text{(B.3)} \\
&-\Gamma_{si_1i_1}\begin{pmatrix} s=\nu_t+\omega & \nu_s=(t+\omega-\nu_t)/2 & \nu'_s=(\omega-t-\nu_t)/2 \\ t=\nu_t-\omega & \nu_t=(t+\nu_t+\omega)/2 & \nu'_t=(\nu_t-t+\omega)/2 \\ u=t & \nu_u=\omega & \nu'_u=\nu_t \end{pmatrix}\times \\
&\times\Gamma_{si_1i_2}\begin{pmatrix} s=\nu'_t+\omega & \nu_s=(-t-\nu'_t+\omega)/2 & \nu'_s=(\nu'_t-t-\omega)/2 \\ t=t & \nu_t=\omega & \nu'_t=\nu'_t \\ u=-\nu'_t+\omega & \nu_u=(\nu'_t-t+\omega)/2 & \nu'_u=(\nu'_t+t+\omega)/2 \end{pmatrix} \\
&+\Gamma_{di_1i_1}\begin{pmatrix} s=\nu_t+\omega & \nu_s=(t+\omega-\nu_t)/2 & \nu'_s=(\omega-t-\nu_t)/2 \\ t=\nu_t-\omega & \nu_t=(t+\nu_t+\omega)/2 & \nu'_t=(\nu_t-t+\omega)/2 \\ u=t & \nu_u=\omega & \nu'_u=\nu_t \end{pmatrix}\times \\
&\times\Gamma_{si_1i_2}\begin{pmatrix} s=\nu'_t+\omega & \nu_s=(-t-\nu'_t+\omega)/2 & \nu'_s=(\nu'_t-t-\omega)/2 \\ t=t & \nu_t=\omega & \nu'_t=\nu'_t \\ u=-\nu'_t+\omega & \nu_u=(\nu'_t-t+\omega)/2 & \nu'_u=(\nu'_t+t+\omega)/2 \end{pmatrix} \\
&\Big\}\Big(P(\omega+\frac{t}{2},\omega-\frac{t}{2})+P(\omega+\frac{t}{2},\omega-\frac{t}{2})\Big)
\end{aligned}
$$

B.2.3 u-channel

$$
\begin{aligned}
\dot{g}^{\mathrm{u}}_{\mathrm{s}i_1i_2}\left(u,\nu_u,\nu'_u\right) = \frac{1}{2\pi}\int \mathrm{d}\omega \Bigg\{ & \\
& 2\Gamma_{\mathrm{s}i_1i_2}\begin{pmatrix} s=\nu_u+\omega & \nu_s=(\nu_u+u-\omega)/2 & \nu'_s=(-u+\nu_u-\omega)/2 \\ t=\omega-\nu_u & \nu_t=(\omega+u+\nu_u)/2 & \nu'_t=(-u+\nu_u+\omega)/2 \\ u=u & \nu_u=\nu_u & \nu'_u=\omega \end{pmatrix}\times \\
& \times\Gamma_{\mathrm{s}i_1i_2}\begin{pmatrix} s=\nu'_u+\omega & \nu_s=(\omega+u-\nu'_u)/2 & \nu'_s=(-u+\omega-\nu'_u)/2 \\ t=\nu'_u-\omega & \nu_t=(\nu'_u+\omega+u)/2 & \nu'_t=(-u+\omega+\nu'_u)/2 \\ u=u & \nu_u=\omega & \nu'_u=\nu'_u \end{pmatrix} \\
& +\Gamma_{\mathrm{s}i_1i_2}\begin{pmatrix} s=\nu_u+\omega & \nu_s=(\nu_u+u-\omega)/2 & \nu'_s=(-u+\nu_u-\omega)/2 \\ t=\omega-\nu_u & \nu_t=(\omega+u+\nu_u)/2 & \nu'_t=(-u+\nu_u+\omega)/2 \\ u=u & \nu_u=\nu_u & \nu'_u=\omega \end{pmatrix}\times \\
& \times\Gamma_{\mathrm{d}i_1i_2}\begin{pmatrix} s=\nu'_u+\omega & \nu_s=(\omega+u-\nu'_u)/2 & \nu'_s=(-u+\omega-\nu'_u)/2 \\ t=\nu'_u-\omega & \nu_t=(\nu'_u+\omega+u)/2 & \nu'_t=(-u+\omega+\nu'_u)/2 \\ u=u & \nu_u=\omega & \nu'_u=\nu'_u \end{pmatrix} \\
& +\Gamma_{\mathrm{d}i_1i_2}\begin{pmatrix} s=\nu_u+\omega & \nu_s=(\nu_u+u-\omega)/2 & \nu'_s=(-u+\nu_u-\omega)/2 \\ t=\omega-\nu_u & \nu_t=(\omega+u+\nu_u)/2 & \nu'_t=(-u+\nu_u+\omega)/2 \\ u=u & \nu_u=\nu_u & \nu'_u=\omega \end{pmatrix}\times \\
& \times\Gamma_{\mathrm{s}i_1i_2}\begin{pmatrix} s=\nu'_u+\omega & \nu_s=(\omega+u-\nu'_u)/2 & \nu'_s=(-u+\omega-\nu'_u)/2 \\ t=\nu'_u-\omega & \nu_t=(\nu'_u+\omega+u)/2 & \nu'_t=(-u+\omega+\nu'_u)/2 \\ u=u & \nu_u=\omega & \nu'_u=\nu'_u \end{pmatrix} \\
& \Bigg\}\left(P(\omega-\frac{u}{2}u,\omega+\frac{u}{2})+P(\omega+\frac{u}{2},\omega-\frac{u}{2})\right)
\end{aligned}
\tag{B.4}
$$

B.3 Densityvertex Flow

B.3.1 s-channel

$$
\begin{aligned}
\dot{g}^{\mathrm{s}}_{\mathrm{d}i_1i_2}\left(s,\nu_s,\nu'_s\right) = \frac{1}{2\pi}\int \mathrm{d}\omega \Bigg\{ & \\
& 3\Gamma_{\mathrm{s}i_1i_2}\begin{pmatrix} s=s & \nu_s=\nu_s & \nu'_s=-\omega \\ t=\omega-\nu_s & \nu_t=(s+\omega+\nu_s)/2 & \nu'_t=(s-\nu_s-\omega)/2 \\ u=\omega+\nu_s & \nu_u=(s+\nu_s-w)/2 & \nu'_u=(s-\nu_s+\omega)/2 \end{pmatrix}\times \\
& \times\Gamma_{\mathrm{s}i_1i_2}\begin{pmatrix} s=s & \nu_s=\omega & \nu'_s=\nu'_s \\ t=-\nu'_s-\omega & \nu_t=(s+\omega-\nu'_s)/2 & \nu'_t=(s-\omega+\nu'_s)/2 \\ u=-\nu'_s+\omega & \nu_u=(s+w+\nu'_s)/2 & \nu'_u=(s-\omega-\nu'_s)/2 \end{pmatrix} \\
& +\Gamma_{\mathrm{d}i_1i_2}\begin{pmatrix} s=s & \nu_s=\nu_s & \nu'_s=-\omega \\ t=\omega-\nu_s & \nu_t=(s+\omega+\nu_s)/2 & \nu'_t=(s-\nu_s-\omega)/2 \\ u=\omega+\nu_s & \nu_u=(s+\nu_s-w)/2 & \nu'_u=(s-\nu_s+\omega)/2 \end{pmatrix}\times \\
& \times\Gamma_{\mathrm{d}i_1i_2}\begin{pmatrix} s=s & \nu_s=\omega & \nu'_s=\nu'_s \\ t=-\nu'_s-\omega & \nu_t=(s+\omega-\nu'_s)/2 & \nu'_t=(s-\omega+\nu'_s)/2 \\ u=-\nu'_s+\omega & \nu_u=(s+w+\nu'_s)/2 & \nu'_u=(s-\omega-\nu'_s)/2 \end{pmatrix} \\
& \Bigg\}\left(P(\frac{s}{2}+\omega,\frac{s}{2}-\omega)+P(\frac{s}{2}-\omega,\frac{s}{2}+\omega)\right)
\end{aligned}
\tag{B.5}
$$

B.3.2 t-channel

$$
\begin{aligned}
\dot{g}^{\mathrm{t}}_{\mathrm{d}i_1i_2}\left(t,\nu_t,\nu'_t\right) = \frac{1}{2\pi}\int \mathrm{d}\omega \sum_j \Bigg\{ & -2\Gamma_{\mathrm{d}i_1j}\begin{pmatrix} s=\nu_t+\omega & \nu_s=(\nu_t-t-\omega)/2 & \nu'_s=(\omega-\nu_t-t)/2 \\ t=t & \nu_t=\nu_t & \nu'_t=\omega \\ u=-\omega+\nu_t & \nu_u=(w+\nu_t-t)/2 & \nu'_u=(w+t+\nu_t)/2 \end{pmatrix}\times \\
& \times\Gamma_{\mathrm{d}ji_2}\begin{pmatrix} s=\nu'_t+\omega & \nu_s=(\omega-t-\nu'_t)/2 & \nu'_s=(\nu'_t-t-\omega)/2 \\ t=t & \nu_t=\omega & \nu'_t=\nu'_t \\ u=-\nu'_t+\omega & \nu_u=(\nu'_t-t+\omega)/2 & \nu'_u=(t+\omega+\nu'_t)/2 \end{pmatrix} \\
& +3\Gamma_{\mathrm{d}i_1i_2}\begin{pmatrix} s=\nu_t+\omega & \nu_s=(\nu_t-t-\omega)/2 & \nu'_s=(\omega-t-\nu_t)/2 \\ t=t & \nu_t=\nu_t & \nu'_t=\omega \\ u=-\omega+\nu_t & \nu_u=(\omega-t+\nu_t)/2 & \nu'_u=(t+\nu_t+\omega)/2 \end{pmatrix}\times \\
& \times\Gamma_{\mathrm{s}i_2i_2}\begin{pmatrix} s=\nu'_t+\omega & \nu_s=(\nu'_t+t-\omega)/2 & \nu'_s=(\nu'_t-t-\omega)/2 \\ t=w-\nu'_t & \nu_t=(\nu'_t+t+\omega)/2 & \nu'_t=(\nu'_t-t+\omega)/2 \\ u=t & \nu_u=\nu'_t & \nu'_u=\omega \end{pmatrix}
\end{aligned}
$$

$$
\begin{aligned}
&+\Gamma_{\mathrm{d}i_1i_2}\begin{pmatrix} s=\nu_t+\omega & \nu_s=(\nu_t-t-\omega)/2 & \nu'_s=(\omega-t-\nu_t)/2 \\ t=t & \nu_t=\nu_t & \nu'_t=\omega \\ u=-\omega+\nu_t & \nu_u=(\omega-t+\nu_t)/2 & \nu'_u=(t+\nu_t+\omega)/2 \end{pmatrix}\times \\
&\times\Gamma_{\mathrm{d}i_2i_2}\begin{pmatrix} s=\nu'_t+\omega & \nu_s=(\nu'_t+t-\omega)/2 & \nu'_s=(\nu'_t-t-\omega)/2 \\ t=w-\nu'_t & \nu_t=(\nu'_t+t+\omega)/2 & \nu'_t=(\nu'_t-t+\omega)/2 \\ u=t & \nu_u=\nu'_t & \nu'_u=\omega \end{pmatrix} \qquad \text{(B.6)} \\
&+3\Gamma_{\mathrm{s}i_1i_1}\begin{pmatrix} s=\nu_t+\omega & \nu_s=(t+\omega-\nu_t)/2 & \nu'_s=(\omega-t-\nu_t)/2 \\ t=\nu_t-\omega & \nu_t=(t+\nu_t+\omega)/2 & \nu'_t=(\nu_t-t+\omega)/2 \\ u=t & \nu_u=\omega & \nu'_u=\nu_t \end{pmatrix}\times \\
&\times\Gamma_{\mathrm{d}i_1i_2}\begin{pmatrix} s=\nu'_t+\omega & \nu_s=(-t-\nu'_t+\omega)/2 & \nu'_s=(\nu'_t-t-\omega)/2 \\ t=t & \nu_t=\omega & \nu'_t=\nu'_t \\ u=-\nu'_t+\omega & \nu_u=(\nu'_t-t+\omega)/2 & \nu'_u=(\nu'_t+t+\omega)/2 \end{pmatrix} \\
&+\Gamma_{\mathrm{d}i_1i_1}\begin{pmatrix} s=\nu_t+\omega & \nu_s=(t+\omega-\nu_t)/2 & \nu'_s=(\omega-t-\nu_t)/2 \\ t=\nu_t-\omega & \nu_t=(t+\nu_t+\omega)/2 & \nu'_t=(\nu_t-t+\omega)/2 \\ u=t & \nu_u=\omega & \nu'_u=\nu_t \end{pmatrix}\times \\
&\times\Gamma_{\mathrm{d}i_1i_2}\begin{pmatrix} s=\nu'_t+\omega & \nu_s=(-t-\nu'_t+\omega)/2 & \nu'_s=(\nu'_t-t-\omega)/2 \\ t=t & \nu_t=\omega & \nu'_t=\nu'_t \\ u=-\nu'_t+\omega & \nu_u=(\nu'_t-t+\omega)/2 & \nu'_u=(\nu'_t+t+\omega)/2 \end{pmatrix} \\
&\Big\}\left(P(\omega+\frac{t}{2},\omega-\frac{t}{2})+P(\omega+\frac{t}{2},\omega-\frac{t}{2})\right)
\end{aligned}
$$

B.3.3 u-channel

$$
\begin{aligned}
\dot{g}^{\mathrm{u}}_{\mathrm{s}i_1i_2}(s,t,u)\,(u,\nu_u,\nu'_u) = \frac{1}{2\pi}\int \mathrm{d}\omega \Bigg\{ & \\
& 3\Gamma_{\mathrm{s}i_1i_2}\begin{pmatrix} s=\nu_u+\omega & \nu_s=(\nu_u+u-\omega)/2 & \nu'_s=(-u+\nu_u-\omega)/2 \\ t=\omega-\nu_u & \nu_t=(\omega+u+\nu_u)/2 & \nu'_t=(-u+\nu_u+\omega)/2 \\ u=u & \nu_u=\nu_u & \nu'_u=\omega \end{pmatrix}\times \\
& \times\Gamma_{\mathrm{s}i_1i_2}\begin{pmatrix} s=\nu'_u+\omega & \nu_s=(\omega+u-\nu'_u)/2 & \nu'_s=(-u+\omega-\nu'_u)/2 \\ t=\nu'_u-\omega & \nu_t=(\nu'_u+\omega+u)/2 & \nu'_t=(-u+\omega+\nu'_u)/2 \\ u=u & \nu_u=\omega & \nu'_u=\nu'_u \end{pmatrix} \\
& +\Gamma_{\mathrm{d}i_1i_2}\begin{pmatrix} s=\nu_u+\omega & \nu_s=(\nu_u+u-\omega)/2 & \nu'_s=(-u+\nu_u-\omega)/2 \\ t=\omega-\nu_u & \nu_t=(\omega+u+\nu_u)/2 & \nu'_t=(-u+\nu_u+\omega)/2 \\ u=u & \nu_u=\nu_u & \nu'_u=\omega \end{pmatrix}\times \\
& \times\Gamma_{\mathrm{d}i_1i_2}\begin{pmatrix} s=\nu'_u+\omega & \nu_s=(\omega+u-\nu'_u)/2 & \nu'_s=(-u+\omega-\nu'_u)/2 \\ t=\nu'_u-\omega & \nu_t=(\nu'_u+\omega+u)/2 & \nu'_t=(-u+\omega+\nu'_u)/2 \\ u=u & \nu_u=\omega & \nu'_u=\nu'_u \end{pmatrix} \\
& \Bigg\}\left(P(\omega-\frac{u}{2}u,\omega+\frac{u}{2})+P(\omega+\frac{u}{2},\omega-\frac{u}{2})\right)
\end{aligned}
\tag{B.7}
$$

B.4 Susceptibility

$$
\begin{aligned}
\chi_{i_1j_2}(\nu) = & -\frac{1}{4\pi}\int \mathrm{d}\omega G(\omega-\nu/2)G(\omega+\nu/2) \\
& -\frac{1}{8\pi^2}\int \mathrm{d}\omega \int \mathrm{d}\omega' G(\omega-\nu/2)G(\omega+\nu/2)G(\omega'-\nu/2)G(\omega'+\nu/2) \\
& (2\Gamma_{\mathrm{s}i_1i_2}\begin{pmatrix} s=\omega+\omega' & \nu_s=(\omega-\omega'-\nu)/2 & \nu'_s=(\omega'-\omega-\nu)/2 \\ t=\nu & \nu_t=\omega & \nu'_t=\omega' \\ u=\omega'-\omega & \nu_u=(\omega+\omega'-\nu)/2 & \nu'_u=(\omega+\omega'+\nu)/2 \end{pmatrix} \\
& +\Gamma_{\mathrm{s}i_1i_1}\begin{pmatrix} s=\omega+\omega' & \nu_s=(\omega-\omega'-\nu)/2 & \nu'_s=(\omega-\omega'-\nu)/2 \\ t=\omega'-\omega & \nu_t=(\omega+\omega'-\nu)/2 & \nu'_t=(\omega+\omega'+\nu)/2 \\ u=\nu & \nu_u=\omega & \nu'_u=\omega' \end{pmatrix}\delta_{i_1i_2} \\
& -\Gamma_{\mathrm{d}i_1i_1}\begin{pmatrix} s=\omega+\omega' & \nu_s=(\omega-\omega'-\nu)/2 & \nu'_s=(\omega-\omega'-\nu)/2 \\ t=\omega'-\omega & \nu_t=(\omega+\omega'-\nu)/2 & \nu'_t=(\omega+\omega'+\nu)/2 \\ u=\nu & \nu_u=\omega & \nu'_u=\omega' \end{pmatrix}\delta_{i_1i_2})
\end{aligned}
\tag{B.8}
$$

APPENDIX C

Collection of real space lattices

In this appendix, we collect the Bravais lattice and basis vectors of a selection of two-dimensional (2D) and three-dimensional (3D) lattices.

C.1 Two-dimensional lattices

C.1.1 Square lattice

The square lattice is a 2D Bravais lattice with lattice vectors

$$\boldsymbol{a}_1 = \begin{pmatrix} 1 \\ 0 \end{pmatrix} \quad \boldsymbol{a}_2 = \begin{pmatrix} 0 \\ 1 \end{pmatrix} \tag{C.1}$$

and the single basis point

$$\boldsymbol{b}_1 = \begin{pmatrix} 0 \\ 0 \end{pmatrix}. \tag{C.2}$$

It tiles the plane with squares.

C.1.2 Triangular lattice

The triangular lattice is a 2D Bravais lattice with lattice vectors

$$\boldsymbol{a}_1 = \begin{pmatrix} 1 \\ 0 \end{pmatrix} \quad \boldsymbol{a}_2 = \begin{pmatrix} \frac{1}{2} \\ \frac{\sqrt{3}}{2} \end{pmatrix} \tag{C.3}$$

and the single basis point

$$\boldsymbol{b}_1 = \begin{pmatrix} 0 \\ 0 \end{pmatrix}. \tag{C.4}$$

It is a triangular tiling of the plane.

C.1.3 Honeycomb lattice

The honeycomb lattice is a 2D lattice with the triangular lattice vectors

$$\boldsymbol{a}_1 = \begin{pmatrix} \frac{3}{2} \\ \frac{\sqrt{3}}{2} \end{pmatrix} \quad \boldsymbol{a}_2 = \begin{pmatrix} \frac{3}{2} \\ -\frac{\sqrt{3}}{2} \end{pmatrix} \tag{C.5}$$

and the two basis points

$$\boldsymbol{b}_1 = \begin{pmatrix} 0 \\ 0 \end{pmatrix} \quad \boldsymbol{b}_2 = \begin{pmatrix} 1 \\ 0 \end{pmatrix}. \tag{C.6}$$

The lattice is build from edge sharing hexagons.

C.1.4 Kagome lattice

The honeycomb lattice is a 2D lattice with the triangular lattice vectors

$$\boldsymbol{a}_1 = \begin{pmatrix} 2 \\ 0 \end{pmatrix} \quad \boldsymbol{a}_2 = \begin{pmatrix} 1 \\ \sqrt{3} \end{pmatrix} \tag{C.7}$$

and the three basis points

$$\boldsymbol{b}_1 = \begin{pmatrix} 0 \\ 0 \end{pmatrix} \quad \boldsymbol{b}_2 = \begin{pmatrix} 1 \\ 0 \end{pmatrix} \quad \boldsymbol{b}_3 = \begin{pmatrix} \frac{1}{2} \\ \frac{\sqrt{3}}{2} \end{pmatrix}. \tag{C.8}$$

The lattice consists of corner sharing triangles, which surround a hexagon. Alternatively it can be viewed as removing every fourth point out of a triangular lattice in a regular fashion.

C.2 Three-dimensional lattices

C.2.1 Simple cubic lattice

The simple cubic lattice is a 3D Bravais lattice with lattice vectors

$$\boldsymbol{a}_1 = \begin{pmatrix} 1 \\ 0 \\ 0 \end{pmatrix} \quad \boldsymbol{a}_2 = \begin{pmatrix} 0 \\ 1 \\ 0 \end{pmatrix} \quad \boldsymbol{a}_= \begin{pmatrix} 0 \\ 0 \\ 1 \end{pmatrix} \tag{C.9}$$

and the single basis point

$$\boldsymbol{b}_1 = \begin{pmatrix} 0 \\ 0 \\ 0 \end{pmatrix}. \tag{C.10}$$

C.2.2 Body-centered cubic lattice

The body-centered cubic (BCC) lattice is a 3D Bravais lattice with lattice vectors

$$\boldsymbol{a}_1 = \begin{pmatrix} \frac{1}{2} \\ \frac{1}{2} \\ -\frac{1}{2} \end{pmatrix} \quad \boldsymbol{a}_2 = \begin{pmatrix} -\frac{1}{2} \\ \frac{1}{2} \\ \frac{1}{2} \end{pmatrix} \quad \boldsymbol{a}_3 = \begin{pmatrix} \frac{1}{2} \\ -\frac{1}{2} \\ \frac{1}{2} \end{pmatrix} \tag{C.11}$$

and the single basis point

$$\boldsymbol{b}_1 = \begin{pmatrix} 0 \\ 0 \\ 0 \end{pmatrix}. \tag{C.12}$$

The lattice's most symmetric unit cell is a cube, where the body-center point is added as a lattice point in addition to the eight corners.

C.2.3 Face-centered cubic lattice

The face-centered cubic (FCC) lattice is a 3D Bravais lattice with lattice vectors

$$\boldsymbol{a}_1 = \begin{pmatrix} 0 \\ \frac{1}{\sqrt{2}} \\ \frac{1}{\sqrt{2}} \end{pmatrix} \quad \boldsymbol{a}_2 = \begin{pmatrix} \frac{1}{\sqrt{2}} \\ 0 \\ \frac{1}{\sqrt{2}} \end{pmatrix} \quad \boldsymbol{a}_3 = \begin{pmatrix} \frac{1}{\sqrt{2}} \\ \frac{1}{\sqrt{2}} \\ 0 \end{pmatrix} \tag{C.13}$$

and the single basis point

$$\boldsymbol{b}_1 = \begin{pmatrix} 0 \\ 0 \\ 0 \end{pmatrix}. \tag{C.14}$$

The most symmetric unit cell of the FCC lattice is a cube, where in addition to the eight corners the midpoint of all six faces are added as lattice points.

C.2.4 Diamond lattice

The diamond lattice is a 3D lattice with the FCC lattice vectors

$$\boldsymbol{a}_1 = \begin{pmatrix} 0 \\ \frac{2}{\sqrt{3}} \\ \frac{2}{\sqrt{3}} \end{pmatrix} \quad \boldsymbol{a}_2 = \begin{pmatrix} \frac{2}{\sqrt{3}} \\ 0 \\ \frac{2}{\sqrt{3}} \end{pmatrix} \quad \boldsymbol{a}_3 = \begin{pmatrix} \frac{2}{\sqrt{3}} \\ \frac{2}{\sqrt{3}} \\ 0 \end{pmatrix} \tag{C.15}$$

and the two basis points

$$\boldsymbol{b}_1 = \begin{pmatrix} 0 \\ 0 \\ 0 \end{pmatrix} \quad \boldsymbol{b}_2 = \begin{pmatrix} \frac{1}{\sqrt{3}} \\ \frac{1}{\sqrt{3}} \\ \frac{1}{\sqrt{3}} \end{pmatrix}. \tag{C.16}$$

The lattice decomposes into two interpenetrating FCC lattices separated by the basis vector $\boldsymbol{b}_2$ from each other.

C.2.5 Pyrochlore lattice

The Pyrochlore lattice is a 3D lattice with the FCC lattice vectors

$$\boldsymbol{a}_1 = \begin{pmatrix} 0 \\ \frac{1}{2} \\ \frac{1}{2} \end{pmatrix} \quad \boldsymbol{a}_2 = \begin{pmatrix} \frac{1}{2} \\ 0 \\ \frac{1}{2} \end{pmatrix} \quad \boldsymbol{a}_3 = \begin{pmatrix} \frac{1}{2} \\ \frac{1}{2} \\ 0 \end{pmatrix} \tag{C.17}$$

and the four basis points

$$\boldsymbol{b}_1 = \begin{pmatrix} 0 \\ 0 \\ 0 \end{pmatrix} \quad \boldsymbol{b}_2 = \begin{pmatrix} 0 \\ \frac{1}{4} \\ \frac{1}{4} \end{pmatrix} \quad \boldsymbol{b}_3 = \begin{pmatrix} \frac{1}{4} \\ 0 \\ \frac{1}{4} \end{pmatrix} \quad \boldsymbol{b}_2 = \begin{pmatrix} \frac{1}{4} \\ \frac{1}{4} \\ 0 \end{pmatrix}. \tag{C.18}$$

The Pyrochlore lattice is built from corner-sharing tetrahedra and in this regard a 3D generalization of the Kagome lattice.

Appendix D

Exact integration of interpolating functions

Guided by the idea behind the common, non-adaptive integration routines, we will employ a different approach to the frequency integrals. As we know the exact form of the interpolating functions we used for integration so far, we can use this information to integrate them analytically, resulting in a quadrature rule tailored to our functions.

Within the central part of the Vertex function, we have to do a trilinear interpolation within the frequency cuboid $[\omega_i, \omega_{i+1}] \times [\omega_j, \omega_{j+1}] \times [\omega_k, \omega_{k+1}]$. Therefore the interpolation within one of these cuboids in for one of the factors in the integral generically is a third-order polynamial

$$\Gamma(a + b\omega, c + d\omega, e + f\omega) = a_3\omega^3 + a_2\omega^2 + a_1\omega + a_0. \tag{D.1}$$

If less of the arguments are integrated over or the arguments are large enough, that we have to use asymptotics, we will end up with a lower order polynomial, depending on the number of integrated arguments.

Worst case, the integrand in the Katnin part consists of two vertices, which are third-order polynomials, the derivative of the self-energy (first-order polynomial), and three propagators (inverse first-order polynomials), which are multiplied together. This rational function, therefore, is a polynomial of seventh order divided by one of third order. Mathematica will help to do the integral, but the formula is lengthy.

In practice we have to find the intervals in ω, where the as and bs are constant, i.e. all frequency arguments of all functions are in between two discretization points. This means, we have to integrate between all points, where one of the shifted frequency arguments is on the discretization mesh. Calling the definite integral from ω_l to ω_h of the rational function defined above $F(\vec{a}, \vec{b}, \omega_l, \omega_h)$ and the discrete frequencies $\vec{\omega}$, the algorithm to integrate between ω_i and ω_f is

1. Shift $\vec{\omega}$ for each argument of all functions, such that we plug in a point on the mesh.
2. Take the union $\vec{\omega}_u$ of these and cut the list such, that $\omega_i < \omega_u^i < \omega_f$
3. Collect $\vec{a}^i$ and $\vec{b}^i$, such that these are valid on the interval $[\omega_u^i, \omega_u^{i+1}]$
4. The full integral is then given by $\sum_i F(\vec{a}^i, \vec{b}^i, \omega_u^i, \omega_u^{i+1})$

Remarks

- Caching of $\vec{a}^i$ and $\vec{b}^i$ can be done independent of external s, ν_s, ν'_s and these can be implemented as a shift. They will vetorize over all lattice points, as frequency integration is independent of it.
- $\partial_\Lambda \Sigma = 0$ for $\omega \to \infty$, due to asymptotics. This cuts effectively the Katanin integral for high frequencies.

- Multi-Loop integrations will go to infty, but are well controlled. Orders of polynomials will be lower there.

Appendix E

Truncated unity in frequency space

Similar to the decomposition into lattice harmonics in functional renormalization group (FRG) for itinerant fermions in truncated unity FRG we here want to sketch a similar scheme in frequency space.

E.1 Spectral decomposition of functions

We want to consider a decomposition of the vertex in the fermionic frequencies into a basis of (scaled) polynomials. To this end, let us first fix notation. Let $p_a(x)$, with $a \in \mathbb{N}_0$ be a complete orthonormal polynomial basis in the interval $[-1, 1]$. We define orthonormality with respect to a scalar product involving a weight function $w(x)$ as

$$< p_a, p_b >= \int_{-1}^{1} \mathrm{d}x p_a(x) p_b(x) w(x) = \delta_{a,b} \,. \tag{E.1}$$

As the vertex functions are defined for all frequencies, we use the function $m : \mathbb{R} \to [-1, 1]$ to map the frequency arguments to the interval the polynomials are orthogonal in. Choices one could consider as basis fucntions are the Legendre Polynomials

$$p_a^L(x) = \sqrt{\frac{2a+1}{2}} P_a(x) \quad \text{with} \quad w(x) = 1 \tag{E.2}$$

where we introduced a factor to normalize them. Another common choice for orthogonal polynomials in numerics are the Chebyshev polynomials

$$p_a^T(x) = \sqrt{\frac{1}{\pi}} T_a(x) \quad \text{with} \quad w(x) = \sqrt{1 - x^2}. \tag{E.3}$$

Note, that in this convention $< p_0^T, p_0^T >= 2$.
For the mapping function we consider

$$m(\omega) = \frac{\omega}{\sqrt{\omega^2 - 1}} \quad m^{-1}(x = \frac{x}{\sqrt{1 - x^2}} \,. \tag{E.4}$$

Any function $f(\omega)$ can then be expanded in terms of the polynomials as

$$f(\omega) = \sum_{a=0}^{\infty} c_a p_a(x), \tag{E.5}$$

where

$$c_a = \int_{-1}^{1} \mathrm{d}x\, p_a(x) f(m^{-1}(x)) w(x)\,. \tag{E.6}$$

This spectral decomposition can subsequently be used to construct an approximation to f by truncating the sum in eq. (E.5).

E.2 Expansion of the flow equations

We want to use the spectral decomposition defined above for the fermionic frequencies in each channel c of the vertex function Γ. A major part of the discussion is based on Reference [278]. The reason we do not consider an expansion of the bosonic frequency axis is for now mainly numerical: expanding also this frequency would necessitate a projection onto the basis functions, i.e. an additional integration, for each component in each step of the flow. This we can circumvent by treating the bosonic variable as continuous. For the self-energy, there is another reason: the mapped polynomials decay at least as $1/\omega^2$ for $\omega \to \infty$, but the self-energy physically should decay as $1/\omega$, which can only be achieved by considering a large number of basis functions. Therefore, we expand the Vertex function in the c-channel ($c = s/t/u$) as

$$g^{\mathrm{c}}_{s/d,i_1i_2}(c, \nu_c, \nu_c') = \sum_{a,b} \Gamma^{\mathrm{c};ab}_{s/d,i_1i_2}(c) p_a(m(\nu_c)) p_b(m(\nu_c'))\,. \tag{E.7}$$

Plugging this expansion into the flow equations we find in the s-channel

$$\begin{aligned} \dot{g}^{\mathrm{s};ab}_{s,i_1i_2}(s) = \frac{1}{2\pi} \sum_{c,d} \big\{ &-2\Gamma^{ac}_{s,i_1i_2}(s)\Gamma^{db}_{s,i_1i_2}(s) \\ &+\Gamma^{ac}_{d,i_1i_2}(s)\Gamma^{db}_{s,i_1i_2}(s) \\ &+\Gamma^{ac}_{s,i_1i_2}(s)\Gamma^{db}_{d,i_1i_2}(s)\big\}\Pi^{cd}_s(s) \end{aligned} \tag{E.8}$$

$$\begin{aligned} \dot{g}^{\mathrm{s};ab}_{d,i_1i_2}(s) = \frac{1}{2\pi} \sum_{c,d} \big\{ &3\Gamma^{ac}_{s,i_1i_2}(s)\Gamma^{db}_{s,i_1i_2}(s) \\ &+\Gamma^{ac}_{d,i_1i_2}(s)\Gamma^{db}_{d,i_1i_2}(s)\big\}\Pi^{cd}_s(s), \end{aligned} \tag{E.9}$$

where we defined the s-bubble function

$$\Pi^{cd}_s(s) = \int \mathrm{d}\omega\, p_c(m(-\omega)) p_d(m(\omega)) P\left(\frac{s}{2} + \omega, \frac{s}{2} - \omega\right)\,. \tag{E.10}$$

Similarly, we get in the t-channel

$$\begin{aligned} \dot{g}^{\mathrm{t};ab}_{s,i_1i_2}(t) = \frac{1}{2\pi} \sum_{c,d} \big\{ &-2\sum_j \Gamma^{ac}_{s,i_1j}(t)\Gamma^{db}_{s,j\,i_2}(t) \\ &-\Gamma^{ac}_{s,i_1i_2}(t)\Gamma^{bd}_{s,i_2i_2}(u=t) \\ &+\Gamma^{ac}_{s,i_1i_2}(t)\Gamma^{db}_{d,i_2i_2}(u=t) \\ &-\Gamma^{ca}_{s,i_1i_1}(u=t)\Gamma^{db}_{s,i_1i_2}(t) \\ &+\Gamma^{ca}_{d,i_1i_1}(u=t)\Gamma^{db}_{s,i_1i_2}(t)\big\}\Pi^{cd}_t(t) \end{aligned} \tag{E.11}$$

$$\begin{aligned}\dot{g}^{\mathrm{t};ab}_{d,i_1i_2}(t) = \frac{1}{2\pi}\sum_{c,d}\Big\{ -2\sum_j \Gamma^{ac}_{d,i_1j}(t)\Gamma^{db}_{d,j\ i_2}(t) \\ +3\Gamma^{ac}_{d,i_1i_2}(t)\Gamma^{bd}_{s,i_2i_2}(u=t) \\ +\Gamma^{ac}_{d,i_1i_2}(t)\Gamma^{db}_{d,i_2i_2}(u=t) \\ +3\Gamma^{ca}_{s,i_1i_1}(u=t)\Gamma^{db}_{d,i_1i_2}(t) \\ +\Gamma^{ca}_{d,i_1i_1}(u=t)\Gamma^{db}_{d,i_1i_2}(t)\Big\}\Pi^{cd}_t(t)\end{aligned} \tag{E.12}$$

with the t-bubble

$$\Pi^{cd}_t(t) = \int \mathrm{d}\omega\, p_c(m(\omega))p_d(m(\omega))P\left(\omega+\frac{t}{2},\omega-\frac{t}{2}\right). \tag{E.13}$$

Finally, the u-channel reads

$$\begin{aligned}\dot{g}^{\mathrm{u};ab}_{s,i_1i_2}(u) = \frac{1}{2\pi}\sum_{c,d}\Big\{2\Gamma^{ac}_{s,i_1i_2}(u)\Gamma^{db}_{s,i_1i_2}(u) \\ +\Gamma^{ac}_{d,i_1i_2}(u)\Gamma^{db}_{s,i_1i_2}(u) \\ +\Gamma^{ac}_{s,i_1i_2}(u)\Gamma^{db}_{d,i_1i_2}(u)\Big\}\Pi^{cd}_u(u)\end{aligned} \tag{E.14}$$

$$\begin{aligned}\dot{g}^{\mathrm{u};ab}_{d,i_1i_2}(u) = \frac{1}{2\pi}\sum_{c,d}\Big\{3\Gamma^{ac}_{s,i_1i_2}(u)\Gamma^{db}_{s,i_1i_2}(u)) \\ +\Gamma^{ac}_{d,i_1i_2}(u)\Gamma^{db}_{d,i_1i_2}(u)\Big\}\Pi^{cd}_s(s),\end{aligned} \tag{E.15}$$

where the u-bubble is the same as the t-bubble

$$\Pi^{cd}_u(u) = \Pi^{cd}_t(u). \tag{E.16}$$

If the polynoials fulfill

$$p_a(-x) = (-1)^a p_a(x), \tag{E.17}$$

i.e., p_a is even(odd), if a is even(odd), then

$$\Pi^{cd}_s(s) = (-1)^{c+1}\Pi^{cd}_t(s), \tag{E.18}$$

as p is antisymmetric in each of its arguments separately.

E.3 Rotation between frequency parametrizations

To complete the picture of the spectral decomposition, we need to know how to rotate between the different frequency parametrizations, as in the right-hand side of the flow equations in Section E.2 we need the full vertex in the antural parametrizations. This amounts to plugging in the relations between the frequency arguments and projecting onto the respective basis functions. We find

$$\begin{aligned}\Gamma^{ab}_{s/,i_1i_2}(s) = \int_{-\infty}^{\infty}\mathrm{d}\omega\mathrm{d}\omega' \sum_{c,d}\Gamma^{cd}_{s/,i_1i_2}(t=-\omega-\omega')p_c\left(m\left(\frac{s+\omega-\omega'}{2}\right)\right)p_d\left(m\left(\frac{s-\omega+\omega'}{2}\right)\right) \\ p_a(m(\omega))p_b(m(\omega))m'(\omega)m'(\omega')\end{aligned} \tag{E.19}$$

$$= \int_{-\infty}^{\infty} \mathrm{d}\omega\mathrm{d}\omega' \sum_{c,d} \Gamma^{cd}_{s/,i_1i_2}(u = \omega - \omega') p_c\left(m\left(\frac{s+\omega+\omega'}{2}\right)\right) p_d\left(m\left(\frac{s-\omega-\omega'}{2}\right)\right)$$
$$p_a(m(\omega)) p_b(m(\omega)) m'(\omega) m'(\omega') \tag{E.20}$$

for the projection to the s-parametrization,

$$\Gamma^{ab}_{s/,i_1i_2}(t) = \int_{-\infty}^{\infty} \mathrm{d}\omega\mathrm{d}\omega' \sum_{c,d} \Gamma^{cd}_{s/,i_1i_2}(s = \omega + \omega') p_c\left(m\left(\frac{-t+\omega-\omega'}{2}\right)\right) p_d\left(m\left(\frac{-t-\omega+\omega'}{2}\right)\right)$$
$$p_a(m(\omega)) p_b(m(\omega)) m'(\omega) m'(\omega') \tag{E.21}$$
$$= \int_{-\infty}^{\infty} \mathrm{d}\omega\mathrm{d}\omega' \sum_{c,d} \Gamma^{cd}_{s/,i_1i_2}(u = \omega - \omega') p_c\left(m\left(\frac{-t+\omega+\omega'}{2}\right)\right) p_d\left(m\left(\frac{t+\omega+\omega'}{2}\right)\right)$$
$$p_a(m(\omega)) p_b(m(\omega)) m'(\omega) m'(\omega') \tag{E.22}$$

when projecting onto t and finally

$$\Gamma^{ab}_{s/,i_1i_2}(u) = \int_{-\infty}^{\infty} \mathrm{d}\omega\mathrm{d}\omega' \sum_{c,d} \Gamma^{cd}_{s/,i_1i_2}(s = \omega + \omega') p_c\left(m\left(\frac{u+\omega-\omega'}{2}\right)\right) p_d\left(m\left(\frac{-u+\omega-\omega'}{2}\right)\right)$$
$$p_a(m(\omega)) p_b(m(\omega)) m'(\omega) m'(\omega') \tag{E.23}$$
$$= \int_{-\infty}^{\infty} \mathrm{d}\omega\mathrm{d}\omega' \sum_{c,d} \Gamma^{cd}_{s/,i_1i_2}(t = -\omega + \omega') p_c\left(m\left(\frac{u+\omega+\omega'}{2}\right)\right) p_d\left(m\left(\frac{-u+\omega+\omega'}{2}\right)\right)$$
$$p_a(m(\omega)) p_b(m(\omega)) m'(\omega) m'(\omega') \tag{E.24}$$

projecting onto u.

E.4 Numerical considerations

As an algorithmic implementation of a single RG-step, one can follow how similar calculations are done in TUFRG:

1. Compute bubbles
2. Compute derivative in respective channel parametrization via matrix multiplication
3. Rotate derivatives in other parametrizations, to update full vertex in available in all three frequency parametrizations

This means, in contrast to conventional PFFRG one would track the full vertex in three parametrizations instead of the three channels separately. Therefore, the main work is shifted from integrating the bubble functions (which now will be a relatively easy task) to rotating the vertex contributions, which will be one double integral per rotation. In this regard, effort should be similar.

However, as shown in Reference [278] for fermionic systems, a low number of basis functions, there 16, but only 8 nonzero coefficients, is enough to capture the frequency content of the vertex. This would free up computational

resources from the fermionic frequencies, where complexity scales as N_ν^2, which can be used to increase resolution in bosonic frequency. Additionally, the interpolation effort is significantly reduced, as interpolation has to be done only in the bosonic frequency.

Considering implementation effort, Legendre polynomials are readily available in Julia, for example via the C library GSL, wrapped in GSL.jl. However, if convergence in Chebyshev polynomials is also good, we can rely on more sophisticated methods to calculate the coefficients for vertex rotations. These algorithms need only n function evaluations to construct a Chebyshev approximation with n polynomials and no integrations whatsoever.

Bibliography

[1] É. du Trémolet de Lacheisserie, D. Gignoux, and M. Schlenker, "*Magnetism, from the Dawn of Civilization to Today*", *Magnetism*, (Springer, New York, NY, 2002) pp. 3–18.

[2] J. M. Coey, *Magnetism and magnetic materials*, (Cambridge University Press, 2010) pp. 1–617.

[3] P. Weiss and J. Kunz, "*Les variations thermiques de l'aimantation de la pyrrhotine*", Journal de Physique Théorique et Appliquée **4**, 847 (1905).

[4] J. H. V. Vleck, "*The Theory of Electric and Magnetic Susceptibilities.*", The Mathematical Gazette **18**, 328 (1934).

[5] B. Sriram Shastry and B. Sutherland, "*Exact ground state of a quantum mechanical antiferromagnet*", Physica B+C **108**, 1069 (1981).

[6] P. Ghosh, T. Müller, and R. Thomale, "*Another Exact Ground State of a 2D Quantum Antiferromagnet*" (2021), arXiv: 2112.05137.

[7] P. W. Anderson, "*Resonating valence bonds: A new kind of insulator?*", Materials Research Bulletin **8**, 153 (1973).

[8] P. Fazekas and P. W. Anderson, "*On the ground state properties of the anisotropic triangular antiferromagnet*", Philosophical Magazine **30**, 423 (1974).

[9] B. Bernu, P. Lecheminant, C. Lhuillier, and L. Pierre, "*Exact spectra, spin susceptibilities, and order parameter of the quantum Heisenberg antiferromagnet on the triangular lattice*", Physical Review B **50**, 10048 (1994), arXiv: 9407028 [cond-mat].

[10] P. W. Anderson, "*The resonating valence bond state in La_2CuO_4 and superconductivity*", Science **235**, 1196 (1987).

[11] L. Balents, "*Spin liquids in frustrated magnets*", Nature **464**, 199 (2010).

[12] L. Savary and L. Balents, "*Quantum spin liquids: A review*", Reports on Progress in Physics **80** (2017), arXiv: 1601.03742.

[13] Y. Zhou, K. Kanoda, and T. K. Ng, "*Quantum spin liquid states*", Reviews of Modern Physics **89**, 25003 (2017), arXiv: 1607.03228.

[14] V. Kalmeyer and R. B. Laughlin, "*Equivalence of the resonating-valence-bond and fractional quantum Hall states*", Physical Review Letters **59**, 2095 (1987).

[15] G. Baskaran, Z. Zou, and P. W. Anderson, "*The resonating valence bond state and high-T_c superconductivity – A mean field theory*", Solid State Communications **63**, 973 (1987).

[16] X. G. Wen, "*Mean-field theory of spin-liquid states with finite energy gap and topological orders*", Physical Review B **44**, 2664 (1991).

[17] X. G. Wen, "*Quantum orders and symmetric spin liquids*", Physical Review B **65**, 1 (2002), arXiv: 0107071 [cond-mat].

[18] J. Hubbard, "*Electron correlations in narrow energy bands*", Proceedings of the Royal Society of London. Series A. Mathematical and Physical Sciences **276**, 238 (1963).

[19] J. Hubbard, "*Electron correlations in narrow energy bands. II. The degenerate band case*", Proceedings of the Royal Society of London. Series A. Mathematical and Physical Sciences **277**, 237 (1964).

[20] J. Hubbard, "*Electron correlations in narrow energy bands III. An improved solution*", Proceedings of the Royal Society of London. Series A. Mathematical and Physical Sciences **281**, 401 (1964).

[21] J. Hubbard, "*Electron correlations in narrow energy bands - IV. The atomic representation*", Proceedings of the Royal Society of London. Series A. Mathematical and Physical Sciences **285**, 542 (1965).

[22] J. Hubbard, "*Electron correlations in narrow energy bands V. A perturbation expansion about the atomic limit*", Proceedings of the Royal Society of London. Series A. Mathematical and Physical Sciences **296**, 82 (1967).

[23] J. Hubbard, "*Electron correlations in narrow energy bands VI. The connexion with many-body perturbation theory*", Proceedings of the Royal Society of London. Series A. Mathematical and Physical Sciences **296**, 100 (1967).

[24] C. L. Cleveland and R. Medina A., "*Obtaining a Heisenberg Hamiltonian from the Hubbard model*", American Journal of Physics **44**, 44 (1976).

[25] Y. Iqbal, F. Becca, S. Sorella, and D. Poilblanc, "*Gapless spin-liquid phase in the kagome spin-$\frac{1}{2}$ Heisenberg antiferromagnet*", Physical Review B **87**, 60405 (2013), arXiv: 1209.1858.

[26] Y. C. He, M. P. Zaletel, M. Oshikawa, and F. Pollmann, "*Signatures of Dirac cones in a DMRG study of the Kagome Heisenberg model*", Physical Review X **7**, 1 (2017), arXiv: 1611.06238.

[27] Y. Iqbal, F. Ferrari, A. Chauhan, A. Parola, D. Poilblanc, and F. Becca, "*Gutzwiller projected states for the Heisenberg model on the Kagome lattice: Achievements and pitfalls*", Physical Review B **104**, 1 (2021), arXiv: 2108.02847.

[28] S. R. White, "*Density matrix formulation for quantum renormalization groups*", Physical Review Letters **69**, 2863 (1992).

[29] U. Schollwöck, "*The density-matrix renormalization group*", Reviews of Modern Physics **77**, 259 (2005), arXiv: 0409292 [cond-mat].

[30] F. L. Buessen, M. Hering, J. Reuther, and S. Trebst, "*Quantum Spin Liquids in Frustrated Spin-1 Diamond Antiferromagnets*", Physical Review Letters **120**, 57201 (2018), arXiv: 1706.06299.

[31] Y. Iqbal, T. Müller, P. Ghosh, M. J. Gingras, H. O. Jeschke, S. Rachel, J. Reuther, and R. Thomale, "*Quantum and Classical Phases of the Pyrochlore Heisenberg Model with Competing Interactions*", Physical Review X **9**, 11005 (2019), arXiv: 1802.09546.

[32] P. Ghosh, T. Müller, F. P. Toldin, J. Richter, R. Narayanan, R. Thomale, J. Reuther, and Y. Iqbal, "*Quantum paramagnetism and helimagnetic orders in the Heisenberg model on the body centered cubic lattice*", Physical Review B **100** (2019), arXiv: 1902.01179.

[33] Y. Iqbal, T. Müller, H. O. Jeschke, R. Thomale, and J. Reuther, "*Stability of the spiral spin liquid in $MnSc_2S_4$*", Physical Review B **98**, 1 (2018), arXiv: 1802.00357.

[34] P. Ghosh, Y. Iqbal, T. Müller, R. T. Ponnaganti, R. Thomale, R. Narayanan, J. Reuther, M. J. Gingras, and H. O. Jeschke, "*Breathing chromium spinels: a showcase for a variety of pyrochlore Heisenberg Hamiltonians*", npj Quantum Materials **4**, 1 (2019), arXiv: 1903.01928.

[35] S. Chillal *et al.*, "*Evidence for a three-dimensional quantum spin liquid in $PbCuTe_2O_6$*", Nature Communications **11** (2020), arXiv: 1712.07942.

[36] T. A. Kaplan and N. Menyuk, "*Spin ordering in three-dimensional crystals with strong competing exchange interactions*", Philosophical Magazine **87**, 3711 (2007).

[37] S. R. Sklan and C. L. Henley, "*Nonplanar ground states of frustrated antiferromagnets on an octahedral lattice*", Physical Review B **88**, 24407 (2013), arXiv: 1209.1381.

[38] M. F. Lapa and C. L. Henley, "*Ground States of the Classical Antiferromagnet on the Pyrochlore Lattice*", ArXiv e-prints (2012), arXiv: 1210.6810.

[39] K. Millard and H. S. Leff, "*Infinite-spin limit of the quantum Heisenberg model*", Journal of Mathematical Physics **12**, 1000 (1971).

[40] E. H. Lieb, "*The classical limit of quantum spin systems*", Communications in Mathematical Physics **31**, 327 (1973).

[41] P. M. Pardalos and S. A. Vavasis, "*Quadratic programming with one negative eigenvalue is NP-hard*", Journal of Global Optimization **1**, 15 (1991).

[42] J. M. Luttinger and L. Tisza, "*Theory of dipole interaction in crystals*", Physical Review **70**, 954 (1946).

[43] J. M. Luttinger, "*A note on the ground state in antiferromagnetics*", Physical Review **81**, 1015 (1951).

[44] D. H. Lyons and T. A. Kaplan, "*Method for determining ground-state spin configurations*", Physical Review **120**, 1580 (1960).

[45] J. Villain, "*La structure des substances magnetiques*", Journal of Physics and Chemistry of Solids **11**, 303 (1959).

[46] J. C. Domenge, P. Sindzingre, C. Lhuillier, and L. Pierre, "*Twelve sublattice ordered phase in the $J_1 - J_2$ model on the kagomé lattice*", Physical Review B **72**, 1 (2005), arXiv: 0502414 [cond-mat].

[47] J. C. Domenge, C. Lhuillier, L. Messio, L. Pierre, and P. Viot, "*Chirality and $\mathbb{Z}_2$ vortices in a Heisenberg spin model on the kagome lattice*", Physical Review B **77**, 172413 (2008), arXiv: 0711.1497.

[48] J. N. Reimers, A. J. Berlinsky, and A. C. Shi, "*Mean-field approach to magnetic ordering in highly frustrated pyrochlores*", Physical Review B **43**, 865 (1991).

[49] J. N. Reimers, "*Diffuse-magnetic-scattering calculations for frustrated antiferromagnets*", Physical Review B **46**, 193 (1992).

[50] D. A. Garanin and B. Canals, "*Classical spin liquid: Exact solution for the infinite-component antiferromagnetic model on the kagomé lattice*", Physical Review B **59**, 443 (1999), arXiv: 9805362 [cond-mat].

[51] B. Canals and D. Garanin, "*Spin-liquid phase in the pyrochlore anti-ferromagnet*", Canadian Journal of Physics **79**, 1323 (2001), arXiv: 0102237 [cond-mat].

[52] S. V. Isakov, K. Gregor, R. Moessner, and S. L. Sondhi, "*Dipolar Spin Correlations in Classical Pyrochlore Magnets*", Physical Review Letters **93**, 167204 (2004), arXiv: 0407004 [cond-mat].

[53] H. B. Curry, "*The method of steepest descent for non-linear minimization problems*", Quarterly of Applied Mathematics **2**, 258 (1944).

[54] G. C. Wick, "*The evaluation of the collision matrix*", Physical Review **80**, 268 (1950).

[55] Y. L. Wang, S. Shtrikman, and H. Callen, "*Wick's theorem for spin operators, with an application to spin waves in antiferromagnets*", Physical Review **148**, 419 (1966).

[56] Y. L. Wang, S. Shtrikman, and H. Callen, "*Wick's theorem for spin operators and its relation to the coupled-fermion representation*", Journal of Applied Physics **37**, 1451 (1966).

[57] A. A. Abrikosov, "*Electron scattering on magnetic impurities in metals and anomalous resistivity effects*", Physics Physique Fizika **2**, 5 (1965).

[58] I. Affleck, Z. Zou, T. Hsu, and P. W. Anderson, "*SU(2) gauge symmetry of the large-U limit of the Hubbard model*", Physical Review B **38**, 745 (1988).

[59] F. L. Buessen, "*A Functional Renormalization Group Perspective on Quantum Spin Liquids in Three-Dimensional Frustrated Magnets*", **21**, 499 (2019).

[60] F. J. Wegner and A. Houghton, "*Renormalization group equation for critical phenomena*", Physical Review A **8**, 401 (1973).

[61] J. Polchinski, "*Renormalization and effective lagrangians*", Nuclear Physics, Section B **231**, 269 (1984).

[62] C. Wetterich, "*Exact evolution equation for the effective potential*", Physics Letters B **301**, 90 (1993), arXiv: 1710.05815.

[63] K. G. Wilson, "*II. Phase-Space Cell Analysis of Critical Behavior*", Physical Review B **4**, 3184 (1971).

[64] K. G. Wilson and J. Kogut, "*The renormalization group and the ϵ expansion*", Physics Reports **12**, 75 (1974).

[65] M. Reuter and C. Wetterich, "*Running gauge coupling in three dimensions and the electroweak phase transition*", Nuclear Physics, Section B **408**, 91 (1993).

[66] B. J. Schaefer and J. Wambach, "*Renormalization group approach towards the QCD phase diagram*", Physics of Particles and Nuclei **39**, 1025 (2008), arXiv: 0611191 [hep-ph].

[67] M. F. Li and M. Luo, "*Functional renormalization flow and dynamical chiral symmetry breaking of QCD*", Physical Review D - Particles, Fields, Gravitation and Cosmology **85**, 1 (2012).

[68] B. J. Schaefer, "*Fluctuations and the QCD phase diagram*", Physics of Atomic Nuclei **75**, 741 (2012).

[69] T. Yokota, T. Kunihiro, and K. Morita, "*Functional renormalization group analysis of the soft mode at the QCD critical point*", Progress of Theoretical and Experimental Physics **2016**, 1 (2016), arXiv: 1603.02147.

[70] A. Eichhorn and T. Koslowski, "*Continuum limit in matrix models for quantum gravity from the functional renormalization group*", Physical Review D - Particles, Fields, Gravitation and Cosmology **88**, 1 (2013), arXiv: 1309.1690.

[71] A. Castro and T. A. Koslowski, "*Renormalization Group Approach to the Continuum Limit of Matrix Models of Quantum Gravity With Preferred Foliation*", Frontiers in Physics **9**, 1 (2021).

[72] K. G. Wilson, "*The renormalization group: Critical phenomena and the Kondo problem*", Reviews of Modern Physics **47**, 773 (1975).

[73] R. Hedden, V. Meden, T. Pruschke, and K. Schönhammer, "*A functional renormalization group approach to zero-dimensional interacting systems*", Journal of Physics Condensed Matter **16**, 5279 (2004).

[74] C. Karrasch, T. Enss, and V. Meden, "*Functional renormalization group approach to transport through correlated quantum dots*", Physical Review B **73**, 1 (2006).

[75] C. Karrasch, R. Hedden, R. Peters, T. Pruschke, K. Schönhammer, and V. Meden, "*A finite-frequency functional renormalization group approach to the single impurity Anderson model*", Journal of Physics Condensed Matter **20** (2008).

[76] C. Karrasch, S. Andergassen, and V. Meden, "*Supercurrent through a multilevel quantum dot close to singlet-triplet degeneracy*", Physical Review B **84**, 1 (2011).

[77] S. Andergassen, T. Enss, V. Meden, W. Metzner, U. Schollwöck, and K. Schönhammer, "*Functional renormalization group for Luttinger liquids with impurities*", Physical Review B **70**, 1 (2004), arXiv: 0403517 [cond-mat].

[78] S. Andergassen, T. Enss, V. Meden, W. Metzner, U. Schollwöck, and K. Schönhammer, "*Renormalization-group analysis of the one-dimensional extended Hubbard model with a single impurity*", Physical Review B **73**, 1 (2006).

[79] W. Metzner, "*Functional renormalization group computation of interacting fermi systems*", Progress of Theoretical Physics Supplement **160**, 58 (2005).

[80] C. J. Halboth and W. Metzner, "*Renormalization-group analysis of the two-dimensional Hubbard model*", Physical Review B **61**, 7364 (2000).

[81] C. Hille, F. B. Kugler, C. J. Eckhardt, Y. Y. He, A. Kauch, C. Honerkamp, A. Toschi, and S. Andergassen, "*Quantitative functional renormalization group description of the two-dimensional Hubbard model*", Physical Review Research **2**, 33372 (2020), arXiv: 2002.02733.

[82] C. Hille, D. Rohe, C. Honerkamp, and S. Andergassen, "*Pseudogap opening in the two-dimensional Hubbard model: A functional renormalization group analysis*", Physical Review Research **2**, 33068 (2020), arXiv: 2003.01447.

[83] D. Zanchi and H. Schulz, "*Weakly correlated electrons on a square lattice: Renormalization-group theory*", Physical Review B **61**, 13609 (2000).

[84] C. Honerkamp and M. Salmhofer, "*Temperature-flow renormalization group and the competition between superconductivity and ferromagnetism*", Physical Review B **64** (2001), arXiv: 0105218 [cond-mat].

[85] C. Honerkamp, M. Salmhofer, N. Furukawa, and T. M. Rice, "*Breakdown of the landau-fermi liquid in two dimensions due to umklapp scattering*", Physical Review B **63**, 1 (2001).

[86] C. Honerkamp, "*Electron-doping versus hole-doping in the 2D $t - t'$ Hubbard model*", European Physical Journal B **21**, 81 (2001), arXiv: 0103172 [cond-mat].

[87] C. Honerkamp, "*Density waves and cooper pairing on the honeycomb lattice*", Physical Review Letters **100**, 1 (2008).

[88] S. Uebelacker and C. Honerkamp, "*Self-energy feedback and frequency-dependent interactions in the functional renormalization group flow for the two-dimensional Hubbard model*", Physical Review B **86**, 1 (2012), arXiv: 1209.3947.

[89] A. Eberlein and W. Metzner, "*Superconductivity in the two-dimensional t - t' -Hubbard model*", Physical Review B **89**, 1 (2014), arXiv: 1308.4845.

[90] A. Tagliavini, C. Hille, F. B. Kugler, S. Andergassen, A. Toschi, and C. Honerkamp, "*Multiloop functional renormalization group for the two-dimensional Hubbard model: Loop convergence of the response functions*", SciPost Physics **6**, 1 (2019), arXiv: 1807.02697.

[91] C. Platt, W. Hanke, and R. Thomale, "*Functional renormalization group for multi-orbital Fermi surface instabilities*", Advances in Physics **62**, 453 (2013), arXiv: 1310.6191.

[92] H. Zhai, F. Wang, and D. H. Lee, "*Antiferromagnetically driven electronic correlations in iron pnictides and cuprates*", Physical Review B **80**, 1 (2009), arXiv: 0905.1711.

[93] R. Thomale, C. Platt, W. Hanke, J. Hu, and B. A. Bernevig, "*Exotic d-wave superconducting state of strongly hole-doped $K_xBa_{1-x}Fe_2As_2$*", Physical Review Letters **107**, 1 (2011).

[94] R. Thomale, C. Platt, W. Hanke, and B. A. Bernevig, "*Mechanism for explaining differences in the order parameters of FeAs-based and FeP-based pnictide superconductors*", Physical Review Letters **106**, 1 (2011).

[95] C. Platt, R. Thomale, C. Honerkamp, S. C. Zhang, and W. Hanke, "*Mechanism for a pairing state with time-reversal symmetry breaking in iron-based superconductors*", Physical Review B **85**, 3 (2012), arXiv: 1106.5964.

[96] C. Platt, G. Li, M. Fink, W. Hanke, and R. Thomale, "*Evolution of superconducting gap anisotropy in hole-doped 122 iron pnictides*", Physica Status Solidi (B) Basic Research **254** (2017), arXiv: 1607.00412.

[97] M. Klett *et al.*, "*From high T_c to low T_c: Multiorbital effects in transition metal oxides*", Physical Review B **104**, 1 (2021), arXiv: 2101.04689.

[98] J. Reuther and P. Wölfle, "*J_1-J_2 frustrated two-dimensional Heisenberg model: Random phase approximation and functional renormalization group*", Physical Review B **81**, 144410 (2009), arXiv: 0912.0860.

[99] J. Reuther, "*Frustrated quantum Heisenberg antiferromagnets: functional renormalization-group approach in auxiliary-fermion representation*", PhD thesis, 2011.

[100] M. Salmhofer, C. Honerkamp, W. Metzner, and O. Lauscher, "*Renormalization group flows into phases with broken symmetry*", Progress of Theoretical Physics **112**, 943 (2004).

[101] W. Metzner, M. Salmhofer, C. Honerkamp, V. Meden, and K. Schönhammer, "*Functional renormalization group approach to correlated fermion systems*", Reviews of Modern Physics **84**, 299 (2012), arXiv: 1105.5289.

[102] N. Dupuis, L. Canet, A. Eichhorn, W. Metzner, J. M. Pawlowski, M. Tissier, and N. Wschebor, "*The nonperturbative functional renormalization group and its applications*", Physics Reports **910**, 1 (2021), arXiv: 2006.04853.

[103] P. Kopietz, L. Bartosch, and F. Schütz, *Introduction to the Functional Renormalization Group*, vol. 798, Lecture Notes in Physics, (Berlin, Heidelberg: Springer Berlin Heidelberg, 2010) arXiv: 1211.6245.

[104] H. J. Maris and L. P. Kadanoff, *Teaching the renormalization group*, 1993.

[105] J. W. Negele and H. Orland, "*Quantum many-particle systems*", Quantum Many-Particle Systems, 1 (2018).

[106] A. A. Katanin, "*Fulfillment of Ward identities in the functional renormalization group approach*", Physical Review B **70**, 115109 (2004), arXiv: 0402602 [cond-mat].

[107] V. Meden, *Functional Renormalization Group*, URL: https://www.statphys.rwth-aachen.de/go/id/qygs/lidx/1/.

[108] E. Noether, "*Invariante Variationsprobleme*", Nachrichten von der Gesellschaft der Wissenschaften zu Göttingen, Mathematisch-Physikalische Klasse, 248 (1918).

[109] M. Hering, "*New States of Matter in Strongly Frustrated Quantum Magnets*", PhD thesis, 2018.

[110] M. L. Baez, "*Numerical methods for frustrated magnetism : From quantum to classical spin systems*", PhD thesis, 2018.

[111] F. L. Buessen, V. Noculak, S. Trebst, and J. Reuther, "*Functional renormalization group for frustrated magnets with nondiagonal spin interactions*", Physical Review B **100**, 125164 (2019), arXiv: 1905.04190.

[112] F. L. Buessen and S. Trebst, "*Competing magnetic orders and spin liquids in two- and three-dimensional kagome systems: Pseudofermion functional renormalization group perspective*", Physical Review B **94**, 235138 (2016), arXiv: 1609.01650.

[113] M. Hering and J. Reuther, "*Functional renormalization group analysis of Dzyaloshinsky-Moriya and Heisenberg spin interactions on the kagome lattice*", Physical Review B **95**, 54418 (2017), arXiv: 1610.09149.

[114] A. Keleş and E. Zhao, "*Renormalization group analysis of dipolar Heisenberg model on square lattice*", Physical Review B **97**, 1 (2018), arXiv: 1803.02904.

[115] A. Keleş and E. Zhao, "*Absence of Long-Range Order in a Triangular Spin System with Dipolar Interactions*", Physical Review Letters **120**, 187202 (2018), arXiv: 1801.00842.

[116] F. L. Buessen and Y. B. Kim, "*Functional renormalization group study of the Kitaev-Γ model on the honeycomb lattice and emergent incommensurate magnetic correlations*", Physical Review B **103**, 1 (2021), arXiv: 2101.04685.

[117] M. Hering, V. Noculak, F. Ferrari, Y. Iqbal, and J. Reuther, "*Dimerization tendencies of the pyrochlore Heisenberg antiferromagnet: A functional renormalization group perspective*", **054426**, 1 (2021), arXiv: 2110.08160.

[118] A. Keleş and E. Zhao, "*Rise and fall of plaquette order in the Shastry-Sutherland magnet revealed by pseudofermion functional renormalization group*", Physical Review B **105**, 1 (2022).

[119] J. Reuther and R. Thomale, "*Functional renormalization group for the anisotropic triangular antiferromagnet*", Physical Review B **83**, 24402 (2011), arXiv: 1006.3622.

[120] J. Reuther, D. A. Abanin, and R. Thomale, "*Magnetic order and paramagnetic phases in the quantum J_1-J_2-J_3 honeycomb model*", Physical Review B **84**, 14417 (2011), arXiv: 1103.0859.

[121] J. Reuther, P. Wölfle, R. Darradi, W. Brenig, M. Arlego, and J. Richter, "*Quantum phases of the planar antiferromagnetic J_1-J_2-J_3 Heisenberg model*", Physical Review B **83**, 64416 (2011), arXiv: 1010.3098.

[122] J. Reuther, R. Thomale, and S. Trebst, "*Finite-temperature phase diagram of the Heisenberg-Kitaev model*", Physical Review B **84**, 100406 (2011), arXiv: 1105.2005.

[123] R. Suttner, C. Platt, J. Reuther, and R. Thomale, "*Renormalization group analysis of competing quantum phases in the J_1 - J_2 Heisenberg model on the kagome lattice*", Physical Review B **89**, 20408 (2014), arXiv: 1303.0579.

[124] Y. Iqbal, W. J. Hu, R. Thomale, D. Poilblanc, and F. Becca, "*Spin liquid nature in the Heisenberg J_1-J_2 triangular antiferromagnet*", Physical Review B **93**, 144411 (2016), arXiv: 1601.06018.

[125] Y. Iqbal, R. Thomale, F. Parisen Toldin, S. Rachel, and J. Reuther, "*Functional renormalization group for three-dimensional quantum magnetism*", Physical Review B **94**, 140408 (2016), arXiv: 1604.03438.

[126] Y. Iqbal, P. Ghosh, R. Narayanan, B. Kumar, J. Reuther, and R. Thomale, "*Intertwined nematic orders in a frustrated ferromagnet*", Physical Review B **94**, 224403 (2016), arXiv: 1608.03751.

[127] J. Reuther, R. Thomale, and S. Rachel, "*Spiral order in the honeycomb iridate Li_2IrO_3*", Physical Review B **90**, 100405 (2014), arXiv: 1404.5818.

[128] K. Iida *et al.*, "*$q = 0$ long-range magnetic order in centennialite $CaCu_3(OD)_6Cl_2 \cdot 0.6\,D_2O$: A spin-$\frac{1}{2}$ perfect kagome antiferromagnet with J_1–J_2–J_d*", Physical Review B **101**, 220408 (2020).

[129] D. Kiese, F. L. Buessen, C. Hickey, S. Trebst, and M. M. Scherer, "*Emergence and stability of spin-valley entangled quantum liquids in moiré heterostructures*", Physical Review Research **2**, 1 (2020), arXiv: 1907.09490.

[130] M. Hering, F. Ferrari, A. Razpopov, I. I. Mazin, R. Valenti, H. O. Jeschke, and J. Reuther, "*Distorted kagome antiferromagnet: Phase diagram and application to Y-kapellasite*", 1 (2021), arXiv: 2107.13570.

[131] Y. Iqbal, H. O. Jeschke, J. Reuther, R. Valentí, I. I. Mazin, M. Greiter, and R. Thomale, "*Paramagnetism in the kagome compounds (Zn, Mg, Cd)$Cu_3(OH)_6Cl_2$*", Physical Review B **92**, 1 (2015), arXiv: 1506.03436.

[132] I. Rousochatzakis, J. Reuther, R. Thomale, S. Rachel, and N. B. Perkins, "*Phase diagram and quantum order by disorder in the kitaev K_1 - K_2 honeycomb magnet*", Physical Review X **5**, 1 (2015), arXiv: 1506.09185.

[133] C. Balz *et al.*, "*Physical realization of a quantum spin liquid based on a complex frustration mechanism*", Nature Physics **12**, 942 (2016), arXiv: 1606.06463.

[134] Y. Iqbal, T. Müller, K. Riedl, J. Reuther, S. Rachel, R. Valentí, M. J. Gingras, R. Thomale, and H. O. Jeschke, "*Signatures of a gearwheel quantum spin liquid in a spin-$\frac{1}{2}$ pyrochlore molybdate Heisenberg antiferromagnet*", Physical Review Materials **1**, 71201 (2017), arXiv: 1705.05291.

[135] A. Revelli *et al.*, "*Spin-orbit entangled $j = \frac{1}{2}$ moments in Ba_2CeIrO_6: A frustrated fcc quantum magnet*", Physical Review B **100**, 1 (2019), arXiv: 1901.06215.

[136] G. Li, N. Wentzell, P. Pudleiner, P. Thunström, and K. Held, "*Efficient implementation of the parquet equations: Role of the reducible vertex function and its kernel approximation*", Physical Review B **93**, 1 (2016), arXiv: 1510.03330.

[137] N. Wentzell, G. Li, A. Tagliavini, C. Taranto, G. Rohringer, K. Held, A. Toschi, and S. Andergassen, "*High-frequency asymptotics of the vertex function: Diagrammatic parametrization and algorithmic implementation*", Physical Review B **102**, 85106 (2020), arXiv: 1610.06520.

[138] C. Honerkamp, D. Rohe, S. Andergassen, and T. Enss, "*Interaction flow method for many-fermion systems*", Physical Review B **70**, 1 (2004).

[139] D. Kiese, T. Müller, Y. Iqbal, R. Thomale, and S. Trebst, "*Multiloop functional renormalization group approach to quantum spin systems*" (2020), arXiv: 2011.01269.

[140] J. Thoenniss, M. K. Ritter, F. B. Kugler, J. von Delft, and M. Punk, "*Multiloop pseudofermion functional renormalization for quantum spin systems: Application to the spin-$\frac{1}{2}$ kagome Heisenberg model*" (2020), arXiv: 2011.01268.

[141] T. R. Morris, "*The Exact Renormalization Group and Approximate Solutions*", International Journal of Modern Physics A **09**, 2411 (1994), arXiv: 9308265 [hep-ph].

[142] K. U. Giering and M. Salmhofer, "*Self-energy flows in the two-dimensional repulsive Hubbard model*", Physical Review B **86**, 1 (2012).

[143] J. Reuther and R. Thomale, "*Cluster functional renormalization group*", Physical Review B **89**, 024412 (2014), arXiv: 1309.3262.

[144] D. Bergeron and A. M. Tremblay, "*Algorithms for optimized maximum entropy and diagnostic tools for analytic continuation*", Physical Review E **94**, 1 (2016), arXiv: 1507.01012.

[145] D. Roscher, N. Gneist, M. M. Scherer, S. Trebst, and S. Diehl, "*Cluster functional renormalization group and absence of a bilinear spin liquid in the J_1-J_2 Heisenberg model*", Physical Review B **100**, 125130 (2019), arXiv: 1905.01060.

[146] V. N. Popov and S. A. Fedotov, "*The functional-integration method and diagram technique for spin systems*", Zh. Eksp. Teor. Fiz **22**, 183 (1987).

[147] N. V. Prokofev and B. V. Svistunov, "*From the Popov-Fedotov case to universal fermionization*", Physical Review B **84**, 1 (2011).

[148] M. L. Baez and J. Reuther, "*Numerical treatment of spin systems with unrestricted spin length S: A functional renormalization group study*", Physical Review B **96**, 45144 (2017), arXiv: 1612.05074.

[149] F. L. Buessen, D. Roscher, S. Diehl, and S. Trebst, "*Functional renormalization group approach to SU(N) Heisenberg models: Real-space renormalization group at arbitrary N*", Physical Review B **97**, 1 (2018), arXiv: 1711.02182.

[150] D. P. Arovas and A. Auerbach, "*Functional integral theories of low-dimensional quantum Heisenberg models*", Physical Review B **38**, 316 (1988).

[151] D. Roscher, F. L. Buessen, M. M. Scherer, S. Trebst, and S. Diehl, "*Functional renormalization group approach to SU(N) Heisenberg models: Momentum-space RG for the large-N limit*", Physical Review B **97**, 064416 (2017), arXiv: 1711.02183.

[152] R. Thomale, E. Kapit, D. F. Schroeter, and M. Greiter, "*Parent Hamiltonian for the chiral spin liquid*", Physical Review B **80**, 1 (2009).

[153] F. B. Kugler and J. Von Delft, "*Multiloop functional renormalization group for general models*", Physical Review B **97**, 1 (2018), arXiv: 1707.04536.

[154] I. Diatlov, V. Sudakov, and K. Ter-Martirosian, "*Asymptotic Meson-Meson Scattering Theory*", Soviet Physics JETP **Vol: 5**, 631 (1957).

[155] F. B. Kugler and J. Von Delft, "*Multiloop Functional Renormalization Group That Sums Up All Parquet Diagrams*", Physical Review Letters **120**, 57403 (2018), arXiv: 1703.06505.

[156] F. B. Kugler and J. V. Delft, "*Derivation of exact flow equations from the self-consistent parquet relations*", New Journal of Physics **20**, 099601 (2018), arXiv: 1807.02898.

[157] M. Rück and J. Reuther, "*Effects of two-loop contributions in the pseudofermion functional renormalization group method for quantum spin systems*", Physical Review B **97**, 1 (2018), arXiv: 1712.02535.

[158] A. Eberlein, "*Fermionic two-loop functional renormalization group for correlated fermions: Method and application to the attractive Hubbard model*", Physical Review B **90**, 1 (2014), arXiv: 1406.3178.

[159] A. A. Katanin, "*Two-loop functional renormalization group approach to the one- and two-dimensional Hubbard model*", Physical Review B **79**, 1 (2009).

[160] K. Veschgini and M. Salmhofer, "*Schwinger-Dyson renormalization group*", Physical Review B **88** (2013), arXiv: 1306.4346.

[161] F. L. Buessen, "*The SpinParser software for pseudofermion functional renormalization group calculations on quantum magnets*", 1 (2021), arXiv: arXiv:2109.13317v1.

[162] D. Kiese, T. Müller, and L. Gresista, *PFFRGSolver.jl repository*, URL: https://github.com/dominikkiese/PFFRGSolver.jl.

[163] M. K. Ritter, D. Kiese, T. Müller, F. B. Kugler, R. Thomale, S. Trebst, and J. v. Delft, "*Benchmark Calculations of Multiloop Pseudofermion fRG*" (2022), arXiv: arXiv:2203.13007v1.

[164] P. Bogacki and L. F. Shampine, "*A 3(2) pair of Runge - Kutta formulas*", Applied Mathematics Letters **2**, 321 (1989).

[165] J. Beyer, F. Goth, and T. Müller, "*Better Integrators for Functional Renormalization Group Calculations*" (2022), arXiv: 2203.15306v1.

[166] P. Sindzingre, L. Seabra, N. Shannon, and T. Momoi, "*Phase diagram of the spin-1/2 J_1-J_2-J_3 Heisenberg model on the square lattice with ferromagnetic J_1*", Journal of Physics: Conference Series **145** (2009).

[167] P. Sindzingre, N. Shannon, and T. Momoi, "*Phase diagram of the spin-1/2 J_1-J_2-J_3 Heisenberg model on the square lattice*", Journal of Physics: Conference Series **200**, 8 (2010), arXiv: 0907.4163.

[168] R. Schmidt, J. Schulenburg, J. Richter, and D. D. Betts, "*Spin-$\frac{1}{2}$ J_1-J_2 model on the body-centered cubic lattice*", Physical Review B **66**, 1 (2002), arXiv: 0203085 [cond-mat].

[169] J. Villain, "*A magnetic analogue of stereoisomerism : application to helimagnetism in two dimensions*", Journal de Physique **38**, 385 (1977).

[170] B. Danu, G. Nambiar, and R. Ganesh, "*Extended degeneracy and order by disorder in the square lattice J_1-J_2-J_3 model*", Physical Review B **94**, 1 (2016), arXiv: 1603.06599.

[171] A. N. Ignatenko and V. Y. Irkhin, "*Frustrated Heisenberg antiferromagnets on cubic lattices: Magnetic structures, exchange gaps, and non-conventional critical behaviour*", Journal of Siberian Federal University - Mathematics and Physics **9**, 454 (2016), arXiv: 1611.06305.

[172] E. F. Shender, "*Anti-Ferromagnetic Garnets with Fluctuation-Like Interacting Sub-Lattices*", Sov. Phys. JETP **56**, 178 (1982).

[173] P. Müller, J. Richter, A. Hauser, and D. Ihle, "*Thermodynamics of the frustrated J_1-J_2 Heisenberg ferromagnet on the body-centered cubic lattice with arbitrary spin*", European Physical Journal B **88** (2015), arXiv: 1505.07219.

[174] R. A. Tahir-Kheli and H. S. Jarrett, "*Ferromagnetic Curie temperature in cubic lattices with next-nearest-neighbor interaction*", Physical Review **135**, 1096 (1964).

[175] D. J. Farnell, O. Götze, and J. Richter, "*Ground-state ordering of the J_1-J_2 model on the simple cubic and body-centered cubic lattices*", Physical Review B **93**, 1 (2016), arXiv: 1606.00388.

[176] K. Majumdar and T. Datta, "*Non-linear spin wave theory results for the frustrated S=$\frac{1}{2}$ Heisenberg antiferromagnet on a body-centered cubic lattice*", Journal of Physics: Condensed Matter **21**, 406004 (2009), arXiv: 0906.0960.

[177] M. R. Pantić, D. V. Kapor, S. M. Radošević, and P. M. Mali, "*Phase diagram of spin-$\frac{1}{2}$ quantum Heisenberg J_1 - J_2 antiferromagnet on the body-centered-cubic lattice in random phase approximation*", Solid State Communications **182**, 55 (2014), arXiv: 1310.4961.

[178] J. Oitmaa and W. Zheng, "*Phase diagram of the bcc $S = \frac{1}{2}$ Heisenberg antiferromagnet with first and second neighbor exchange*", Physical Review B **69**, 1 (2004), arXiv: 0310054 [cond-mat].

[179] E. Nagaev, "*First-order magnetic phase transitions and meta-magnetism of quantum origin*", JETP Lett **39** (1984).

[180] M. I. Kaganov and A. V. Chubukov, "*Interacting magnons*", Soviet Physics - Uspekhi **30**, 1015 (1987).

[181] G. S. Rushbrooke, G. A. Baker Jr., and P. A. Wood, "*Heisenberg Model*", *Phase transitions and critical phenomena*, (1974) pp. 246–356.

[182] J. Oitmaa and E. Bornilla, "*High-temperature-series study of the spin-$\frac{1}{2}$ Heisenberg ferromagnet*", Physical Review B **53**, 14228 (1996).

[183] J. Oitmaa and W. Zheng, "*Curie and Néel temperatures of quantum magnets*", Journal of Physics Condensed Matter **16**, 8653 (2004), arXiv: 0409041 [cond-mat].

[184] J. Richter, P. Müller, A. Lohmann, and H. J. Schmidt, "*High-temperature Expansion for Frustrated Magnets: Application to the J_1-J_2 Model on the BCC Lattice*", Physics Procedia **75**, 813 (2015), arXiv: 1609.06837.

[185] K. Chen, A. M. Ferrenberg, and D. P. Landau, "*Static critical behavior of three-dimensional classical Heisenberg models: A high-resolution Monte Carlo study*", Physical Review B **48**, 3249 (1993).

[186] R. Moessner and J. T. Chalker, "*Properties of a classical spin liquid: The heisenberg pyrochlore antiferromagnet*", Physical Review Letters **80**, 2929 (1998), arXiv: 9712063 [cond-mat].

[187] R. Moessner and J. Chalker, "*Low-temperature properties of classical geometrically frustrated antiferromagnets*", Physical Review B **58**, 12049 (1998), arXiv: 9807384 [cond-mat].

[188] A. P. Ramirez, A. Hayashi, R. J. Cava, R. Siddharthan, and B. S. Shastry, "*Zero-point entropy in 'spin ice'*", Nature **399**, 333 (1999).

[189] S. T. Bramwell and M. J. Gingras, "*Spin ice state in frustrated magnetic pyrochlore materials*", Science **294**, 1495 (2001), arXiv: 0201427 [cond-mat].

[190] L. Pauling, "*The Structure and Entropy of Ice and of Other Crystals with Some Randomness of Atomic Arrangement*", Journal of the American Chemical Society **57**, 2680 (1935).

[191] D. Tsuneishi, M. Ioki, and H. Kawamura, "*Novel ordering of the pyrochlore Heisenberg antiferromagnet with the ferromagnetic next-nearest-neighbour interaction*", Journal of Physics Condensed Matter **19** (2007), arXiv: 0609655 [cond-mat].

[192] T. Nakamura and D. Hirashima, "*Classical antiferromagnet on the pyrochlore lattice*", Journal of Magnetism and Magnetic Materials **310**, 1297 (2007).

[193] G. W. Chern, R. Moessner, and O. Tchernyshyov, "*Partial order from disorder in a classical pyrochlore antiferromagnet*", Physical Review B **78**, 144418 (2008), arXiv: 0803.2332.

[194] T. Okubo, T. H. Nguyen, and H. Kawamura, "*Cubic and noncubic multiple-q states in the Heisenberg antiferromagnet on the pyrochlore lattice*", Physical Review B **84**, 144432 (2011), arXiv: 1107.5440.

[195] L. Messio, C. Lhuillier, and G. Misguich, "*Lattice symmetries and regular magnetic orders in classical frustrated antiferromagnets*", Physical Review B **83**, 184401 (2011), arXiv: 1101.1212.

[196] B. Canals and C. Lacroix, "*Pyrochlore antiferromagnet: A three-dimensional quantum spin liquid*", Physical Review Letters **80**, 2933 (1998), arXiv: 9807407 [cond-mat].

[197] B. Canals and C. Lacroix, "*Quantum spin liquid: The Heisenberg antiferromagnet on the three-dimensional pyrochlore lattice*", Physical Review B **61**, 1149 (2000).

[198] Y. Huang, K. Chen, Y. Deng, N. Prokof'Ev, and B. Svistunov, "*Spin-Ice State of the Quantum Heisenberg Antiferromagnet on the Pyrochlore Lattice*", Physical Review Letters **116**, 177203 (2016), arXiv: 1511.08285.

[199] M. Taillefumier, O. Benton, H. Yan, L. D. Jaubert, and N. Shannon, "*Competing spin liquids and hidden spin-nematic order in spin ice with frustrated transverse exchange*", Physical Review X **7**, 41057 (2017), arXiv: 1705.00148.

[200] V. R. Ravi Chandra and J. Sahoo, "*Spin-$\frac{1}{2}$ Heisenberg antiferromagnet on the pyrochlore lattice: An exact diagonalization study*", Physical Review B **97**, 1 (2018), arXiv: 1710.11316.

[201] P. Müller, A. Lohmann, J. Richter, and O. Derzhko, "*Thermodynamics of the pyrochlore-lattice quantum Heisenberg antiferromagnet*", Physical Review B **100**, 1 (2019), arXiv: 1901.09194.

[202] C. Liu, G. B. Halász, and L. Balents, "*Symmetric U(1) and $\mathbb{Z}_2$ spin liquids on the pyrochlore lattice*", Physical Review B **104** (2021), arXiv: 2105.12726.

[203] J. H. Kim and J. H. Han, "*Chiral spin states in the pyrochlore Heisenberg magnet: Fermionic mean-field theory and variational Monte Carlo calculations*", Physical Review B **78**, 180410 (2008).

[204] F. J. Burnell, S. Chakravarty, and S. L. Sondhi, "*Monopole flux state on the pyrochlore lattice*", Physical Review B **79**, 144432 (2009), arXiv: 0809.0528.

[205] B. Schneider, J. C. Halimeh, and M. Punk, " *Projective symmetry group classification of chiral $\mathbb{Z}_2$ spin liquids on the pyrochlore lattice: Application to the spin-$\frac{1}{2}$ XXZ Heisenberg model* ", Physical Review B **105**, 1 (2022), arXiv: 2107.13574.

[206] A. B. Harris, A. J. Berlinsky, and C. Bruder, "*Ordering by quantum fluctuations in a strongly frustrated Heisenberg antiferromagnet*", Journal of Applied Physics **69**, 5200 (1991).

[207] B. Normand and Z. Nussinov, "*Fermionic spinon and holon statistics in the pyrochlore quantum spin liquid*", Physical Review B **93**, 115122 (2016).

[208] M. Isoda and S. Mori, "*Valence-bond crystal and anisotropic excitation spectrum on 3-dimensionally frustrated pyrochlore*", Journal of the Physical Society of Japan **67**, 4022 (1998).

[209] A. Koga and N. Kawakami, "*Frustrated Heisenberg antiferromagnet on the pyrochlore lattice*", Physical Review B **63**, 144432 (2001), arXiv: 0010138 [cond-mat].

[210] H. Tsunetsugu, "*Antiferromagnetic Quantum Spins on the Pyrochlore Lattice*", Journal of the Physical Society of Japan **70**, 640 (2001), arXiv: 0103231 [cond-mat].

[211] H. Tsunetsugu, "*Spin-singlet order in a pyrochlore antiferromagnet*", Physical Review B **65**, 1 (2002).

[212] J. B. Fouet, M. Mambrini, P. Sindzingre, and C. Lhuillier, "*Planar pyrochlore: A valence-bond crystal*", Physical Review B **67**, 54411 (2003), arXiv: 0108070 [cond-mat].

[213] E. Berg, E. Altman, and A. Auerbach, "*Singlet Excitations in Pyrochlore: A Study of Quantum Frustration*", Physical Review Letters **90**, 4 (2003), arXiv: 0206384 [cond-mat].

[214] R. Moessner, S. L. Sondhi, and M. O. Goerbig, "*Quantum dimer models and effective Hamiltonians on the pyrochlore lattice*", Physical Review B **73**, 94430 (2006), arXiv: 0508504 [cond-mat].

[215] B. Normand and Z. Nussinov, "*Hubbard model on the pyrochlore lattice: A 3D quantum spin liquid*", Physical Review Letters **112**, 207202 (2014), arXiv: 1308.3186.

[216] I. Hagymasi, R. Schafer, R. Moessner, and D. J. Luitz, "*Possible Inversion Symmetry Breaking in the $S = 1/2$ Pyrochlore Heisenberg Magnet*", Physical Review Letters **126**, 117204 (2021), arXiv: 2010.03563.

[217] N. Astrakhantsev, T. Westerhout, A. Tiwari, K. Choo, A. Chen, M. H. Fischer, G. Carleo, and T. Neupert, "*Broken-Symmetry Ground States of the Heisenberg Model on the Pyrochlore Lattice*", Physical Review X **11**, 41021 (2021), arXiv: 2101.08787.

[218] P. H. Conlon and J. T. Chalker, "*Absent pinch points and emergent clusters: Further neighbor interactions in the pyrochlore Heisenberg antiferromagnet*", Physical Review B **81**, 224413 (2010), arXiv: 1003.4176.

[219] C. L. Henley, "*Ordering due to disorder in a frustrated vector antiferromagnet*", Physical Review Letters **62**, 2056 (1989).

[220] A. V. Chubukov, "*On the quantum effects in helimagnets*", Journal of Physics C: Solid State Physics **17** (1984).

[221] P. Müller, A. Lohmann, J. Richter, O. Menchyshyn, and O. Derzhko, "*Thermodynamics of the pyrochlore Heisenberg ferromagnet with arbitrary spin S*", Physical Review B **96**, 174419 (2017), arXiv: 1707.01529.

[222] M. Troyer, F. Alet, and S. Wessel, "*Histogram methods for quantum systems: From reweighting to Wang-Landau sampling*", Brazilian Journal of Physics **34**, 377 (2004).

[223] S. Wessel, "*Critical entropy of quantum Heisenberg magnets on simple-cubic lattices*", Physical Review B **81**, 52405 (2010), arXiv: 0912.3990.

[224] K. Soldatov, K. Nefedev, Y. Komura, and Y. Okabe, "*Large-scale calculation of ferromagnetic spin systems on the pyrochlore lattice*", Physics Letters, Section A: General, Atomic and Solid State Physics **381**, 707 (2017), arXiv: 1612.08312.

[225] P. Peczak, A. M. Ferrenberg, and D. P. Landau, "*High-accuracy Monte Carlo study of the three-dimensional classical Heisenberg ferromagnet*", Physical Review B **43**, 6087 (1991).

[226] A. Lohmann, H. J. Schmidt, and J. Richter, "*Tenth-order high-temperature expansion for the susceptibility and the specific heat of spin-s Heisenberg models with arbitrary exchange patterns: Application to pyrochlore and kagome magnets*", Physical Review B **89**, 14415 (2014), arXiv: 1309.0940.

[227] T. Hutak, P. Müller, J. Richter, T. Krokhmalskii, and O. Derzhko, "*The spin-1/2 Heisenberg ferromagnet on the pyrochlore lattice: A Green's function study*", Condensed Matter Physics **21**, 33705 (2018), arXiv: 1809.09951.

[228] S. V. Tyablikov, *Methods in the Quantum Theory of Magnetism*, (Plenum, New York, 1967)

[229] D. Schmalfuß, J. Richter, and D. Ihle, "*Green's function theory of quasi-two-dimensional spin-half Heisenberg ferromagnets: Stacked square versus stacked kagomé lattices*", Physical Review B **72**, 3 (2005), arXiv: 0504662 [cond-mat].

[230] P. Müller, J. Richter, and D. Ihle, "*Thermodynamics of frustrated ferromagnetic spin-$\frac{1}{2}$ Heisenberg chains: Role of interchain coupling*", Physical Review B **95**, 134407 (2017), arXiv: 1703.04573.

[231] D. A. Huse, W. Krauth, R. Moessner, and S. L. Sondhi, "*Coulomb and liquid dimer models in three dimensions*", Physical Review Letters **91**, 167004 (2003), arXiv: 0305318 [cond-mat].

[232] R. Moessner and L. Sondhi, "*Three-dimensional resonating-valence-bond liquids and their excitations*", Physical Review B **68**, 1 (2003), arXiv: 0307592 [cond-mat].

[233] C. L. Henley, "*The "Coulomb phase" in frustrated systems*", Annual Review of Condensed Matter Physics **1**, 179 (2010), arXiv: 0912.4531.

[234] K. W. Plumb, H. J. Changlani, A. Scheie, S. Zhang, J. W. Krizan, J. A. Rodriguez-Rivera, Y. Qiu, B. Winn, R. J. Cava, and C. L. Broholm, "*Continuum of quantum fluctuations in a three-dimensional $S = 1$ Heisenberg magnet*", Nature Physics **15**, 54 (2019), arXiv: 1711.07509.

[235] S. Zhang, H. J. Changlani, K. W. Plumb, O. Tchernyshyov, and R. Moessner, "*Dynamical Structure Factor of the Three-Dimensional Quantum Spin Liquid Candidate $NaCaNi_2F_7$*", Physical Review Letters **122**, 167203 (2019), arXiv: 1810.09481.

[236] R. Schäfer, I. Hagymási, R. Moessner, and D. J. Luitz, "*Pyrochlore $S{=}\frac{1}{2}$ Heisenberg antiferromagnet at finite temperature*", Physical Review B **102**, 1 (2020), arXiv: 2003.04898.

[237] C. Liu, G. B. Halász, and L. Balents, "*Competing orders in pyrochlore magnets from a $\mathbb{Z}_2$ spin liquid perspective*", Physical Review B **100**, 75125 (2019), arXiv: 1905.00460.

[238] A. W. Sandvik, "*Critical temperature and the transition from quantum to classical order parameter fluctuations in the three-dimensional heisenberg antiferromagnet*", Physical Review Letters **80**, 5196 (1998), arXiv: 9804234 [cond-mat].

[239] M. Salmhofer and C. Honerkamp, "*Fermionic renormalization group flows: Technique and theory*", Progress of Theoretical Physics **105**, 1 (2001).

[240] M. Hering, J. Sonnenschein, Y. Iqbal, and J. Reuther, "*Characterization of quantum spin liquids and their spinon band structures via functional renormalization*", Physical Review B **99**, 1 (2019), arXiv: 1806.05021.

[241] N. Niggemann, M. Hering, and J. Reuther, "*Classical spiral spin liquids as a possible route to quantum spin liquids*", Journal of Physics Condensed Matter **32** (2020), arXiv: 1905.11318.

[242] J. Reuther, R. Thomale, and S. Rachel, "*Magnetic ordering phenomena of interacting quantum spin Hall models*", Physical Review B **86**, 1 (2012), arXiv: 1206.3103.

[243] D. Bergman, J. Alicea, E. Gull, S. Trebst, and L. Balents, "*Order-by-disorder and spiral spin-liquid in frustrated diamond-lattice antiferromagnets*", Nature Physics **3**, 487 (2007), arXiv: 0612001 [cond-mat].

[244] S. Gao *et al.*, "*Spiral spin-liquid and the emergence of a vortex-like state in $MnSc_2S_4$*", Nature Physics **13**, 157 (2017), arXiv: 1605.04199.

[245] S. B. Lee and L. Balents, "*Theory of the ordered phase in A-site antiferromagnetic spinels*", Physical Review B **78**, 1 (2008), arXiv: 0808.3010.

[246] L. Savary, E. Gull, S. Trebst, J. Alicea, D. Bergman, and L. Balents, "*Impurity effects in highly frustrated diamond-lattice antiferromagnets*", Physical Review B **84**, 1 (2011).

[247] J. B. Fouet, P. Sindzingre, and C. Lhuillier, "*An investigation of the quantum J_1-J_2-J_3 model on the honeycomb lattice*", Eur. Phys. J. B **20**, 241 (2001).

[248] A. Mulder, R. Ganesh, L. Capriotti, and A. Paramekanti, "*Spiral order by disorder and lattice nematic order in a frustrated Heisenberg antiferromagnet on the honeycomb lattice*", Physical Review B **81**, 1 (2010), arXiv: 1004.1119.

[249] J. Villain, R. Bidaux, J. P. Carton, and R. Conte, "*Order As an Effect of Disorder.*", Journal de physique Paris **41**, 1263 (1980).

[250] V. Fritsch, J. Hemberger, N. Büttgen, E. W. Scheidt, H. A. Krug Von Nidda, A. Loidl, and V. Tsurkan, "*Spin and Orbital Frustration in $MnSc_2S_4$ and $FeSc_2S_4$*", Physical Review Letters **92**, 2 (2004).

[251] S. Giri, H. Nakamura, and T. Kohara, "*Classical antiferromagnetism in $MnSc_2S_4$: A ^{45}Sc NMR study*", Physical Review B **72**, 3 (2005).

[252] A. Krimmel, M. Mücksch, V. Tsurkan, M. M. Koza, H. Mutka, C. Ritter, D. V. Sheptyakov, S. Horn, and A. Loidl, "*Magnetic ordering and spin excitations in the frustrated magnet $MnSc_2S_4$*", Physical Review B **73**, 1 (2006).

[253] G. M. Kalvius, O. Hartmann, D. R. Noakes, F. E. Wagner, R. Wäppling, U. Zimmermann, C. Baines, A. Krimmel, V. Tsurkan, and A. Loidl, "*A μ SR magnetic study of frustrated $FeSc_2S_4$ and $MnSc_2S_4$*", Physica B: Condensed Matter **378-380**, 592 (2006).

[254] M. Mücksch *et al.*, "*Multi-step magnetic ordering in frustrated thiospinel $MnSc_2S_4$*", Journal of Physics Condensed Matter **19** (2007).

[255] P. J. Brown, A. G. Fox, E. N. Maslen, M. A. O'Keefe, and B. T. M. Willis, "*Intensity of diffracted intensities*", International Tables for Crystallography, 554 (2006).

[256] A. N. Yaresko, "*Electronic band structure and exchange coupling constants in ACr_2X_4 spinels (A=Zn, Cd, Hg; X=O, S, Se)*", Physical Review B **77**, 1 (2008).

[257] Y. V. Tymoshenko *et al.*, "*Pseudo-goldstone magnons in the frustrated S=3/2 heisenberg helimagnet $ZnCr_2Se_4$ with a Pyrochlore Magnetic Sublattice*", Physical Review X **7**, 41049 (2017), arXiv: 1705.04642.

[258] J. E. Greedan, M. Sato, X. Yan, and F. S. Razavi, "*Spin-glass-like behavior in $Y_2Mo_2O_7$, a concentrated, crystalline system with negligible apparent disorder*", Solid State Communications **59**, 895 (1986).

[259] M. J. Gingras, C. V. Stager, N. P. Raju, B. D. Gaulin, and J. E. Greedan, "*Static Critical Behavior of the Spin-Freezing Transition in the Geometrically Frustrated Pyrochlore Antiferromagnet $Y_2Mo_2O_7$*", Physical Review Letters **78**, 947 (1997).

[260] J. S. Gardner, B. D. Gaulin, S. H. Lee, C. Broholm, N. P. Raju, and J. E. Greedan, "*Glassy statics and dynamics in the chemically ordered pyrochlore antiferromagnet $Y_2Mo_2O_7$*", Physical Review Letters **83**, 211 (1999).

[261] K. Miyoshi, Y. Nishimura, K. Honda, K. Fujiwara, and J. Takeuchi, "*Successive spin freezing behavior in a pyrochlore antiferromagnet $Y_2Mo_2O_7$ under magnetic fields*", Journal of the Physical Society of Japan **69**, 3517 (2000).

[262] N. Hanasaki, K. Watanabe, T. Ohtsuka, I. Kézsmárki, S. Iguchi, S. Miyasaka, and Y. Tokura, "*Nature of the transition between a ferromagnetic metal and a spin-glass insulator in pyrochlore molybdates*", Physical Review Letters **99**, 7 (2007).

[263] L. Clark, G. J. Nilsen, E. Kermarrec, G. Ehlers, K. S. Knight, A. Harrison, J. P. Attfield, and B. D. Gaulin, "*From Spin glass to quantum spin liquid ground states in molybdate pyrochlores*", Physical Review Letters **113**, 117201 (2014), arXiv: 1405.3172.

[264] H. J. Silverstein *et al.*, "*Liquidlike correlations in single-crystalline $Y_2Mo_2O_7$: An unconventional spin glass*", Physical Review B **89**, 54433 (2014).

[265] J. G. Rau and M. J. Gingras, "*Frustrated quantum rare-earth pyrochlores*", Annual Review of Condensed Matter Physics **10**, 357 (2019), arXiv: 1806.09638.

[266] C. Hickey, L. Cincio, Z. Papić, and A. Paramekanti, "*Emergence of chiral spin liquids via quantum melting of noncoplanar magnetic orders*", Physical Review B **96**, 1 (2017), arXiv: 1705.05381.

[267] I. Dzyaloshinsky, "*A thermodynamic theory of "weak" ferromagnetism of antiferromagnetics*", Journal of Physics and Chemistry of Solids **4**, 241 (1958).

[268] T. Moriya, "*Anisotropic superexchange interaction and weak ferromagnetism*", Physical Review **120**, 91 (1960).

[269] M. Elhajal, B. Canals, R. Sunyer, and C. Lacroix, "*Ordering in the pyrochlore antiferromagnet due to Dzyaloshinsky-Moriya interactions*", Physical Review B **71**, 94420 (2005).

[270] V. N. Kotov, M. Elhajal, M. E. Zhitomirsky, and F. Mila, "*Dzyaloshinsky-Moriya-induced order in the spin-liquid phase of the $S = 1/2$ pyrochlore antiferromagnet*", Physical Review B **72**, 1 (2005).

[271] S. Depenbrock, I. P. McCulloch, and U. Schollwöck, "*Nature of the spin-liquid ground state of the S=1/2 Heisenberg model on the kagome lattice*", Physical Review Letters **109**, 67201 (2012).

[272] T. Yavors'kii, T. Fennell, M. J. Gingras, and S. T. Bramwell, "*$Dy_2Ti_2O_7$ spin ice: A test case for emergent clusters in a frustrated magnet*", Physical Review Letters **101**, 1 (2008), arXiv: 0707.3477.

[273] S. H. Lee, C. Broholm, W. Ratcliff, G. Gasparovic, Q. Huang, T. H. Kim, and S. W. Cheong, "*Emergent excitations in a geometrically frustrated magnet*", Nature **418**, 856 (2002).

[274] S. Okumura, H. Kawamura, T. Okubo, and Y. Motome, "*Novel spin-liquid states in the frustrated heisenberg antiferromagnet on the honeycomb lattice*", Journal of the Physical Society of Japan **79**, 1 (2010), arXiv: 1004.4441.

[275] S. Bieri, L. Messio, B. Bernu, and C. Lhuillier, "*Gapless chiral spin liquid in a kagome Heisenberg model*", Phys. Rev. B **92**, 60407 (2015).

[276] S. Bieri, C. Lhuillier, and L. Messio, "*Projective symmetry group classification of chiral spin liquids*", Physical Review B **93**, 94437 (2016), arXiv: 1512.00324.

[277] C. J. Eckhardt, G. A. Schober, J. Ehrlich, and C. Honerkamp, "*Truncated-unity parquet equations: Application to the repulsive Hubbard model*", Physical Review B **98**, 1 (2018), arXiv: 1802.09797.

[278] N. K. Yirga and D. K. Campbell, "*Frequency-dependent functional renormalization group for interacting fermionic systems*", Physical Review B **103**, 1 (2021), arXiv: 2010.02163.

[279] L. V. Keldysh, "*Diagram technique for nonequilibrium processes*", Sov. Phys. JETP **20** (1965).

[280] R. Gezzi, T. Pruschke, and V. Meden, "*Functional renormalization group for nonequilibrium quantum many-body problems*", Physical Review B **75**, 1 (2007).

[281] C. Karrasch, M. Pletyukhov, L. Borda, and V. Meden, "*Functional renormalization group study of the interacting resonant level model in and out of equilibrium*", Physical Review B **81**, 31 (2010), arXiv: 0911.5165.

[282] S. G. Jakobs, M. Pletyukhov, and H. Schoeller, "*Nonequilibrium functional renormalization group with frequency-dependent vertex function: A study of the single-impurity Anderson model*", Physical Review B **81**, 1 (2010).

[283] J. Potten, "*Frequency-resolved functional renormalization group studies of two-dimensional quantum magnets*", MA thesis, 2022.

[284] N. Niggemann, B. Sbierski, and J. Reuther, "*Frustrated Quantum Spins at finite Temperature: Pseudo-Majorana functional RG approach*", Physical Review B **103**, 104431 (2020), arXiv: 2012.14836.

[285] N. Niggemann, J. Reuther, and B. Sbierski, "*Quantitative functional renormalization for three-dimensional quantum Heisenberg models*", 1 (2021), arXiv: 2112.08104.

[286] T. Mizoguchi, L. D. Jaubert, R. Moessner, and M. Udagawa, "*Magnetic clustering, half-moons, and shadow pinch points as signals of a proximate Coulomb phase in frustrated Heisenberg magnets*", Physical Review B **98**, 1 (2018), arXiv: 1806.08534.

[287] O. Benton, L. D. Jaubert, R. R. Singh, J. Oitmaa, and N. Shannon, "*Quantum Spin Ice with Frustrated Transverse Exchange: From a π-Flux Phase to a Nematic Quantum Spin Liquid*", Physical Review Letters **121**, 67201 (2018), arXiv: 1802.09198.

List of acronyms

1D one-dimensional.
2D two-dimensional.
3D three-dimensional.

AF antiferromagnetic.

BCC body-centered cubic.
BZ Brillouin zone.

CS cuboctahedral stack.

DFT density functional theory.
DMRG density matrix renormalization group.
DT double-twist.

FCC face-centered cubic.
FM ferromagnetic.
FRG functional renormalization group.

MMS multiply-modulated spiral.

NN nearest neighbor.
NNN next-to-nearest neighbor.
NNNN next-to-next-to-nearest neighbor.

PFFRG pseudo-fermion functional renormalization group.

QMC quantum Monte-Carlo.

RG renormalization group.
RVB resonating valence bond.

Acknowledgements

Over the years of my Ph.D., there have accumulated a lot of people, that contributed to my studies in one way or another. After six years, the following is deemed to be an incomplete one, but nevertheless, I would like to use this space to mention some people.

Firstly, I have to thank Ronny Thomale for giving me the opportunity to work in his group and introducing me to the wonderful world of pseudo-fermion functional renormalization group (PFFRG), frustrated magnetism, and everything else in physics. He from the beginning allowed me to pick and work on the topics I was interested in, which led to the development of many of the tools used in this thesis. Although we only recently managed to start work on the particular project we initially planned for my thesis, I am positive, that it will give fruitful results in the coming years.

The next person, I am indebted to is my co-supervisor Yasir Iqbal. Especially in the beginning, he was the one introducing me to the intricacies of implementing PFFRG. It is due to him, that I was part of a plethora of fascinating projects and collaborations, only some of which made their way into this thesis. I also enjoyed our off-topic discussions a lot, who else could have taught me, that India is indeed the world's largest exporter of beef?

A special thanks to Dominik Kiese, with whom I had the pleasure to intensively work on the multi-loop implementation and the `PFFRGSolver.jl` code. Our discussions were always helpful and I hope we will have the opportunity to collaborate as closely again in the future.

Two groups outside of Würzburg deserve a special mention: Firstly Jan von Delft and his students Julian Thoenniss and Marc Ritter. Our exchange of ideas, results and even code led to both a thorough benchmarking of our respective codes and to further refinement of our numerics.

The second group is Johannes Reuther in Berlin and his then students Laura Baez and Max Hering. The insights into PFFRG I got from you, especially into two-loop implementations, laid the foundations for the multi-loop code developed in this thesis.

What would my time at the chair have been without my office mates? Beginning with Michi Klett and David Riegler, who have been there from the beginning. Although your old-couple-style discussions were not always easy to handle, it was always fun to discuss with you physics, programming, or anything else happening at the institute or in the world. The same is true for the newest members of our office, Hendrik and Yanik. All the best for your Ph.D. studies!

Thank you also to the rest of our group currently Tobi, Tobi, Tilman, Armando, Yasin, Alex, Alex, and Lavi. Without you and all, who already have left, the work would not have been nearly as enjoyable.

A special nod to Martin Greiter, although we did not always agree on the utilization of resources, I benefitted greatly from his excellent lectures and knowledge of physics.

From the other end of our floor, there has to be specially mentioned Flo Goth, who always was there to help with any technical problems and provided many excellent ideas for numerics, which unfortunately most of the time were dropped due to time constraints.

A special thanks to Janik and, first and foremost, Michi, for relentlessly proofreading this thesis up to the last minute before submission.

Outside of the theory department, there are also a lot of people to thank: all the ones from Fachschaft and its Dunstkreis, who I spent a lot of time with, especially Adi, Lux, Andy, Rafa, Oha, and many more, that I cannot list exhaustively here.

Last, but everything but least, I have to thank my family: My parents and siblings for supporting me through all those years, hardly knowing what I was working on at all. And of course my own little family: Jorik and Leni, for making me happy every day, although they exhaust me from time to time. Also, the one to be, you really were the last push of motivation needed. And, first and foremost: Jacky, my wife, for her love and unconditional support while working on this thesis, when shifting my deadline time after time, and for just being there for me.